Self-organized Interfacial Instabilities of Thin Films: Influence of Charge Leakage, Dielectric Anisotropy, and Confinement

A thesis submitted

in partial fulfillment of the requirements

for the degree of

Doctor of Philosophy

by

Kartick Mondal

Thesis Supervisor

Dr. Dipankar Bandyopadhyay

Department of Chemical Engineering

Indian Institute of Technology Guwahati

January 2014

C E R T I F I C A T E

It is certified that the work contained in this thesis entitled ***"Self-organized Interfacial Instabilities of Thin Films: Influence of Charge Leakage, Dielectric Anisotropy, and Confinement"****, by Mr. Kartick Mondal, has been carried out under my supervision and that this work has not been submitted elsewhere for a degree.*

Thesis Supervisor:

Dr. Dipankar Bandyopadhyay
Assistant Professor
Department of Chemical Engineering
Indian Institute of Technology Guwahati

January 2014

ACKNOWLEDGEMENT

Working for PhD has been an unforgettable experience for me and it would not possible without these people.

First and foremost, I would like to thank my thesis supervisor **Dr. Dipankar Bandyopadhyay** for giving me an opportunity to work in a very interesting area of research. I am very grateful to Dr. Dipankar Bandyopadhyay for his continuous guidance, important advices and stimulating discussions. In spite of his busy schedule, he always happily spends time to analyze problems and gave needed suggestions for the betterment of my work. Some of his remarkable qualities such as, patience during work, his depth of perfection and attractive presentation skills, will always continue to inspire me. The experience of working with him will have far-reaching influence in my future life. I consider it an honor to work under him.

I am thankful to all the Professors of Chemical Engineering Department. I am also thankful to **Prof. Pallab Ghosh** for his course on Colloid and Interface Science. It is a pleasure to acknowledge to **Dr. Tapas Kr. Mandal** for his encouragement and supporting me during this work.

I would like to thank my doctoral committee members, **Dr. Kaustubha Mohanty**, **Dr. Subrata K. Majumder**, Department of Chemical Engineering and **Dr. Padma Kumar Padmanabhan,** Department of Physics, for their valuable suggestion and effort which made my thesis successful.

My sincere thanks to **Dr. A. Ananth Praveen Kumar**, for his co-operative assistance in learning the basics concepts and provided me constant source of encouragement throughout my PhD.

I am particularly grateful to **Mr. Abhiram Hens, Mr. Abir Ghosh, Mr. Prashant Kumar, Mr. Himanshu, Mr. Anjishnu, Ms. Anwesha, Ms. Sunita,** and **Ms. Manisha** for their support in computation.

I am also thankful to present research group members **Ms. Abhijna Das., Mr. Abhinav Sharma, Mr. Amit Kumar Singh, Mr. Bolledu Ravi, Mr. Jayant Borana,**

Mr. Joydip Chaudhuri, Mr. Mitradip Bhattacharjee, Mr. Nilanjan Mandal, Mr. Saptak Rarotra, Ms. Satarupa Dutta, Mr. Seim Timung, Ms. Snigdha Chakraborty, Mr. Sunny Kumar, Mr. Venkatanarayana Prasad S, Mr. Vijeet Tiwari, Mr. Vineet Kumar, and last but not the least **Mr. Viswanath Pasumarthi.**

I would like to thank my fellow research scholars **Mr. Mriganka Sekhar Manna, Mr. D. Vasanth, Mr. Venkata Swamy Nalajala**.

I cannot forget to thank my friends **Mr. Ardhendu Sekhar Giri, Mr. Arya Das, Mr. Arnab Ghosh, Mr. Avijit Ghosh, Mr. Barun Gorain, Mr. Himadri Nayak, Mr. Kaushik Mondal, Mr. Kalyan Manna, Mr. Niladri Set, Mr. Purnendu Kumar Mandal, Mr. Santu Das, Mr. Sayantan Samanta, Mr Somnath Mondal,** for the lovely support in making my stay at IIT Guwahati memorable.

Above all, I would like to thank my **parents, and family members** for their love and support throughout everything, as always.

I dedicate this thesis to *My Family.*

KARTICK MONDAL

SYNOPSIS

Self-organized Interfacial Instabilities of Thin Films: Influence of Charge Leakage, Dielectric Anisotropy, and Confinement

The interfacial instabilities of thin films can lead to useful patterns with the periodicity ranging from a few microns to the nanoscale under the controlled guidance of the intermolecular interactions and external fields. For example, when an ultra-thin (< 100 nm) polymer film annealed to its glass transition temperature, it can spontaneously undergo a Rayleigh-Taylor instability under the destabilizing influence of the van der Waals interaction to form holes, droplets, and bicontinuous structures. Then again, soft polymer surfaces can deform into periodic columns, holes, stripes, and channels when exposed to a destabilizing electrostatic field. From the technological perspective, one of the key challenges associated with the self-organized patterns on a homogeneous surface is the spatial randomness of the patterns, which is resolved by the use of periodic physical and chemical patterns decorated on the bounding surfaces. Further, although the self-organization processes have edge in developing extremely complex structures employing less number of steps, the periodicity of the patterns is still at the higher side as compared to the other competing techniques. The present focus in the thin film research is on the reduction of the pattern periodicity to nanoscale domain because highly compact and ordered patterns find important applications as memory devices, solar panels, sensors, micro/nano fluidic devices, and drug delivery modules, among many others. In this direction, a simple route is to empower the destabilizing force field together with the reduction in the strength of the stabilizing influences.

Herein, we consider four different configurations in which we employ different techniques to engender patterns with smaller periodicity. In the first problem of the thesis, we

consider a pair of immiscible elastic and viscous films confined between a pair of electrodes. The common interface between the soft elastic film and the liquid layers is deformable under the influence of an external electrostatic field. The configuration ensures that the elastic-viscous interface imparts a lesser stabilizing influence as compared to the similar single viscous or elastic films. Further, any of the elastic and the viscous films is made leaky dielectric in order to increase the strength of the destabilizing stress at the elastic-viscous interface. A complete linear stability analysis of the configuration identifies the conditions for the development of the miniaturized patterns. In the second configuration of the thesis, we extend the previous problem to a viscous bilayer with a pair of deformable liquid-liquid and liquid-air interfaces. In this case, we studied the effects of charge leakage at the liquid layers. A complete linear suability analysis alongside long-wave two-dimensional (2-D) and three-dimensional (3-D) nonlinear simulations are performed to uncover the regimes of nanoscale pattern formation and interesting complex structures that can be fabricated through this configurations. For the third configuration discussed in the thesis, we consider the effect of the dielectric anisotropy on the pattern periodicity. For this purpose, the free-surface of a single liquid crystal film bounded by a non-influential fluid like air is allowed to deform under the influence of external electrostatic field. A comprehensive linear stability analysis for this configuration uncovers that indeed the dielectric anisotropy can lead to reduction in pattern spacing. In the last configuration discussed in the thesis, we consider a pair of immiscible liquid films undergoing instability due to the long-range Lifschitz-van der Waals interaction. A comparative study has been performed through molecular dynamic and continuum simulations to uncover salient features of this configuration. The study shows that the extremely thin liquid films with a common deformable interface having weak stabilizing

capillary force can generate nanoscale structures. Further, a long-range order to this nanoscale patterns can be imposed when the surfaces are decorated with physical and chemical patterns. Concisely, the thesis reports some scientific and technologically important avenues for pattern miniaturization through charge leakage, dielectric anisotropy, and confinement in different configurations composed of thin single and bilayer of films.

1. Electro-Capillary Instabilities of Thin Elastic-Viscous Bilayers: The Influence of Charge leakage

A few recent theoretical works suggests that a bilayer with a common deformable interface can lead to miniaturized patterns under the influence of an external electrostatic field because of the weaker capillarity at the interface owing to the reduced interfacial tension. In such a situation, use of leaky dielectric materials as films can enhance the destabilizing stress at the interface and reduce the spacing between the patterns. A very recent experimental work suggest that application of an electric field on an elastic layer confined under a bulk conducting layer could lead to interesting crease or crater or wrinkle type surface morphologies on the elastic film under different regimes of field intensity. The study also infers that a transition of length scale from shorter to longer wavelength regime takes place alongside the morphological transition. However, the theoretical basis for this transition of length scale from longer to shorter wavelength regime is yet to be identified. A number of previous studies show that an elastic film of micron scale thickness (h) can show short-wave features (length scale ~ $3h$) under the exposure of the destabilizing electric field. The length scale shifts towards the longer wavelength regime as the film thickness is progressively reduced and the influence of the stabilizing surface tension force is enhanced. However, the experiments uncover that even a smaller feature

size in the short wave domain is possible when an elastic film deforms under a bulk conducting liquid layer such as salt water.

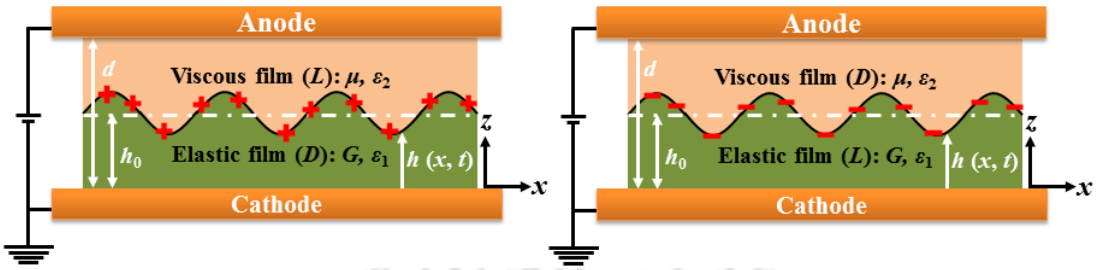

Figure 1: Schematic diagram of an elastic-viscous bilayer exposed to an electric field. The left (right) image shows that the liquid (elastic) layer is leaky dielectric material.

In the thesis, we focus to unveil the electric field induced instabilities of a confined bilayer composed of a soft elastic layer and a viscous layer with a common deformable elastic-viscous interface and confined between two electrodes, as shown schematically in Figure 1. In particular, we consider two different configurations, (i) a purely dielectric elastic layer confined by a leaky dielectric liquid layer, namely, the V^L configuration and (ii) a leaky dielectric elastic layer confined by a purely dielectric liquid layer, namely, the E^L configuration. The formulation considers a general description of the electric field and a comprehensive linear stability analysis unveils the different long to short wavelength regimes of the electric field induced instabilities of both E^L and V^L configurations. The results reported show a transition from long wave to short wave instabilities as the charge leakage in any of the elastic and the liquid layers is enhanced. Further, the results corroborate that these two configurations can indeed lead to nanoscale patterns under the influence of an external electric field. Importantly, the requirement of field intensity is observed to be much smaller than the single layer elastic film configurations. The results obtained for the V^L bilayer closely resembles the experimental observations while the E^L

bilayer opens up another avenue to fabricate miniaturized holes, columns, creases, craters, and wrinkles employing the elastic-viscous bilayers.

2. Electric Field Induced Instabilities of Thin Leaky Bilayers: Pathways to Unique Morphologies and Miniaturization

Electric field induced patterns on the free-surface of a polymer film are essentially the outcome of the dominance of the applied electrostatic stress over the stabilizing capillary force. A simple route for high-density patterns is to empower the destabilizing electric field together with the reduction in the stabilizing influence arising from the surface tension force. Since the applied field strength can be increased to a limit by increasing the applied voltage bias or by reducing the distance between the electrodes, the onus is to find alternative routes. In this direction, recent studies show that the electric field induced instabilities of the thin bilayers or trilayers can make useful contributions. Figure 2 schematically shows a typical bilayer under the influence of an externally applied electric field in which a pair of films is stacked on an electrode and a confining electrode form the top maintains an air gap with the upper layer.

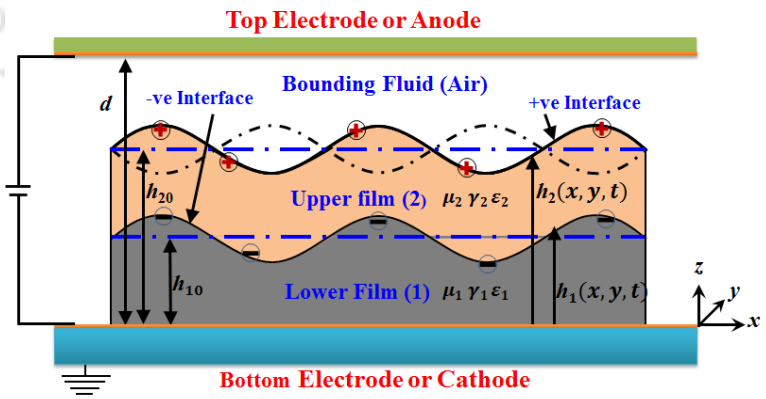

Figure 2: Schematic illustration of a leaky bilayer exposed to an electrostatic field.

The key advantages of the electric field induced instabilities of a bilayer are, (i) the destabilizing filed strength can be internally tuned by changing the thickness, viscosity,

and dielectric permittivity of the films, which provide a larger parameter space to regulate the time and length scales, (ii) can develop unique embedded and encapsulated interfacial patterns, and (iii) a significant reduction in length scale is expected when the instability is dominated by the deformation of the embedded soft interface having weaker stabilizing interfacial tension. Importantly, when the applied field strength is kept constant, the destabilizing field at the interfaces of a bilayer can further be enhanced by the introduction of weakly conducting liquid layers. In such a situation, the larger electrical stress can be attributed to the coupled electrical stresses at the interface due to the accumulation of the free charges together with the induced charge separation. In the thesis work, we compare and contrast the salient features of the electric field induced instabilities of thin bilayers composed of, (i) a pair of purely dielectric films (DD), (ii) a leaky dielectric lower layer below a purely dielectric upper layer (LD), (iii) a leaky dielectric upper layer on a purely dielectric lower layer (DL), and (iv) a pair of leaky dielectric films (LL). We perform a general linear stability analysis (GLSA) of the conservation laws incorporating the full descriptions of the Maxwell stresses. The sensitivity of the length and time scales on the parameters such as the thickness, dielectric permittivity, and viscosity ratios of the films are studied. The GLSA shows that the additional interfacial stresses originating from the free charge accumulation and induced charge separation can together shift the instability in the shorter wavelength regime. Importantly, the GLSA also predicts that the length scales of the instabilities of the leaky bilayers can in fact reduce to the nanoscale regime to open up the possibility of pattern miniaturization. In the regime where the instability has long-wave characteristics, 2-D and 3-D (three-dimensional) nonlinear simulations are performed to uncover the spatiotemporal evolution and the subsequent charge distribution at the interfaces. Unlike the purely dielectric bilayers where the electrical stresses due to

the induced charge separation across the interface dictate the deformation, the nonlinear simulations reveal that the presence of charged interfaces can lead to considerably different interfacial patterns for the leaky dielectric bilayers. For example, when the interfaces are of same (opposite) charge they are expected to deform toward the same (opposite) electrode, which can lead to interesting interfacial patterns when in competition with the stress because of the induced charge separation. Exploiting these features a host of periodic interfacial patterns such as core-shell columns, holes encapsulated by columns, a bundle of columns embedded inside a shell, a collection of holes embedded under columns, and 'caged' columns are obtained, which are rather difficult to assemble using other competing patterning techniques. The results reported can be of importance in the diverse areas of micro/nanotechnology.

3. Electric Field Induced Instabilities of Thin Liquid Crystal Films: Influence of Dielectric Anisotropy

The theoretical understanding of the electric field induced instabilities of LC films is in its infancy owing to the complexity of the physics associated with the topic. A previous theoretical work studied analytically the influence of magnetic field at the NI interface to explain the available experimental results. Later, Tavener *et al.* employed Ericksen-Leslie theoretical model to study the electric field induced convective instabilities of thin nematic LC films. In the thesis, within the similar framework we uncover the free-surface instabilities of a thin nematic LC film, as schematically shown in Figure 3.

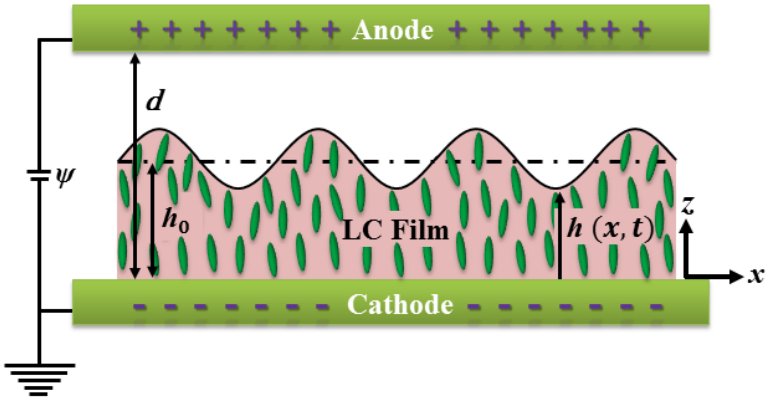

Figure 3: Schematic illustration of a liquid crystal (LC) film exposed to an electric field.

For the sake of simplicity in the mathematical operations we assume that the LC film is isothermal, non-conducting, and deforming under the influence of an external DC field. The configuration under consideration resembles the system employed by Schäffer *et al.* with the exception that the film is composed of a LC material. The coupled Ericksen-Leslie equations with full description of the Maxwell stresses together with appropriate boundary conditions are linearized to estimate the length and time scales of the instabilities. The numerical results are validated against an approximate analytical long-wave analysis in the isotropic as well as in the anisotropic limit. In particular, we focus on solving the director field with different combinations of angular, homeotropic, and planer boundary conditions at the LC-air and LC-substrate interfaces. Following this, we show the salient features of the dielectric anisotropy on the length and the time scales of the instabilities. The study highlights that the free surface of a nematic LC film show a long-wave interfacial instability, which does not require a critical field intensity to set in. Further, the dielectric anisotropy of the film can not only alter the length and the times scale of the instabilities but also can enforce pattern miniaturization. Concisely, the study

makes a useful contribution in studying the field induced instabilities and subsequent pattern formation of thin LC films.

4. Self-organized Pathways to Nano-Patterns Exploiting the Instabilities of Ultrathin Confined Bilayers

The instabilities of ultrathin bilayers can lead to interesting embedded and encapsulated patterns. The structures find important applications in, (i) transistors – when a N-type material is embedded inside or encapsulated by a P-type material, (ii) drug-delivery modules – drugs encapsulated by polymers, and embedded micro/nano channels – for the transport of functional fluids in microchips, among many others. Importantly, when the instability of a dewetting bilayer is dictated by the deformation of the confined liquid-liquid interface, the reduced interfacial tension opens up the possibility of decorating patterns with nanoscale periodicity. Figure 4 schematically shows a typical confined bilayer where a pair of ultrathin liquid films is bounded between two rigid surfaces.

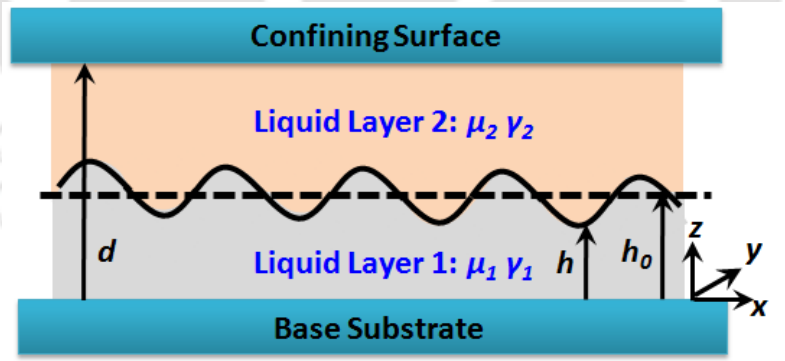

Figure 4: Schematic diagram of a bilayer confined between two rigid substrates.

The major advantage of this configuration over the other single and bilayer arrangements is the presence of a very weak stabilizing interfacial tension at the common deformable liquid-liquid interface, which can significantly reduce the periodicity of the dewetted structures. The periodicity of the patterns can further be reduced by decreasing the thickness of the films because the strength of the destabilizing intermolecular force

increases explosively as the films become thinner. The study reported in the thesis illustrates the instability and spatiotemporal dynamics of an ultrathin-confined bilayer. The major focus here is to explore the different routes to nanostructure formation exploiting the instabilities of a confined bilayer composed of extremely thin (< 5 nm) liquid films. The bilayers are classified based on the high to low surface energies of the confining surfaces and the films. For this purpose, we have chosen benzene (B) and water (W) as liquid films having low and high surface energies confined between, (a) Case I – a pair of high surface energy substrates (e.g. Platinum - Pt), (b) Case II – a pair of low surface energy substrates (e.g. rubber - R), and (c) Case III – a combination of high and low surface energy substrates. The continuum simulations of the configurations clearly show the different spatiotemporal stages of dewetting, such as the hole-formation in the short time, then the hole-growth followed by hole-coalescence stage, and finally the formation of nanostructures at the later phase. The length scales of the patterns from the continuum simulations are compared with a linear stabilities analysis (LSA) and MD simulations. Interestingly, the LSA together with the continuum and MD simulations convey that indeed the increase destabilizing intermolecular interaction due to the thinness of the films together with a weak interfacial tension at the deformable water-benzene interface leads to structures with nanoscale periodicity. In addition, the study shows that the dewetted structures can be guided by the physical and chemical patterns on the substrates to form ordered nanoscale droplets, stripes, and channels, which can be of significant technological importance. The results reported can encourage future experiments on the patterning and fabrication of nanostructures employing ultrathin confined bilayers.

In summary, the thesis focuses on the theoretical understanding of the stability, dynamics, and morphologies of the thin functional films with special properties due to the presence of charge leakage, dielectric anisotropy, and confinement. The research work is expected to improve the basic understandings of the dynamics of the thin films, which can contribute to the development of diverse areas of micro- and nano-technology.

CONTENTS

	List of tables	**xxi**
	List of figures	**xxiii**
	Nomenclature	**xxxix**
1	**Introduction**	**1**
	1.1 Overview	3
	1.2 Major objectives	4
	1.3 References	12
2	**Electro-Capillary Instabilities of Thin Elastic-Viscous Bilayer: The Influence of Charge leakage**	19
	Abstract	21
	2.1 Introduction	22
	2.2 Problem formulation	23
	2.3 General Linear stability analysis	26
	2.3.1 Base-state analysis	26
	2.3.2 Perturbed-state analysis	27
	2.4 Results and discussion	30
	2.5 Summary	41
	2.6 References	42
3	**Electric Field Induced Instabilities of Thin Leaky Bilayers: Pathways to Unique Morphologies and Miniaturization**	**45**
	Abstract	47
	3.1 Introduction	48
	3.2 Problem formulation	49
	3.2.1 Electric Field	50
	3.2.2 Electrohydrodynamic field	51
	3.3 General Linear stability analysis	52
	3.3.1 Base-state analysis	52
	3.3.2 Perturbed-state analysis	53
	3.4 Nonlinear Evolution Equations	56
	3.5 Results and discussion	62

3.5.1 Linear Stability Analysis 63
3.5.2 Nonlinear Simulations 69
3.6 Summary 79
3.7 References 80
4 Electro-Capillary Instabilities of Thin Liquid Crystal Films: Influence of Dielectric Anisotropy 83
Abstract 85
4.1 Introduction 87
4.2 Theoretical model 88
4.3 Dimensionless form 92
4.3.1 Long-wave analysis 95
Linear stability analysis 96
4.4 4.4.1 Base-state analysis 97
4.4.2 Perturbed-state analysis 98
4.5 Numerical analysis 100
4.6 Results and discussion 102
4.7 Summary 116
4.8 References 117
5 Self-organized pathways to nanopatterns exploiting the instabilities of ultrathin confined bilayers 119
Abstract 121
5.1 Introduction 123
5.2 Problem formulation 124
5.2.1 Continuum modeling 125
5.2.1.1 Governing Equations 125
5.2.1.2 Linear stability analysis 127
5.2.1.3 Nonlinear evolution equation 129
5.2.2 Molecular modeling 132
5.3 Results and discussion 135
5.3.1 Linear stability analysis 137
5.3.2 Molecular dynamics and continuum simulations 139
5.3.3 Spatiotemporal scales and morphologies from the continuum 145

and MD approaches

5.3.4 Patterning of dewetted structures 145

5.4 Summary 151

5.5 References 153

6 Conclusion and scope for future work 157

6.1 Conclusions 159

6.1.1 Electro-capillary instabilities of thin elastic-viscous bilayer 159

6.1.2 Electric field induced instabilities of thin leaky bilayers 160

6.1.3 Electro-capillary instabilities of thin liquid crystal films 161

6.1.4 Self-organized nanopatterns from the unstable ultrathin confined bilayers 162

6.2 Future scope of research 164

Appendix 167

LIST OF TABLES

Table No.		Page No.
3.1	Typical values of bilayer parameters	60
4.1	Typical parametric values used in the calculations for the nematic film	103
5.1	The following Hamaker constants, surface energies, and viscosities are used for calculations of the reported different cases.	136
5.2	Length and time scales, morphologies from continuum (CD) and MD approaches for different cases. The lighter shades in the images show smaller height.	145

LIST OF FIGURES

Figure No.		Page No.
1.1	Schematic diagram of an elastic-viscous bilayer exposed to an electric field. The left (right) image shows that the liquid (elastic) layer is leaky dielectric material.	7
1.2	Schematic illustration of a leaky bilayer exposed to an electrostatic field.	8
1.3	Schematic illustration of a liquid crystal (LC) film exposed to an electric field.	10
1.4	Schematic diagram of a bilayer confined between two rigid substrates.	11
2.1	Schematic diagram of elastic-viscous bilayers exposed to an external electric field. The left (right) image shows that the viscous (elastic) layer is leaky dielectric material. The symbols G, μ *and* ε_i are elastic shear modulus of the elastic film, viscosity of the liquid film, and dielectric constant of elastic (i = *1*) and viscous (i = *2*) films. The mean and the local thicknesses of the soft elastic film are denoted by h_0 and h (x, t), respectively, and the distance between the electrodes is d.	22
2.2	Plot (a) shows variation of linear growth coefficient (ω) with wave number (k) for a purely dielectric liquid film deforming under the influence of external electric field. The curves 1 and 2 show the results from the LWLSA and GLSA, respectively, when d = 193 nm, h = 150 nm, ψ = 70 V, μ = 1 Pa s, γ = 0.038 Nm^{-1}, and ε_2 = 2.5. The curves 1 and 2 in the plot (b) show the bifurcation diagrams of a purely dielectric elastic film deforming under the influence of external electric field. The curves 1 and 2 show the results from the LWLSA and GLSA, respectively, when d = 1.5 μm, h = 1 μm, G = 10^5 Pa, γ = 0.02 Nm^{-1}, and ε_1 = 3.	32
2.3	GLSA results show the contours of critical parameters of	33

confined elastic-viscous bilayers in the γ vs. h plane. Plots (a) – (c) show the contours for D configuration, plots (d) – (f) show the contours for V^L configuration, and plots (g) – (i) for E^L configuration. The plots (a), (d), and (g) show the contours of E_c , plots (b), (e), and (h) show the contours of λ_c , and plots (c), (f), and (i) show the contours of λ_c/h. The other essential parameters for plots are, d = 30 μm, ε_1 = 3, and ε_2 = 5.

2.4 GLSA results show the contours of critical parameters of confined elastic-viscous bilayers in the G vs. h plane. Plots (a) – (c) show the contours for D configuration, plots (d) – (f) show the contours for V^L configuration, and plots (g) – (i) for E^L configuration. The plots (a), (d), and (g) show the contours of E_c, plots (b), (e), and (h) show the contours of λ_c , and plots (c), (f), and (i) show the contours of λ_c/h. The other essential parameters for plots are, d = 30 μm, ε_1 = 3, and ε_2 = 5. 36

2.5 GLSA results for the elastic-viscous confined bilayers in presence of external electric field. The plots (a) and (c) show the influence of applied voltage (ψ) and elastic film thickness (h), respectively, on dominant growth coefficient (ω_m). The plots (b) and (d) show the variation corresponding dominant wave length (λ_m) and normalized dominant wave length (λ_m/h_0), respectively with ψ and h, respectively. The solid lines, evenly broken lines, and unevenly broken lines indicate D, V^L, and E^L confined elastic-viscous bilayers. In plots (a) – (d), the curves with darker and lighter shades represent $\varepsilon_1(5.0) > \varepsilon_2(3.0)$ and $\varepsilon_1(3.0) > \varepsilon_2(5.0)$, respectively. For plots (a) – (b) h = 1.0 μm, d = 1.5 μm and for plots (c) – (d) ψ = 400 V, d = 2.0 μm. The other necessary parameters for the plots (a) – (d) are G = 10^3 Pa., γ = 0.001 N m^{-1}, μ = 100 Pa s, and s_i = 1.0 × 10^{-11} S m^{-1}. 37

2.6 GLSA results for the elastic-viscous confined bilayers in presence of external electric field. The plots (a) and (b) show 39

	the influence of $\varepsilon_r = \varepsilon_2 / \varepsilon_1$ on ω_m and λ_m, respectively. The solid lines, evenly broken lines and dashed-dotted lines indicate *D*, V^L, and E^L confined elastic-viscous bilayers. In plots (a) – (b), curves with darker (lighter) shades represent the results when ε_2 (= 3.0) [ε_1 (=3.0)] is constant and ε_1 (ε_2) is varied to get ε_r. The other parameters for the plots are, G = 10^4 Pa., γ = 0.001 N m^{-1}, μ = 100. Pa. s., h = 1.0 μm, d = 1.5 μm, ψ = 300 V, and s_i =1.0 × 10^{-11} S m^{-1}.	
2.7	LSA results for the elastic-viscous confined bilayers in presence of external electric field. The plots (a) – (c) [(d) – (f)] show the variation of $E_c / \sqrt{G/\varepsilon_1\varepsilon_0}$ (λ_c / h_0) with γ / Gh_0 by varying *G*, h_0 and γ, respectively. The square symbols in each plot are experimental results in previous study. The solid and evenly broken lines in the plots (a) – (f), represent LSA results for V^L configuration using LWP and GP, respectively. The parameters used for the plots are, G = 10 Pa – 10^6 Pa, h_0 = 0.1 μm – 100 μm, γ = 0.001 N m^{-1} – 0.05 N m^{-1}, μ = 0.001 Pa s, h_s = 125 μm, d = 250 μm, ε_s = 3.5, ε_1 = 2.65, ε_2 = 80 and σ_2 = 1.0 × 10^{-11} S m^{-1}.	40
3.1	A schematic diagram of a leaky bilayer under the influence of an external electric field. The mean and the local thicknesses of the lower layer are denoted by h_{10} and $h_1(x,t)$, respectively, and the same for the composite layers are denoted by h_{20} and $h_2(x,t)$, respectively. The symbols γ_i, μ_i, and ε_i denote the surface energy, viscosity, and dielectric permittivity of the lower (i = 1) and upper (i = 2) layers, respectively. The distance between the electrodes is d. The positive and negative signs signify the free charges at the interface.	49
3.2	The lines with darker (lighter) shade show the results from the GLSA (LWLSA). The plots (a) and (d) show the variation of	59

dominant linear growth coefficient (ω_m) with the thickness ratio of the films ($\beta = h_{30} / h_{10}$) and the applied voltage (ψ). Plots (b) and (e) show the variation of dominant wavelength (λ_m) with β and ψ. Plots (c) and (f) show the variation of normalized dominant wavelength (λ_m / h_{20}) with β and ψ. The β is obtained by fixing h_{20} (= 0.5 μm) and then changing h_{10} or h_{30}. The notation ε_{12} represents $\varepsilon_1(3.0) > \varepsilon_2(2.0)$ and ε_{21} represents $\varepsilon_1(3.0) < \varepsilon_2(2.0)$. The other necessary parameters are shown in the SET I of Table 3.1.

3.3 The lines with darker (lighter) shade show the results from the GLSA (LWLSA). The solid, evenly broken, dash-dot and dash-dot-dot lines indicate bilayers with, dielectric films (DD), lower layer leaky-upper layer dielectric (LD), lower layer dielectric-upper layer leaky (DL) and both layer leaky (LL), respectively. The plots (a), (b), and (c) show the variations of ω_m , λ_m and λ_m / h_{20}, respectively, with β when $\varepsilon_1(3.0) > \varepsilon_2(2.0)$. The plots (d), (e), and (f) show the variations of ω_m , λ_m and λ_m / h_{20}, respectively, with β when $\varepsilon_2(3.0) > \varepsilon_1(2.0)$. The β is obtained by fixing h_{20} (= 0.5 μm) and then changing either h_{10} or h_{30}. The other necessary parameters are shown in the SET I of Table 3.1. 63

3.4 GLSA results showing the influence of electric field potential (ψ). The solid, evenly broken, dash-dot and dash-dot-dot lines indicate the DD, LD, DL, and LL bilayers, respectively. The plots (a), (b) and (c) show the variations of ω_m , λ_m, and λ_m / h_{20} respectively, with ψ when $\varepsilon_1(3.0) > \varepsilon_2(2.0)$. The plots (d), (e) and (f) show the variations of ω_m , λ_m, and λ_m / h_{20}, respectively, with ψ when $\varepsilon_2(3.0) > \varepsilon_1(2.0)$. The other necessary parameters 65

are shown in the SET I of Table 4.1.

3.5 GLSA results showing the influence of $\varepsilon_r = \varepsilon_2 / \varepsilon_1$. The solid, evenly broken, dash-dot and dash-dot-dot lines indicate the DD, LD, DL, and LL bilayers, respectively. The plots (a), (b) and (c) show the variations of ω_m , λ_m, and λ_m / h_{20}, respectively, with ε_r when ε_1(=5.5) constant . The plots (d), (e) and (f) show the variations of ω_m , λ_m, and λ_m / h_{20}, respectively, with ε_r when $\varepsilon_2 (= 5.5)$ constant. The other necessary parameters are shown in the SET II of Table 3.1. 66

3.6 GLSA results showing the influence of $\mu_r = \mu_2 / \mu_1$ and $\sigma_r = \sigma_2 / \sigma_1$. For the plots (a) – (f), the solid, evenly broken, dash-dot and dash-dot-dot lines indicate the DD, LD, DL, and LL bilayers, respectively. The plots (a), (b), and (c) show the variations of ω_m, λ_m, and λ_m / h_{20}, respectively, with μ_r when $\varepsilon_1(5.5) > \varepsilon_2(3.0)$. The plots (d), (e), and (f) show the variations of ω_m , λ_m, and λ_m / h_{20}, respectively, with μ_r when $\varepsilon_2(5.5) > \varepsilon_1(3.0)$. For the plots (g) – (i), the solid (broken) line represent σ_1 (σ_2) is fixed at 10^{-11} S/m. The plots (g), (h), and (i) show the variations of ω_m, λ_m and λ_m / h_{20} with conductivity ratio (σ_r) for the LL bilayer. In the other plots, the conductivity of the films is fixed to 10^{-11} S/m. The other necessary parameters used for all plots are shown in SET II of Table 4.1. 68

3.7 2-D spatiotemporal evolution of bilayers over a 3Λ domain when d = 0.5 μm and ε_1 (3.0) > ε_2 (2.0). Plots (a) and (b) correspond to a DD bilayer, plots (c) and (d) correspond to a LD bilayer, plots (e) and (f) correspond to a DL bilayer, and plots (g) and (h) correspond to a LL bilayer. The curves 1 – 3 in the plots (a), (c), (e), and (g) indicate the evolution of H_1 and H_2 whereas the same in the plots (b), (d), (f), and (h) show the 70

evolution of Q_1 and Q_2. The curves 1 – 3 in the plots (a) and (b) correspond to T = 6.6 × 10^4, 7.7 × 10^4, and 9.7 × 10^4; in the plots (c) and (d) correspond to T = 6.8 × 10^3, 10.5 × 10^3, and 10.7 × 10^3; in the plots (e) and (f) correspond to T = 1.1 × 10^4, 1.4 × 10^4, and 1.1 × 10^6; and in the plots (g) and (h) correspond to T = 913, 954, and 1095. The other necessary parameters are shown in the SET I of Table 3.1.

3.8 2-D spatiotemporal evolution of bilayers over a 3Λ domain when d = 0.5 μm and ε_1 (2.0) < ε_2 (3.0). Plots (a) and (b) correspond to a DD bilayer, plots (c) and (d) correspond to a LD bilayer, plots (e) and (f) correspond to a DL bilayer and plots (g) and (h) correspond to a LL bilayer. The curves 1 – 3 in the plots (a), (c), (e), and (g) indicate the evolution of H_1 and H_2 whereas the same in the plots (b), (d), (f), and (h) show the evolution of Q_1 and Q_2. The curves 1 – 3 in the plots (a) and (b) correspond to T = 7.1 × 10^4, 8.4 × 10^4, and 9.6 × 10^4; in the plots (c) and (d) correspond to T = 4.0 × 10^3, 4.6 × 10^3, and 5.3 × 10^3; in the plots (e) and (f) correspond to T = 0.7 × 10^4, 0.8 × 10^4, and 4.2 × 10^5; and in the plots (g) and (h) correspond to T = 862, 954, and 1084. The other necessary parameters are shown in the SET I of Table 3.1. 72

3.9 Final morphologies from the 3-D simulations over a 3Λ × 3Λ domain when d = 0.5 μm. The columns (a) and (b) correspond to ε_1(3.0) > ε_2 (2.0) [(c) and (d) correspond to ε_1(2.0) < ε_2 (3.0)]. Rows (I) and (II) show DD bilayers, rows (III) and (IV) show LD bilayers, and rows (V) and (VI) show LL bilayers. Rows (I), (III), and (V) show the top view [(II), (IV), and (VI) show 3-D surface profiles]. Images (Ia), (Ib), (IIa), and (IIb) correspond to T = 8.3 × 10^4; images (Ic), (Id), (IIc), and (IId) correspond to T = 7.5 × 10^4; images (IIIa), (IIIb), (IVa), and (IVb) correspond to T = 9.3 × 10^3; images (IIIc), (IIId), (IVc), and (IVd) correspond to T = 4.3 × 10^3; images (Va), (Vb), 74

(V1a), and (V1b) correspond to $T = 10^3$; images (Vc), (Vd), (VIc), and (VId) correspond to $T = 10^3$. The other necessary parameters are shown in the SET I of Table 3.1.

3.10 2-D spatiotemporal evolution of bilayers over a 3Λ domain when $d = 0.3$ μm and $h_{20} = 0.26$ μm for (a) – (d) [$h_{20} = 0.25$ μm for (e) – (h)]. Plots (a), (b), (e) and (f) correspond to ε_1 (3.0) > ε_2 (2.0) [(c), (d), (g) and (h) correspond to ε_1 (2.0) < ε_2 (3.0)]. Plots (a) – (d) correspond to LD bilayers whereas the plots (e) – (h) correspond to DL bilayers. The curves 1 – 3 in the plots (a), (c), (e), and (g) indicate the evolution of H_1 and H_2 whereas the same in the plots (b), (d), (f), and (h) show the evolution of Q_1 and Q_2. The curves 1 – 3 in the plots (a) and (b) correspond to T = 8.5, 13.0, and 14.7; in the plots (c) and (d) correspond to T = 2.2, 5.0, and 6.9; in the plots (e) and (f) T = 4.2, 25.1, and 55.8; and in the plots (g) and (h) correspond to T = 10.0, 15.3, and 36.4. The other necessary parameters are shown in the SET I of Table 3.1. 76

3.11 Final 3-D morphologies over a 3Λ × 3Λ domain when $d = 0.3$ μm. Images in the columns (a) and (b) correspond to ε_1 (2.0) > ε_2 (3.0) [(c) and (d) correspond to ε_1 (2.0) < ε_2 (3.0)]. Rows (I) and (III) show the top view [(II) and (IV) show 3-D surface profiles]. Images (Ia) – (IId) correspond to LD bilayers where columns (a) and (b) correspond to T = 12.4 [columns (c) and (d) correspond to T = 3.8]. Images (IIIa) – (IVd) correspond to DL bilayers where columns (a) and (b) correspond to T = 3.5 [columns (c) and (d) correspond to T = 12.5]. The other necessary parameters are shown in the SET I of Table 4.1. 77

4.1 Schematic diagram of a nematic liquid crystal (LC) film deforming under the influence of an external electric field. The mean and the local thicknesses of the LC film are denoted by h_0 and h (x, t), respectively, and the distance between the electrodes is d. The anode and the film surface are separated by 88

a dielectric material such as air.

4.2 Variation of linear growth coefficient (ω) with wave number (k) from the present analysis. Plot (a) shows a comparison between the LWLSA (lighter shade, curve-1) and GLSA (darker shade-curve-2) when the film is isotropic, d = 193 nm, h = 100 nm, ψ = 70 V, μ = 1 Pa s, and ε = 2.5. Plot (b) shows the results from the LWLSA (lighter shade curve-1) and GLSA (darker shade curve-2) for a nematic film when d = 2 μm, h = 1.0 μm, ψ = 20 V, and ε_a = 0.5. The inset in the plot (b) shows a situation where GLSA and LWLSA varies significantly when h = 0.5 μm. The other necessary parameters for the plot (b) are shown in the Table 4.1. 103

4.3 The GLSA plots show the variations of ω with k for the electric field induced instabilities (ψ = 20 V) of a thin nematic film (h = 1.5 μm). The director fields at NS (z = 0) and NI (z = h) interfaces are in homeotropic alignment (θ_i = 0^o), as schematically shown in the left hand side or the first row. In plot (a) the lines 1–3 represent ε_a = – 0.7, 0, and 5, respectively. The curve 'i' show a comparative ω vs. k plot for a similar isotropic film (ε = 6). Plots (b) – (f) show the influences of the bulk elastic constant (K_f) and the Leslie coefficients (α_i) on the length and time scales. In the plot (b), $K_f, \alpha_4 \neq 0$ and $\alpha_1, \alpha_2, \alpha_3, \alpha_5 = 0$ in which curves 1–3 represent K_f = 3×10^{-12} N, 6 $\times10^{-12}$ N, and 10 $\times10^{-12}$ N, respectively; plot (c) $K_f, \alpha_4, \alpha_1 \neq 0$ and $\alpha_2, \alpha_3, \alpha_5 = 0$ in which curves 1–3 represent α_1 = 0.003 Pa s, 0.007 Pa s, and 0.01 Pa s, respectively; plot (d) $K_f, \alpha_4, \alpha_2 \neq 0$ and $\alpha_1, \alpha_3, \alpha_5 = 0$ in which curves 1–3 represent α_2 = – 0.007 Pa s, – 0.03 Pa s, and – 0.05 Pa s, respectively); plot (e) $K_f, \alpha_4, \alpha_3 \neq 0$ and $\alpha_1, \alpha_2, \alpha_5 = 0$, in 105

which the curves 1–3 represent α_3 = – 0.001 Pa s, – 0.003 Pa s, and – 0.006 Pa s, respectively; and plot (f) $K_f, \alpha_4, \alpha_5 \neq 0$ and $\alpha_1, \alpha_2, \alpha_3 = 0$ in which the curves 1–3 represent α_5 = 0.03 Pa s, 0.05 Pa s, and 0.07 Pa s, respectively. The other necessary parameters for the plots are shown in the table 4.1.

4.4 The GLSA plots show the variations of ω with *k* for the electric field induced instabilities (ψ = 20 V) of a thin nematic film (*h* = 1.5 μm). The director fields at NS (*z* = 0) is in homeotropic alignment (θ_1 = 0°) and at NI (*z* = *h*) interface is in planer alignment (θ_2 = 90°), as schematically shown in the left hand side or the first row. In plot (a) the lines 1–3 represent ε_a = – 0.7, 0, and 5, respectively. The curve '*i*' show a comparative ω vs. *k* plot for a similar isotropic film (ε = 6). In the plot (b), *h* = 0.1 μm , $K_f, \alpha_4 \neq 0$ and $\alpha_1, \alpha_2, \alpha_3, \alpha_5 = 0$, in which the curves 1–3 represent K_f = 3×10^{-12} N, 6×10^{-12} N, and 10×10^{-12} N, respectively; plot (c) $K_f, \alpha_4, \alpha_1 \neq 0$ and $\alpha_2, \alpha_3, \alpha_5 = 0$ in which the curves 1–3 represent α_1 = 0.003 Pa s, 0.007 Pa s, and 0.01 Pa s, respectively; plot (d) $K_f, \alpha_4, \alpha_2 \neq 0$ and $\alpha_1, \alpha_3, \alpha_5 = 0$ in which the curves 1–3 represent α_2 = - 0.007 Pa s, 0.015 Pa s, and 0.02 Pa s, respectively; plot (e) $K_f, \alpha_4, \alpha_3 \neq 0$ and $\alpha_1, \alpha_2, \alpha_5 = 0$ in which the curves 1–3 represent α_3 = - 0.001 Pa s, - 0.003 Pa s, and - 0.006 Pa s, respectively; and plot (f) $K_f, \alpha_4, \alpha_5 \neq 0$ and $\alpha_1, \alpha_2, \alpha_3 = 0$ in which the curves 1–3 represent α_5 = 0.03 Pa s, 0.05 Pa s, and 0.07 Pa s, respectively. The other necessary parameters for the plots are shown in the Table 4.1. 107

4.5 The GLSA results when the director fields at NS (*z* = 0) and NI (*z* = *h*) interfaces are in homeotropic alignment (θ_i = 0°). The applied field strength is ψ = 20 V. Plot (a) shows the variation 109

of θ at the base state along the *z*-axis, as schematically shown in the left hand side or the first row. The plots (b) – (d) show the variations of π_{EF}, ω_m, and λ_m with ε_a. The solid, evenly broken and solid curves represent , h = 1.0 µm, 1.3 µm, and 1.5 µm, respectively. The plots (e) – (g) show the variations in π_{EF}, ω_m, and λ_m with h. The solid, evenly broken, and unevenly broken curves represent ε_a = – 0.7, 0, and 5, respectively. The other necessary parameters for the plots are shown in the Table 4.1.

4.6 The GLSA results when the director fields at NS (z = 0) and NI ($z = h$) interfaces are in planer alignment ($\theta_i = 90^o$). The applied field strength is ψ = 20 V. Plot (a) shows the variation of θ at the base state along the *z*-axis, as schematically shown in the left hand side or the first row. The plots (b) – (d) show the variations in π_{EF}, ω_m, and λ_m with ε_a. The solid, evenly broken and unevenly broken curves represent h = 1.0 µm, 1.3 µm, and 1.5 µm, respectively. The plots (e) – (g) show the variations in π_{EF}, ω_m, and λ_m with h. The solid, evenly broken, and unevenly broken curves represent ε_a = 4, 6, and 8, respectively. The other necessary parameters for the plots are shown in the Table 4.1. 111

4.7 The GLSA results when the director fields at NS (z = 0) is in homeotropic alignment ($\theta_1 = 0^o$) and at NI ($z = h$) interface is in planer alignment ($\theta_2 = 90^o$). The applied field strength is ψ = 20 V. Plots (a) and (b) shows the variation of θ at the base state along the *z*-axis with the change in the ε_a and h, respectively, as schematically shown in the left hand side or the first row. In plot (a) the curve 1 represent ε_a = 0, the evenly broken and unevenly broken curves 2 and 3 of darker shade (lighter shade) represent ε_a = 0.5 and 5 (– 0.1 and – 0.7), respectively. In plot 112

(b) the solid curves 1 and 2 represent ε_a = 0. The evenly broken and unevenly broken curves 3 and 4 of darker shade represent (lighter shade) h = 1 μm, and 1.5 μm, respectively and ε_a = 0, 5 (– 0.7), respectively. The plots (c) – (e) show the variations in π_{EF}, π_{ES}, ω_m, and λ_m with ε_a. The solid, evenly broken and unevenly broken curves represent h = 1.0 μm, 1.3 μm, and 1.5 μm, respectively. In plot (b) the curves with darker shades (lighter shade) show the variation of π_{EF} (π_{ES}) and y-axis to the left (right) contains the range of variation. The plots (f) – (h) show the variations in π_{EF}, π_{ES}, ω_m, and λ_m with h. The solid, evenly broken, and unevenly broken curves represent ε_a = – 0.7, 0, and 5, respectively. The other necessary parameters for the plots are shown in the Table 4.1.

4.8 The GLSA results when the director fields at the NS (z = 0) is in planer alignment (θ_1 = 0°) and at NI (z = h) interface is in homeotropic (θ_2 = 90°). The applied field strength is ψ = 20 V. Plots (a) and (b) shows the variation of θ at the base state along the z-axis with the change in the ε_a and h, respectively, as schematically shown in the left hand side or the first row. In plot (a) the curve 1 represent ε_a = 0, the evenly broken and unevenly broken curves 2 and 3 of darker shade (lighter shade) represent ε_a = 0.5 and 5 (– 0.1 and – 0.7), respectively. In plot (b) the solid curves 1 and 2 represent ε_a = 0. The evenly broken and unevenly broken curves 3 and 4 of darker shade represent (lighter shade) h = 1 μm, and 1.5 μm, respectively and ε_a = 0, 5 (– 0.7), respectively. The plots (c) – (e) show the variations in π_{EF}, π_{ES}, ω_m, and λ_m with ε_a. The solid, evenly broken and unevenly broken curves represent h = 1.0 μm, 1.3 μm, and 1.5 μm, respectively. In plot (b) the curves with darker shades 114

(lighter shade) show the variation of π_{EF} (π_{ES}) and *y*-axis to the left (right) contains the range of variation. The plots (f) – (h) show the variations in π_{EF}, π_{ES}, ω_m, and λ_m with h. The solid, evenly broken, and unevenly broken curves represent ε_a = – 0.7, 0, and 5, respectively. The other necessary parameters for the plots are shown in the Table 4.1.

5.1 Schematic diagram of a bilayer confined between two rigid substrates. 123

5.2 Figure 5.2 The LSA results for the confined bilayers. Plots (a) – (c) show the variations of ω_m, λ_m and $\partial\pi/\partial h$ with *h*. Rows (I) – (III) correspond to cases (I) – (III). Curves 1 – 3 represent a constant d = 1.5 nm, 1.75 nm, and 2.0 nm, respectively. The other parameters required for the plots are shown in Table 5.1. 137

5.3 The simulation results for case I (Pt-B-W-Pt). Images (a) – (d) show the continuum evolution over a 3Λ × 3Λ domain when the benzene (water) film is 0.75 nm (1.0 nm) thick (λ_m = 3.14 nm). Images in the first (second) row show the top view (3D surface profiles) at T = 4.8, 5.2, 5.8, and 6.4, respectively. Images (e) – (h) show the spatiotemporal MD evolution, where the first, second, and third rows show the evolution of the benzene, water, and combined layers, after t = 0, 15, 30, and 45 ps, respectively. In images (a) – (h), the benzene (water) layer is 0.75 nm (1.0 nm) thick. In images (i) – (k), the first row shows the morphologies after 45 ps when the benzene (water) film is 0.75 nm (0.75 nm) thick and the second row shows the same benzene (water) film thickness is 1 nm (0.75 nm). 139

5.4 The results for case II (R-W-B-R). Images (a) – (d) show the continuum evolution over a 3Λ × 3Λ domain (λ_m = 9.13 nm) of a confined bilayer when the benzene and water films are equally thick (0.75 nm). Images in the first (second) row show the top view (3-D surface profiles) at T = 4.5, 4.73, 5.08, and 5.4, 142

respectively. Images (e) – (h) show the continuum simulation when the benzene (water) film is 1.0 nm (0.5 nm) thick over a 3Λ × 3Λ domain (λ_m = 6 nm). Images in the first (second) row show the top view (3-D surface profiles) at T = 13.4, 15.1, 16.3, and 17.6, respectively. Images (i)–(p) show the MD evolution. Images show the evolution of the benzene layers after t = 0 ps, 25 ps, 50 ps, and 100 ps, respectively. In images (i) – (l), the benzene (water) layer is 0.75 nm (0.75 nm) thick and in images (m) – (p), the benzene (water) layer is 1 nm (0.5 nm) thick.

5.5 The simulation results for case III (R-W-B-Pt). Images (a) – (d) show the continuum evolution over a 3Λ × 3Λ domain (λ_m = 4.1 nm) when the benzene and water films are 0.75 nm thick. Images in the first (second) row show the top view (3-D) surface profiles) at T = 0.15, 0.17, 0.201, and 0.23, respectively. Images (e) – (h) show the continuum simulation over a 3Λ × 3Λ domain (λ_m = 4.8 nm) when the benzene (water) film is 1.0 nm (0.5 nm) thick. Images in the first (second) row show the top view (3-D surface profiles) at T = 4.8, 5.2, 5.7, and 6.7, respectively. Images (i) – (p) show the spatiotemporal MD evolution. The first, second, and third rows show the evolution of the benzene, water, and combined layers aftert = 0, 15, 30, and 45 ps, respectively. In images (i) – (l), the benzene (water) layer is 0.75 nm (0.75 nm) thick and in images (m)–(p), the benzene (water) layer is 1 nm (0.5 nm) thick. 144

5.6 Images (a) – (f) are referenced in Table 5.2. Plots (g) – (i) show gray scale vs distance plots obtained from the image analysis of plots (a) – (f). Plot (g) corresponds to images (a) and (b) of case (I), plot (h) corresponds to images (c) and (d) of case (II), and plot (i) corresponds to images (e) and (f) of case (III). The line with darker (lighter) shade corresponds to the continuum (MD) simulations. 145

5.7 The simulation results for a case I (Pt-W-B-Pt) bilayer on 148

physically patterned surfaces. Images (a) – (d) show the continuum evolution of a confined bilayer over $\Lambda \times \Lambda$ domain on cross-patterned surface. Image (a) in the first (second) row shows the top view (3-D profiles) of cross-patterned surface and images (b) – (d) in the first (second) row show the top view (3-D profiles) of the evolving interface at T = 3.3, 12.4, and 28.05, respectively. Images (e) – (h) show the continuum simulation over $\Lambda \times \Lambda$ domain on striped patterned surface. Image (e) in the first (second) row shows the top view (3-D profiles) of striped patterned surface and images (f) – (h) in the first (second) row show the top view (3-D profiles) of the evolving interface at T = 2.03, 5.3, and 37.7, respectively. Images (i) and (j) show the MD morphologies of the benzene layer after 50 ps. In all plots, h = 1.0 nm, d = 2.0 nm, and the defect height is 0.4 nm.

5.8 The continuum simulation results of spatiotemporal evolution of liquid-liquid interface for case I (Pt-W-B-Pt) and case III (Ru-W-B-Pt) bilayers composed of water (d – h = 1 nm) and benzene (h = 2 nm) layers on a striped Pt substrate with varying height of striped. The first (second) row in images (a) – (d) show top view (side view) of striped Pt substrate. Width of the striped in all the cases is 1.50 nm and its height increases from left to right and for case I (Case III) are 0.0 nm, 0.02 nm, 0.1 nm, and 0.2 nm, (0.0 nm, 0.02 nm, 0.1 nm, and 0.3 nm) respectively. Images (e) - (h) show the morphologies after T = 93.8, 31.2, 66.1 and 23.8 respectively and images (i) - (l) show that after T = 69.0, 79.4, 75.2 and 31.1 respectively. Other necessary parameters are $A_1 = -1.2 \times 10^{-19}$, $A_2 = 2.67 \times 10^{-19}$ for Case I and $A_1 = 4.41 \times 10^{-21}$, $A_2 = 2.67 \times 10^{-19}$ for Case III. 149

5.9 The continuum simulation results of spatiotemporal evolution of liquid-liquid interface for case I (Pt-W-B-Pt) and case III (Ru-W-B-Pt) bilayers composed of water (d – h = 1 nm) and benzene (h = 1 nm) layers on a chemically striped Pt substrate. 151

Images (a) – (c) show side view of a chemically patterned substrate with different patterned width (0.0 nm, 0.08 nm and 0.2 nm). Images (d) - (f) show the morphologies after T = 44.1, 37.8, and 44.6, respectively, and images (g) - (i) show that after T = 44.6, 36.0, and 39.8, respectively. The bottom row shows the side view of the respective Pt substrates. Other necessary parameters are $A_1 = -1.2\times10^{-19}$, $A_2 = 2.67 \times 10^{-19}$, and $A_{2C} = 4.0 \times 10^{-19}$ for Case I and $A_1 = 4.41 \times 10^{-21}$, $A_2 = 2.67\times10^{-19}$, and $A_{2C} = 4.0 \times 10^{-19}$ for Case III.

NOMENCLATURE

$\mu\,(\mu_i)$	Viscosity of the liquid (Viscosity of the i^{th} layer)
G	Elastic shear modulus
γ, γ_{21}	Surface tension/Interfacial tension
γ_2	Surface tension
Γ	Dimensionless Surface tension
E_r	Ericksen number
ε_0	Dielectric permittivity of free space
ε_i	Dielectric constant of the i^{th} layer
ψ, ψ_0	Applied voltage between the electrodes
ω, ω_m	Growth-coefficient, Dominant Growth-coefficient
Ω, Ω_m	Dimensionless Growth-coefficient, Dominant Growth-coefficient
λ, λ_m, λ_c	Linear wavelength, Dominant wavelength, Critical wave length
λ, λ_m, λ_c	Wavenumber, Dominant Wavenumber, Critical Wavenumber
h_0	Mean thickness of the Elastic/nematic LC film layer
h_{10}	Mean thickness of the lower layer
h_{20}	Mean thickness of the composite layers in free bilayer system
h_{30}	Mean thickness of the upper layer
h	Local thickness of the Elastic/nematic LC film layer
h_1	Local thickness of the lower layer
h_2	Local thickness of the composite layers in free bilayer system

h_2	Local thickness of the upper layer
d	Distance between the electrodes
H_0	Dimensionless mean thickness of the lower layer
H_1	Dimensionless thickness of the lower layer
H_2	Dimensionless of the composite layers in free bilayer system
H_3	Dimensionless of the upper layer
D	Dimensionless Distance between the electrodes
t	Dimensional time
T	Dimensionless time
x, y, z	Dimensional x-axis, y-axis, z-axis
X, Y, Z	Dimensionless: X-axis, Y-axis, Z-axis
A_1, A_2	Hamaker constant
S_{ijk}	Spreading coefficient

Chapter 1

Introduction

1.1 OVERVIEW

In the present thesis, we consider four different thin film configurations to engender patterns with smaller periodicity. In the **Chapter 2**, we consider a pair of immiscible soft elastic and viscous films confined between a pair of electrodes. The common interface between the soft elastic film and the liquid layer is deformable under the influence of an external electrostatic field. The configuration ensures that the elastic-viscous interface is under a lesser stabilizing influence as compared to the similar single viscous or elastic films. Further, when any of the elastic or viscous film is a leaky dielectric material, the strength of the destabilizing stress is larger at the elastic-viscous interface. The analysis identifies the conditions to develop the sub-micron patterns. In the **Chapter 3**, we consider a viscous bilayer with a pair of deformable liquid-liquid and liquid-air interfaces. In this case, we study the effects of charge leakage at the liquid layers. A linear suability analysis alongside long-wave two-dimensional (2-D) and three-dimensional (3-D) nonlinear simulations uncover the regimes of nanoscale patterns. In the **Chapter 4**, we consider the effect of the dielectric anisotropy on the pattern periodicity. For this purpose, the free-surface of a single liquid crystal film bounded by a non-influential fluid like air is allowed to deform under the influence of external electrostatic field. Linear stability analysis for this configuration uncovers that indeed the dielectric anisotropy can lead to reduction in pattern spacing as compared to the similar isotropic films. In the **Chapter 5**, a pair of immiscible liquid films undergoing instability due to the long-range Lifschitz-van der Waals interaction is considered. A comparative study has been performed through molecular dynamic and continuum simulations to uncover salient features. The study shows that the extremely thin liquid films with a common deformable interface having weak stabilizing capillary force can generate nano-droplets or stripes. A long-range order

to this nanoscale patterns can be imposed when the surfaces are decorated with physical and chemical patterns. Finally, in the **Chapter 6,** we conclude the thesis with important outcomes from this work with the scope of future research.

1.2 MAJOR OBJECTIVES

The interfacial instabilities of thin films can lead to useful patterns with the periodicity ranging from a few microns to the sub-micron scale under the controlled guidance of the intermolecular interactions and external fields. For example, when an ultra-thin (< 100 nm) polymer film is annealed above glass transition temperature, it can spontaneously undergo a Rayleigh-Taylor instability under the destabilizing influence of the van der Waals interaction to form holes, droplets, and bicontinuous structures.[1–12] The soft polymer surfaces can also deform into periodic columns, holes, stripes, and channels when exposed to a destabilizing electrostatic field.[13–24] From the technological perspective, one of the key challenges associated with the self-organized patterns on a homogeneous surface is the spatial randomness of the patterns, which is regulated by the use of periodic physical and chemical patterns decorated on the bounding surfaces.[17,18,22,25–33] Although the self-organization processes can be superior in developing extremely complex structures employing less number of steps, the periodicity of the patterns remained at the higher side, if compared with the other competing techniques such as lithography, ion beam etching, etc. The present focus in the thin film research is to reduce the pattern periodicity to nanoscale domain because highly compact and ordered patterns find important applications as memory devices, solar panels, sensors, micro/nano fluidic devices, and drug delivery modules.[34–41]

The electrohydrodynamic (EHD) free surface instabilities of thin films with micron-scale to sub-micron thicknesses significantly differ from the similar macroscopic configurations because of the absence of the gravitational influence.[42,43] In particular, the thin viscous films are found to show a long-wave character, as the shorter wavelength modes are stabilized by the capillary force while the electric field can only destabilize the remaining longer wavelength modes.[22,44,45] The rheological properties are found to influence the kinetics of these instabilities. For example, the films with frequency dependent elasticity show a faster kinetics of deformation with increase in the relaxation time as compared to the similar viscous films.[46,47] In contrast, the frequency independent elastomer films or the purely elastic Hookean films shows a finite wavenumber character because the elastic stiffness can also stabilize the modes in the long-wave regime[47–52] Therefore, the films with permanent elasticity were unstable only beyond a critical field strength when the destabilizing electric field can overcome the combined influence of the elastic and capillary forces. The electric field induced instabilities are also found to be influenced by the electrical properties of the films. For example, the use of leaky dielectric films in place of dielectric films can reduce the spacing between the patterns because of the additional destabilizing stress originating from the free-charge accumulation at the surface alongside the induced charge separation.[44,53–57] Further, leaky and perfectly dielectric materials are also found to show significantly different length and time scales under the direct (DC) and alternating current (AC) fields.[58,59] Complex embedded, encapsulated, and phase-inverted structures, with reduced pattern periodicity were fabricated when multiple layers employed.[60–70]

Recent theoretical works[51,71–73] show that a bilayer with a common deformable interface could lead to miniaturized patterns under the influence of an external electrostatic field

because of the weaker capillarity at the interface originating from the reduced interfacial tension. In such a situation, use of leaky dielectric materials as films enhance the destabilizing stress at the interface and can reduce the spacing between the patterns.[50,51] More recent experimental works[74,75] suggest that application of an electric field on an elastic layer confined under a bulk conducting layer can lead to interesting crease or crater or wrinkle type surface morphologies on the elastic film under different regimes of field intensity. The study infers that a transition of length scale from shorter to longer wavelength regime can take place alongside the morphological transition. However, the theoretical basis for this transition of length scale from longer to shorter wavelength regime is still to be identified. A number of previous studies show that an elastic film of micron scale thickness (h) can develop short-wave features (length scale ~ $3h$) under the exposure of the destabilizing electric field.[50,52] The length scale shifts towards the longer wavelength regime as the film thickness is progressively reduced and the influence of the stabilizing surface tension force is enhanced.[50,52] However, the experiments[74,75] uncover that even a smaller feature size in the short-wave domain is possible when an elastic film deforms under a conducting salt water layer.

In the thesis, we unveil the electric field induced instabilities of a confined bilayer composed of soft elastic and viscous layers with a common deformable elastic-viscous interface, as shown schematically in the Figure 1.1. In particular, we consider two different configurations, (i) a purely dielectric elastic layer confined by a leaky dielectric liquid layer, namely, the V^L configuration and (ii) a leaky dielectric elastic layer confined by a purely dielectric liquid layer, namely, the E^L configuration. The formulation considers a general description of the electric field and the linear stability analysis unveils

the different long to short wavelength regimes of the electric field induced instabilities of both the E^L and V^L configurations.

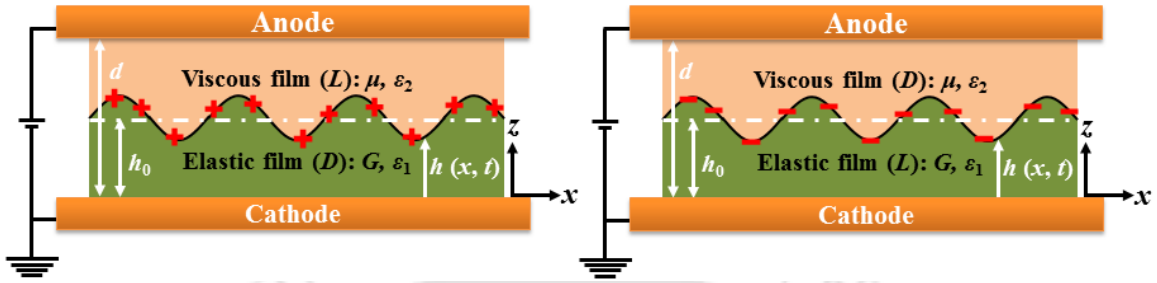

Figure 1.1 Schematic diagram of an elastic-viscous bilayer exposed to an electric field. The left (right) image shows that the liquid (elastic) layer is leaky dielectric material.

The results reported in this work show a transition from long to short wave instabilities as the charge leakage in any of the elastic and the liquid layers is enhanced. Further, the results corroborate that these two configurations can indeed lead to sub-micron patterns under the influence of an external electric field. Importantly, the requirement of field intensity is much smaller to initiate the instabilities in the elastic-viscous bilayers, as compared to the single layer elastic film configurations. The results obtained for the V^L bilayer closely resembles the length scales predicted in the experiments[52,53] while the E^L bilayer opens up another avenue to fabricate sub-micron holes, columns, creases, craters, and wrinkles employing the elastic-viscous bilayers.

As compared to the configurations with elastic layers, the electric field induced patterns on the free-surface of a thin viscous film are essentially the outcome of the dominance of the applied electrostatic stress over the stabilizing surface tension force.[13,14] A simple route for high-density patterns is to empower the destabilizing electric field together with the reduction in the stabilizing influence arising from the surface tension force. Since the applied field strength could be increased to a limit by increasing the applied voltage bias or by reducing the distance between the electrodes, the onus is to find alternative routes.

Recent studies showed that the electric field induced instabilities of the thin bilayers or trilayers could make useful contributions.[60–70,76–78]

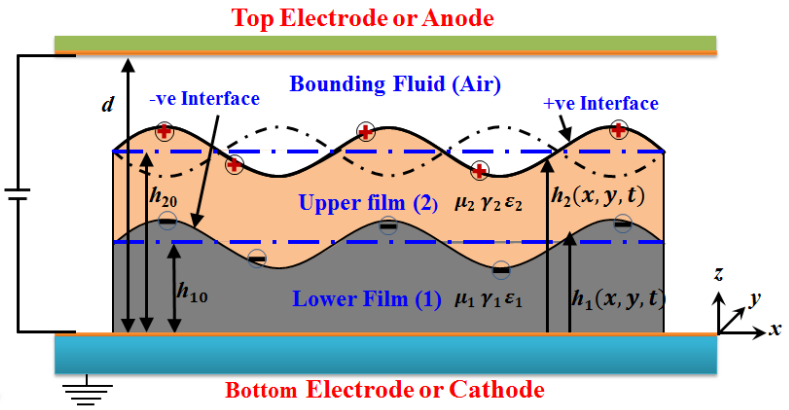

Figure 1.2 Schematic illustration of a leaky bilayer exposed to an electrostatic field.

Figure 1.2 schematically shows a typical bilayer under the influence of an externally applied electric field in which a pair of films is stacked on an electrode and a confining electrode form the top maintains an air gap with the upper layer. The key advantages of the electric field induced instabilities of a bilayer are, (i) the destabilizing filed strength can be internally tuned by changing the thickness, viscosity, and dielectric permittivity of the films, which provide a larger parameter space to regulate the time and length scales, (ii) can develop unique embedded and encapsulated interfacial patterns, and (iii) a significant reduction in length scale is expected when the instability is dominated by the deformation of the embedded soft interface having weaker stabilizing interfacial tension. Importantly, when the applied field strength is kept constant, the destabilizing field at the interfaces of a bilayer can further be enhanced by the introduction of weakly conducting liquid layers, as observed for a few recent works on other configurations.[53,56–59,79] In such a situation, the larger electrical stress can be attributed to the coupled electrical stresses at the interface due to the accumulation of the free charges together with the induced charge separation. The physics associated with the deformation of the soft interfaces under these

coupled electrical stresses is far more complex but exciting as compared to the purely dielectric bilayers where the electrical stress appears purely due to the induced charge separation. The results reported in this work not only highlight the above mentioned issues but also show the interesting interfacial morphologies of the viscous bilayers composed of leaky dielectric films.

The field induced deformations of the orientationally isotropic viscous or elastic or viscoelastic thin films are completely different from the same of the anisotropic liquid crystal (LC) films. De Gennes[80] and Faetti and Palleschi[81] is among the pioneers to show that the surface of a nematic LC film can deform into hill and valley shaped structures when the director field is distorted by an external magnetic field. The instability originated from the competition between destabilizing Ericksen stress engendered by the magnetic field and the stabilizing capillary and gravitational forces. Later, Yokoyama, Kobayashi & Kamei[82] have shown that even an AC electric field acting perpendicular to a nematic-isotropic (NI) interface can also produce periodic hill and valleys beyond critical field strength. Recent experimental studies[83,84] unveil that the NI interface can develop two different types of instabilities under the exposure of an external AC field, (i) the interface immediately shapes into undulated patterns resembling the EHD instabilities reported by Schäffer et al.,[13,14] and (ii) periodic patterns develop only beyond a critical field strength. The length scales of the instabilities are correlated to the interplay between the stabilizing thermal and capillary forces with the destabilizing Maxwell stresses originating from the electric field. However, the theoretical understanding of the electric field induced instabilities of LC films is in its infancy owing to the complexity of the physics associated with the topic. A previous theoretical work[85] studied analytically the influence of magnetic field at the NI interface to explain the available experimental results.[81] Later, Tavener et

al.[86] employed Ericksen-Leslie theoretical model[80,87–93] to study the electric field induced convective instabilities of thin nematic LC films.

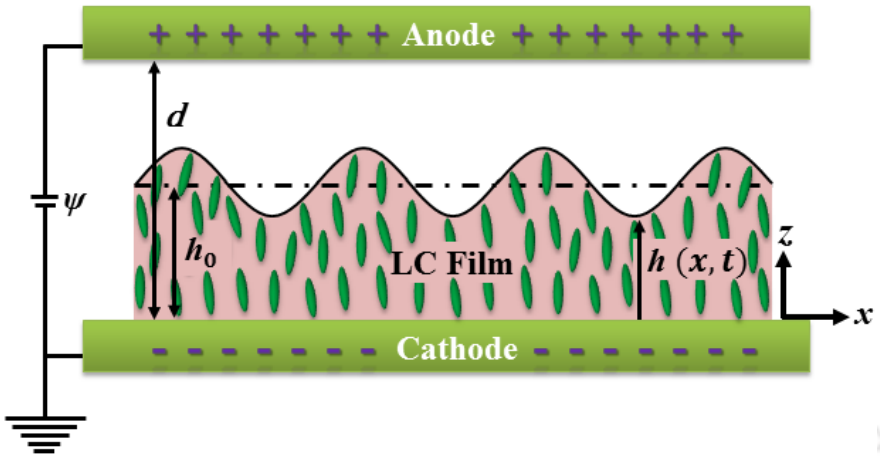

Figure 1.3 Schematic illustration of a nematic liquid crystal (LC) film exposed to an electric field.

In the thesis, within the similar framework we uncover the free-surface instabilities of a thin nematic LC film, as schematically shown in Figure 1.3. The major focus is on understanding the influence of the orientational anisotropy of the molecules on the length and the time scales of the instabilities.

Apart from the influence of the electric field, the intermolecular interactions can also engender instabilities in thin films when the thickness is below 100 nm. The instabilities of ultrathin bilayers can lead to interesting embedded and encapsulated patterns.[94-118] The structures find important applications in, (i) transistors – when a N-type material is embedded inside or encapsulated by a P-type material, (ii) drug-delivery modules – drugs encapsulated by polymers, and embedded micro/nano channels – for the transport of functional fluids in microchips, among many others. Importantly, when the instability of a dewetting bilayer is dictated by the deformation of the confined liquid-liquid interface, the reduced interfacial tension opens up the possibility of decorating patterns with nanoscale

periodicity. Figure 1.4 schematically shows a typical confined bilayer where a pair of ultrathin liquid films is bounded between two rigid surfaces.

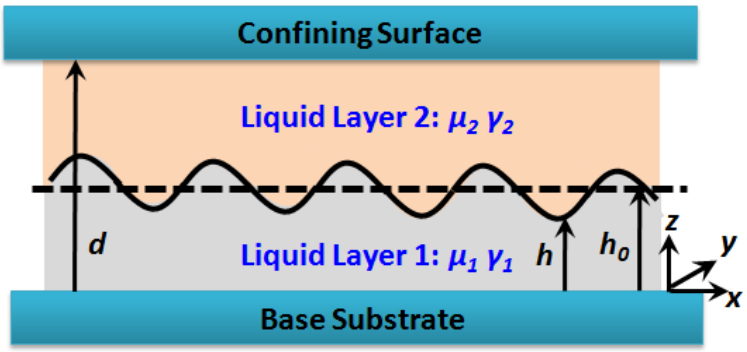

Figure 1.4 Schematic diagram of a bilayer confined between two rigid substrates.

The major advantage of this configuration over the other single and bilayer arrangements is the presence of a very weak stabilizing interfacial tension at the common deformable liquid-liquid interface, which can significantly reduce the periodicity of the dewetted structures. The periodicity of the patterns can further be reduced by decreasing the thickness of the films because the strength of the destabilizing intermolecular force increases explosively as the films become thinner. Motivated by these features, a number of research groups has explored the salient features of the instabilities of free and confined bilayers under the destabilizing influence of electric field, van der Waals forces, and solutal and thermal Marangoni effects.[56,57,60,119–123] However, most of the theoretical studies employ the Derjaguin, Landau, Verwey and Overbeek (DLVO) theory to calculate the contribution from the destabilizing intermolecular force and employ a long-wave continuum approach to study the key features of these instabilities that essentially lead to micron scale patterns. Importantly, with reduction in the thickness of the film (<5 nm) the spacing between the dewetted structures reduces significantly and the predictions from the long-wave approach remain no longer valid. In this regard, some recent studies[124–127] show those molecular dynamics (MD) simulations can quantitatively resolve the spatiotemporal

dynamics of the self-organized instabilities of ultrathin films by considering a more comprehensive intermolecular force field. The study reported in the thesis illustrates the instability and spatiotemporal dynamics of an ultrathin-confined bilayer. The major focus here is to explore the different routes to nanostructure formation exploiting the instabilities of a confined bilayer composed of extremely thin (< 5 nm) liquid films. The length scales of the patterns from the continuum simulations are compared with a linear stabilities analysis (LSA) and MD simulations.

In summary, the thesis focuses on the theoretical understanding of the stability, dynamics, and morphologies of the thin functional films with special properties due to the presence of charge leakage, dielectric anisotropy, and confinement. The outcome of this study is expected to improve the basic understandings of the dynamics of the thin films, which can contribute to the development of diverse areas of micro- and nano-technology.

1.3 REFERENCES

1. E. Ruckenstein and R. K. Jain, J. Chem. Soc., Faraday Trans. **2** 70, 132 (1974).
2. P. G. de Gennes, Rev. Mod. Phys. **57**, 827 (1985).
3. G. Reiter, Phys. Rev. Lett. **68**, 75 (1992).
4. F. Brochard-Wyart, P. Martin and C. Redon, Langmuir **9**, 3682 (1993).
5. A. Sharma, Langmuir **9**, 861 (1993).
6. G. Reiter, Langmuir **9**, 1344 (1993).
7. A. Oron, S. H. Davis and S. G. Bankoff, Rev. Mod. Phys. **69**, 931 (1997).
8. Sharma and R. Khanna, Phys. Rev. Lett. **81**, 3463 (1998).
9. Oron and S. G. Bankoff, J. Colloid Interface Sci. **218**, 152 (1999).
10. U. Thiele, M. G. Velarde and K. Neuffer, Phys. Rev. Lett. **87**, 016104 (2001).
11. G. Narsimhan, J. Colloid Interface Sci. **287**, 624 (2005).
12. M. H. Yang, S. Y. Hou, Y. L. Chang and A. C.-M. Yang, Phys. Rev. Lett. **96**, 066105 (2006).

13. E. Schaffer, T. Thurn-Albrecht, T. P. Russell and U. Steiner, Nature (London) **403**, 874 (2000).
14. E. Schäffer, T. Thurn-Albrecht, T.P.Russell and U. Steiner, Europhys. Lett. **53**, 518 (2001).
15. P. Deshpande, X. Sun and S. Y. Chou, Appl. Phys. Lett., **79**, 1688 (2001).
16. T. Xu, C. J. Hawker and T. P. Russell, Macromolecules **36**, 6178 (2003).
17. S. Harkema and U. Steiner, Adv. Funct. Mater. **15**, 2016 (2005).
18. N. Wu, L. F. Pease and W. B. Russel, Adv. Funct. Mater. **16**, 1992 (2006).
19. N. Wu and W. B. Russel, Nano Today **4**, 180 (2009).
20. S. Herminghaus, Phys. Rev. Lett. **83**, 2359 (1999).
21. L. Wu and S. Y. Chou, J. Non-Newtonian Fluid Mech. **125**, 91 (2005).
22. R. Verma, A. Sharma, K. Kargupta and J. Bhaumik, Langmuir **21**, 3710 (2005).
23. K. John, P. Hänggi and U. Thiele, Soft Matter **4**, 1183 (2008).
24. B. Uma and R. Usha, Phys. Rev. E **82**, 016305 (2010).
25. A. M. Higgins and R. A. L. Jones, Nature **404**, 476 (2000).
26. R. Konnur, K. Kargupta and A. Sharma, Phys. Rev. Lett. **84**, 931 (2000).
27. K. Kargupta and A. Sharma, Phys. Rev. Lett. **86**, 4536 (2001).
28. Simmons and A. Chauhan, J. Colloid Interface Sci. **295**, 472 (2006).
29. S. Saprykin, P. M. J. Trevelyan, R. J. Koopmans and S. Kalliadasis, Phys. Rev. E **75**, 026306 (2007).
30. R. D. Lenz and S. Kumar, J. Fluid Mech. **571**, 33 (2007).
31. G. Reiter, P. Auroy and L. Auvray, Macromolecules **29**, 2150 (1996).
32. A. Sehgal, V. Ferreiro, J. F. Douglas, E. J. Amis and A. Karim, Langmuir **18**, 7041 (2002).
33. R. Mukherjee, D. Bandyopadhyay and A. Sharma, Soft Matter **4**, 2086 (2008).
34. A. Lafuma and D. Quéré, Nat. Mater. **2**, 457 (2003).
35. R. Blossey, Nat. Mater. **2**, 301 (2003).
36. R. Langer and D. A. Tirrell, Nature **428**, 487 (2004).
37. T. M. Squires and S. R. Quake, Rev. Mod. Phys. **77**, 977 (2005).
38. Z. Hu, M. Tian, B. Nysten, and A. M. Jonas, Nat. Mater. **8**, 62 (2009).
39. Z. Nie and E. Kumacheva, Nature Materials **7**, 277 (2008).

40. M. A. C. Stuart, W. T. S. Huck, J. Genzer, M. Müller, C. Ober, M. Stamm, G. B. Sukhorukov, I. Szleifer, V. V. Tsukruk, M. Urban, F. Winnik, S. Zauscher, I. Luzinov, and S. Minko, Nat. Mater. **9**, 101 (2010).
41. J. K. W. Yang, Y. S. Jung, J.-B. Chang, R. A. Mickiewicz, A. Alexander-Katz, C. A. Ross, and K. K. Berggren, Nat. Nanotech. **5**, 256 (2010).
42. J. R. Melcher, and G. I. Taylor, Annu. Rev. Fluid Mech. **1**, 111 (1969).
43. A. Saville, Annu. Rev. Fluid Mech. **29**, 27 (1997).
44. L. F. Pease and W. B. Russel, J. Chem. Phys. **118**, 3790 (2003).
45. N. Wu, L. F. Pease, and W. B. Russel, Langmuir **21**, 12290 (2005).
46. G. Tomar, V. Shankar, A. Sharma and G. Biswas, J. Non-Newtonian Fluid Mech. **143**, 120 (2007).
47. D. Bandyopadhyay, P. D. S. Reddy, and A. Sharma, Phys. Fluids **24**, 074106 (2012).
48. N. Arun, A. Sharma, V. B. Shenoy and K. S. Narayan, Adv. Mater. **18**, 660 (2006).
49. N. Arun, A. Sharma, P. S. G. Pattader, I. Banerjee, H. M. Dixit, and K. S. Narayan, Phys. Rev. Lett. **102**, 254502 (2009).
50. J. Sarkar, A. Sharma, and V. B. Shenoy, Phys. Rev. E **77**, 031604 (2008).
51. D. Bandyopadhyay, A. Sharma, and V. Shankar, J. Chem. Phys. 128, 154909 (2008).
52. J. Sarkar, and A. Sharma, Langmuir **26**, 8464 (2010).
53. L. F. Pease and W. B. Russel, J. Non-Newtonian Fluid Mech. **102**, 233 (2002).
54. L. F. Pease and W. B. Russel, Langmuir **20**, 795 (2004).
55. L. F. Pease, and W. B. Russel, J. Chem. Phys. **125**, 184716 (2006).
56. V. Shankar and A. Sharma, J. Colloid Interface Sci. **274**, 294 (2004).
57. R. V. Craster and O. K. Matar, Phys. Fluids **17**, 032104 (2005).
58. S. A. Roberts and S. Kumar, J. Fluid Mech. 631, 255 (2009).
59. S. A. Roberts, and S. Kumar, Phys. Fluids **22**, 122102 (2010).
60. Z. Lin, T. Kerle, S. M. Baker, D. A. Hoagland, E. Schäffer, U. Steiner and T. P. Russell, J. Chem. Phys. **114**, 2377 (2001).
61. Z. Lin, T. Kerle, T. P. Russell, E. Schäffer and U. Steiner, Macromolecules **35**, 3971 (2002).

62. Z. Lin, T. Kerle, T. P. Russell, E. Schäffer and U. Steiner, Macromolecules **35**, 6255 (2002).

63. M. D. Morariu, N. E. Voicu, E. Schäffer, Z. Lin, T. P. Russell and U. Steiner, Nat. Mater. **2**, 48 (2003).

64. K. A. Leach, S. Gupta, M. D. Dickey, C. G. Willson and T. P. Russell, Chaos **15**, 047506 (2005).

65. M. D. Dickey, S. Gupta, K. A. Leach, E. Collister, C. G. Willson and T. P. Russell, Langmuir **22**, 4315 (2006).

66. D. Bandyopadhyay, A. Sharma, U. Thiele and P. D. S. Reddy, Langmuir **25**, 9108 (2009).

67. P. D. S. Reddy, D. Bandyopadhyay and A. Sharma, J. Phys. Chem. C **114**, 21020 (2010).

68. P. D. S. Reddy, D. Bandyopadhyay, and A. Sharma, J. Phys. Chem. C **116,** 22847 (2012).

69. S. Srivastava, D. Bandyopadhyay and A. Sharma, Langmuir **26**, 10943 (2010).

70. S. Srivastava, P. D. S. Reddy, C. Wang, D. Bandyopadhyay, and A. Sharma, J. Chem. Phys. **132**, 174703 (2010).

71. D. Bandyopadhyay, A. Sharma and V. Shankar, EPL **89**, 36002 (2010).

72. P. Gambhire, and R. M. Thaokar, Eur. Phys. J. E **34**, 84(1) (2011).

73. P. Gambhire, and R. M. Thaokar, Phys. Rev. E **86**, 036301 (2012).

74. Q. Wang, L. Zhang, and X. Zhao, Phys. Rev. Lett. **106**, (2011).

75. Q. Wang, and X. Zhao, Phys. Rev. E. **88**, 042403 (2013).

76. A. Atta, D. G. Crawford, C. R. Koch and S. Bhattacharjee, Langmuir **27**, 12472 (2011).

77. G. Amarandei, P. Beltrame, I. Clancy, C. O'Dwyer, A. Arshak, U. Steiner, D. Corcoran and U. Theile, Soft Matter **8**, 6333 (2012).

78. P. G. Oppenheimer, S. Mahajan and U. Steiner, Adv. Optical Mater. **24**, 175 (2012).

79. M. F. El-Sayed, M. H. M. Moussa, A. A. A. Hassan and N. M. Hafez, ISRN Applied Mathematics **2011**, 1 (2011).

80. P. G. de Gennes, and J. Prost, "The Physics of Liquid Crystals" Oxford University Press Walton Street, (1993).

81. S. Faetti, and V. Palleschi, V. J. Phys. France, **46**, 415 (1985).

82. H. Yokoyama, S. Kobayashi, and H. Kamei, Mol. Cryst. Liq. Cryst. **129,** 109 (1985).
83. P. Oswald, EPL **90**, 16005 (2010).
84. P. Oswald, Eur. Phys. J. E **33**, 69 (2010).
85. V. A. Raghunathan, Phys. Rev. E **51,** 896 (1995).
86. S. J. Tavener, T. Mullin, G. I. Blake, and K. A. Cliffe, Phys. Rev. E **63**, 011708 (2000).
87. C. Frank, Discuss. Faraday Soc. **25**, 19 (1958).
88. J. L. Ericksen, Archive for Rational Mechanics and Analysis **9**, 371 (1962).
89. J. L. Ericksen, Trans. Soc. Rheol. **11**, 5 (1967).
90. M. Leslie, Continuum Mech. Thermodyn. **4**, 167 (1992).
91. S. Chandrasekhar, "Liquid Crystals" Cambridge University Press (1992).
92. T.-S. Lin, L. J. Cummings, A. J. Archer, L. Kondic, and U. Thiele, Phys. Fluids **25**, 082102 (2013).
93. T.-S. Lin, L. Kondic, U. Thiele, and L. J. Cummings, J. Fluid Mech. **729**, 214 (2013).
94. P. Lambooy, K. C. Phelan, O. Haugg and G. Krausch, Phys. Rev. Lett. **76**, 1110 (1996).
95. Q. Pan, K. I. Winey, H. H. Hu and R. J. Composto, Langmuir **13**, 1758 (1997).
96. R. A. Segalman and P. F. Green, Macromolecules **32**, 801 (1999).
97. C. Wang, G. Krausch and M. Geoghegan, Langmuir **17**, 6269 (2001).
98. H. Kang, S.-H. Lee, S. Kim and K. Char, Macromolecules **36**, 8579 (2003).
99. D. Bandyopadhyay, R. Gulabani and A. Sharma, Ind. Eng. Chem. Res. **44**, 1259 (2005).
100. D. Bandyopadhyay and A. Sharma, J. Chem. Phys. **125**, 054711 (2006).
101. J. Léopoldès and P. Damman, Nat. Mater. **5**, 957 (2006).
102. R. Mukherjee, R. Pangule, A. Sharma and G. Tomar, Adv. Funct. Mater. **17**, 2356 (2007).
103. J. P. de Silva, M. Geoghegan, A. M. Higgins, G. Krausch, M.-O. David and G. Reiter, Phys. Rev. Lett. **98**, 267802 (2007).
104. D. Bandyopadhyay, A. Sharma and C. Rastogi, Langmuir **24**, 14048 (2008).

105. R. Paul, U. Karabiyik, M. C. Swift, J. R. Hottle and A. R. Esker, Langmuir **24**, 4676 (2008).
106. L. Xu, D. Bandyopadhyay, A. Sharma and S. W. Joo, Soft Matter **7**, 8056 (2011).
107. L. Xu, D. Bandyopadhyay, T. Shi, L. An, A. Sharma and S. W. Joo, Polymer **52**, 4345 (2011).
108. L. Xu, A. Sharma and S. W. Joo, Macromolecules **44**, 9335 (2011).
109. K. D. Danov, V. N. Paunov, N. Alleborn, H. Raszilliers and F. Durst, Chem. Eng. Sci. **53**, 2809 (1998).
110. K. D. Danov, V. N. Paunov, S. D. Stoyanov, N. Alleborn, H. Raszilliers and F. Durst, Chem. Eng. Sci. **53**, 2823 (1998).
111. V. N. Paunov, K. D. Danov, N. Alleborn, H. Raszilliers and F. Dursts, Chem. Eng. Sci. **53**, 2839 (1998).
112. S. Kumar and O. K. Matar, J. Colloid Interface Sci. **273** 581 (2004).
113. O. K. Matar, V. Gkanis and S. Kumar, J. Colloid Interface Sci. **286**, 319 (2005).
114. A. Pototsky, M. Bestehorn, D. Merkt and U. Thiele, J. Chem. Phys. **122**, 224711 (2005).
115. L. S. Fisher and A. A. Golovin, J. Colloid Interface Sci. **291**, 515 (2005).
116. A. Pototsky, M.Bestehorn, D. Merkt and U. Thiele, Europhys. Lett. **74**, 665 (2006).
117. A. A. Nepomnyashchy and I. Simanovskii, Phys. Rev. Lett. **102**, 164501 (2009).
118. R. D. Lenz and S. Kumar, J. Colloid Interface Sci. **316**, 660 (2007).
119. P. D. S. Reddy, D. Bandyopadhyay, S. W. Joo, A. Sharma and S. Qian, Phys. Rev. E **83**, 036313 (2011).
120. Z. Lin, T. Kerle, S. M. Baker, D. A. Hoagland, E. Sch¨ affer, U. Steiner, and T. P. Russell,J. Chem. Phys. **114**, 2377 (2001).
121. D. Merkt, A. Pototsky, M. Bestehorn, and U. Thiele, Phys. Fluids **17**, 064104 (2005).
122. R. Verma, A. Sharma, I. Banerjee, and K. Kargupta, J. Colloid Interface Sci. **296**, 220 (2006).
123. H. Luo and D. Gersappe, Macromolecules **37**, 5792 (2004).
124. H. Liu, A. Bhattacharya, and A. Chakrabarti, J. Chem. Phys. **109**, 8607 (1998).
125. E. Bertrand, T. D. Blake, and J. D. Coninck, Eur. Phys. J. (Special Topics) **166**, 173 (2009).

126. J. Koplik and J. R. Banavar, Phys. Rev. Lett. 84, 4401 (**2000)**.

127. C.-C. Hwang, J.-Y. Hsieh, K.-H. Chang, and J.-J. Liao, Physica A**256**, 333 (1998).

Chapter 2

Electro-Capillary Instabilities of Thin Elastic-Viscous Bilayer: The Influence of Charge leakage

ABSTRACT

Charge leakage at any of the weakly conducting layer of a thin elastic-viscous bilayer can engender interesting interfacial instabilities when exposed to an external electrostatic field. A general linear stability analysis including the full descriptions of the Maxwell stresses uncovers the key short to long-wave features of the instabilities of the elastic-viscous composite bilayers with purely dielectric films, and a combination of leaky and dielectric films. The study highlights that the presence of a leaky elastic or viscous layer in an elastic-viscous bilayer can impart additional electrostatic stress due to the presence of free charges at the interface, which can significantly reduce the length scales to enforce pattern miniaturization. Unlike the purely dielectric bilayers where the accumulation of induced dipoles due to the dielectric-contrast across the interface dictates the direction of the interfacial deformation, for leaky bilayers the presence of the free charge (positive or negative) can determine the deformation towards or away from the electrodes (anode or cathode). The general linear analysis uncover that a transition from long- to short-wave instabilities take place with progressive increase in the strength of the destabilizing stress, reduction in the capillary forces at the interface, and with increase in the thickness of the leaky layer. The general analysis shown here could reproduce the previously predicted length scales especially with a long-wave potential. Further, the use of a more generic potential in the present work can indeed predict the recently reported experimental length scales of the electric field induced instabilities of elastic viscous bilayers. The results reported can be of importance in the diverse areas of micro/nanotechnology.

The manuscript of this chapter is under preparation

2.1 INTRODUCTION

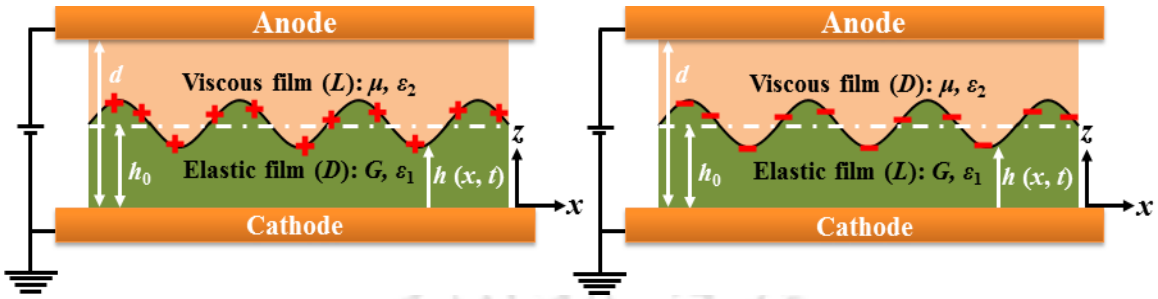

Figure 2.1 Schematic diagram of elastic-viscous bilayers exposed to an external electric field. The left (right) image shows that the viscous (elastic) layer is leaky dielectric material. The symbols *G, μ and* ε_i are elastic shear modulus of the elastic film, viscosity of the liquid film, and dielectric constant of elastic (*i = 1*) and viscous (*i = 2*) films. The mean and the local thicknesses of the soft elastic film are denoted by h_0 and *h* (*x, t*), respectively, and the distance between the electrodes is *d*.

In the present chapter, we focus to unveil the electric field induced instabilities of a confined bilayer composed of a soft elastic layer and a viscous layer with a common deformable elastic-viscous interface. The bilayer is confined between two electrodes, as shown schematically in Figure 2.1 In particular, we consider two different configurations, (i) a purely dielectric elastic layer confined by a leaky dielectric liquid layer, namely, the V^L configuration and (ii) a leaky dielectric elastic layer confined by a purely dielectric liquid layer, namely, the E^L configuration. The formulation considers a general description of the electric field[1-6] and a comprehensive linear stability analysis unveils the different long to short wavelength regimes of the electric field induced instabilities of both E^L and V^L configurations. The results obtained for the V^L bilayer closely resemble the experimental observations from Wang, Zhang & Zhao, Wang & Zhao[7,8] while the E^L bilayer opens up another avenue to fabricate miniaturized holes, columns, creases, craters, and wrinkles employing the elastic-viscous bilayers. Concisely, the study shows the short-wave features of the electric field induced instabilities of the elastic-viscous bilayers, which is not reported by the previous theoretical works. The results reported here can be

of importance in miniaturization of the electric field induced patterns fabricated on the surface of a thin polymer film.

2.2 PROBLEM FORMULATION

A Cartesian two-dimensional (2-D) coordinate system is employed with the origin located at the substrate (z = 0) and the unit base vectors $(\mathbf{e}_x, \mathbf{e}_z)$ are directed to the x- and z-directions, respectively. Figure 2.1 schematically shows the elastic-viscous configuration considered in the present work. The films are confined between a pair of electrodes separated by the distance, d and the thicknesses of the elastic and the liquid films are denoted by h and (d – h), respectively. The characteristic times for the electrical, magnetic, and friction dominated flow fields are, $t_E = \varepsilon_i \varepsilon_0 / \sigma_i$, $t_M = \mu_i \mu_0 \sigma_i l^2$, and $t_P = \rho_i l^2 / \eta_i$, respectively, where l is the characteristic length scale (~ 10^{-4} m). For the leaky dielectric fluids the typical orders of magnitudes for the fluids are, the electrical conductivity σ_i ~10^{-6} - 10^{-9} S m^{-1}, the magnetic permeability $\mu_i \mu_0$ ~ 10^{-6} S m^{-1}, and the electrical permeability $\varepsilon_i \varepsilon_0$ ~ 10^{-11} C^2 N^{-1} m^{-2}. The present phenomenon ensures a parameter space, $t_P >> t_E > t_M$.[6] The dimensionless number $\Lambda = \varepsilon \varepsilon_0 E_0 / e l \sqrt{n_0 K} << 1$ for the elastic-viscous configuration also ensures that the fluids are electrically neutral in which the typical field intensity (E_0), charge of an electron (e), and the ionic concentration ($\sqrt{n_0 K}$) can be considered as, ~10^6 V m^{-1}, ~10^{-19} C and ~10^{20}, respectively.[6] Thus, we can assume that the time scale for the magnetic phenomena is much smaller than the same for electrostatic processes and electro-neutrality prevails within the bulk.[6] The resulting governing equations for the electric field, $\mathbf{E}_i$, in the elastic and viscous layers (i = *1* and *2*) are,

$$\nabla \cdot \mathbf{E}_i = 0,\ \nabla \times \mathbf{E}_i = 0. \tag{2.2.1}$$

The irrotational electric field can be expressed in terms of the potential function as, $\mathbf{E}_i = -\nabla \psi_i$, which leads to the following Laplace equation for the ith layer when replaced in Eq. (2.2.1),

$$\nabla^2 \psi_i = 0. \tag{2.2.2}$$

The boundary conditions enforced for the electric field are, (i) at the cathode (z = 0), $\psi_1 = 0$ and anode (z = 0), $\psi_2 = \psi$; (ii) at the elastic-viscous interface ($z = h$), the normal [$\varepsilon_0 \varepsilon_2 \left(\mathbf{E}_2 \cdot \mathbf{n}\right) - \varepsilon_0 \varepsilon_1 \left(\mathbf{E}_1 \cdot \mathbf{n}\right) = q$] and tangential [$\mathbf{E}_1 \cdot \mathbf{t} = \mathbf{E}_2 \cdot \mathbf{t}$] component balances. The symbol ε_0 represents the dielectric permittivity of free space, 8.854 × 10^{-12} C^2/N m^2.

The films are composed of a purely Newtonian liquid (i = 2) with constant viscosity (μ) and a purely Hookean elastic solid with constant elastic shear modulus (G). The dielectric permittivity (ε_i) and the electrical conductivity s_i of the films are also assumed to be constant. The conservation of mass and momentum for the incompressible elastic and liquid films are expressed by,

$$-\nabla p_1 + \nabla \cdot \left(\boldsymbol{\tau}_1 + \mathbf{M}_1\right) = 0,\ \nabla \cdot \mathbf{u}_1 = 0. \tag{2.2.3}$$

$$-\nabla p_2 + \nabla \cdot \left(\boldsymbol{\sigma}_2 + \mathbf{M}_2\right) = 0,\ \nabla \cdot \mathbf{v}_2 = 0. \tag{2.2.4}$$

The inertial terms are neglected owing to the thinness of the films. The constitutive relations for the Hookean-elastic solid, $\boldsymbol{\tau}_1 = G\left(\nabla \mathbf{u}_1 + \nabla \mathbf{u}_1^{\,T}\right)$, is expressed in terms of displacement vector, $\mathbf{u}_1 = \left(u_1^{(x)},\ u_1^{(z)}\right)$ in which the bracketed superscripts denote the x- and the z-components. The Newtonian behavior of the liquid film, $\boldsymbol{\sigma}_2 = \mu_2\left(\nabla \mathbf{v}_2 + \nabla \mathbf{v}_2^{\,T}\right)$, is expressed in terms of velocity vector, $\mathbf{v}_2 = \left(v_2^{(x)},\ v_2^{(z)}\right)$. The Maxwell stresses from the

external electric field, $\mathbf{M}_i = \varepsilon_0 \varepsilon_i \left[\mathbf{E}_i \otimes \mathbf{E}_i - 0.5 \left(\mathbf{E}_i \cdot \mathbf{E}_i \right) \mathbf{I} \right]$, are also integrated to the equations of motion to describe the EHD field. The irrotational and divergence free electric field ensure the electro-neutrality at the bulk ($\nabla \cdot \mathbf{M}_i = 0$).

No slip, impermeability, and constant potential boundary conditions are enforced at the cathode ($z = 0$) and anode ($z = d$),

$$\mathbf{u}_1 = 0, \tag{2.2.5}$$

$$\mathbf{v}_2 = 0. \tag{2.2.6}$$

At the deformable elastic-viscous interface ($z = h$), continuity of x- and z- components of velocities, normal and tangential stress balances, and the kinematic conditions for the height (h) and free charge density (q) are enforced as,

$$\dot{\mathbf{u}}_1 = \mathbf{v}_2, \tag{2.2.7}$$

$$-p_2 + \mathbf{n} \cdot \left(\boldsymbol{\sigma}_2 + \mathbf{M}_2 \right) \cdot \mathbf{n} + p_1 - \mathbf{n} \cdot \left(\boldsymbol{\tau}_1 + \mathbf{M}_1 \right) \cdot \mathbf{n} = \gamma \kappa, \tag{2.2.8}$$

$$\mathbf{n} \cdot \boldsymbol{\tau}_1 \cdot \mathbf{t} - \mathbf{n} \cdot \boldsymbol{\sigma}_2 \cdot \mathbf{t} - q \mathbf{E}_2 = 0, \tag{2.2.9}$$

$$\dot{h} + \left(\dot{\mathbf{u}}_1 \cdot \nabla_s \right) h = \dot{\mathbf{u}}_1 \cdot \mathbf{n}, \tag{2.2.10}$$

$$\dot{q} + \dot{\mathbf{u}}_1 \cdot \nabla_s q - q \mathbf{n} \cdot \left(\mathbf{n} \cdot \nabla \right) \mathbf{u} = s_1 \mathbf{E}_1 \cdot \mathbf{n} - s_2 \mathbf{E}_2 \cdot \mathbf{n}. \tag{2.2.11}$$

The curvature of the interface is defined as, $\kappa = \nabla_s \cdot \mathbf{n}$. The symbols ∇ and ∇_s are the gradient operators. The symbol ε_0 represents the dielectric permittivity of free-space, 8.854×10^{-12} C^2/Nm^2. The unit outward normal ($\mathbf{n}$) and tangent ($\mathbf{t}$) vectors at the elastic-viscous are, $\left(-h_x / \sqrt{1+h_x^2}, 1/\sqrt{1+h_x^2} \right)$ and $\left(1/\sqrt{1+h_x^2}, h_x / \sqrt{1+h_x^2} \right)$.

2.3 GENERAL LINEAR STABILITY ANALYSIS

The general linear stability analysis (GLSA) is performed based on the assumptions that the kinematics of deformation is small.

2.3.1 Base-state analysis

A quiescent base-state is considered with stationary liquid, $v_{20}^{(x)} = v_{20}^{(z)} = 0$, and elastic, $u_{10}^{(x)} = u_{10}^{(z)} = 0$, layers with constant film thicknesses, (d - h_0) and h_0, respectively. The bilayer at base-state is under a continuous exposure of the electric field potential ψ_i with a constant interfacial charge concentration, q_0. The resulting expression for the base-state potential is, $\psi_{i0} = F_{1i} z + F_{2i}$, from the governing equation, $\psi_{i0zz} = 0$ in which the subscript z denotes differentiation. The following base-state boundary conditions are employed to evaluate the constants, F_{ji} s (i = *1* and *2*; j = *1* and *2*): (i) at the cathode (z = 0), ψ_{10} = 0 and at anode (z = d), $\psi_{20} = \psi$; at the elastic-viscous interface (z = h_0), the balances of the normal ($\varepsilon_0 \varepsilon_1 \psi_{10z} - \varepsilon_0 \varepsilon_2 \psi_{20z} = q_0$) and the tangential ($\psi_{10} = \psi_{20}$) components of the electric field.

The base-state z-momentum balance for the EHD field leads to the expression, $p_{i0z} = 0$, for the for each layer i = *1* and *2*, which has a solution, $p_{i0} = D_i$, where D_i s (i = *1* and *2*) are the constants. The base-state normal stress balance, $p_{10} - p_{20} + 0.5\left(\varepsilon_0 \varepsilon_2 \psi_{20z} - \varepsilon_0 \varepsilon_1 \psi_{10z}\right)$, at the elastic-viscous (z = h_0) interface is enforced to evaluate these constants. In the process we obtain the base-state pressure for the i^{th} layer, p_{i0}. The kinematic equation for the conservation of charge density at the base-state, $s_2 \psi_{20z}\big|_h - s_1 \psi_{10z}\big|_h = 0$, yields the base-state free charge density at the interface for the E^L

bilayer, $q_0 = -\varepsilon_0\varepsilon_2\psi/(d-h_0)$, and for the V^L bilayer, $q_0 = \varepsilon_0\varepsilon_1\psi/h_0$. Clearly, the expressions suggest that the increase in the thickness of leaky layer and dielectric permittivity of the dielectric layer (either elastic or viscous) and applied field intensity leads to a larger base-state charge density. This results in a larger electrical stress at the elastic-viscous interface for both the E^L and V^L configurations.

2.3.2 Perturbed-state analysis

The governing equations and the boundary conditions in the Eqs. (2.2.2) – (2.2.11) are linearized by employing the normal linear modes, $\mathbf{u}_1 = \tilde{\mathbf{u}}_1 e^{\omega t + \mathbf{i}kx}$, $\mathbf{v}_2 = \tilde{\mathbf{v}}_2 e^{\omega t + \mathbf{i}kx}$, $\psi_i = \psi_{i0} + \tilde{\psi}_i e^{\omega t + \mathbf{i}kx}$, $p_i = p_{i0} + \tilde{p}_i e^{\omega t + \mathbf{i}kx}$, $h = h_0 + \tilde{h} e^{\omega t + \mathbf{i}kx}$ and $q = q_0 + \tilde{q} e^{\omega t + \mathbf{i}kx}$, where the symbols ω and k represent the linear growth coefficient and the wave number of the disturbance, respectively, where the tilde symbols denote the perturbed variables. The linearized perturbed electric field Eq. (2.2.2) is,

$$\tilde{\psi}_{izz} - k^2\tilde{\psi}_i = 0. \tag{2.3.1}$$

The general solution of the Eq. (2.3.1) is,

$$\tilde{\psi}_i = C_{1i}\, e^{kz} + C_{2i}\, e^{-kz}. \tag{2.3.2}$$

Here the coefficients C_{ji} (i = *1* and *2*; j = *1* and *2*) are constants. The constants C_{ji} s can be evaluated by employing the linearized perturbed boundary conditions: (i) at the cathode (z = 0), $\tilde{\psi}_1 = 0$ and at the anode (z = d), $\tilde{\psi}_2 = 0$; (ii) at the elastic-liquid interface (z = h_0), the normal [$\varepsilon_0\varepsilon_1\tilde{\psi}_{1z} - \varepsilon_0\varepsilon_2\tilde{\psi}_{2z} = \tilde{q}$] and the tangential [$(\tilde{\psi}_1 - \tilde{\psi}_2) + \tilde{h}(\psi_{10z} - \psi_{20z}) = 0$] component balances.

The linearized forms of the governing Eqs. (2.2.3) are,

$$-\mathbf{i}k\tilde{p}_1 + G\left(\frac{d^2\tilde{u}_1^{(x)}}{dz^2} - k^2\tilde{u}_1^{(x)}\right) = 0, \tag{2.3.3}$$

$$-\frac{d\tilde{p}_1}{dz} + G\left(\frac{d^2\tilde{u}_1^{(z)}}{dz^2} - k^2\tilde{u}_1^{(z)}\right) = 0, \tag{2.3.4}$$

$$\mathbf{i}k\tilde{u}_1^{(x)} + \frac{d\tilde{u}_1^{(x)}}{dz} = 0. \tag{2.3.5}$$

The linearized forms of the governing Eqs. (2.2.4) are,

$$-\mathbf{i}k\tilde{p}_2 + \mu\left(\frac{d^2\tilde{v}^{(x)}}{dz^2} - k^2\tilde{v}^{(x)}\right) = 0, \tag{2.3.6}$$

$$-\frac{d\tilde{p}_2}{dz} + \mu\left(\frac{d^2\tilde{v}^{(z)}}{dz^2} - k^2\tilde{v}^{(z)}\right) = 0, \tag{2.3.7}$$

$$\mathbf{i}k\tilde{v}^{(x)} + \frac{d\tilde{v}^{(z)}}{dz} = 0. \tag{2.3.8}$$

Eliminating $\tilde{p}_i$ from the linearized governing Eqs. (2.3.3) – (2.3.5) and (2.3.6 – (2.3.8) results in the following biharmonic equations for the elastic and the viscous layers,

$$\frac{d^4\tilde{u}^{(z)}}{dz^4} - 2k^2\frac{d^2\tilde{u}^{(z)}}{dz^2} + k^4\tilde{u}^{(z)} = 0, \tag{2.3.9}$$

$$\frac{d^4\tilde{v}^{(z)}}{dz^4} - 2k^2\frac{d^2\tilde{v}^{(z)}}{dz^2} + k^4\tilde{v}^{(z)} = 0. \tag{2.3.10}$$

The general solutions for the Eqs. (2.3.9) and (2.3.10) are,

$$\tilde{u}^{(z)} = (A_{1i} + B_{2i}z)e^{kz} + (A_{3i} + A_{4i}z)e^{-kz}, \tag{2.3.11}$$

$$\tilde{v}^{(z)} = (B_{1i} + B_{2i}z)e^{kz} + (B_{3i} + B_{4i}z)e^{-kz}. \tag{2.3.12}$$

Here the coefficients A_{ji} and B_{ji} (i = *1* and *2*; j = *1* to *4*) are constants. The boundary conditions are also linearized employing the normal linear modes. The following are the linearized no slip and impermeability conditions at z = 0,

$$\tilde{u}^{(x)} = \tilde{u}^{(z)} = 0. \tag{2.3.13}$$

The linearized continuity of velocities, the tangential and normal stress balances, and the kinematic conditions at z = h_0 reduce to the forms,

$$\omega\tilde{u}^{(x)} = \tilde{v}^{(x)},\ \omega\tilde{u}^{(z)} = \tilde{v}^{(z)}, \tag{2.3.14}$$

$$G\left(\frac{d\tilde{u}_1^{(x)}}{dz} + \mathbf{i}k\tilde{u}_1^{(z)}\right) - \mu\left(\frac{d\tilde{v}_2^{(x)}}{dz} + \mathbf{i}k\tilde{v}_2^{(z)}\right) + \mathbf{i}kq_0\left(\tilde{\psi}_2 + \tilde{h}\frac{d\psi_{20}}{dz}\right) = 0, \tag{2.3.15}$$

$$\tilde{p}_1 - \tilde{p}_2 - 2G\frac{d\tilde{u}_1^{(z)}}{dz} + 2\mu\frac{d\tilde{v}_2^{(z)}}{dz} + \varepsilon_0\left(\varepsilon_2\frac{d\psi_{20}}{dz}\frac{d\tilde{\psi}_2}{dz} - \varepsilon_1\frac{d\psi_{10}}{dz}\frac{d\tilde{\psi}_1}{dz}\right) - k^2\gamma\tilde{h} = 0, \tag{2.3.16}$$

$$\tilde{h} = \tilde{u}_1^{(z)}, \tag{2.3.17}$$

$$\tilde{q} = \frac{1}{\omega}\left(s_2\frac{d\tilde{\psi}_2}{dz} - s_1\frac{d\tilde{\psi}_1}{dz}\right) - \mathbf{i}kq_0\tilde{u}_1^{(x)}. \tag{2.3.18}$$

The linearized tangential and normal stress balances, and the kinematic conditions at *z* = *d*,

$$\tilde{v}_2^{(x)} = \tilde{v}_2^{(z)} = 0. \tag{2.3.19}$$

The general solution for $\tilde{u}_1^{(z)}$ and $\tilde{v}_2^{(z)}$, Eqs. (2.3.11) and (2.3.12), are used to obtain expressions for the remaining linearized variables, $\tilde{u}_1^{(x)}$, $\tilde{v}_2^{(x)}$, and $\tilde{p}_i$. Replacing the expressions of these variables ($\tilde{u}_1^{(x)}$, $\tilde{u}_1^{(z)}$, $\tilde{v}_2^{(x)}$, $\tilde{v}_2^{(z)}$ and $\tilde{p}_i$) in the boundary conditions, Eqs. (2.3.13) – (2.3.19), lead to a set of eight homogeneous linear algebraic equations with eight unknown constants, A_{ji} and B_{ji} (*i* = *1* and *2*; *j* = *1* to *4*). Equating the determinant of the coefficient matrix of the linear equations to zero leads to the general dispersion relation, which is cumbersome and not supplied with the text. The analytical solution of the dispersion relation is, $\omega = f(k)$, which is solved to obtain the dominant growth coefficient (ω_m) by finding out the global maxima of ω and the corresponding

wavelength (λ_m). As limiting cases, we have validated the results from the dispersion relation for a single viscous dielectric (leaky-dielectric) film under air,[9] a single elastic dielectric (leaky-dielectric) film under air. All the algebraic operations in the derivations are done with the help of the commercial package Mathematica™.

Long wave potential: In previous theoretical study they have used long wave potential for electric field by applying lubricating approximation. The governing Eq. (2.2.2) becomes $\psi_{izz}=0$. The long wave boundary conditions for the electric field are, (i) at the cathode (z = 0), $\psi_1=0$ and anode (z = d), $\psi_2=\psi$; (ii) at the elastic-viscous interface ($z=h$), the normal [$\varepsilon_0\varepsilon_1\psi_{1z}-\varepsilon_0\varepsilon_2\psi_{2z}=q$] and tangential [$\psi_1=\psi_2$] component balances. The excess pressures originating from the applied electric field at elastic-viscous interface is

$$\pi=\frac{-d^2q^2\varepsilon_1+2dq\varepsilon_1\left(hq-\varepsilon_0\varepsilon_2\psi\right)+\left(\varepsilon_1-\varepsilon_2\right)\left(-h^2q^2+\varepsilon_0^2\varepsilon_1\varepsilon_2\psi^2\right)}{2\varepsilon_0\left[d\varepsilon_1+h\left(\varepsilon_2-\varepsilon_1\right)\right]^2}. \qquad (2.3.20)$$

The excess pressure π is a function of h and q. It is expanded in Taylor series about its base-state (h_0, q_0) and taken up to first order term. The linearized excess pressure is then used in normal stress balance, Eq. (2.3.16).

2.4 RESULTS AND DISCUSSION

Figure 2.1 schematically shows the two different elastic-viscous configurations, (i) the V^L bilayer – composed of a purely dielectric elastic layer confined by a leaky dielectric liquid layer and (ii) the E^L – bilayer consists of a leaky dielectric elastic layer confined by a purely dielectric liquid layer. In both the configurations, the stiffness of the elastic film and the capillary force at the interface act as stabilizing influences against the destabilizing

external electric field. The exposure of electric field ensures that the elastic-viscous interface is under the exposure of the two different types of stresses owing to the accumulation of the bound and free charges. In particular, as compared to the similar dielectric bilayers, the free charge accumulation at the interface develops an additional electrostatic interaction (attraction or repulsion) between the charged-interface (positive or negative) and the electrodes. Interestingly, the experiments on the electric field induced instabilities of the elastic-viscous bilayers can be performed in two different ways: (i) the external electric field is slowly ramped up until the deformation at the interface is initiated, and (ii) the electric field is ramped up abruptly to a very high value. In the first situation, the length and the times scales of the instability is driven by the neutral stability condition (critical mode – symbolized by subscript 'c') in which the combined stabilizing elastic and capillary forces nearly balance the destabilizing electric field force. However, in the latter case, the imbalance of the stronger electric field over the weaker stabilizing forces destabilizes a band of modes in which the fastest growing one (dominant mode – symbolized by subscript 'm') determines the length and time scales of the deformation. Herein we discuss the salient features of both the critical and the dominant modes of the electric field induced instabilities of elastic-viscous bilayers. In particular, we compare and contrast the critical and the dominant length scales on the E^L and V^L bilayers with a purely dielectric bilayer, denoted by the notation *D* in the script and figures.

In Figure 2.2, a comparison between the LWLSA and GLSA results are shown by the curves 1 and 2. The plot (a) shows variation of linear growth coefficient (ω) with wave number (*k*) of the electric field induced instability of a dielectric liquid layer whereas the plot (b) shows a bifurcation diagram of a dielectric elastic film deforming under the

influence of the electric field. The curves confirm that the LWLSA can only predict the correct eigenvalues when the instability is essentially long-wave ($k \rightarrow 0$). However, the GLSA with a more generic electric field potential is more accurate in predicting the unstable modes when the instability shows shorter wavelength features. Figure 2.2 corroborates the necessity of the GLSA in predicting the time and length scales of the electric field induced instabilities of this kind of configurations.

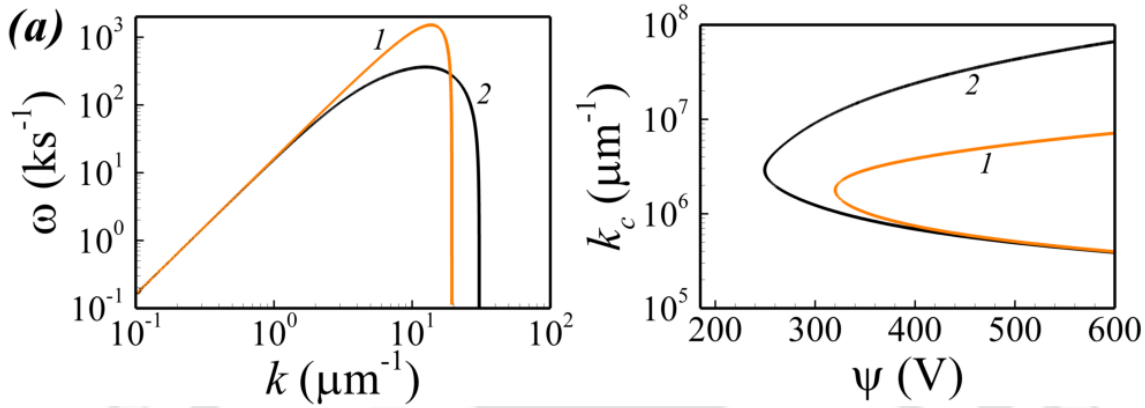

Figure 2.2 Plot (a) shows variation of linear growth coefficient (ω) with wave number (k) for a purely dielectric liquid film deforming under the influence of external electric field. The curves 1 and 2 show the results from the LWLSA and GLSA, respectively, when d = 193 nm, h = 43 nm, ψ = 70 V, μ = 1 Pa s, γ = 0.038 N m^{-1}, and ε_2 = 2.5. The curves 1 and 2 in the plot (b) show the bifurcation diagrams of a purely dielectric elastic film deforming under the influence of external electric field. The curves 1 and 2 show the results from the LWLSA and GLSA, respectively, when d = 1.5 μm, h = 1 μm, G = 10^5 Pa, γ = 0.02 N m^{-1}, and ε_1 = 3.

Figure 2.3 shows the contours of the minimum field intensity required to initiate the instability (E_c), the corresponding critical length scale (λ_c), and the normalized critical length scale with respect to the elastic film thickness (λ_c/h), in the interfacial tension (γ) vs. elastic film thickness (h) plane. Plots (a) – (c) in the first row represent an elastic-viscous bilayer with dielectric films – a 'D' bilayer, plots (d) – (f) in the second row represent an elastic-viscous bilayer with leaky viscous film – a 'V^L' bilayer, and the plots (g) – (i) in the third row represent an elastic-viscous bilayer with leaky elastic film – a 'E^L'

bilayer.

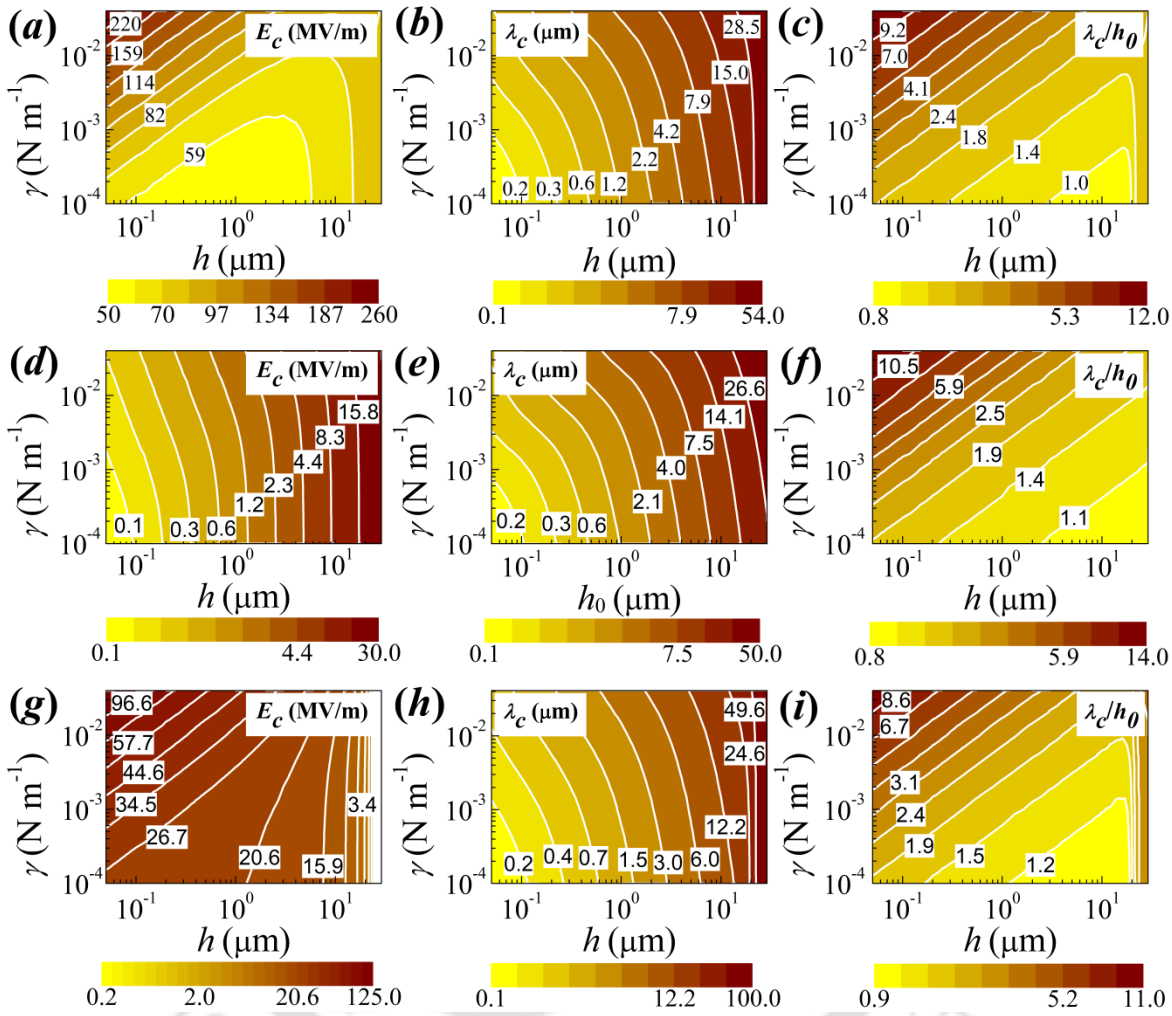

Figure 2.3 GLSA results show the contours of critical parameters of confined elastic-viscous bilayers in the γ vs. h plane. Plots (a) – (c) show the contours for D configuration, plots (d) – (f) show the contours for V^L configuration, and plots (g) – (i) for E^L configuration. The plots (a), (d), and (g) show the contours of E_c , plots (b), (e), and (h) show the contours of λ_c , and plots (c), (f), and (i) show the contours of λ_c/h. The other essential parameters for plots are, d = 30 μm, ε_1 = 3, and ε_2 = 5.

The plots (a) in the first column report E_c, which is a measure of the minimum field strength required to initiate instability in an elastic-viscous configuration. The contour plots suggest that 'D' bilayer requires a much stronger external field than any of the 'V^L' or 'E^L' bilayer, which endorses the requirement of smaller field intensity when any of the

layers of an elastic-viscous bilayer is leaky. For a purely dielectric elastic-viscous bilayer a larger electrode distance (d) ensures a weaker field intensity to be active across the interface to engender instability. In contrast, when any of the film is leaky, the effective electrode distance for the applied potential reduces by an amount equaling the thickness of the leaky layer. This is because, the presence of the leaky layer ensures enough accumulation of the electrons or holes at the interface layer to keep a constant potential across the film. In addition, the base-state free charge density at the interface for the E^L, $q_0 = -\varepsilon_0\varepsilon_2\psi/(d-h_0)$, and V^L bilayers, $q_0 = \varepsilon_0\varepsilon_1\psi/h_0$ clearly shows the increase in the free charge density with increase in the thickness of the leaky layer and applied potential. Thus, the elastic-viscous bilayers having a leaky dielectric layer is always unstable at much lower field intensity as compared to a purely dielectric layer because the effective field intensity acting on the elastic-viscous interface is much stronger. In addition, the plots suggest that as the magnitude of the capillary force at the elastic-viscous interface reduces the critical field intensity required to initiate the instability also reduces. Interestingly, the plot (d) suggests that a thick leaky dielectric viscous layer (high $d - h$) on a thin purely dielectric elastic layer (low h) require a significantly small E_c to become unstable. The E_c is found to be many fold larger for an elastic-viscous bilayer with very thick (high h) leaky elastic layer and a thin viscous layer (low $d - h$), as shown in the plot (g). The plots (b), (e), and (h) suggest that although the elastic-viscous configurations with a thick elastic layer (high h) show a similar λ_c but with reduction in the elastic layer thickness and the interfacial tension, the bilayers even show λ_c even in the sub-micron regime. The plots (c), (f), and (i) suggest that a thinner elastic film with higher interfacial tension shows a long-wave instability as $\lambda_c/h \sim 20$ for all the cases. However, with increase in h and reduction in γ lead to a transition from long- to short-wave, as the length

scale becomes, $\lambda_c/h \sim 1$. In case of the configurations with thinner elastic film the longer wavelength regime of the instability is expected as the surface tension effects are more pronounced whereas as the elastic film becomes thicker the progressive reduction in the influence of the capillary force shifts the instability towards the shorter wavelength regime.[10] Importantly, the short-wave instabilities is expected to show a further shorter wavelength regime for the present configurations because of the enhancement of the destabilizing stress owing to the free charges accumulation at the interface. It may be noted here that although the previous works predicted the transition from long- to short-wave with increase in h and reduction in γ, they could not correctly predict the length scale especially at the short-wave.[10] A recent experimental work shows the similar mismatch in between the experiments and the theoretical predictions with the use of long-wave electric field potential in the general linear stability analysis.[7,8] In the present work we consider the complete electric field potential in the GLSA, which not only helps in predicting the accurate transition from the long- to short-wave but also could predict the length scales accurately to the order, $\lambda_c/h \sim 1$.

Figure 2.4 shows the contours of E_c, λ_c, and λ_c/h in shear modulus (G) vs. h plane. Plots (a) – (c) represent an elastic-viscous bilayer with dielectric films – a 'D' bilayer, plots (d) – (f) represent an elastic-viscous bilayer with leaky viscous film – a 'V^L' bilayer, and the plots (g) – (i) represent an elastic-viscous bilayer with leaky elastic film – a 'E^L' bilayer. The plots (a) in the first column report E_c, which suggest that 'D' bilayer requires a much stronger external field than any of the 'V^L' or 'E^L' bilayers. In addition, as the magnitude of G reduces the E_c also reduces. Interestingly, the plot (d) suggests that a thick leaky dielectric viscous layer (high $d - h$) on a thin purely dielectric elastic layer (low h) require a significantly small E_c to become unstable. The E_c is found to be many fold larger for an

elastic-viscous bilayer with very thick (high h) leaky elastic layer and a thin viscous layer (low $d - h$), as shown in the plot (g). The plots (b), (e), and (h) suggest that although the

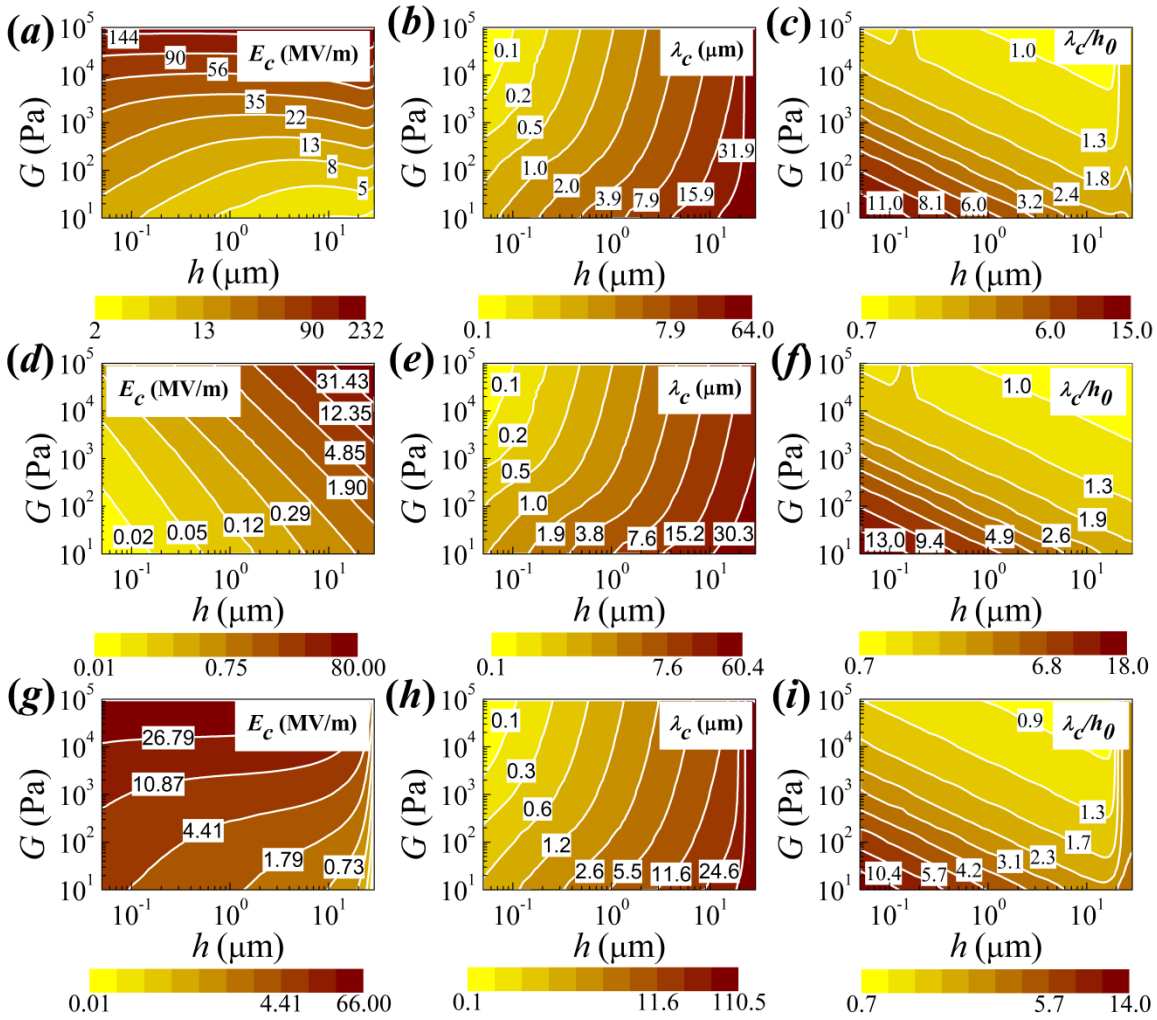

Figure 2.4 GLSA results show the contours of critical parameters of confined elastic-viscous bilayers in the G vs. h plane. Plots (a) – (c) show the contours for D configuration, plots (d) – (f) show the contours for V^L configuration, and plots (g) – (i) for E^L configuration. The plots (a), (d), and (g) show the contours of E_c, plots (b), (e), and (h) show the contours of λc , and plots (c), (f), and (i) show the contours of $\lambda c/h$. The other essential parameters for plots are, d = 30 μm, ε_1 = 3, and ε_2 = 5.

elastic-viscous configurations with a thick elastic layer (high h) show a similar λ_c. However, with reduction in the elastic layer thickness and increase in G the bilayers even show a critical length scale in the sub-micron regime. The plots (c), (f), and (i) suggest that a thinner elastic film with lower G shows a long-wave instability as $\lambda_c/h > 20$ for all

the cases. With increase in the elastic film thickness and G leads to a transition from long- to short-wave takes place as, $\lambda_c/h \sim 1$.

Concisely, the Figures 2.3 and 2.4 together shows that the use of a more generic electric field potential can accurately predict the length and the time scales of the electric field induced instabilities of thin elastic-viscous bilayers, which commensurate with the recently found experimental results.[7,8]

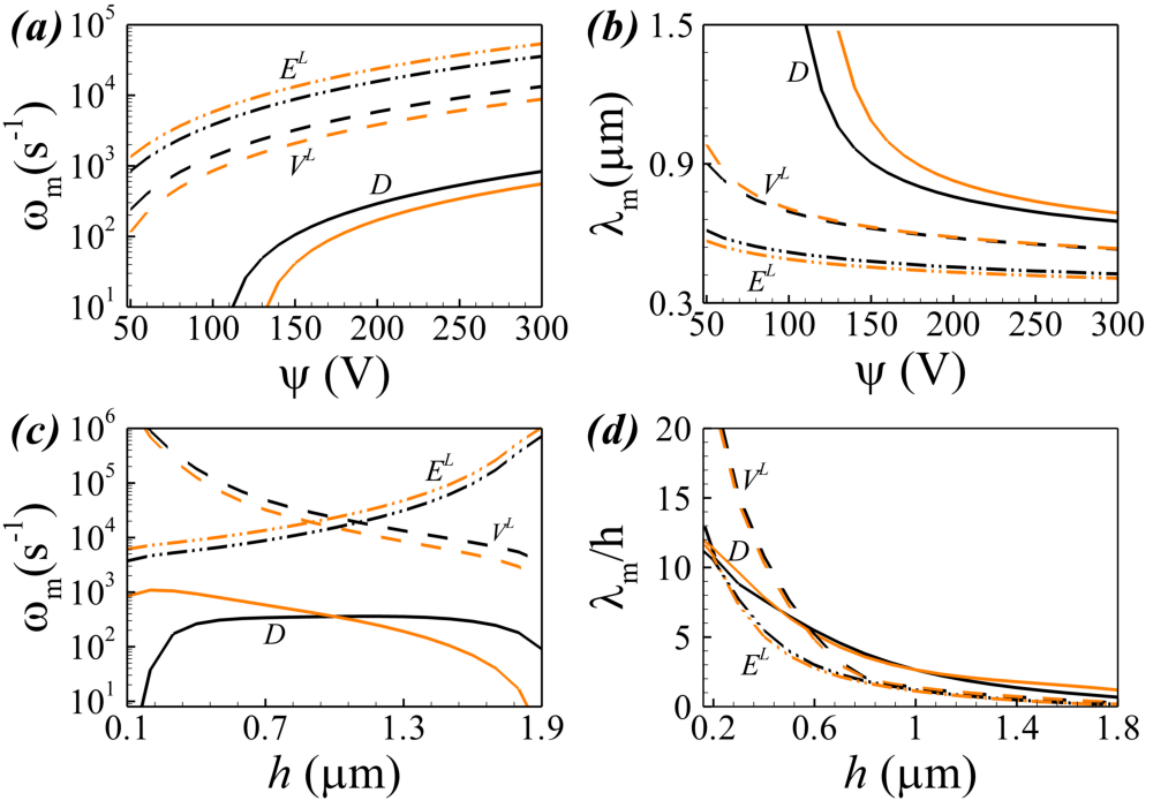

Figure 2.5 GLSA results for the elastic-viscous confined bilayers in presence of external electric field. The plots (a) and (c) show the influence of applied voltage (ψ) and elastic film thickness (h), respectively, on dominant growth coefficient (ω_m). The plots (b) and (d) show the variation corresponding dominant wave length (λ_m) and normalized dominant wave length (λ_m/h_0), respectively with ψ and h, respectively. The solid lines, evenly broken lines, and unevenly broken lines indicate D, V^L, and E^L confined elastic-viscous bilayers. In plots (a) – (d), the curves with darker and lighter shades represent $\varepsilon_1(5.0) > \varepsilon_2(3.0)$ and $\varepsilon_1(3.0) > \varepsilon_2(5.0)$, respectively. For plots (a) – (b) h = 1.0 μm, d = 1.5 μm and for plots (c) – (d) ψ = 400 V, d = 2.0 μm. The other necessary parameters for the plots (a) – (d) are G = 10^3 Pa, γ = 0.001 N m^{-1}, μ = 100 Pa s, and s_i = 1.0 × 10^{-11} S m^{-1}.

As mentioned previously, that the interface of an elastic-viscous bilayer can adopt the dominant mode of instability when abruptly exposed to an external electrostatic field. Figures 2.5 and 2.6 summarize the details of such occurrences from the GLSA.

In Figure 2.5 the plots (a) and (c) show the influence of applied voltage (ψ) and elastic film thickness (h), respectively, on dominant growth coefficient (ω_m). The plots (b) and (d) show the variation corresponding dominant wavelength (λ_m) and normalized dominant wave length (λ_m/h_0), respectively, with ψ and h, respectively. The solid lines, evenly broken lines and unevenly broken lines indicate D, V^L, and E^L confined elastic-viscous bilayers. The plots clearly suggest that the length and time scales are much smaller when one of the films of a purely dielectric elastic-viscous bilayer is replaced by a leaky elastic or viscous layer. The smallest time and length scales are shown by the bilayer where the elastic layer is leaky layer. A recent experiment has already shown the reduction in the length scales in an elastic-viscous bilayer with a leaky viscous bilayer. [7,8] The present work predicts that instead of the viscous layer, use of elastic layer can further reduce the length scales of the features, as shown in the plot (b). In addition, the plot (b) also highlights that these configurations can lead to sub-micron scale patterns at reasonably low field intensity on the surface of the elastic film.

The plots (a) and (b) in Figure 2.6 show the influence of $\varepsilon_r = \varepsilon_2 / \varepsilon_1$ on ω_m and λ_m, respectively. The plots clearly show that while the dielectric contrast across the interface is an absolute necessity to develop patterns interface of a purely dielectric elastic-viscous bilayer, the bilayers with leaky dielectric elastic or viscous layers can show instabilities even when the dielectric contrast is absent. In addition, the length and the time scales remain significant small under such a situation. The Figures 2.5 and 2.6 together show

some interesting features of the dominant mode of instabilities of an elastic-viscous bilayer.

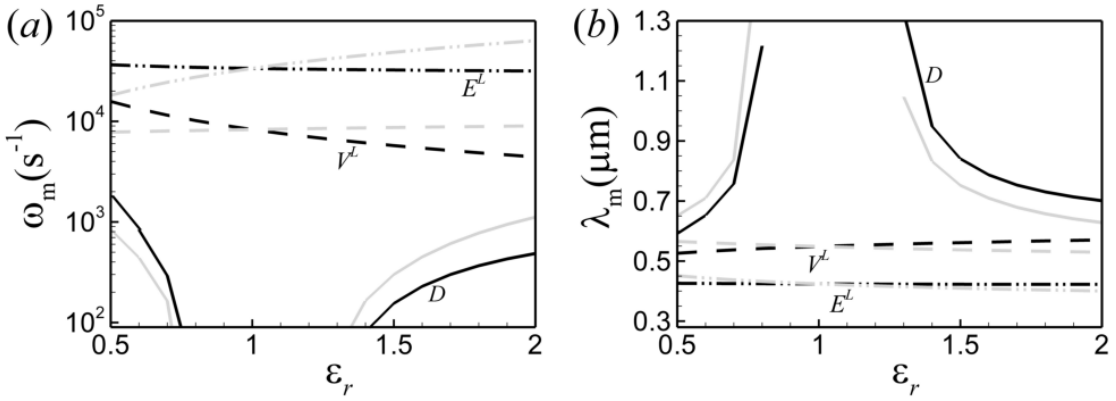

Figure 2.6 GLSA results for the elastic-viscous confined bilayers in presence of external electric field. The plots (a) and (b) show the influence of $\varepsilon_r = \varepsilon_2 / \varepsilon_1$ on ω_m and λ_m, respectively. The solid lines, evenly broken lines and dashed-dotted lines indicate *D*, V^L, and E^L confined elastic-viscous bilayers. In plots (a) – (b), curves with darker (lighter) shades represent the results when ε_2 (= 3.0) [ε_1 (=3.0)] is constant and ε_1 (ε_2) is varied to get ε_r. The other parameters for the plots are, G = 10^4 Pa, γ = 0.001 N m^{-1}, μ = 100 Pa s, h = 1.0 μm, d = 1.5 μm, ψ = 300 V, and s_i =1.0 × 10^{-11} S m^{-1}.

In Figure 2.7 the discrete square symbols show the experimental results, [7,8] the curve 1 shows the length scales predicted theoretically employing LWP,[7,8] and the curve 2 depicts the length scales predicted by the GLSA performed in the present formulation. Plot (a) shows the variation in the dimensionless critical field intensity ($E_c / \sqrt{G\varepsilon_1\varepsilon_0}$) with the dimensionless parameter, γ / Gh_0, obtained by varying G, h_0 and γ, respectively. The dimensionless number, γ / Gh_0, signifies the relative strength of the restoring surface tension and elastic forces inside the film. The plot (b) shows the variation in the normalized critical length scale (λ_c / h_0) with, γ / Gh_0, obtained by varying *G*, h_0 and γ, respectively. The dimensionless groups are borrowed from the previous study[49,50] to compare and contrast the results obtained in this work.

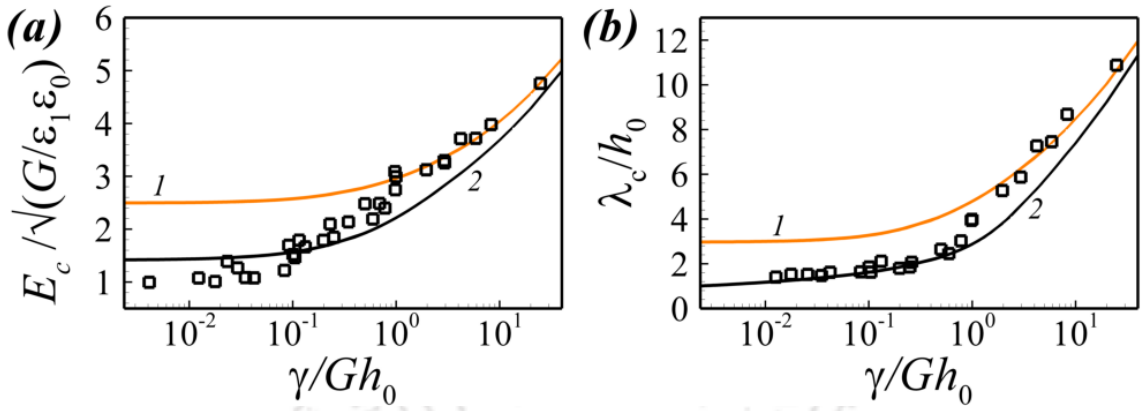

Figure 2.7 LSA results for the elastic-viscous confined bilayers in presence of external electric field. The plots (a) and (b) show the variation of $E_c/\sqrt{G/\varepsilon_1\varepsilon_0}$ and, (λ_c/h_0) respectively, with γ/Gh_0 by varying *G*, h_0 and γ, respectively. The square symbols in each plot are experimental results in previous study. The curves 1 and 2 represent LSA results for V^L configuration using LWP and GP, respectively. The parameters used for the plots are, *G* = 161 Pa – 155 k Pa, h_0 = 10 ± 2 μm – 59 ± 4 μm, γ = 0.0047 N m^{-1} and 0.04 N m^{-1}, μ = 0.001 Pa s, *d* = 250 μm, ε_1 = 2.65, ε_2 = 80 and σ_2 = 1.0 × 10^{-11} S m^{-1}.

The plot (a) suggests the larger restoring forces in the thinner and less compliant elastic films with larger elastic-stiffness and interfacial tension (larger γ/Gh_0) require a larger field intensity ($E_c/\sqrt{G\varepsilon_1\varepsilon_0}$) to engender instability. In comparison, with reduction in γ/Gh_0 (increase in h_0 and reduction in γ and *G*) the instability can be initiated at much lower electric field intensity ($E_c = \psi_c/h_0$). The plot (b) suggests that the weaker interfacial tension also ensures shorter wavelength instability ($\lambda_c/h_0 \sim 1$) for the thicker films with larger elastic-stiffness (smaller γ/Gh_0). A transition from shorter to longer wavelength regime is observed with increasing γ/Gh_0 because the effect of the capillary forces become predominant for the less compliant elastic films with smaller thickness and larger elastic modulus. Remarkably, the normalized critical field intensity ($E_c/\sqrt{G\varepsilon_1\varepsilon_0}$) and length scale ($\lambda_c/h_0$) predicted by the present work (solid line) can not only predict the

transitions from the long- to short-wave modes but also closely resemble the experimental length scales.[49,50] In comparison, the LWLSA can only accurately predict the length scales in the long-wave regime. The additional second term in the left hand side of the Eq. (3.1) for the electric field stress is the major reason behind the difference in the predictions from the LWP and GLSA. It may be noted here that the transition in the length scale from short to long-wave regime is also associated with a transition in pattern, as suggested by the experiments.[49,50] Concisely, the figure highlights the accuracy of the GLSA in predicting the experimental length scales of the electric field induced interfacial patterns of elastic-viscous bilayers with a weakly conducting liquid and purely dielectric elastic layer.

2.5 SUMMARY

A general linear stability analysis of the electric field induced instabilities of elastic-viscous bilayers is performed including the full descriptions of the Maxwell stresses uncovers the key short to long-wave features. The study highlights,

(i) Presence of a leaky elastic or viscous layer in the bilayer can impart additional electrostatic stress due to the presence of free charges at the interface(s), which can significantly reduce the length scales to develop submicron patterns. Unlike the purely dielectric bilayers where the accumulation of induced dipoles due to the dielectric-contrast across the interface dictates the direction of the interfacial deformation, for leaky bilayers the presence of the free charge (positive or negative) can determine the deformation towards or away from the electrodes (anode or cathode).

(ii) The study uncover that a transition from long- to short-wave instabilities take place with progressive increase in the strength of the destabilizing stress, reduction in the capillary forces at the interface, and with increase in the thickness of the leaky layer.

(iii) The general analysis shown here could reproduce the previously predicted length scales especially with a long-wave potential.[10] Further, the use of a more generic potential in the present work can indeed predict the recently reported experimental length scales of the electric field induced instabilities of elastic viscous bilayers.[7,8]

(iv) A recent experiment has already shown the reduction in the length scales in an elastic-viscous bilayer with a leaky viscous bilayer.[7,8] The present work predicts that instead of the viscous layer, use of elastic layer can further reduce the length scales of the features. In addition, the study uncovers that the elastic-viscous configurations with one leaky layer can indeed lead to sub-micron scale patterns at reasonably low field intensity on the surface of the elastic film.

In summary, the study motivates future applications on the self-organized patterning to basic understanding of electric field induced instabilities of thin elastic-viscous bilayers composed of leaky materials.

2.6 REFERENCE

1. P. Gambhire, and R. M. Thaokar, Eur. Phys. J. E **34**, 84(1) (2011).
2. P. Gambhire, and R. M. Thaokar, Phys. Rev. E **86**, 036301 (2012).
3. K. Mondal, P. Kumar, and D. Bandyopadhyay, J. Chem. Phys. **138**, 024705 (2013).
4. O. Ozen, N. Aubry, D. T. Papageorgiou and P. G. Petropoulos, Electrochimica Acta **51**, 5316 (2006).
5. F. Li, O. Ozen, N. Aubry, D. T. Papageorgiou, and P. G. Petropoulos, J. Fluid Mech. **583**, 347 (2007).
6. D. A. Saville, Annu. Rev. Fluid Mech. **29**, 27 (1997).
7. Q. Wang, L. Zhang, and X. Zhao, Phys. Rev. Lett. **106**, 118301 (2011).
8. Q. Wang, and X. Zhao, Phys. Rev. E **88**, 042403 (2013).
9. R. Verma, A. Sharma, K. Kargupta and J. Bhaumik, Langmuir **21**, 3710 (2005).
10. J. Sarkar, A. Sharma, and V. B. Shenoy, Phys. Rev. E **77**, 031604 (2008).

11. G. Tomar, V. Shankar, A. Sharma, and G. Biswas, J. Non-Newtonian Fluid Mech. **143**, 120 (2007).
12. D. Bandyopadhyay, P. D. S. Reddy, and A. Sharma, Phys. Fluids **24**, 074106 (2012).
13. N. Arun, A. Sharma, V. B. Shenoy, and K. S. Narayan, Adv. Mater. **18**, 660 (2006).
14. N. Arun, A. Sharma, P. S. G. Pattader, I. Banerjee, H. M. Dixit, and K. S. Narayan, Phys. Rev. Lett. **102**, 254502 (2009).
15. D. Bandyopadhyay, A. Sharma, and V. Shankar, J. Chem. Phys. **128**, 154909 (2008).
16. J. Sarkar, and A. Sharma, Langmuir **26**, 8464 (2010).
17. R. V. Craster, and O. K. Matar, Phys. Fluids **17**, 032104 (2005).
18. S. A. Roberts, and S. Kumar, Phys. Fluids **22**, 122102 (2010).
19. D. Bandyopadhyay, A. Sharma, U. Thiele, and P. D. S. Reddy, Langmuir **25**, 9108 (2009).
20. P. D. S. Reddy, D. Bandyopadhyay, and A. Sharma, J. Phys. Chem. C **114,** 21020 (2010).
21. P. D. S. Reddy, D. Bandyopadhyay, and A. Sharma, J. Phys. Chem. C **116,** 22847 (2012).
22. D. Bandyopadhyay, A. Sharma and V. Shankar, EPL, **89,** 36002 (2010).

Chapter 3

Electric Field Induced Instabilities of Thin Leaky Bilayers: Pathways to Unique Morphologies and Miniaturization

ABSTRACT

Charge leakage of the weakly conducting liquid layers in a thin bilayer can engender interesting interfacial instabilities when exposed to an external electrostatic field. A general linear stability analysis including the full descriptions of the Maxwell stresses uncovers the key short to long-wave features of the instabilities of the bilayers composed of purely dielectric films, leaky dielectric films, and a combination of leaky and dielectric films. The study highlights that for the leaky bilayers the additional electrostatic stress due to the presence of free charges at the interface(s) can significantly reduce the length scale to enforce pattern miniaturization. Unlike a purely dielectric bilayer where the dielectric-contrast across the interfaces dictates the direction of the interfacial deformations, for leaky bilayers the nature of the charge (positive or negative) at the interface can also contribute to the deformation towards or away from the electrodes (anode or cathode). Nonlinear simulations uncover that the interfaces can develop unique morphologies when the spatiotemporal variation of the attractive or repulsive force at the charged interface act together or against the electrical stress due to the induced charge separation across the interface. Exploiting these features a host of periodic interfacial patterns such as core-shell columns, a hole encapsulated by a column, a bundle of columns embedded inside a single column, a collection of holes embedded under a column, and 'caged' columns are obtained, which are rather difficult to assemble using other conventional patterning techniques. The results reported can be of importance in the diverse areas of micro/nanotechnology.

This chapter is published in J. Chem. Phys. **138**, 024705 (2013).

3.1 INTRODUCTION

In the present chapter, we explore the salient features of the electric field induced instabilities of thin bilayers composed of, (i) a pair of purely dielectric films (DD), (ii) a leaky dielectric lower layer below a purely dielectric upper layer (LD), (iii) a leaky dielectric upper layer on a purely dielectric lower layer (DL), and (iv) a pair of leaky dielectric films (LL). The work is motivated by a recent study[1] on the alternating current (AC) induced interfacial instabilities of a bilayer where long-wave linear stability analysis (LWLSA) together with 2-D (two-dimensional) nonlinear simulations briefly discuss the influence of charge leakage under the direct current (DC) field in one of the asymptotic limits. In comparison, we perform a general wavenumber linear stability analysis (GLSA) of the conservation laws incorporating the full descriptions of the Maxwell stresses. The sensitivity of the length and time scales on the parameters such as the thickness, dielectric permittivity, and viscosity ratios of the films are explored. The GLSA shows that the additional interfacial stresses originating from the free charge accumulation and induced charge separation can together shift the instability in the shorter wavelength regime where the LWLSA is no longer valid. Importantly, the GLSA also predicts that the length scales of the instabilities of the leaky bilayers can in fact reduce to the nanoscale regime to open up the possibility of pattern miniaturization. In the regime where the instability has long-wave characteristics, 2-D and 3-D (three-dimensional) nonlinear simulations are performed to uncover the spatiotemporal evolution of the interfaces and the subsequent charge distribution. Unlike the purely dielectric bilayers where the electrical stresses due to the induced charge separation across the interface dictate the deformation, the nonlinear simulations reveal that the presence of charged interfaces can lead to considerably different interfacial patterns for the leaky dielectric bilayers. For example, when the

interfaces are of same (opposite) charge they are expected to deform toward the same (opposite) electrode, which can lead to interesting interfacial patterns when in competition with the stress because of the induced charge separation. Further, the spatiotemporal variation of the charge concentration can dynamically influence the interfacial deformations to develop some unique interfacial patterns. The results discussed can be of significant importance in the future studies related to the fabrication of some unique submicron patterns exploiting the electric field induced instabilities of the thin leaky dielectric bilayers.

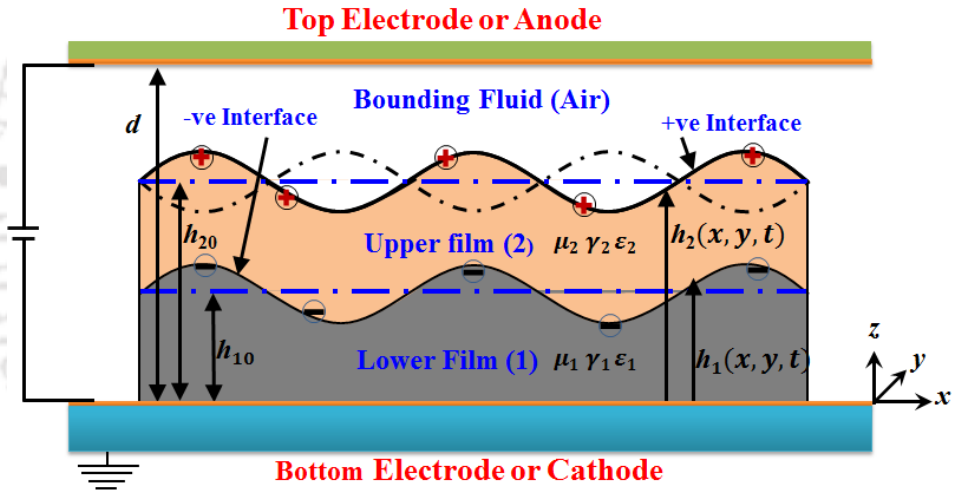

Figure 3.1 A schematic diagram of a leaky bilayer under the influence of an external electric field. The mean and the local thicknesses of the lower layer are denoted by h_{10} and $h_1(x,t)$, respectively, and the same for the composite layers are denoted by h_{20} and $h_2(x,t)$, respectively. The symbols γ_i, μ_i, and ε_i denote the surface energy, viscosity, and dielectric permittivity of the lower (i = 1) and upper (i = 2) layers, respectively. The distance between the electrodes is d. The positive and negative signs signify the free charges at the interface.

3.2 PROBLEM FORMULATION

In the formulation, the x and y coordinates are in parallel and the z coordinate is normal to the substrate (Figure 3.1). The notation t represents time, the bracketed superscripts are vector components, the superscript dot represents time derivative, the subscripts x, y, and z

denote the derivatives, and the subscript $i = 1$ ($i = 2$) denotes lower (upper) layer/interface. The lower, upper, and combined film thicknesses are denoted by h_1, h_3, and h_2 ($= h_1 + h_3$), respectively. The respective base-state values are denoted by h_{10}, h_{30}, and h_{20}, respectively. The distance between the electrodes is defined by d. The symbols $\boldsymbol{\sigma}_i$, $\mathbf{M}_i$, κ_i, p_i, ε_i, μ_i, π_i, q_i, s_i, and γ_i are the Newtonian stress tensor for fluids, Maxwell stress tensor, curvature, isotropic static pressure, dielectric permittivity, viscosity, excess pressure because of electric field, charge concentration, conductivity, and surface energy of the ith fluid layer, respectively. The unit outward normal and tangent vectors are represented by, $\mathbf{n}_i\left[-h_{ix}/\sqrt{1+h_{ix}^2}, 1/\sqrt{1+h_{ix}^2}\right]$ and $\mathbf{t}_i\left[1/\sqrt{1+h_{ix}^2}, h_{ix}/\sqrt{1+h_{ix}^2}\right]$, respectively.

3.2.1 Electric Field

We assume that the electric field is irrotational and electro-neutrality prevails within the bulk of the films. Further, the characteristic flow time is assumed to be much larger than the time scales for the electrically induced and magnetic effects.[2-5] Thus, the governing equations, $\nabla \cdot \mathbf{E}_i = 0$ and $\nabla \times \mathbf{E}_i = 0$, are valid for the electric field, $\mathbf{E}_i$, in the fluids i = 1, 2 and a. Here subscript 'a' denotes a non-viscous perfectly dielectric fluid such as air. The irrotational electric field is expressed in terms of a potential function, ψ_i as, $\mathbf{E}_i = -\nabla\psi_i$, leading to the Laplace equation for ith layer,

$$\nabla^2\psi_i = 0. \qquad (3.2.1)$$

The boundary conditions enforced for the electric field are, (i) at the cathode ($z = 0$), $\psi_1 = 0$ and anode ($z = d$), $\psi_a = \psi$; (ii) at the liquid-liquid interface ($z = h_1$), the normal $[\varepsilon_0\varepsilon_2(\mathbf{E}_2 \cdot \mathbf{n}_1) - \varepsilon_0\varepsilon_1(\mathbf{E}_1 \cdot \mathbf{n}_1) = q_1]$ and the tangential $[\mathbf{E}_1 \cdot \mathbf{t}_1 = \mathbf{E}_2 \cdot \mathbf{t}_1]$ component balances; (iii) at the liquid-air interface ($z = h_2$), the normal

$[\varepsilon_0(\mathbf{E}_a\cdot\mathbf{n}_2)-\varepsilon_0\varepsilon_2(\mathbf{E}_2\cdot\mathbf{n}_2)=q_2]$ and the tangential $[\mathbf{E}_2\cdot\mathbf{t}_2=\mathbf{E}_a\cdot\mathbf{t}_2]$ component balances. The symbol ε_0 represents the dielectric permittivity of free space, 8.854×10^{-12} $C^2/N\,m^2$.

3.2.2 Electrohydrodynamic Field

The electrohydrodynamic (EHD) of a thin leaky dielectric film is governed by the Stokes equations of motion coupled with Maxwell stresses and conservation of current at the weakly conducting interface.[2-5] The films are considered to be Newtonian and incompressible liquids. The following continuity equation and the equations of motion describe the EHD of the leaky dielectric bilayer,

$$\nabla\cdot\mathbf{u}_i=0, \tag{3.2.2}$$

$$-\nabla p_i+\nabla\cdot(\boldsymbol{\sigma}_i+\mathbf{M}_i)=0. \tag{3.2.3}$$

Where the constitutive relation for a Newtonian fluid, $\boldsymbol{\sigma}_i=\mu_i(\nabla\mathbf{u}_i+\nabla\mathbf{u}_i^{T})$, is expressed in terms of velocity vector, $\mathbf{u}_i=(u_i^{(x)},\ u_i^{(z)})$, and the Maxwell stress because of the external electric field is, $\mathbf{M}_i=\varepsilon_0\varepsilon_i\left[\mathbf{E}_i\otimes\mathbf{E}_i-0.5(\mathbf{E}_i\cdot\mathbf{E}_i)\mathbf{I}\right]$. The Maxwell stresses arise only at the interfaces because electroneutrality prevails at the bulk ($\nabla\cdot\mathbf{M}_i=0$).

The lower layer is assumed to be non-slipping on the impermeable substrate [$\mathbf{u}_1=0$ at $z=0$]. At the liquid-liquid interface [$z=h_1$], continuity of *x*- and *z*-components of velocities [$\mathbf{u}_1=\mathbf{u}_2$], normal stress balance $[-p_2+\mathbf{n}_1\cdot(\boldsymbol{\sigma}_2+\mathbf{M}_2)\cdot\mathbf{n}_1+p_1-\mathbf{n}_1\cdot(\boldsymbol{\sigma}_1+\mathbf{M}_1)\cdot\mathbf{n}_1=\gamma_{21}\kappa_1]$, tangential stress balance $[\mathbf{n}_1\cdot\boldsymbol{\sigma}_1\cdot\mathbf{t}_1-\mathbf{n}_1\cdot\boldsymbol{\sigma}_2\cdot\mathbf{t}_1-q_1\mathbf{E}_2=0]$, and the kinematic conditions for the height and free charge concentration, $\dot{h}_1+u_1^{(x)}h_{1x}+u_1^{(y)}h_{1y}=u_1^{(z)}$ and $\dot{q}_1+\mathbf{u}_1\cdot\nabla_s q_1-q_1\mathbf{n}_1\cdot(\mathbf{n}_1\cdot\nabla)\mathbf{u}_1=s_1\mathbf{E}_1\cdot\mathbf{n}_1-s_2\mathbf{E}_2\cdot\mathbf{n}_1$, are enforced. The normal stress

balance, $[-p_0+\mathbf{n}_2\cdot\mathbf{M}_a\cdot\mathbf{n}_2+p_2-\mathbf{n}_2\cdot(\boldsymbol{\sigma}_2+\mathbf{M}_2)\cdot\mathbf{n}_2=\gamma_2\kappa_2]$, tangential stress balance, $[\mathbf{n}_2\cdot\boldsymbol{\sigma}_2\cdot\mathbf{t}_2-q_2\mathbf{E}_a=0]$, and the kinematic conditions for height and free charge concentration, $\dot{h}_2+u_2^{(x)}h_{2x}+u_2^{(y)}h_{2y}=u_2^{(z)}$ and $\dot{q}_2+\mathbf{u}_2\cdot\nabla_s q_2-q_2\mathbf{n}_2\cdot(\mathbf{n}_2\cdot\nabla)\mathbf{u}_2=s_2\mathbf{E}_2\cdot\mathbf{n}_2$, are applied as boundary conditions at the liquid-air interface [$z=h_2$]. The curvature of the interface *i* is defined as, $\kappa_i=\nabla_s\cdot\mathbf{n}_i$.

3.3 GENERAL LINEAR STABILITY ANALYSIS

The GLSA is performed based on the assumptions that the kinematics of deformation is small.

3.3.1 Base-state analysis

A quiescent base-state is considered with stationary fluid layers, $u_{i0}^{(x)}=u_{i0}^{(z)}=0$, with film thickness, h_{i0}, interfacial charge concentration, q_{i0}, and under the exposure of an electric field potential ψ_{i0}. The expression for the electric potential for each layer *i = 1*, *2* and *a* is,

$$\psi_{i0zz}=0. \tag{3.3.1}$$

The general solution of Eq. (3.3.1) is,

$$\psi_{i0}=A_{1i}z+A_{2i}. \tag{3.3.2}$$

The boundary conditions employed to evaluate A_{ij}s (*i = 1*, *2*; *j = 1*, *2* and *a*) are: (i) at the solid-liquid interface (*z* = 0), $\psi_{10}=0$ and at the electrode-air interface (*z* = d), $\psi_{a0}=\psi$; (ii) at the liquid-liquid interface ($z=h_{10}$), the normal [$\varepsilon_0\varepsilon_1\psi_{10z}-\varepsilon_0\varepsilon_2\psi_{20z}=q_{10}$] and the tangential [$\psi_{10}=\psi_{20}$] component balances; (iii) at the liquid-air interface ($z=h_{20}$), the normal [$\varepsilon_0\varepsilon_2\psi_{20z}-\varepsilon_0\psi_{a0z}=q_{20}$] and the tangential [$\psi_{20}=\psi_{a0}$] component balances.

The base-state EHD expression for the z-momentum balance for each layer *i = 1* and *2* is,

$$p_{i0z} = 0 . \tag{3.3.3}$$

The general solution of Eq. (3.3.3) is,

$$p_{i0} = D . \tag{3.3.4}$$

The linear boundary conditions employed to evaluate D_i s (i = *1* and *2*) are: (i) at the liquid-liquid interface ($z = h_{10}$), the normal balance [$p_{10} = p_{20} - 0.5\varepsilon_0 \left(\varepsilon_2 A_{12}^2 - \varepsilon_1 A_{11}^2\right)$]; (ii) at the liquid-air interface ($z = h_{20}$), the normal component balance [$p_{20} = p_0 - 0.5\varepsilon_0 \left(A_{1a}^2 - \varepsilon_2 A_{12}^2\right)$].

The base-state conservation of charge concentrations at the liquid-liquid and liquid-air interfaces reduce to, $s_2 \psi_{20z}\big|_{h_{10}} - s_1 \psi_{10z}\big|_{h_{10}} = 0$ and $s_2 \psi_{20z}\big|_{h_{20}} = 0$, which are solved to obtain q_{10} and q_{20} .The final expressions of the base-state charges for a, DD bilayer are, $q_{10} = q_{20} = 0$; LD bilayer are, $q_{10} = -\varepsilon_0 \varepsilon_2 \psi / \left[\left(h_{20} - h_{10}\right) + \varepsilon_2 \left(d - h_{20}\right)\right]$ and $q_{20} = 0$; DL bilayer are, $q_{10} = \varepsilon_0 \varepsilon_1 \psi / \left[h_{10} + \varepsilon_1 \left(d - h_{20}\right)\right]$ and $q_{20} = -\varepsilon_0 \varepsilon_1 \psi / \left[h_{10} + \varepsilon_1 \left(d - h_{20}\right)\right]$; LL bilayer are, $q_{10} = 0$ and $q_{20} = -\varepsilon_0 \psi / \left(d - h_{20}\right)$.

3.3.2 Perturbed-state analysis

The governing equations and the boundary conditions are linearized by employing the normal linear modes, $u_i^{(x)} = \tilde{u}_i^{(x)} e^{\omega t + \mathbf{i} k x}$, $u_i^{(z)} = \tilde{u}_i^{(z)} e^{\omega t + \mathbf{i} k x}$, $\psi_i = \psi_{i0} + \tilde{\psi}_i e^{\omega t + \mathbf{i} k x}$, $p_i = p_{i0} + \tilde{p}_i e^{\omega t + \mathbf{i} k x}$, $h_i = h_{i0} + \tilde{\delta}_i e^{\omega t + \mathbf{i} k x}$, and $q_i = q_{i0} + \tilde{\theta}_i e^{\omega t + \mathbf{i} k x}$ where the symbols ω and k represent the linear growth coefficient and the wave number of the disturbance, respectively. The variables $\tilde{u}_i^{(x)}$, $\tilde{u}_i^{(z)}$, $\tilde{\psi}_i$, and $\tilde{p}_i$ in the normal modes are $f\left(z\right)$ only. The

symbols $\tilde{\delta}_i$ and $\tilde{\theta}_i$ are the infinitesimal perturbation of height and charge concentration at the interfaces. The linearized perturbed electric field Eq. (3.2.1) is,

$$\tilde{\psi}_{izz} - k^2\tilde{\psi}_i = 0\,. \tag{3.3.5}$$

The general solution of the Eq. (8) is,

$$\tilde{\psi}_i = C_{1i}e^{kz} + C_{2i}e^{-kz}\,. \tag{3.3.6}$$

Here the coefficients C_{ij} (i = *1*, *2* and *a*; j = *1* and *2*) are constants. The constants C_{ij} s can be evaluated by employing the linearized perturbed boundary conditions: (i) at the solid-liquid interface (z = 0), $\tilde{\psi}_1 = 0$ and at the electrode-air interface (z = d), $\tilde{\psi}_a = 0$; (ii) at the liquid-liquid interface ($z = h_{10}$), the normal [$\varepsilon_0\varepsilon_1\tilde{\psi}_{1z} - \varepsilon_0\varepsilon_2\tilde{\psi}_{2z} = \tilde{\theta}_1$] and the tangential [$\left(\tilde{\psi}_1 - \tilde{\psi}_2\right) + \tilde{\delta}_1\left(\psi_{10z} - \psi_{20z}\right) = 0$] component balances; (iii) at the liquid-air interface ($z = h_{20}$), the normal [$\varepsilon_0\varepsilon_2\tilde{\psi}_{2z} - \varepsilon_0\tilde{\psi}_{az} = \tilde{\theta}_2$] and the tangential [$\left(\tilde{\psi}_2 - \tilde{\psi}_a\right) + \tilde{\delta}_2\left(\psi_{20z} - \psi_{a0z}\right) = 0$] component balances.

The linearized forms of the governing Eqs. (3.2.2) and (3.2.3) are,

$$-\mathbf{i}k\tilde{p}_i + \mu_i\left(-k^2\tilde{u}_i^{(x)} + \frac{d^2\tilde{u}_i^{(x)}}{dz^2}\right) = 0\,, \tag{3.3.7}$$

$$-\frac{d\tilde{p}_i}{dz} + \mu_i\left(-k^2\tilde{u}_i^{(z)} + \frac{d^2\tilde{u}_i^{(z)}}{dz^2}\right) = 0\,, \tag{3.3.8}$$

$$\mathbf{i}k\tilde{u}_i^{(x)} + \frac{d\tilde{u}_i^{(z)}}{dz} = 0\,. \tag{3.3.9}$$

Eliminating $\tilde{p}_i$ from the linearized governing Eqs. (3.3.7) – (3.3.9) results in the following biharmonic equation for each layer,

$$\frac{d^4\tilde{u}_i^{(z)}}{dz^4} - 2k^2\frac{d^2\tilde{u}_i^{(z)}}{dz^2} + k^4\tilde{u}_i^{(z)} = 0\,. \tag{3.3.10}$$

The general solution of Eq. (3.3.10) is,

$$\tilde{u}_i^{(z)} = (B_{1i} + B_{2i} z) e^{kz} + (B_{3i} + B_{4i} z) e^{-kz} . \tag{3.3.11}$$

Here the coefficients B_{ji} (i = *1* and *2*; j = *1* to *4*) are constants. The boundary conditions are also linearized employing the normal linear modes. The following are the linearized no slip and impermeability conditions at $z = 0$,

$$\tilde{u}_1^{(x)} = \tilde{u}_1^{(z)} = 0 . \tag{3.3.12}$$

The linearized continuity of velocities, the tangential and normal stress balances, and the kinematic conditions at $z = h_{10}$ reduce to the forms,

$$\tilde{u}_1^{(x)} = \tilde{u}_2^{(x)},\ \tilde{u}_1^{(z)} = \tilde{u}_2^{(z)}, \tag{3.3.13}$$

$$\mu_1 \left(\frac{d\tilde{u}_1^{(x)}}{dz} + \mathbf{i}k\tilde{u}_1^{(z)} \right) - \mu_2 \left(\frac{d\tilde{u}_2^{(x)}}{dz} + \mathbf{i}k\tilde{u}_2^{(z)} \right) + \mathbf{i}kq_{10} \left(\tilde{\psi}_2 + \tilde{\delta}_1 \frac{d\psi_{20}}{dz} \right) = 0 , \tag{3.3.14}$$

$$\tilde{p}_1 - \tilde{p}_2 - 2\mu_1 \frac{d\tilde{u}_1^{(z)}}{dz} + 2\mu_2 \frac{d\tilde{u}_2^{(z)}}{dz} + \varepsilon_0 \left(\varepsilon_2 \frac{d\psi_{20}}{dz} \frac{d\tilde{\psi}_2}{dz} - \varepsilon_1 \frac{d\psi_{10}}{dz} \frac{d\tilde{\psi}_1}{dz} \right) - k^2 \gamma_{21} \tilde{\delta}_1 = 0 , \tag{3.3.15}$$

$$\tilde{\delta}_1 = \frac{\tilde{u}_1^{(z)}}{\omega} , \tag{3.3.16}$$

$$\tilde{\theta}_1 = \frac{1}{\omega} \left(s_2 \frac{d\tilde{\psi}_2}{dz} - s_1 \frac{d\tilde{\psi}_1}{dz} - \mathbf{i}kq_{10} \tilde{u}_1^{(x)} \right) . \tag{3.3.17}$$

The linearized tangential and normal stress balances, and the kinematic conditions at $z = h_{20}$,

$$\mu_2 \left(\frac{d\tilde{u}_2^{(x)}}{dz} + \mathbf{i}k\tilde{u}_2^{(z)} \right) + \mathbf{i}kq_{20} \left(\tilde{\psi}_a + \tilde{\delta}_2 \frac{d\psi_{a0}}{dz} \right) = 0 , \tag{3.3.18}$$

$$\tilde{p}_2 - 2\mu_2 \frac{d\tilde{u}_2^{(z)}}{dz} + \varepsilon_0 \left(\frac{d\psi_{a0}}{dz} \frac{d\tilde{\psi}_a}{dz} - \varepsilon_2 \frac{d\psi_{20}}{dz} \frac{d\tilde{\psi}_2}{dz} \right) - k^2 \tilde{\delta}_2 \gamma_2 = 0 , \tag{3.3.19}$$

$$\tilde{\delta}_2 = \frac{\tilde{u}_2^{(z)}}{\omega}, \tag{3.3.20}$$

$$\tilde{\theta}_2 = -\frac{1}{\omega}\left(s_2 \frac{d\tilde{\psi}_2}{dz} + \mathbf{i}kq_{20}\tilde{u}_2^{(x)} \right). \tag{3.3.21}$$

The general solution for $\tilde{u}_i^{(z)}$ [Eq. (3.2.11)] is used to obtain expressions for the remaining linearized variables $\tilde{u}_i^{(x)}$ and $\tilde{p}_i$. Replacing the expressions of these variables ($\tilde{u}_i^{(z)}$, $\tilde{u}_i^{(x)}$ and $\tilde{p}_i$) in the boundary conditions [Eqs. (3.3.12) − (3.3.21)] lead to a set of eight homogeneous linear algebraic equations with eight unknown constants B_{ji} (*i* = *1*, *2* and *j* = *1* to *4*). Equating the determinant of the coefficient matrix of the linear equations to zero leads to the dispersion relation, which is cumbersome and not supplied with the text. The analytical solution of the dispersion relation is, $\omega = f(k)$, which is solved to obtain the dominant growth coefficient (ω_m) by finding out the global maxima of ω and the corresponding wavelength (λ_m). As limiting cases, we have validated the results from the dispersion relation for a single viscous dielectric film under air,[6] confined dielectric and leaky bilayers,[7] and dielectric[8] and leaky[1] bilayers under air. All the algebraic operations in the derivations are done with the help of the commercial package Mathematica™.

3.4 NONLINEAR EVOLUTION EQUATIONS

The coupled evolution equations for the liquid-liquid and liquid-air interfaces are derived under the long-wave approximation. Thus, the Stokes equations of motion, $\mu_i u_i^{(x)}{}_{zz} = p_{ix}$, $\mu_i u_i^{(y)}{}_{zz} = p_{iy}$, and $p_{iz} = 0$, the continuity equation, $u_{ix}^{(x)} + u_{iy}^{(y)} + u_{iz}^{(z)} = 0$, the kinematic conditions for the thicknesses and charge concentrations, $h_{it} + u_i^{(x)}\big|_{h_i} h_{ix} + u_i^{(y)}\big|_{h_i} h_{iy} = u_i^{(z)}\big|_{h_i}$,

$q_{1t}+\left(q_1u_1^{(x)}\right)_x+\left(q_1u_1^{(y)}\right)_y=s_2\psi_{2z}\big|_{h_1}-s_1\psi_{1z}\big|_{h_1}$, and $q_{2t}+\left(q_2u_2^{(x)}\right)_x+\left(q_2u_2^{(y)}\right)_y=-s_2\psi_{2z}\big|_{h_2}$, together with the boundary conditions at the interfaces lead to the evolution equations, $h_i=h_i\left(x,y,t\right)$ and $q_i=q_i\left(x,y,t\right)$. The boundary conditions employed for this derivation are: $\mu_2u_{2z}^{(x)}+q_2\left(\psi_{ax}+h_{2x}\psi_{az}\right)=0$ and $\mu_2u_{2z}^{(y)}+q_2\left(\psi_{ay}+h_{2y}\psi_{az}\right)=0$, at $z=h_2$ (tangential stress balance at liquid-air interface); $u_1^{(x)}=u_2^{(x)}$, $u_1^{(y)}=u_2^{(y)}$, $\mu_1u_1^{(x)}-\mu_2u_2^{(x)}+q_1\left(\psi_{2x}+h_{1x}\psi_{2z}\right)=0$ and, $\mu_1u_1^{(y)}-\mu_2u_2^{(y)}+q_1\left(\psi_{2y}+h_{1x}\psi_{2z}\right)=0$ at $z=h_1$ (continuity of velocity and shear stress balance at liquid-liquid interface) and $u_1^{(x)}=u_1^{(y)}=u_1^{(z)}=0$, at $z=0$ (no-slip and impermeability at the solid-liquid interface).

The resulting evolution equations are,

$$\frac{\partial h_1}{\partial t}=\nabla\cdot\left[\begin{array}{l}\dfrac{h_1^3}{3\mu_1}\nabla p_1+\dfrac{h_1^2h_3}{2\mu_1}\nabla p_2+\dfrac{h_1^2}{2\mu_1}q_1\left(\nabla\psi_2\big|_{h_1}+\psi_{2z}\big|_{h_1}\nabla h_1\right)\\+\dfrac{h_1^2}{2\mu_1}q_2\left(\nabla\psi_a\big|_{h_2}+\psi_{az}\big|_{h_2}\nabla h_2\right)\end{array}\right],\tag{3.4.1}$$

$$\frac{\partial h_2}{\partial t}=\nabla\cdot\left[\begin{array}{l}\dfrac{h_1^2}{2\mu_1}\left(h_2-\dfrac{h_1}{3}\right)\nabla p_1+\left(\dfrac{h_1h_3}{\mu_1}\left(h_2-\dfrac{h_1}{2}\right)+\dfrac{h_3^{\,3}}{3\mu_2}\right)\nabla p_2\\+\dfrac{h_1}{\mu_1}\left(h_2-\dfrac{h_1}{2}\right)q_1\left(\nabla\psi_2\big|_{h_1}+\psi_{2z}\big|_{h_1}\nabla h_1\right)\\+\left(\dfrac{h_1}{\mu_1}\left(h_2-\dfrac{h_1}{2}\right)+\dfrac{h_3^{\,2}}{2\mu_2}\right)q_2\left(\nabla\psi_a\big|_{h_2}+\psi_{az}\big|_{h_2}\nabla h_2\right)\end{array}\right],\tag{3.4.2}$$

$$\frac{\partial q_1}{\partial t}=\nabla\cdot\left[\frac{q_1h_1}{\mu_1}\left(\begin{array}{l}\dfrac{h_1}{2}\nabla p_1+h_3\nabla p_2+q_1\left(\nabla\psi_2\big|_{h_1}+\psi_{2z}\big|_{h_1}\nabla h_1\right)\\+q_2\left(\nabla\psi_a\big|_{h_2}+\psi_{az}\big|_{h_2}\nabla h_2\right)\end{array}\right)\right]+s_2\psi_{2z}\big|_{h_1}-s_1\psi_{1z}\big|_{h_1},\tag{3.4.3}$$

$$\frac{\partial q_2}{\partial t}=\nabla\cdot\left(\begin{array}{l}\dfrac{h_1^2 q_2}{2\mu_1}\nabla p_1+\left(\dfrac{h_1 h_3}{\mu_1}+\dfrac{h_3^{\,2}}{2\mu_2}\right)\nabla p_2+\dfrac{h_1 q_1 q_2}{\mu_1}\left(\nabla\psi_2\big|_{h_1}+\psi_{2z}\big|_{h_1}\nabla h_1\right)\\ +\left(\dfrac{h_1}{\mu_1}+\dfrac{h_3}{\mu_2}\right)q_2^2\left(\nabla\psi_a\big|_{h_2}+\psi_{az}\big|_{h_2}\nabla h_2\right)\end{array}\right)-s_2\psi_{2z}\big|_{h_2}. \quad (3.4.4)$$

Here the symbols $\alpha\big|_\beta$ denotes the variable α evaluated at β. Eqs. (3.4.1) – (3.4.4) is a set of coupled partial differential equations (PDEs), which describe the stability, dynamics, and morphology of the liquid-liquid $(i=1)$ and the liquid-air $(i=2)$ interfaces. The pressures at the liquid-liquid and liquid-air interfaces are derived from the normal stress balances,

$$p_1-p_2+\pi_1-\pi_2+\gamma_{21}\nabla^2 h_1=0, \quad (3.4.5)$$

$$p_2-p_o+\pi_2+\gamma_2\nabla^2 h_2=0. \quad (3.4.6)$$

Here p_o is the ambient pressure at the air-gap above the upper film. The symbols π_1 and π_2 are the excess pressures originating from the applied electric field and are expressed as,

$$\pi_1=\frac{\left[\varepsilon_1 h_3 q_2+\varepsilon_2\left(h_1 q_T-\varepsilon_0\varepsilon_1\psi\right)\right]^2-\varepsilon_1\left[-h_3 q_1+h_2\varepsilon_2 q_T-\varepsilon_2\left(dq_T+\varepsilon_0\psi\right)\right]^2}{2\varepsilon_0\left[h_1\left(\varepsilon_1-\varepsilon_2\right)+\varepsilon_1\left(h_2\left(\varepsilon_2-1\right)-d\varepsilon_2\right)\right]^2}, \quad (3.4.7)$$
$$-\frac{3B_1}{\left(d-h_2\right)^4}+\frac{3B_2}{h_1^4}$$

$$\pi_2=\frac{\left[\varepsilon_1 h_3 q_2+\varepsilon_2\left(h_1 q_T-\varepsilon_0\varepsilon_1\psi\right)\right]^2-\varepsilon_2\left[h_1 q_1-\varepsilon_1\left(\left(d-h_2\right)q_2+\varepsilon_0\psi\right)\right]^2}{2\varepsilon_0\left[h_1\left(\varepsilon_1-\varepsilon_2\right)+\varepsilon_1\left(h_2\left(\varepsilon_2-1\right)-d\varepsilon_2\right)\right]^2}. \quad (3.4.8)$$
$$-\frac{3B_1}{\left(d-h_2\right)^4}+\frac{3B_3}{h_3^4}$$

Where the total charge concentration at the interfaces is expressed as, $q_T=q_1+q_2$. In order to capture the long-time interfacial evolution of the films and to remove the contact-

line singularities from the simulations, short range repulsion terms are included in the Eqs. (3.4.7) and (3.4.8). The expressions for the constant coefficient B_1 and B_2 (B_1 and B_3) are evaluated employing the condition for the minimum of the free energy, $\pi_1 = \partial(-\Delta G)/\partial h_1 = 0$ [$\pi_2 = \partial(-\Delta G)/\partial h_3 = 0$], at the contact lines, $h_1 = l_0$ and $(d - h_2) = l_0$ [$h_3 = l_0$ and $(d - h_2) = l_0$]. The expression for B_1, B_2, and B_3 are cumbersome and not supplied with the text.

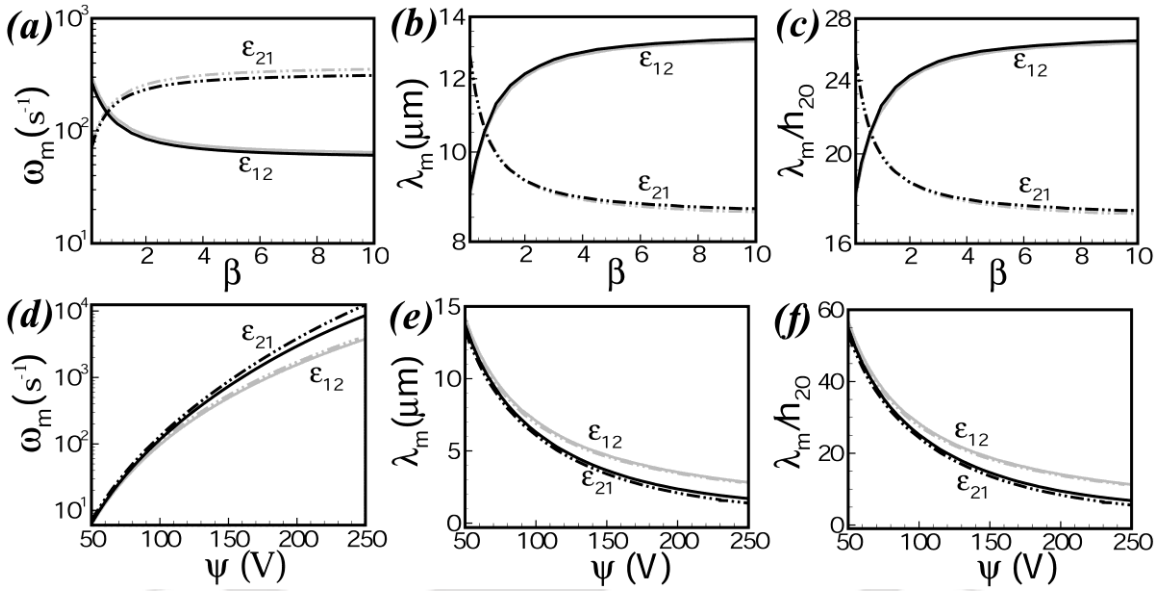

Figure 3.2 The lines with darker (lighter) shade show the results from the GLSA (LWLSA). The plots (a) and (d) show the variation of dominant linear growth coefficient (ω_m) with the thickness ratio of the films ($\beta = h_{30}/h_{10}$) and the applied voltage (ψ). Plots (b) and (e) show the variation of dominant wavelength (λ_m) with β and ψ. Plots (c) and (f) show the variation of normalized dominant wavelength (λ_m/h_{20}) with β and ψ. The β is obtained by fixing h_{20} (= 0.5 μm) and then changing h_{10} or h_{30}. The notation ε_{12} represents $\varepsilon_1(3.0) > \varepsilon_2(2.0)$ and ε_{21}, represents $\varepsilon_1(3.0) < \varepsilon_2(2.0)$. The other necessary parameters are shown in the SET I of Table 3.1.

The evolution Eqs. (3.4.1) – (3.4.4) are perturbed employing the normal modes, $h_i = h_{i0} + \tilde{\delta}_i e^{\omega t + \mathbf{i}kx}$ and $q_i = q_{i0} + \tilde{\theta}_i e^{\omega t + \mathbf{i}kx}$, to obtain the long-wave dispersion relation, which is again cumbersome and not supplied with the text. It may be noted here that the

dispersion relations obtained from the GLSA and LWLSA together with the coupled equations can be reduced and verified to all single layer[6] and bilayer[8] expressions in the respective asymptotic limits. Figure 3.2 shows a comparison between LWLSA and GLSA, in which the results of the electric field induced instabilities of the purely dielectric bilayers are validated against the previous results,[8] in the asymptotic limit where the charges at the interfaces are absent. The plots show that for a purely dielectric bilayer ω_m increases and λ_m reduces as the film with higher dielectric permittivity becomes thicker and the electrical stress increases. The plots (e) and (f) convey that when the electrical stresses are larger at higher ψ, the length scale shifts toward the shorter wavelength regime ($\lambda_m / h_{20} \approx 1$) and GLSA predictions are more accurate than the same from the LWLSA. The figure confirms that the GLSA provides a more accurate time and length scales for the electric field induced instabilities of thin leaky dielectric bilayers.

TABLE 3.1 Typical values of bilayer parameters[8-11]

Variables	SET I	SET II
ψ **(V)**	50	140
γ_{21} **(N m^{-1})**	0.0007	1.5×10^{-5}
γ_2 **(N m^{-1})**	0.03	0.03
μ_1 **(Pa s)**	1	24
μ_2 **(Pa s)**	1	2.3×10^{5}
d **(nm)**	1000	3000
h_{10} **(nm)**	150	500
h_{20} **(nm)**	250	1000
s_i	10^{-11}	10^{-11}

The evolution Eqs. (3.4.1) – (3.4.4) are nondimensionalized for a compact representation of numerical results by introducing, $(X,Y)=K_1(x,y)/h_{10}$, $T=K_2(\gamma_{21}/3\mu_1 h_{10})t$, $Q_i=q_i/\hat{Q}$, $\gamma=\gamma_2/\gamma_{21}$, $R=\mu_1/\mu_2$, $(Z,H_i,D)=(z,h_i,d)/h_{10}$, $(\bar{P}_i,\ \Pi_i)=(p_i,\ \pi_i)/\hat{P}$, $\Psi_i=\psi_i/\psi$, and $S_i=12s_i\mu_1\gamma_{21}h_{10}^3/\varepsilon_0^3\psi^4$, where $\hat{P}=(\varepsilon_0\psi^2/2h_{10}^2)$, $\hat{\mathrm{Q}}=(\varepsilon_0\psi/h_{10})$, $K_1=(\varepsilon_0\psi^2/2h_{10}\gamma_{21})^{0.5}$, and $K_2=K_1^4$.

$$\frac{\partial H_1}{\partial T}=\nabla\cdot\left[\begin{array}{l} H_1^3\nabla\bar{P}_1+\dfrac{3H_1^2H_3}{2}\nabla\bar{P}_2+3H_1^2Q_1\left(\nabla\Psi_2\big|_{H_1}+\Psi_{2Z}\big|_{H_1}\nabla H_1\right)\\ +3H_1^2Q_2\left(\nabla\Psi_a\big|_{H_2}+\Psi_{aZ}\big|_{H_2}\nabla H_2\right)\end{array}\right], \tag{3.4.9}$$

$$\frac{\partial H_2}{\partial T}=\nabla\cdot\left[\begin{array}{l} \dfrac{3H_1^2}{2}\left(H_2-\dfrac{H_1}{3}\right)\nabla\bar{P}_1+3\left(H_1H_3\left(H_2-\dfrac{H_1}{2}\right)+R\dfrac{H_3^{\,3}}{3}\right)\nabla\bar{P}_2\\ +6H_1\left(H_2-\dfrac{H_1}{2}\right)Q_1\left(\nabla\Psi_2\big|_{H_1}+\Psi_{2Z}\big|_{H_1}\nabla H_1\right)\\ +6\left(H_1\left(H_2-\dfrac{H_1}{2}\right)+\dfrac{RH_3^{\,2}}{2}\right)Q_2\left(\nabla\Psi_a\big|_{H_2}+\Psi_{aZ}\big|_{H_2}\nabla H_2\right)\end{array}\right], \tag{3.4.10}$$

$$\frac{\partial Q_1}{\partial T}=\nabla\cdot\left[\begin{array}{l} \dfrac{3H_1^2Q_1}{2}\nabla\bar{P}_1+3H_1H_3Q_1\nabla\bar{P}_2+6H_1Q_1^2\left(\nabla\Psi_2\big|_{H_1}+\Psi_{2Z}\big|_{H_1}\nabla H_1\right)\\ +6H_1Q_1Q_2\left(\nabla\Psi_a\big|_{H_2}+\Psi_{aZ}\big|_{H_2}\nabla H_2\right)\end{array}\right]+S_2\,\Psi_{2Z}\big|_{H_1}-S_1\,\Psi_{1Z}\big|_{H_1}, \tag{3.4.11}$$

$$\frac{\partial Q_2}{\partial T}=\nabla\cdot\left[\begin{array}{l} \dfrac{3H_1^2Q_2}{2}\nabla\bar{P}_1+3\left(H_1H_3+\dfrac{RH_3^{\,2}}{2}\right)Q_2\nabla\bar{P}_2\\ +6H_1Q_1Q_2\left(\nabla\Psi_2\big|_{H_1}+\Psi_{2Z}\big|_{H_1}\nabla H_1\right)\\ +6\left(H_1+RH_3\right)Q_2^2\left(\nabla\Psi_a\big|_{H_2}+\Psi_{aZ}\big|_{H_2}\nabla H_2\right)\end{array}\right]-S_2\,\Psi_{2Z}\big|_{H_2}. \tag{3.4.12}$$

Here the dimensionless upper layer thickness is expressed as, $H_3=H_2-H_1$. Eqs. (3.4.9) – (3.4.12) were solved numerically to obtain the interfacial deformations and the subsequent

spatiotemporal morphologies. The equations were discretized using a central difference scheme in space and the PDEs were reduced to a set of ordinary differential equations (ODEs) in time. Following this, periodic boundary conditions were enforced at the spatial boundaries. The resulting set of stiff ODEs was simulated in time employing the Gear's algorithm (D02EJF subroutine in 2-D and D02NCF subroutine in 3-D) from the NAG library.[6,8] The simulations were initiated with volume preserving random perturbation at the interfaces and the grid independence of the solutions was ensured.

3.5. RESULTS AND DISCUSSION

The physics associated with the electric field induced interfacial instabilities of a bilayer with leaky dielectric film(s) is intricate and exciting because it involves the deformations of twin interfaces under the combined stresses originating from the accumulated free charges at the interface(s) together with the separation of the induced charges across the interface(s). This is unlike the EHD instabilities of a purely dielectric thin bilayer where solely the stress originating from the induced charge separation deforms the soft interfaces towards the material with lower dielectric permittivity. For example, both the interfaces of a purely dielectric bilayer are expected to show periodic columnar structures toward the upper electrode when the lower layer has the highest dielectric permittivity ($\varepsilon_2 < \varepsilon_1$). Following the same rule, the liquid-air (liquid-liquid) interface forms periodic columns (holes) towards the upper (lower) electrode when upper layer is of highest dielectric permittivity ($\varepsilon_2 > \varepsilon_1$). In comparison, for a leaky dielectric bilayer, the positively or negatively charged interface(s) can also be under the attractive or repulsive influence from the electrodes, which can act together or against the stresses due to the induced charge separation. In this section, with the help of GLSA we identify the conditions for which the

destabilizing stresses in the leaky dielectric bilayers can reduce the length scales of the instabilities. Following this, a collection of nonlinear simulations is presented to uncover the interesting morphologies originating from the interplay between the coupled destabilizing electrical stresses at the interfaces of the leaky bilayers.

3.5.1 Linear Stability Analysis

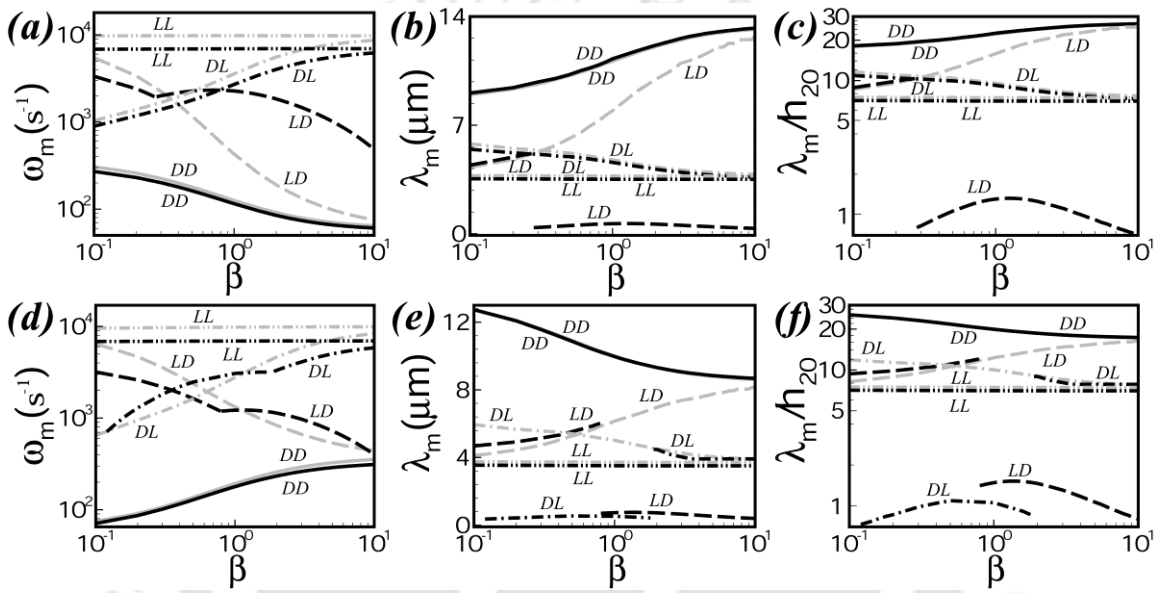

Figure 3.3 The lines with darker (lighter) shade show the results from the GLSA (LWLSA). The solid, evenly broken, dash-dot and dash-dot-dot lines indicate bilayers with, dielectric films (DD), lower layer leaky-upper layer dielectric (LD), lower layer dielectric-upper layer leaky (DL) and both layer leaky (LL), respectively. The plots (a), (b), and (c) show the variations of ω_m, λ_m and λ_m / h_{20}, respectively, with β when $\varepsilon_1(3.0) > \varepsilon_2(2.0)$. The plots (d), (e), and (f) show the variations of ω_m, λ_m and λ_m / h_{20}, respectively, with β when $\varepsilon_2(3.0) > \varepsilon_1(2.0)$. The β is obtained by fixing h_{20} (= 0.5 μm) and then changing either h_{10} or h_{30}. The other necessary parameters are shown in the SET I of Table 3.1.

Figure 3.3 shows the variations in the length (λ_m) and time (ω_m^{-1}) scales of the instabilities from the GLSA (darker shades) and LWLSA (lighter shades) for the DD, LD, DL, and LL bilayers. In these plots the combined thickness of the films (h_{20}) are kept constant and the thickness of the individual layers are varied to obtain the thickness ratio, β. The plots

clearly convey that for a DD bilayer ω_m increases and λ_m reduces with increase in the thickness of the layer with higher dielectric permittivity. In comparison, for LD and DL bilayers, ω_m increases and λ_m reduces with increase in the thickness of the weakly conducting leaky layer. For a LL bilayer, although the magnitude of ω_m increases and λ_m reduces significantly from a DD bilayer, they remain constant with the change in β. The plots (b) and (e) suggest that introduction of charge leakage to any of the layers can reduce the length scale significantly by shifting the dominant mode of instability from the liquid-air (longer wavelength) to liquid-liquid (shorter wavelength) interface having weaker stabilizing interfacial tension. The discontinuity associated with the plots for DL and LD signifies the transition of dominant mode of instability from the liquid-air (longer wavelength) to the liquid-liquid (shorter wavelength) interface or vice versa. The curves show a noticeable 10 – 15 times reduction in the length scales for the LD or DL bilayers as compared to that of a DD bilayer. Clearly, the enhanced destabilizing electrical stress due to the charge leakage alongside a weaker stabilizing interfacial tension at the liquid-liquid interface is the recipe here for the patterns with submicron scale periodicity. More importantly, the plots (c) and (f) convey that, in such a situation, the length scale indeed shifts to the short-wave regime ($\lambda_m / h_{20} \approx 1$) and LWLSA can no longer accurately predict the length and time scales. The LWLSA predictions are found to be more accurate when the dominant mode of instability stays at the liquid-air interface and the length scale is in the long-wave regime ($\lambda_m / h_{20} >> 1$).

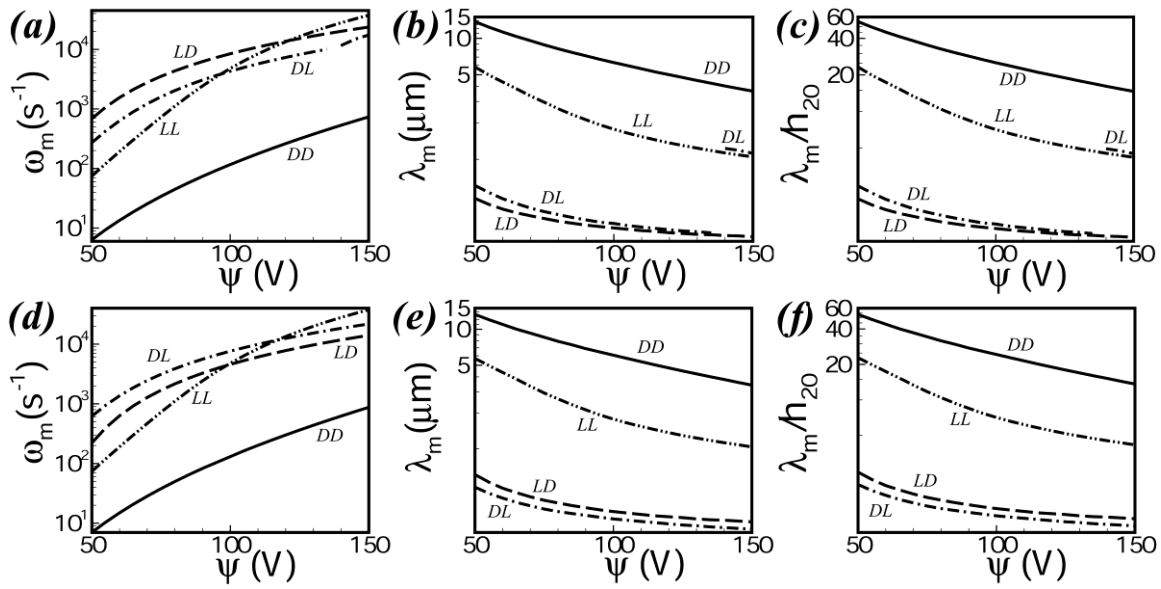

Figure 3.4 GLSA results showing the influence of electric field potential (ψ). The solid, evenly broken, dash-dot and dash-dot-dot lines indicate the DD, LD, DL, and LL bilayers, respectively. The plots (a), (b) and (c) show the variations of ω_m, λ_m, and λ_m / h_{20}, respectively, with ψ when $\varepsilon_1(3.0) > \varepsilon_2(2.0)$. The plots (d), (e) and (f) show the variations of ω_m, λ_m, and λ_m / h_{20}, respectively, with ψ when $\varepsilon_2(3.0) > \varepsilon_1(2.0)$. The other necessary parameters are shown in the SET I of Table 3.1.

Figure 3.4 shows the results from GLSA when ψ is varied. Importantly, the length and time scales for all the LL, DL, and LD bilayers are also found to vary with ψ because the charge concentrations at the interfaces are functions of ψ. The base-state charge concentrations can be estimated from the expressions provided in the Sec. (3.3.1). The plots convey that increase in ψ can lead to 5 – 10 times reduction in the length scales for the leaky bilayers as compared to that for a DD bilayer. The plots (b) and (e) highlight that the LD and DL type bilayers can lead to submicron scale patterns even at moderately high field strength. The GLSA predicts a short-wave instability ($\lambda_m / h_{20} \approx 1$) under these conditions, as depicted in the plots (c) and (f). Thus, in this regime the LWLSA is unable to predict the length and time scales accurately.

Figures 3.3 and 3.4 together show that , in most of the situations, ω_m is highest for the LL bilayers, which means the kinetics of instability is always faster for a LL bilayer as compared to the LD and DL bilayers. However, for the LL bilayers, the dominant mode of instability always stay at the liquid-air interface, which ensures a larger length scale due to higher surface tension. In comparison, for the DL and LD bilayers, the dominant mode of instability can conditionally shift to the liquid-liquid interface having weaker stabilizing interfacial tension. Thus, the DL and LD bilayers can show smaller length scale as compared to the LL bilayers.

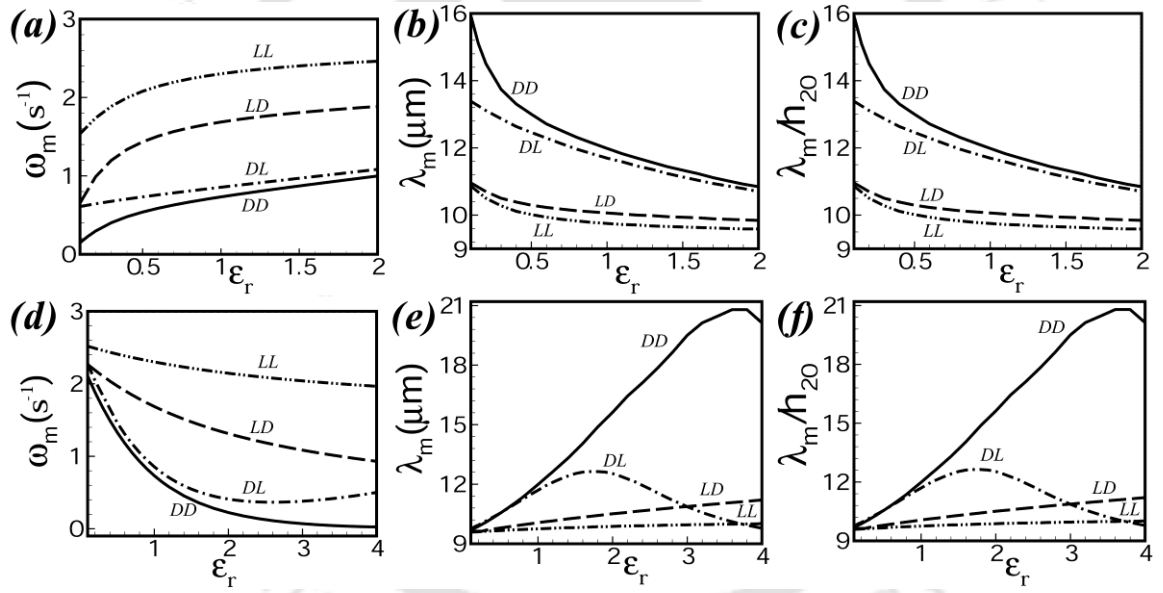

Figure 3.5 GLSA results showing the influence of $\varepsilon_r = \varepsilon_2 / \varepsilon_1$. The solid, evenly broken, dash-dot and dash-dot-dot lines indicate the DD, LD, DL, and LL bilayers, respectively. The plots (a), (b) and (c) show the variations of ω_m, λ_m, and λ_m / h_{20}, respectively, with ε_r when ε_1(=5.5) constant . The plots (d), (e) and (f) show the variations of ω_m, λ_m, and λ_m / h_{20}, respectively, with ε_r when ε_2(= 5.5) constant. The other necessary parameters are shown in the SET II of Table 3.1.

Figure 3.5 shows the results from GLSA when $\varepsilon_r \left(= \varepsilon_2 / \varepsilon_1\right)$ is varied. The plots (a) – (c) show that ω_m increases and λ_m reduces with increase in ε_2 (increasing ε_r) whereas plots (d) – (f) show the same with increase in ε_1 (decreasing ε_r). Increase in ε_2 or ε_1 in a DD

bilayer increases the total capacitance, which increases the destabilizing influence at the interfaces. However, for LD, DL, and LL bilayers the charge concentration at the interfaces are also found to vary with ε_2 or ε_1, as can be estimated from the base-state expressions for the charges in Sec. 3.3.1. Thus, for the leaky bilayers, increase in the permittivity of the layers can enhance free charge accumulation as well as the total capacitance, which can collectively reduce the time and length scales of the instability.

Apart from the thermodynamic parameters such as the ratio of film thickness, applied voltage, and dielectric permittivity of the layers the kinetic parameters such as the viscosity ratio ($\mu_r = \mu_2 / \mu_1$) of the films can also significantly alter the length and time scales of the electric field induced instabilities of leaky bilayers. This is in stark contrast to similar single film scenario where the viscosity can only influence the time scale and does not change the length scale of the instabilities. Figure 3.6 shows the results from GLSA when μ_r is varied. The plots (a) and (d) convey that increase in the viscosity of any of the layers reduces the growth of the instability (ω_m reduces). Interestingly, plots (b) and (e) highlight that tuning the viscosity ratio of the layers the growth-rate of the instability at the interfaces can be controlled and the dominant mode of instability can be shifted from one of the interface to the other. The discontinuities associated with these plots signify this transition. The plots convey that the instability in a DD bilayer with low μ_2 can grow by deformation of the liquid-air interface. With increase in μ_2, as the growth of instability at the upper layer is inhibited by the increased viscous resistance, the dominant mode shifts to the liquid-liquid interface, which also shifts the λ_m to the shorter wavelength regime. At higher μ_2, the instability can again move back to the liquid-air interface because increase

in μ_2 can also restrict the rate of deformation of the liquid-liquid interface. The LD and DL bilayers show similar transitions with μ_r as observed for the DD bilayers whereas the LL bilayers show rather monotonic change with μ_r under similar condition. Importantly, all the leaky bilayers show a much smaller length scale for the instabilities as compared to the DD bilayers at different viscosity ratios.

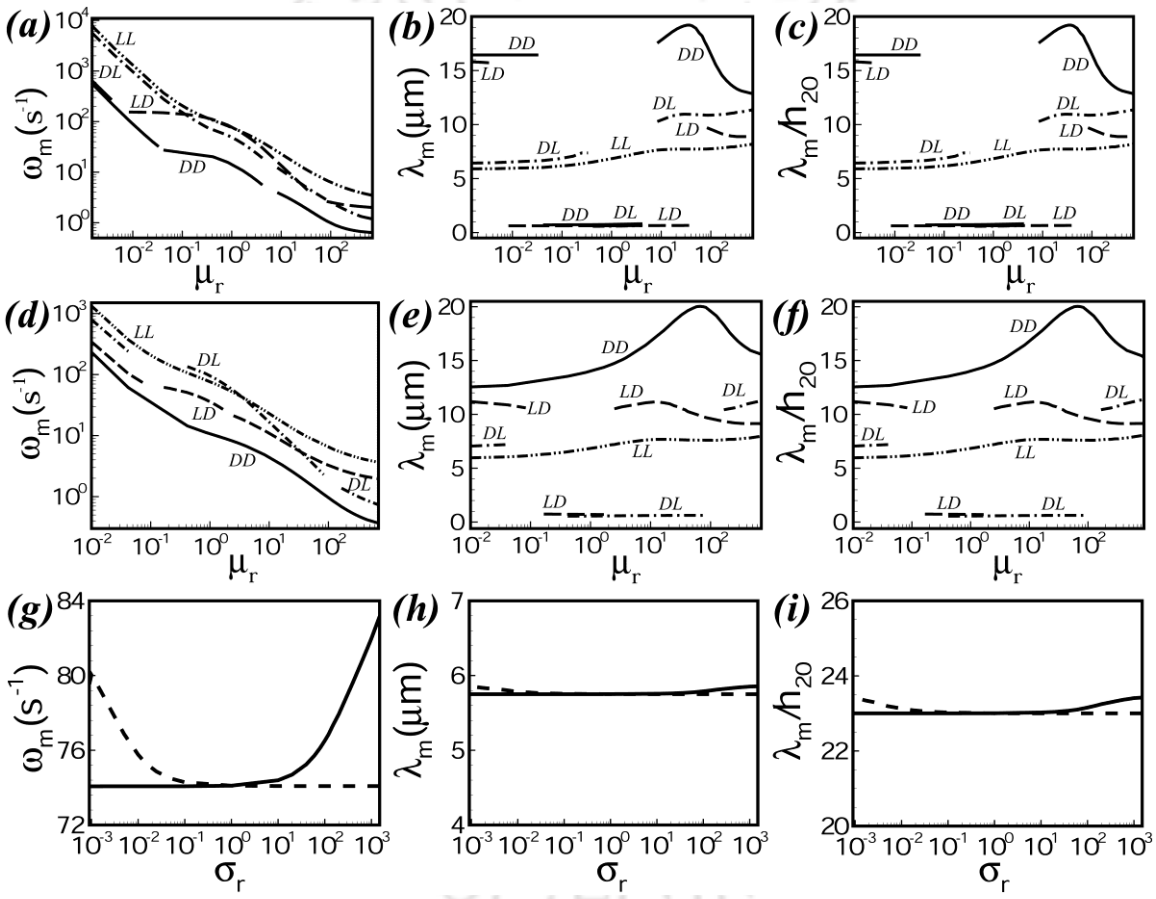

Figure 3.6 GLSA results showing the influence of $\mu_r = \mu_2 / \mu_1$ and $\sigma_r = \sigma_2 / \sigma_1$. For the plots (a) – (f), the solid, evenly broken, dash-dot and dash-dot-dot lines indicate the DD, LD, DL, and LL bilayers, respectively. The plots (a), (b), and (c) show the variations of ω_m, λ_m, and λ_m / h_{20}, respectively, with μ_r when $\varepsilon_1(5.5) > \varepsilon_2(3.0)$. The plots (d), (e), and (f) show the variations of ω_m, λ_m, and λ_m / h_{20}, respectively, with μ_r when $\varepsilon_2(5.5) > \varepsilon_1(3.0)$. For the plots (g) – (i), the solid (broken) line represent σ_1 (σ_2) is fixed at 10^{-11} S/m. The plots (g), (h), and (i) show the variations of ω_m, λ_m, and λ_m / h_{20} with conductivity ratio (σ_r) for the LL bilayer. In the other plots, the conductivity of the films is fixed to 10^{-11} S/m. The other necessary parameters used for all plots are shown in SET II of Table 3.1.

Plots (g) – (i) show that for a LL bilayer although the ratio of conductivities ($\sigma_r = \sigma_2 / \sigma_1$) can significantly alter the time scale of instability, it has hardly any influence on the length scale. Concisely, Figure 3.6 conveys that the patterns with wide range of length scale starting from a few microns to a few hundred nanometers can be fabricated by simply tuning the viscosities of the leaky bilayers. However, tuning the conductivities of the films can only alter the speed at which the structures form.

3.5.2 Nonlinear Simulations

Figures 3.7 – 3.11 summarize the results obtained from the nonlinear simulations in which Figures 3.7, 3.8, and 3.10 show the spatiotemporal 2-D simulations and Figures 3.9 and 3.11 show the 3-D morphologies after long-time evolution. The simulations are performed in the parameter space where the instability has long-wave characteristics. In addition to the interfacial deformations (first column), the 2-D simulations show the time history of the charge accumulation at the interfaces (second column), which conveys the influence of the free charge concentration on the development of various interfacial patterns.

Figure 3.7 shows the 2-D evolution of DD, LD, DL, and LL bilayers when $\varepsilon_1 > \varepsilon_2$. Curves 1 – 3 in plot (a) shows that in response to initial random perturbation, the interfaces of DD bilayer [$Q_1 = Q_2 = 0$ in plot (b)] evolve towards the anode and form an array of concentric core-shell columns with the lower layer as core and the upper layer as shell (curve 3).[8,11] In this situation, the larger electrical stress because of the induced charge separation ensures a faster evolution of liquid-air interface followed by the deformation of the liquid-liquid interface. Plot (c) shows that introduction of charge leakage to the lower layer leads to a negatively charged liquid-liquid interface [$Q_1 < 0$ and $Q_2 = 0$ in the curve 1 of plot (d)]. With time, increase in free charge concentration fuels up a faster deformation of the

liquid-liquid interface towards the upper electrode as compared to the rather slowly evolving liquid-air interface under the sole influence of induced charge separation [curves

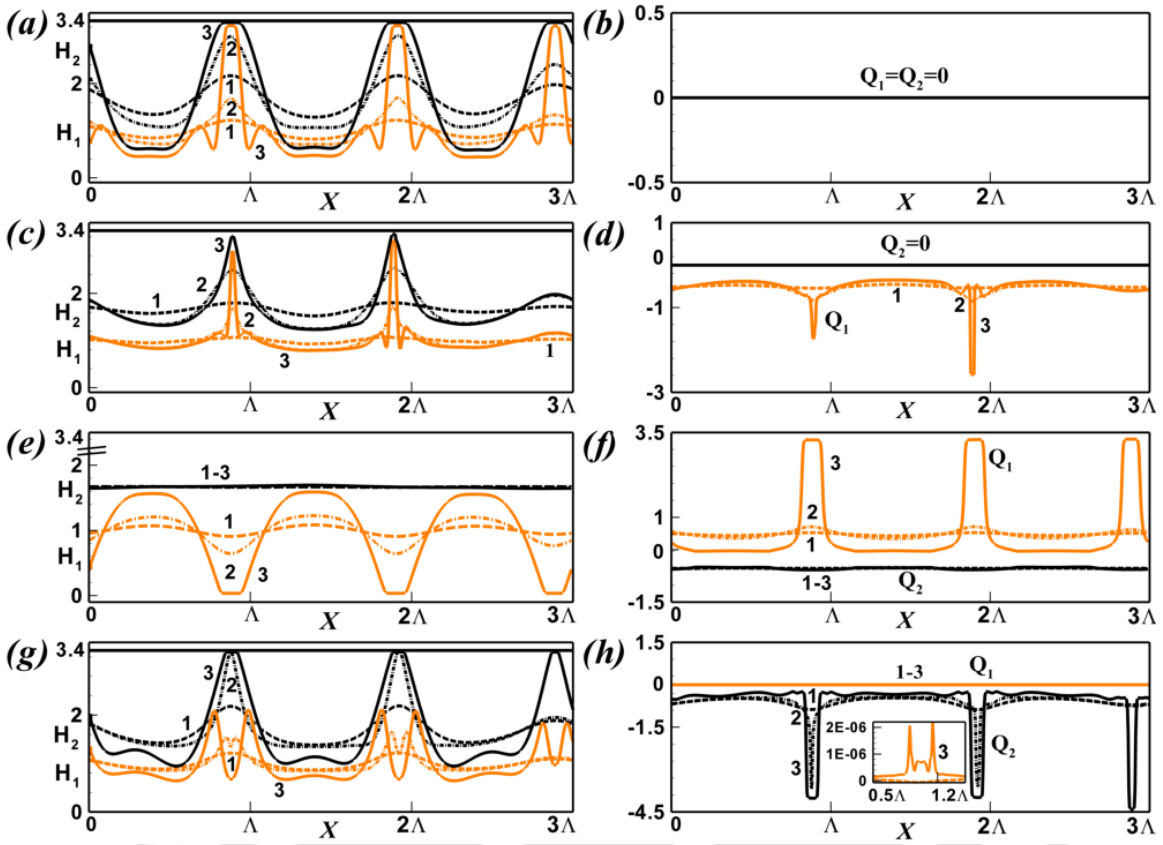

Figure 3.7 2-D spatiotemporal evolution of bilayers over a 3Λ domain when d = 0.5 μm and ε_1 (3.0) > ε_2 (2.0). Plots (a) and (b) correspond to a DD bilayer, plots (c) and (d) correspond to a LD bilayer, plots (e) and (f) correspond to a DL bilayer, and plots (g) and (h) correspond to a LL bilayer. The curves 1 – 3 in the plots (a), (c), (e), and (g) indicate the evolution of H_1 and H_2 whereas the same in the plots (b), (d), (f), and (h) show the evolution of Q_1 and Q_2. The curves 1 – 3 in the plots (a) and (b) correspond to T = 6.6 × 10^4, 7.7 × 10^4, and 9.7 × 10^4; in the plots (c) and (d) correspond to T = 6.8 × 10^3, 10.5 × 10^3, and 10.7 × 10^3; in the plots (e) and (f) correspond to T = 1.1 × 10^4, 1.4 × 10^4, and 1.1 × 10^6; and in the plots (g) and (h) correspond to T = 913, 954, and 1095. The other necessary parameters are shown in the SET I of Table 3.1.

2 and 3 in the plots (c) and (d)]. The columns at the liquid-liquid interface grow exactly at the places where the negative charges accumulate with time. Thus, in contrast to DD bilayers, for the LD bilayers, the 'cores' at the lower layer develop at a much faster pace than the 'shells' at the upper layer. In long time, the cores formed at the lower layer are

expected to pierce through the shells formed at the liquid-air interface. This particular phenomenon could not be captured through the present computational approach because the crossing over of the interfaces is restricted by the repulsion terms in the Eqs. (3.4.7) and (3.4.8), which are essential to avoid the contact line singularities. Plot (e) shows another interesting situation where a DL bilayer with a pair of charged interfaces evolve with time [$Q_1 > 0$ and $Q_2 < 0$ in plot (f)]. The curves 1 – 3 show that a weak interfacial tension together with the attractive force between the positively charged liquid-liquid interface and the cathode can form periodic holes in the lower layer. Since the negatively charged liquid-air interface evolves at a much a slower rate, even after long time evolution the holes remain embedded underneath a rather unperturbed upper layer. Plots (e) and (f) together convey that the temporal growth of the positive charge concentration at the liquid-liquid interface can lead to an array of holes embedded inside the upper layer. Curves 1 – 3 in the plots (g) and (h) show that for a LL bilayer, a negatively (positively) charged liquid-air (liquid-liquid) interface deforms toward the anode (cathode). Interestingly, the curve 1 suggests that the initial deformations of the interfaces are towards the anode when the stresses originating from the induced charge separation across the interface dominates. However, with time the electrical stresses because of free charge accumulation start controlling the deformations. This expedites the growth of the columns at the negatively charged liquid-air interface towards anode and deforms the positively charged liquid-liquid interface towards the cathode. The inset in plot (h) shows the build-up of the positive charge at the liquid-liquid interface at the later stage of evolution. After long time evolution an array of holes in the lower layer is found to be embedded inside an array of the columns in the upper layer. The interfacial morphology shown in the plots (a), (c), (e), and (g) convey that the introduction of the charge leakage to any of the films of a

bilayer can significantly alter the pathway of evolution due to the spatial and temporal variations in the charge concentrations at the interfaces.

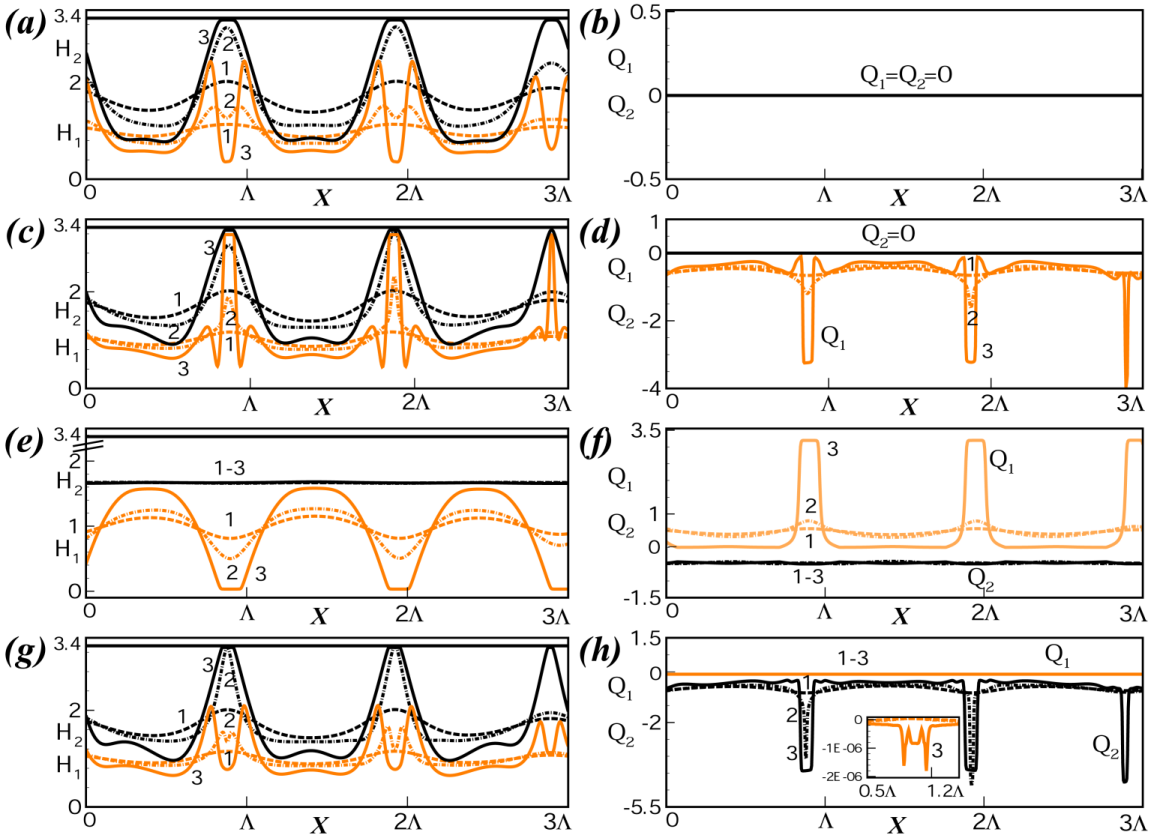

Figure 3.8 2-D spatiotemporal evolution of bilayers over a 3Λ domain when d = 0.5 μm and ε_1 (2.0) < ε_2 (3.0). Plots (a) and (b) correspond to a DD bilayer, plots (c) and (d) correspond to a LD bilayer, plots (e) and (f) correspond to a DL bilayer and plots (g) and (h) correspond to a LL bilayer. The curves 1 – 3 in the plots (a), (c), (e), and (g) indicate the evolution of H_1 and H_2 whereas the same in the plots (b), (d), (f), and (h) show the evolution of Q_1 and Q_2. The curves 1 – 3 in the plots (a) and (b) correspond to T = 7.1 × 10^4, 8.4 × 10^4, and 9.6 × 10^4; in the plots (c) and (d) correspond to T = 4.0 × 10^3, 4.6 × 10^3, and 5.3 × 10^3; in the plots (e) and (f) correspond to T = 0.7 × 10^4, 0.8 × 10^4, and 4.2 × 10^5; and in the plots (g) and (h) correspond to T = 862, 954, and 1084. The other necessary parameters are shown in the SET I of Table 3.1.

Figure 3.8 shows the 2-D nonlinear simulations for DD, LD, DL, and LL bilayers when $\varepsilon_1 < \varepsilon_2$. Curves 1 – 3 in plot (a) show that for a DD bilayer [$Q_1 = Q_2 = 0$ in plot (b)] the liquid-air (liquid-liquid) interface evolves towards the anode (cathode) because of the stress due to the induced charge separation originating from the dielectric-contrast across

the interfaces.[8,11] Plot (c) shows that introduction of charge leakage at the lower layer leads a negatively charged liquid-liquid interface [$Q_1 < 0$ and $Q_2 = 0$ in plot (d)]. In consequence, the liquid-liquid interface is attracted towards the anode and forms an array of core-shell structures (curves 1 – 3) when the stress due to charge accumulation overpowers the stress originating from the induced dipoles. The progressive accumulation of the negative charge at the liquid-liquid interface is shown by the curves 1 – 3 in the plot (d). The plot shows that the columns formed exactly at those places where the negative charge concentration is highest at the liquid-liquid interface. It may be noted here that, in this case, the liquid-air interface deforms towards the anode because in absence of any charge the stresses originating from the induced charge separation dictates the course of deformation. Curves 1 – 3 in plot (e) show that the evolution of a DL bilayer [$q_1 \neq 0$ and $q_2 \neq 0$ in plot (f)] where an attractive force between the positively charged liquid-liquid interface and cathode can form periodic holes in the lower layer embedded under an almost unperturbed upper layer. The positive charge concentration at the liquid-liquid interface shoots up very fast during the time of hole-formation as shown by the plot (f). Curves 1 – 3 in the plots (g) and (h) show that for a LL bilayer a negatively charged liquid-air interface forms columns toward the anode whereas a liquid-liquid interface with very small negative charge concentration [inset plot (h)] forms columns towards the cathode under the influence of the stresses due to the induced charge separation. This particular simulation is an example where the stresses due to induced charge separation overpower the stresses originating from the free charges at the liquid-liquid interface. Thus, after long time evolution, an array of holes in the lower layer embedded inside the columns formed in the upper layer can be observed, as is found for the similar DD

bilayers. The only difference is that the morphologies for the LL bilayers are found to form at a much faster rate as compared to the DD bilayer.

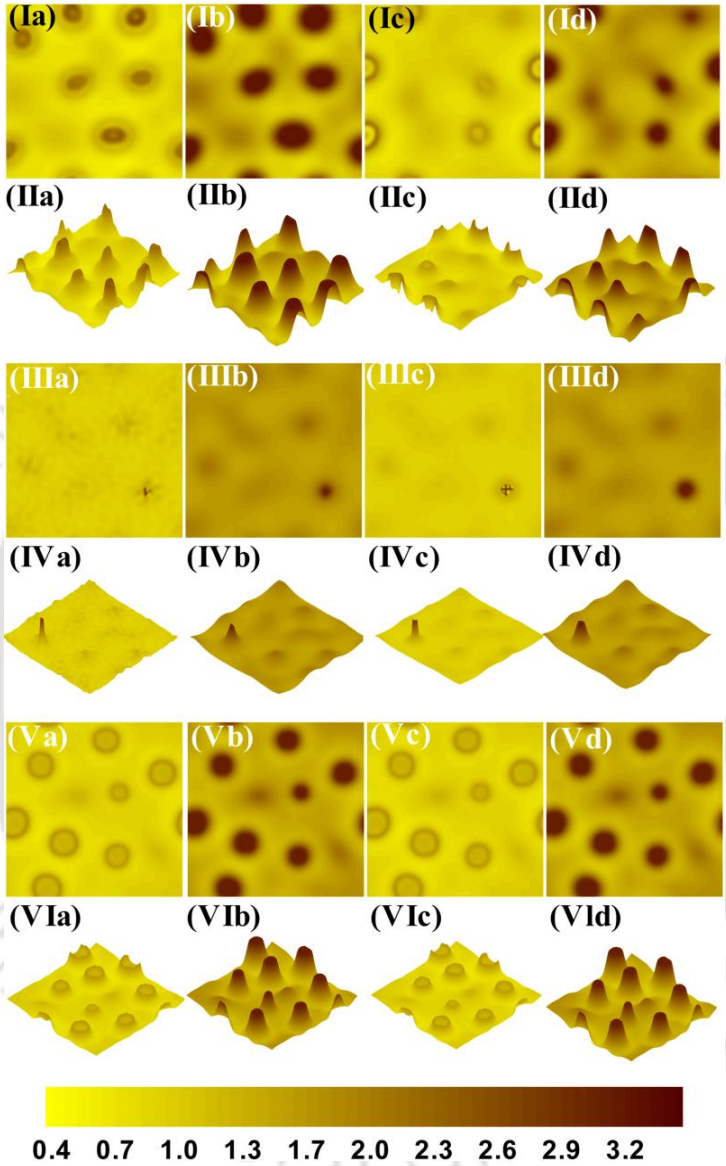

Figure 3.9 Final morphologies from the 3-D simulations over a 3Λ × 3Λ domain when d = 0.5 µm. The columns (a) and (b) correspond to $\varepsilon_1(3.0) > \varepsilon_2(2.0)$ [(c) and (d) correspond to $\varepsilon_1(2.0) < \varepsilon_2(3.0)$]. Rows (I) and (II) show DD bilayers, rows (III) and (IV) show LD bilayers, and rows (V) and (VI) show LL bilayers. Rows (I), (III), and (V) show the top view [(II), (IV), and (VI) show 3-D surface profiles]. Images (Ia), (Ib), (IIa), and (IIb) correspond to $T = 8.3 \times 10^4$; images (Ic), (Id), (IIc), and (IId) correspond to $T = 7.5 \times 10^4$; images (IIIa), (IIIb), (IVa), and (IVb) correspond to $T = 9.3 \times 10^3$; images (IIIc), (IIId), (IVc), and (IVd) correspond to $T = 4.3 \times 10^3$; images (Va), (Vb), (V1a), and (V1b) correspond to $T = 10^3$; images (Vc), (Vd), (VIc), and (VId) correspond to $T = 10^3$. The other necessary parameters are shown in the SET I of Table 3.1.

Figure 3.9 shows the electric field induced long time 3-D morphologies of the configurations simulated in the Figure 3.7 and 3.8. Plots (a) and (b) in the rows (I) and (II) show that a DD bilayer with $\varepsilon_1 > \varepsilon_2$ forms an array of columnar structures with lower layer core and upper layer shell, as previously observed in Figure 3.7a. Plots (c) and (d) in the rows (I) and (II) show that a DD bilayer with $\varepsilon_1 > \varepsilon_2$ forms an array of holes in the lower layer embedded inside the columns in the upper layer, as observed in Figure 8a. Introduction of charge leakage to the lower layer of these bilayers expedites the formation of the columns at the lower layer as can be observed in the rows (III) and (IV). The plots (a) and (b) [(c) and (d)] resemble the 3-D morphologies for the same configuration shown in Figure 3.7c [Figure 3.8c]. Plots (a) and (b) in the rows (V) and (VI) show that for a LL bilayer with $\varepsilon_1 > \varepsilon_2$, the positively charged liquid-liquid interface forms holes at the lower layer and the liquid-air interface deforms toward the anode, as previously observed in the Figure 3.7g. Plots (c) and (d) in the rows (V) and (VI) show that for a LL bilayer with $\varepsilon_1 < \varepsilon_2$, the influence of induced dipoles supersede the influence of charge leakage to deform the liquid-liquid interface towards the cathode whereas the liquid-air interface grows towards the anode, as previously observed in the Figure 3.8g. Figures 3.7 – 3.9 together convey that the presence positively or negatively charged interface(s) in leaky bilayers can show entirely different interfacial patterns as compared to the same observed for the purely dielectric bilayers. In particular, by spatiotemporal variation in the nature and concentration of the free charge at the interface(s), a host of interesting patterns such as an array of core-shell structures, holes underneath columns or holes underneath a continuous layer can be fabricated.

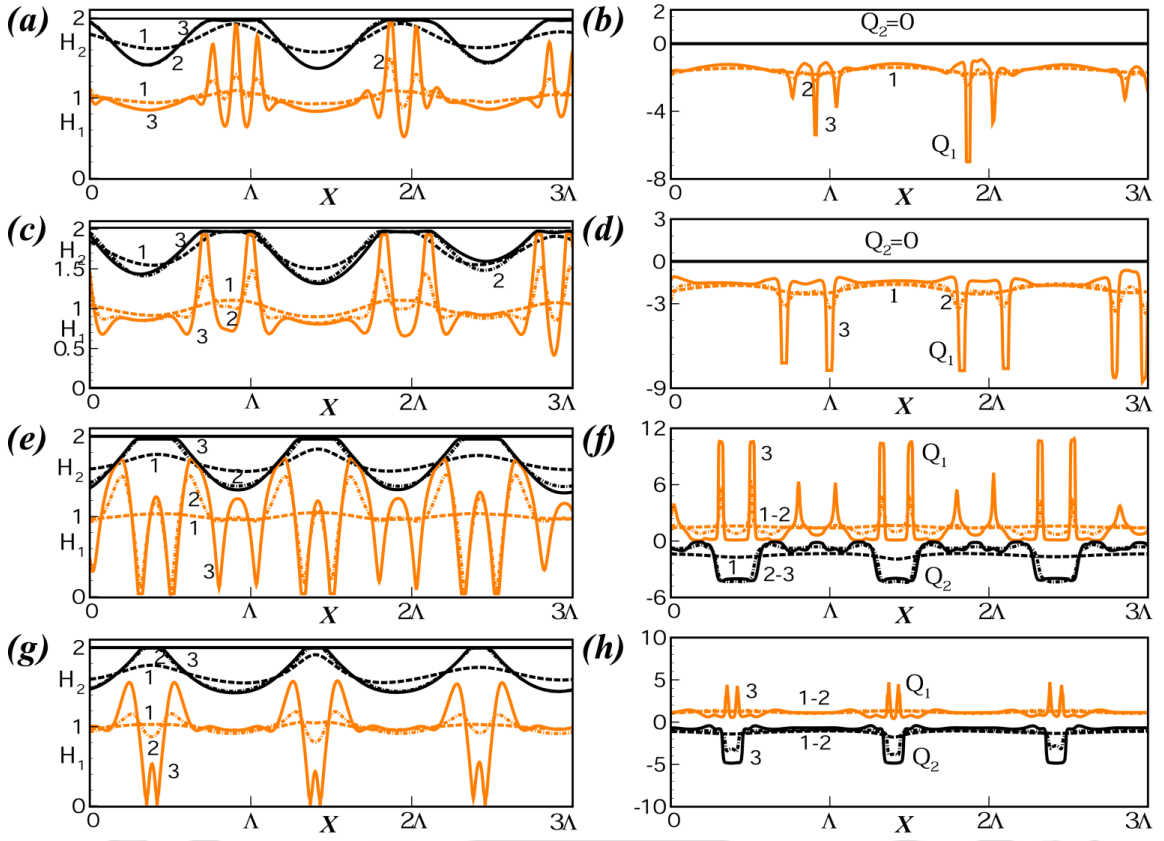

Figure 3.10 2-D spatiotemporal evolution of bilayers over a 3Λ domain when d = 0.3 μm and h_{20} = 0.26 μm for (a) – (d) [h_{20} = 0.25 μm for (e) – (h)]. Plots (a), (b), (e) and (f) correspond to ε_1 (3.0) > ε_2 (2.0) [(c), (d), (g) and (h) correspond to ε_1 (2.0) < ε_2 (3.0)]. Plots (a) – (d) correspond to LD bilayers whereas the plots (e) – (h) correspond to DL bilayers. The curves 1 – 3 in the plots (a), (c), (e), and (g) indicate the evolution of H_1 and H_2 whereas the same in the plots (b), (d), (f), and (h) show the evolution of Q_1 and Q_2. The curves 1 – 3 in the plots (a) and (b) correspond to T = 8.5, 13.0, and 14.7; in the plots (c) and (d) correspond to T = 2.2, 5.0, and 6.9; in the plots (e) and (f) T = 4.2, 25.1, and 55.8; and in the plots (g) and (h) correspond to T = 10.0, 15.3, and 36.4. The other necessary parameters are shown in the SET I of Table 3.1.

Figures 3.10 and 3.11 show some special cases where we could observe morphologies similar to a previous work[12] where the lower layer splits into cage like structures and encapsulates the columns formed in the upper layer. It may be noted here that all the cases selected in these figures show a bimodal behavior in the GLSA, which means the ω vs. k plots possess two maxima. In such a scenario, the interfaces are expected to grow at two different wavelengths.[8,11]

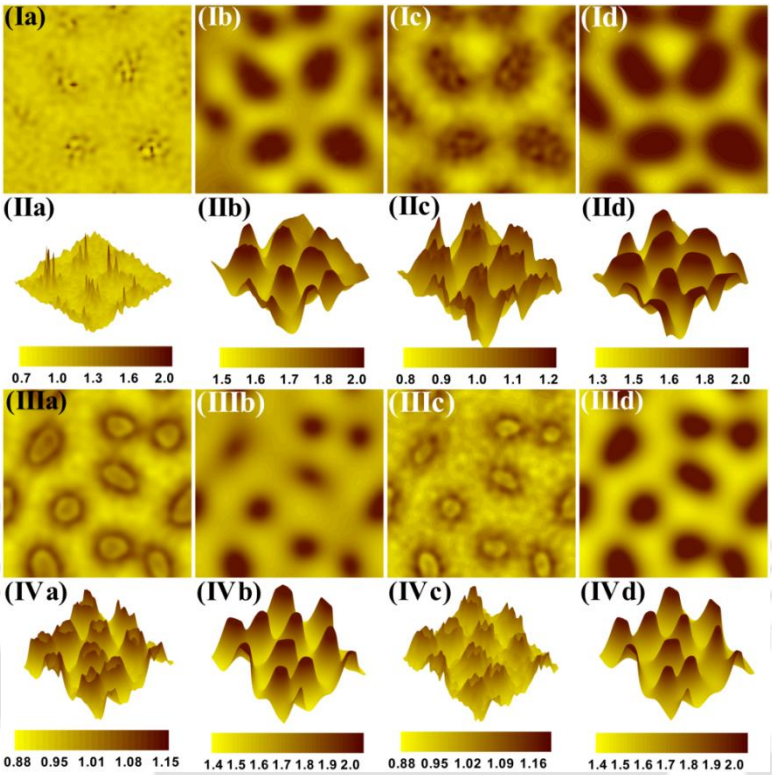

Figure 3.11 Final 3-D morphologies over a 3Λ × 3Λ domain when d = 0.3 μm. Images in the columns (a) and (b) correspond to ε_1 (2.0) > ε_2 (3.0) [(c) and (d) correspond to ε_1 (2.0) < ε_2 (3.0)]. Rows (I) and (III) show the top view [(II) and (IV) show 3-D surface profiles]. Images (Ia) – (IId) correspond to LD bilayers where columns (a) and (b) correspond to T = 12.4 [columns (c) and (d) correspond to T = 3.8]. Images (IIIa) – (IVd) correspond to DL bilayers where columns (a) and (b) correspond to T = 3.5 [columns (c) and (d) correspond to T = 12.5]. The other necessary parameters are shown in the SET I of Table 3.1.

The curves 1 – 3 in Figure 3.10a show that when $\varepsilon_1 > \varepsilon_2$, the charge leakage at the liquid-liquid interface of a LD bilayer can form multiple columns at the lower layer under a single column at the upper layer. Figure 3.10b indicates that the columns are formed exactly at the places where the negative charge concentration grows temporally at the liquid-liquid interface. Plots (a) and (b) in the rows (I) and (II) of Figure 3.11 show the 3-D morphology of a collection of columns in the lower layer embedded inside each single column in the upper layer. In Figure 3.10c we follow exactly the same conditions as set for Figure 3.10a other than $\varepsilon_1 < \varepsilon_2$. In such a situation, the liquid-liquid interface gets

negatively charged (Figure 3.10d) and with time, the interfacial waves get attracted towards the anode and form multiple columns under each column at the upper layer. Plots (c) and (d) in the rows (I) and (II) of Figure 3.11 show 3-D morphologies of a bundle of columns at the lower layer under each upper layer column. Interestingly, the depression adjacent to the bundle of columns at the lower layer form a central hole and the columnar structures surrounding the hole projects out towards the anode, which indicates the onset of the cage like structures at the lower layer encapsulating the upper layer.[12] We could not progress beyond this stage of evolution to exactly capture the cage like structures because that requires crossing over of the interfaces, which is beyond the scope of the present computational approach as mentioned previously. Figure 3.10e shows that a DL bilayer with positively charged liquid-liquid interface (Figure 3.10f) and $\varepsilon_1 > \varepsilon_2$ can deform into multiple holes surrounding a droplet at the center, under a single column at the upper layer. Again, the hole-rims surrounding the holes grow toward the anode to form a bundle of columnar structures. Interestingly, if the conditions are changed to $\varepsilon_1 < \varepsilon_2$, the morphology remains largely similar (Figure 3.10g). The corresponding 3-D interfacial structures for the DL bilayers in the rows (III) and (IV) of Figure 3.11 show the presence of an assembly of holes, droplets, and columns under each upper layer column. The 3-D simulations corroborate the onset of cage like structures surrounding the droplet at the center. The Figures 3.10 and 3.11 convey that interesting interfacial patterns can be fabricated employing the DL and LD bilayers, which are otherwise difficult to obtain from the conventional patterning techniques.

3.6 SUMMARY

We explore the influence of charge leakage on the electric field induced interfacial instabilities of thin bilayers with the help of linear stability analysis together with nonlinear simulations. The major conclusions are,

(i) The general linear stability analysis considers the full descriptions of the Maxwell stresses in the formulation and uncovers the short-wave features of the electric field induced instabilities of thin bilayers with leaky dielectric films. In this regard, the inadequacy of the long-wave analysis is highlighted especially when stronger destabilizing electrical stresses reduce the length scale to the order of film thickness.

(ii) When a bilayer is exposed to an external electrostatic field, a weakly conducting lower layer can develop free charges at the liquid-liquid interface whereas a leaky upper layer can develop free charges at both the interfaces. Importantly, introduction of weakly conducting liquid layers in a bilayer can fuel up coupled electrical stresses at the interface(s) due to the accumulation of the free charges together with the induced charge separation. The GLSA uncovers that the presence of weak conductivity at any of the layers or both the layers can significantly reduce the length scale of the instability. In particular, when the instability is dominated by the deformation of the liquid-liquid interface with a weaker stabilizing interfacial tension, the wavelength of instability can be pushed to the nanoscale regime.

(iii) The charge concentration(s) are found to vary spatiotemporally at the interface(s) to develop a wide range of destabilizing force field with the variations in the thickness, viscosity, and dielectric permittivity of the films. A host of interesting patterns such as arrays of (i) holes or columns or droplets or a combination of these embedded inside the columns, (ii) columns encapsulated by a ‘cage’ of columns, (iii) core-shell columns, and

(iv) holes embedded inside unperturbed layer are obtained by tuning the charge concentrations at the interfaces. Although the patterns shown here are rather randomly distributed, a large area ordering can easily be expected when the electrodes are pre-decorated with physicochemical patterns. Importantly, a wide range of interesting patterns such as an ordered array of open/closed pores, cavities, and channels can be obtained from these embedded/encapsulated structures when one of the layers is selectively removed. The self-organized encapsulated and embedded patterns obtained in this work are difficult to obtain employing the conventional lithographic techniques or from the electric field induced instabilities of a single layer.

In summary, a comprehensive study of electric field induced instabilities of leaky bilayers is presented, which can motivate future experiments together with applications related to self-organized patterning to basic understanding of electric field induced instabilities of leaky materials.

3.7 REFERENCES

1. S. A. Roberts and S. Kumar, Phys. Fluids **22**, 122102 (2010).
2. R. S. Allan and S. G. Mason, Proc. R. Soc. Lond. A **267**, 62 (1962).
3. J. R. Melcher and G. I. Taylor, Annu. Rev. Fluid Mech. **1**, 111 (1969).
4. D. A. Saville, Annu. Rev. Fluid Mech. **29**, 27 (1997).
5. D. J. Griffiths, *Introduction to Electrodynamics* (Prentice Hall of India Pvt. Ltd., New Delhi, 1988).
6. R. Verma, A. Sharma, K. Kargupta and J. Bhaumik, Langmuir **21**, 3710 (2005).
7. V. Shankar and A. Sharma, J. Colloid Interface Sci. **274**, 294 (2004).
8. D. Bandyopadhyay, A. Sharma, U. Thiele and P. D. S. Reddy, Langmuir **25**, 9108 (2009).
9. M. D. Morariu, N. E. Voicu, E. Schäffer, Z. Lin, T. P. Russell and U. Steiner, Nat. Mater. **2**, 48 (2003).

10. K. A. Leach, S. Gupta, M. D. Dickey, C. G. Willson and T. P. Russell, Chaos **15**, 047506 (2005).
11. P. D. S. Reddy, D. Bandyopadhyay and A. Sharma, J. Phys. Chem. C **114**, 21020 (2010).
12. M. D. Dickey, S. Gupta, K. A. Leach, E. Collister, C. G. Willson and T. P. Russell, Langmuir **22**, 4315 (2006).

Chapter 4

Electro-Capillary Instabilities of Thin Liquid Crystal Films: Influence of Dielectric Anisotropy

ABSTRACT

The free surface of a thin anisotropic liquid crystal film can undergo deformation in presence of an electrostatic field when the destabilizing effect due to the applied electric field and Ericksen stress overcome the combined stabilizing influences from the capillary force and the bulk elastic force. A general linear stability analysis of the Ericksen-Leslie governing equations for the flow field and the Maxwell stresses for the anisotropic electric field uncover that the time and the length scales of the interfacial deformations can significantly vary with the dielectric anisotropy and the molecular orientation inside the film. Enforcing a host of different boundary conditions such as homeotropic-homeotropic, planer-planer, homeotropic-planer, and planer-homeotropic at the nematic-solid and nematic-air interfaces, the domain of dominance of the destabilizing Ericksen elastic stress and the external electrostatic field have been identified. The homeotropic-planer combination at the free surface and solid-nematic interface, respectively, shows smaller length and time scales of instability as compared to the similar isotropic cases when the film has a positive dielectric anisotropy. In contrast, enforcing planer-homeotropic combination at the free surface and solid-nematic interface leads to larger length and time scales of instability when the film has a negative dielectric anisotropy. The planer-planer conditions at the boundaries are always found to show larger length and time scales as compared to the films with homeotropic-homeotropic boundaries because in the latter case the molecules are already aligned in the direction of the applied external field. Alongside the boundary conditions, the variation in the applied voltage, film thickness, dielectric anisotropy of the film, and distance between the electrodes are also found to significantly influence the molecular orientations inside the film to change the spatiotemporal scales of the instabilities of nematic films. The general analysis could asymptotically reproduce the

analytical results obtained for the long-wave analysis of the electrohydrodynamic instabilities of the nematic and isotropic films. Concisely, the study highlights some of the fundamental aspects of the influence of molecular orientations on the electric field induced instabilities of a thin nematic film.

The manuscript on this chapter is under preparation.

4.1 INTRODUCTION

In the present chapter, we want to uncover the free-surface instabilities of a thin nematic LC film, as schematically shown in Figure 4.1. For the sake of simplicity in the mathematical operations we assume that the LC film is isothermal, non-conducting, and deforming under the influence of an external DC field. This is contrast to the system studied by Ostwald[1,2] where the film was under the constant exposure of a thermal gradient together with an AC electric field. Further, we replace the confining isotropic liquid with a non-influential fluid like air, which ensured that the configuration under consideration resembles more the system employed by Schäffer et al.,[3] with the exception that the film is composed of a LC material. The coupled Ericksen-Leslie equations with full description of the Maxwell stresses together with appropriate boundary conditions, for example, homeotropic, planer, or a combination of these two at the boundaries, are linearized to estimate the length and time scale of the instabilities. The numerical results are validated against an approximate analytical long-wave analysis in the isotropic as well as in the anisotropic limit. In particular, we focus on solving the director field with different combinations of homeotropic-homeotropic, planer-planer, planer-homeotropic, and homeotropic-planer boundary conditions at the NI (nematic-air) and NS (nematic-solid) interfaces to show the salient features of the molecular orientation on the length and the time scales of the instabilities. The study highlights that the free surface of a nematic LC film can show a long-wave interfacial instability, which does not require a critical field intensity to set in. Further, the dielectric anisotropy of the film can not only alter the length and the times scale of the instabilities but also can enforce pattern miniaturization. Concisely, the study makes a useful contribution in studying the field induced instabilities and subsequent pattern formation of thin LC films.

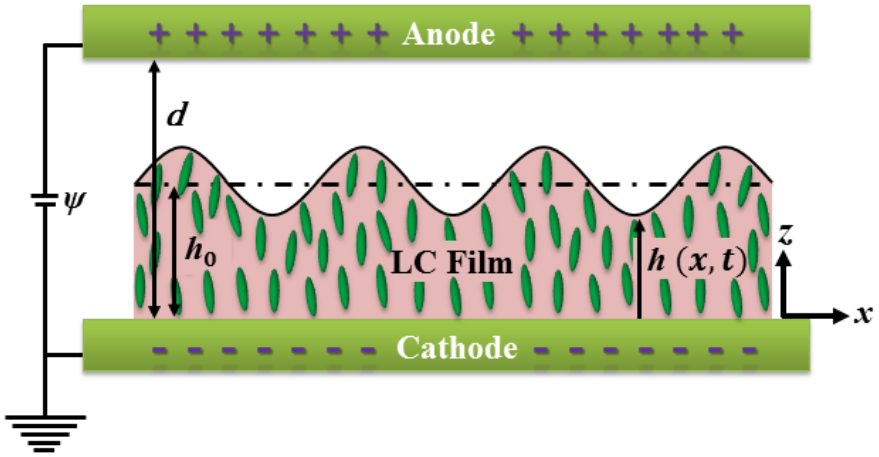

Figure 4.1 Schematic diagram of a nematic liquid crystal (LC) film deforming under the influence of an external electric field. The mean and the local thicknesses of the LC film are denoted by h_0 and h (x, t), respectively, and the distance between the electrodes is d. The anode and the film surface are separated by a dielectric material such as air.

4.2 THEORETICAL MODEL

Figure 4.1 schematically shows a thin nematic film exposed to an external electric filed applied through a pair of electrodes. The film rests on one of the electrodes while the other electrode maintains an air gap from the free-surface of the film. A two-dimensional (2-D) Cartesian coordinate system is employed for the formulation with the origin fixed at the NS interface. In the formulation, x and z are the coordinates parallel and normal to the lower electrode, notation t represents time, the bold variables indicate vectors, the bold variables with over bar indicate tensors, the superscript dot represents time derivative, the subscripts x and z with a comma preceding denote partial differentiation, and subscripts x and z denote components of the vector or the tensor. The variable film thickness is denoted by, $h(x,t)$ while the base-state thickness is denoted by h_0, as shown in Figure 4.1. The symbols $\mathbf{n}$, $\mathbf{u}$, p, κ, F, K_f, α_i, γ, ϕ_e, $\mathbf{g}$, $\mathbf{G}$, $\bar{\mathbf{M}}$, and $\bar{\boldsymbol{\tau}}$ denote the director vector, velocity vector, pressure, curvature, Frank's elastic energy, Frank's constant, Leslie coefficients, surface energy, excess pressure due to the electric field, the intrinsic director

body force, the external director body force, Maxwell stress tensor, and the hydrodynamic stress tensor, respectively. In the LC film the long axes of the rod like molecules largely stay parallel to each other, which lead to a long-range orientational order quantified by the director vector **n,** $\left(n_x = \sin\theta, n_z = \cos\theta\right)$.

The incompressible and isothermal films are assumed to be thin enough to neglect the local and the convective accelerations and the gravitational body forces. The following continuity equation, equations of motion, and balance of couples describe the dynamics of a nematic LC film,[4–10]

$$\mathbf{n}\cdot\mathbf{n} = 1, \tag{4.2.1}$$

$$\nabla\cdot\mathbf{u} = 0, \tag{4.2.2}$$

$$-\nabla\cdot\bar{\mathbf{\Pi}} + \nabla\cdot\left(\bar{\boldsymbol{\tau}} + \bar{\mathbf{M}}\right) = 0, \tag{4.2.3}$$

$$\lambda\mathbf{n} - \frac{\partial F}{\partial \mathbf{n}} + \nabla\cdot\left(\frac{\partial F}{\partial \nabla\mathbf{n}}\right) + \mathbf{G} + \mathbf{g} = 0. \tag{4.2.4}$$

In these expressions the variables for the Frank's free energy (F), the external director body force due to electric field ($\mathbf{G}$), and the intrinsic director body force ($\mathbf{g}$) are defined as,

$$F = 0.5K_f\left[\left(\bar{\nabla}\cdot\mathbf{n}\right)^2 + \left|\bar{\nabla}\times\mathbf{n}\right|^2\right], \tag{4.2.5}$$

$$\mathbf{G} = \varepsilon_0\varepsilon_a\left(\mathbf{E}\cdot\mathbf{n}\right)\mathbf{E}, \tag{4.2.6}$$

$$\mathbf{g} = -\lambda_1\mathbf{N} - \lambda_2\left(\bar{\mathbf{e}}\cdot\mathbf{n}\right). \tag{4.2.7}$$

The symbol ε_0 in these expressions represent the dielectric permittivity of free space and ε_a is the difference in the dielectric constants parallel ($\varepsilon_{\parallel}$) and perpendicular ($\varepsilon_{\perp}$) to the electric field.[11] The notation K_f is the bulk elastic constant of the liquid crystal film within

the domain of one constant approximation.[11] In the Eq. (4.2.7) the strain tensor is defined as, $\bar{\mathbf{e}} = 0.5\left(\nabla\mathbf{u} + \nabla\mathbf{u}^T\right)$, the rotation vector is defined as, $\mathbf{N} = \dot{\mathbf{n}} - \boldsymbol{\omega}\cdot\mathbf{n}$, and the spin tensor is defined as, $\bar{\boldsymbol{\omega}} = 0.5\left(\nabla\mathbf{u} - \nabla\mathbf{u}^T\right)$. The tensor $\bar{\bar{\boldsymbol{\Pi}}}$ is defined as,

$$\bar{\bar{\Pi}} = p\bar{\bar{\mathbf{I}}} + \frac{\partial F}{\partial \nabla\mathbf{n}}\cdot\left(\nabla\mathbf{n}\right)^{\mathbf{T}}. \tag{4.2.8}$$

The constitutive relation for a nematic liquid crystal is defined as,[8–10,12,13]

$$\bar{\boldsymbol{\tau}} = \alpha_1\bar{\mathbf{e}} : \mathbf{nnnn} + \alpha_2\mathbf{nN} + \alpha_3\mathbf{Nn} + \alpha_4\bar{\mathbf{e}} + \alpha_5\mathbf{nn}\cdot\bar{\mathbf{e}} + \alpha_6\bar{\mathbf{e}}\cdot\mathbf{nn}. \tag{4.2.9}$$

Here the Leslie coefficients are denoted by the symbol, α_i. The rotational viscosity and the irrotational torque coefficient[8–10,12,13] in Eq. (4.2.7) are defined as $\lambda_1 = \alpha_3 - \alpha_2$ $\lambda_2 = \alpha_6 - \alpha_5$. The sixth Leslie coefficient, α_6 is evaluated from Onsager-Parodi relation $\lambda_2 = \alpha_6 - \alpha_5 = \alpha_3 + \alpha_5$.

The Maxwell stresses originating from the external electric field are defined as,[14,15]

$$\bar{\mathbf{M}} = \left[\mathbf{DE} - 0.5\left(\mathbf{D}\cdot\mathbf{E}\right)\bar{\mathbf{I}}\right]. \tag{4.2.10}$$

In Eq. 4.2.10 the electric displacement is defined as, $\mathbf{D} = \varepsilon_0\left[\varepsilon_\perp\mathbf{E} + \Delta\varepsilon\left(\mathbf{E}\cdot\mathbf{n}\right)\mathbf{n}\right]$ and the electric field is defined as, $\mathbf{E} = -\nabla\psi$, where ψ denotes the electric field potential.

The nematic film is assumed to be resting on a non-slipping and impermeable surface at $z = 0$,

$$\mathbf{u} = 0. \tag{4.2.11}$$

At the nematic-air interface, $z = h\left(x,t\right)$, the normal and the tangential stress balances together with the kinematic condition are enforced as the boundary conditions,

$$\mathbf{n}_\mathbf{s}\cdot\left(p_0\bar{\mathbf{I}} + \bar{\mathbf{M}}_a\right)\cdot\mathbf{n}_\mathbf{s} - \mathbf{n}_\mathbf{s}\cdot\left(-\bar{\bar{\boldsymbol{\Pi}}} + \bar{\boldsymbol{\tau}} + \bar{\mathbf{M}}\right)\cdot\mathbf{n}_\mathbf{s} = \gamma\kappa, \tag{4.2.12}$$

$$\mathbf{n_s}\cdot\bar{\mathbf{M}}_a\cdot\mathbf{t_s}-\mathbf{n_s}\cdot\left(-\bar{\mathbf{\Pi}}+\bar{\boldsymbol{\tau}}+\bar{\mathbf{M}}\right)\cdot\mathbf{t_s}=0, \tag{4.2.13}$$

$$\dot{h}=w. \tag{4.2.14}$$

Here the symbols h, γ and $\kappa=-\nabla_s\cdot\mathbf{n_s}$ denote the film thickness, surface tension, and the curvature of the deforming free surface. The subscript 'a' denotes the variables corresponding to the bounding fluid air. The notations $\mathbf{n_s}$ and $\mathbf{t_s}$ denote the unit outward normal and tangent vectors, $\nabla h/|\nabla h|$ and $\left(1\Big/\sqrt{\left(1+h_x^2\right)},h_x\Big/\sqrt{\left(1+h_x^2\right)}\right)$, respectively.

The strong anchoring boundary conditions for the director field, **n**, are imposed at NS and NI interfaces. The planar or homeotropic conditions are enforced at the NS interface ($z=0$) as,

$$\mathbf{n}\cdot\mathbf{z}=0 \text{ or } \mathbf{n}\cdot\mathbf{z}=1. \tag{4.2.15}$$

The planar or homeotropic conditions are enforced at NI interface ($z=h$) as,

$$\mathbf{n}\cdot\mathbf{t_s}=1 \text{ or } \mathbf{n}\cdot\mathbf{t_s}=0. \tag{4.2.16}$$

The nematic film is assumed to be non-conducting with a dielectric anisotropy originating from the difference in the dielectric constants in the parallel and normal to the applied field. Thus, the governing equation of an irrational electric field ($\nabla\times\mathbf{E}=0$) for a nematic film can be written as,

$$\nabla\cdot\mathbf{D}=0. \tag{4.2.17}$$

The irrotational ($\nabla\times\mathbf{E}_a=0$) electric field for the purely dielectric bounding film can be described through the following Laplace equation,

$$\nabla^2\psi_a=0. \tag{4.2.18}$$

The constant potential boundary conditions are enforced for the electric field at the cathode ($z = 0$) and anode ($z = d$),

$$\psi = 0,\ \psi_a = \psi_0 . \tag{4.2.19}$$

The normal and the tangential component balances for the electric field are enforced as boundary conditions at the NI free surface ($z = h$),

$$\mathbf{D}_a \cdot \mathbf{n}_s - \mathbf{D} \cdot \mathbf{n}_s = 0,\ \mathbf{E}_a \cdot \mathbf{t}_s = \mathbf{E} \cdot \mathbf{t}_s . \tag{4.2.20}$$

4.3 DIMENSIONLESS FORM

The following expressions are employed to transform the dimensional governing equations and boundary conditions to the dimensionless forms, $(X, Z, H, D) = (x, z, h, d)/h_0$; $T = t\left[\varepsilon_0 \psi_0^2 / 2\mu h_0^2\right]$; $(U, W) = (u, w)\left[2\mu h_0 / \varepsilon_0 \psi_0^2\right]$; $(\Psi, \Psi_a) = (\psi, \psi_a)/\psi_0$; and $(P, P_0) = (p, p_0)\left[2h_0^2 / \varepsilon_0 \psi_0^2\right]$. It may be noted here that the Newtonian viscosity ($0.5\alpha_4 = \mu$) is employed to scale the equations. The resulting dimensionless continuity equation for the nematic film is,

$$U_{,X} + W_{,Z} = 0 . \tag{4.3.1}$$

The dimensionless X- and Z-components of equations of the motion are,

$$\begin{aligned} &-P_{,X} + \left(A_1 U_{,X} + A_2 U_{,Z} + A_3 W_{,X} + A_4 W_{,Z}\right)_{,X} + \left(B_1 U_{,X} + B_2 U_{,Z} + B_3 W_{,X} + B_4 W_{,Z}\right)_{,Z} \\ &-E_r^{-1}\left[\theta_{,X}\left(\theta_{,XX} + \theta_{,ZZ}\right) + 0.5\left(\theta_{,X}^2 + \theta_{,Z}^2\right)_{,X}\right] \\ &-\varepsilon_a \theta_{,X}\left[\left(\Psi_{,X}^2 - \Psi_{,Z}^2\right)\sin 2\theta + 2\cos 2\theta\, \Psi_{,X} \Psi_{,Z}\right] = 0 \end{aligned} , \tag{4.3.2}$$

$$\begin{aligned} &-P_{,Z} + \left(C_1 U_{,X} + C_2 U_{,Z} + C_3 W_{,X} + C_4 W_{,Z}\right)_{,X} + \left(D_1 U_{,X} + D_2 U_{,Z} + D_3 W_{,X} + D_4 W_{,Z}\right)_{,Z} \\ &-E_r^{-1}\left[\theta_{,Z}\left(\theta_{,XX} + \theta_{,ZZ}\right) + 0.5\left(\theta_{,X}^2 + \theta_{,Z}^2\right)_{,Z}\right] \\ &-\varepsilon_a \theta_{,Z}\left[\left(\Psi_{,X}^2 - \Psi_{,Z}^2\right)\sin 2\theta + 2\cos 2\theta\, \Psi_{,X} \Psi_{,Z}\right] = 0 \end{aligned} . \tag{4.3.3}$$

In the above expressions the Ericksen number is defined as, $E_r = \varepsilon_0 \psi_0^2 / K_f$. The complex expressions for the variables A_i, B_i, C_i, and D_i are separately provided in the appendix. The dimensionless X- and Z-components of the balances of the couples are,

$$\begin{aligned}&\Lambda \sin\theta + E_r^{-1}\left[\left(\theta_{,XX}+\theta_{,ZZ}\right)\cos\theta - \left(\theta_{,X}^2+\theta_{,Z}^2\right)\sin\theta\right]\\&+2\varepsilon_a\left(\sin\theta\,\Psi_{,X}^2+\cos\theta\,\Psi_{,X}\Psi_{,Z}\right)\\&+0.5\left[\Lambda_1\cos\theta\left(U_{,Z}-W_{,X}\right)-\Lambda_2\left[2\sin\theta U_{,X}+\cos\theta\left(U_{,Z}+W_{,X}\right)\right]\right]=0\end{aligned}, \tag{4.3.4}$$

$$\begin{aligned}&\Lambda \cos\theta + E_r^{-1}\left[\left(\theta_{,XX}+\theta_{,ZZ}\right)\sin\theta - \left(\theta_{,X}^2+\theta_{,Z}^2\right)\cos\theta\right]\\&+2\varepsilon_a\left(\cos\theta\,\Psi_{,Z}^2+\sin\theta\,\Psi_{,X}\Psi_{,Z}\right)\\&+0.5\left[\Lambda_1\sin\theta\left(U_{,Z}-W_{,X}\right)-\Lambda_2\left[2\cos\theta W_{,Z}+\sin\theta\left(U_{,Z}+W_{,X}\right)\right]\right]=0\end{aligned}. \tag{4.3.5}$$

The first terms in the Eqs. (4.3.4) and (4.3.5) are eliminated to obtain the following balance of couples,[9]

$$\begin{aligned}&E_r^{-1}\left(\theta_{,XX}+\theta_{,ZZ}\right)+\varepsilon_a\left(\sin 2\theta\left[\Psi_{,X}^2-\Psi_{,Z}^2\right]+2\cos 2\theta\,\Psi_{,X}\Psi_{,Z}\right)\\&+0.5\Lambda_1\left(U_{,Z}-W_{,X}\right)-\Lambda_2\left[\cos 2\theta\left(U_{,Z}+W_{,X}\right)-2\sin 2\theta W_{,Z}\right]=0\end{aligned}. \tag{4.3.6}$$

The non-dimensional no-slip and impermeability boundary conditions at the NS interface ($Z = 0$) are,

$$U = W = 0. \tag{4.3.7}$$

The dimensionless normal and tangential stress balances together with the kinematic condition at NI interface ($Z = H$) are,

$$\begin{aligned}&P - P_0 + E_r^{-1}\theta_{,Z}^2 - \left(D_1U_{,X}+D_2U_{,Z}+D_3W_{,X}+D_4W_{,Z}\right)\\&+\left[\varepsilon_a\left(\sin 2\theta\, H_{,X}+\cos^2\theta\right)-\varepsilon_\perp\right]\Psi_{,Z}^2+\Psi_{a,Z}^2+\Gamma H_{,XX}=0\end{aligned}, \tag{4.3.8}$$

$$E_r^{-1}\left(\theta_{,Z}^2 H_{,X}+\theta_{,X}\theta_{,Z}\right)-\left(B_1U_{,X}+B_2U_{,Z}+B_3W_{,X}+B_4W_{,Z}\right)=0, \tag{4.3.9}$$

$$H_{,T}+U\,H_{,X}=W. \tag{4.3.10}$$

In Eq. (4.3.8) the dimensionless number, $\Gamma = 2\gamma h_0 / \varepsilon_0 \psi_0^2$, signifies the ratio of the capillary to the electric field forces. The dimensionless governing equations for the electric field for nematic film and air are,

$$\left[\left(\varepsilon_\perp + \varepsilon_a \sin^2\theta\right)\Psi_{,X}\right]_{,X} + \left[\left(\varepsilon_\perp + \varepsilon_a \cos^2\theta\right)\Psi_{,Z}\right]_{,Z} = -0.5\varepsilon_a\left[\left(\sin 2\theta \Psi_{,Z}\right)_{,X} + \left(\sin 2\theta \Psi_{,X}\right)_{,Z}\right], \quad (4.3.11)$$

$$\Psi_{a,XX} + \Psi_{a,ZZ} = 0. \quad (4.3.12)$$

The dimensionless electric field boundary conditions at cathode ($Z = 0$) and anode ($Z = D$) are,

$$\Psi = 0 \text{ and } \Psi_a = 1. \quad (4.3.13)$$

The non-dimensional normal and tangential component balances of electric field at the NI free surface ($Z = H$) are,

$$\left(\varepsilon_\perp \Psi_{,Z} - \Psi_{a,Z}\right) + \varepsilon_a \cos^2\theta \Psi_{,Z} + 0.5\varepsilon_a \sin 2\theta\left(\Psi_{,X} - H_{,X}\Psi_{,Z}\right) = 0, \quad (4.3.14)$$

$$\left(\Psi_{,X} + H_{,X}\Psi_{,Z}\right) - \left(\Psi_{a,X} + H_{,X}\Psi_{a,Z}\right) = 0. \quad (4.3.15)$$

The strong anchoring boundary conditions for the director field, **n**, are imposed at NS interface and at the free surface. For this purpose, the planar or homeotropic conditions are enforced at NS interface ($Z = 0$) as,

$$\cos\theta = 0 \text{ or } \cos\theta = 1. \quad (4.3.16)$$

The planar or homeotropic conditions are enforced at the NI interface ($Z = H$) as,

$$\sin\theta + H_X \cos\theta = 1 \text{ or } \sin\theta + \delta H_X \cos\theta = 0. \quad (4.3.17)$$

It may be noted here that a long-wave (LWLSA) and a general (GLSA) linear stability analyses have been performed simultaneously in the following sections employing the non-dimensional governing equations and boundary conditions. For this purpose, a scaling

analogous to lubrication approximation has been enforced to the set of governing equations and the boundary conditions, which provides a single framework for both LWLSA and GLSA to identify the time and the length scales of the instabilities. Thus, the Eqs. (4.3.1) – (4.3.17) are rescaled employing the parameters, $\hat{X} = \delta_1 X / h_0$, $\left(\hat{U}, \delta_1 \hat{W}\right) = \left(U, W\right) / \delta_1$, and $\hat{T} = \delta_2 T$, in which, $\delta_1 = \left(\varepsilon_0 \psi^2 / 2\gamma h_0\right)^{0.5}$ and $\delta_2 = \delta_1^{-2}$.

4.3.1 Long-wave analysis

The evolution equation for NI interface can be derived employing the lubrication approximation.[11,12,16,17] For this purpose, the leading order terms of the rescaled governing equations and boundary conditions are retained. The long-wave *X*- and *Z*- components of equations of the motion, balance of couples, and the electric field potential for the nematic film and air are,

$$\left(P + 0.5 E_r^{-1} \theta_{,Z}^2\right)_{,X} = \left(B_2 U_{,Z}\right)_{,Z}, \tag{4.3.18}$$

$$\left(P + 0.5 E_r^{-1} \theta_{,Z}^2\right)_{,Z} = 0, \tag{4.3.19}$$

$$E_r^{-1} \theta_{,ZZ} = 0, \tag{4.3.20}$$

$$\left[\left(\varepsilon_\perp + \varepsilon_a \cos^2\theta\right) \Psi_{,Z}\right]_{,Z} = 0, \tag{4.3.21}$$

$$\Psi_{a,ZZ} = 0. \tag{4.3.22}$$

The leading order no-slip, impermeability for the velocity field, the grounded electric field potential, and the boundary condition at the NS interface ($Z = 0$) are,

$$U = W = \Psi = 0. \tag{4.3.23}$$

The long-wave kinematic condition, normal and tangential stress balances, and the balances of the normal and tangential components of electric field at the NI interface ($Z = H$) are,

$$H_{,T} + U H_{,X} = W, \tag{4.3.24}$$

$$\bar{P} = P_0 - H_{,XX} - 0.5 E_r^{-1} \theta_{,Z}^2 + \left(\varepsilon_\perp + \varepsilon_a \cos^2\theta\right) \Psi_{,Z}^2 - \Psi_{a,Z}^2, \tag{4.3.25}$$

$$U_{,Z} = 0, \tag{4.3.26}$$

$$\left(\varepsilon_\perp + \varepsilon_a \cos^2\theta\right) \Psi_{,Z} = \Psi_{a,Z}, \tag{4.3.27}$$

$$\Psi = \Psi_a. \tag{4.3.28}$$

The boundary condition for the electric field at the anode ($Z = D$) is,

$$\Psi_a = 1. \tag{4.3.29}$$

The director orientation boundary conditions at the substrate ($Z = 0$) and at the NI interface ($Z = H$) are enforced as,

$$\theta = \theta_1, \ \theta = \theta_2. \tag{4.3.30}$$

The final form of evolution equation is,[11,12,16,17]

$$\frac{\partial H}{\partial T} - 2I \frac{\partial}{\partial X}\left(H^3 \frac{\partial \bar{P}}{\partial X} \right) = 0. \tag{4.3.31}$$

Where I is expressed as, $I = \left(\theta_2 - \theta_1\right)^{-3} \int_{\theta_1}^{\theta_2} \frac{\left(\theta_2 - \zeta\right)^2 d\zeta}{k_1 + k_2 \sin^2\zeta - 2\hat{\alpha}_1 \sin^4\zeta}$ in which the constants $k_1 = 2 - \hat{\alpha}_2 + \hat{\alpha}_5$ and $k_2 = 2\left(\hat{\alpha}_1 + \hat{\alpha}_2 + \hat{\alpha}_3\right)$ and variable $\zeta = \theta_1 + \left[\left(\theta_2 - \theta_1\right)/H\right] s$.

4.4 LINEAR STABILITY ANALYSIS

The LWLSA and GLSA are performed based on the deformations at the NI interface follow a small-deformation kinematics and small amplitude perturbations are enforced to

the quiescent bases-state of the nematic film. The quiescent base-state ensures that the *X*- and *Z*-directional base-state velocities are non-existent, $\bar{U} = \bar{W} = 0$, and the unperturbed film thickness is constant, $\bar{H} = 1$. The governing equations and the boundary conditions are perturbed employing the normal linear modes, $\hat{U} = \tilde{U}e^{\Omega T + \mathrm{i}KX}$, $\hat{W} = \tilde{W}e^{\Omega T + \mathrm{i}KX}$, $\left(\Psi, \Psi_a\right) = \left(\bar{\Psi}, \bar{\Psi}_a\right) + \left(\tilde{\Psi}, \tilde{\Psi}_a\right)e^{\Omega T + \mathrm{i}KX}$, $H = \bar{H} + \tilde{H}e^{\Omega T + \mathrm{i}KX}$, and $\theta = \bar{\theta}\left(Z\right) + \tilde{\theta}e^{\Omega T + \mathrm{i}KX}$. Here the symbols *K* and Ω represent the dimensionless wavenumber and growth coefficient of instability, respectively. The variables with over-bar represent the base-state and the variables. The variables $\tilde{U}$, $\tilde{W}$, $\tilde{P}$, $\tilde{\theta}$, $\tilde{\Psi}_a$, $\tilde{\Psi}$, and $\tilde{H}$ represent the perturbed *X*-velocity, *Z*-velocity, pressure, director orientation, electric field potential in the film, and the electric field potential of the bounding fluid, respectively.

4.4.1 Base-state analysis

At the base-state, the governing equations for electric fields at the nematic film and air are,

$$\left[\left(\varepsilon_\perp + \varepsilon_a \cos^2\bar{\theta}\right)\bar{\Psi}_{,Z}\right]_{,Z} = 0, \tag{4.4.1}$$

$$\bar{\Psi}_{a,ZZ} = 0. \tag{4.4.2}$$

The boundary conditions for the electric field at the electrodes (*Z* = 0 and *Z* = *D*) are,

$$\bar{\Psi} = 0 \text{ and } \bar{\Psi}_a = 1. \tag{4.4.3}$$

The boundary conditions for the electric field at the NI interface ($Z = \bar{H}$) are,

$$\left(\varepsilon_\perp + \varepsilon_a \cos^2\bar{\theta}\right)\bar{\Psi}_{,Z} = \bar{\Psi}_{a,Z}, \tag{4.4.4}$$

$$\bar{\Psi} = \bar{\Psi}_a. \tag{4.4.5}$$

The governing equation for the director orientation is,

$$\bar{\theta}_{,ZZ} - E_r\varepsilon_a \sin 2\bar{\theta}\,\bar{\Psi}_{,Z}{}^2 = 0. \tag{4.4.6}$$

The director orientation boundary conditions at the NS (Z = 0) and NI interfaces (Z = H) are,

$$\bar{\theta} = \theta_1 \text{ and } \bar{\theta} = \theta_2 . \tag{4.4.7}$$

In order to obtain the base-state solutions, initially Eq. (4.4.2) is solved analytically to obtain the solution for $\bar{\Psi}_a$. Following this, the coupled Eqs. (4.4.1) and (4.4.6) representing the electric field potential of the nematic film and the director orientation field are solver numerically employing the 4th order Runga-Kutta method to obtain the solutions for $\bar{\Psi}$ and $\bar{\theta}$, enforcing the boundary conditions from Eq. (4.4.3) – (4.4.5) and (4.4.7).

4.4.2. Perturbed-state analysis

The linearized mass balance and linear momentum balance equations (4.3.1) – (4.3.3) lead to the following ordinary differential equations (ODEs),

$$\mathbf{i}K\tilde{U} + \tilde{W}_{,Z} = 0 , \tag{4.4.8}$$

$$-K^2\tilde{P} + L_1^X\tilde{W}_{,ZZZ} + L_2^X\tilde{W}_{,ZZ} + L_3^X\tilde{W}_{,Z} + L_4^X\tilde{W} + L_5^X\tilde{\theta}_{,Z} = 0 , \tag{4.4.9}$$

$$\begin{aligned} &\mathbf{i}K\tilde{P}_{,Z} + L_1^Z\tilde{W}_{,ZZZ} + L_2^Z\tilde{W}_{,ZZ} + L_3^Z\tilde{W}_{,Z} + L_4^Z\tilde{W} \\ &+L_5^Z\tilde{\theta}_{,ZZ} + L_6^Z\tilde{\theta}_{,Z} + L_7^Z\tilde{\theta} + L_8^Z\tilde{\Psi}_{,Z} + L_9^Z\tilde{\Psi} = 0 \end{aligned} . \tag{4.4.10}$$

The expressions for the variables L_i^X and L_i^Z are provided in the appendix. Eliminating the perturbed pressure from the Eqs. (4.4.8) – (4.4.10) the following 4th order ODE is obtained for the nematic film,

$$L_1\tilde{W}_{,ZZZZ} + L_2\tilde{W}_{,ZZZ} + L_3\tilde{W}_{,ZZ} + L_4\tilde{W}_{,Z} + L_5\tilde{W} + L_6\tilde{\theta}_{,ZZ} + L_7\tilde{\theta} + L_8\tilde{\Psi}_{,Z} + L_9\tilde{\Psi} = 0 . \tag{4.4.11}$$

The linearized no-slip and non-permeability boundary conditions at NS interface (Z = 0) are,

$$\tilde{W}_{,Z} = \tilde{W} = 0\,. \tag{4.4.12}$$

At NI interface ($Z = H$), the linearized kinematic equation and the normal and tangential stress balances are,

$$\tilde{H} = \tilde{W}/\Omega, \tag{4.4.13}$$

$$S_1^N \tilde{W} + \Omega \begin{pmatrix} S_2^N \tilde{W}_{,ZZZ} + S_3^N \tilde{W}_{,ZZ} + S_4^N \tilde{W}_{,Z} \\ + S_5^N \tilde{W} + S_6^N \tilde{\theta}_{,Z} + S_7^N \tilde{\theta} + S_8^N \tilde{\Psi}_{,Z} + S_9^N \tilde{\Psi}_{a,Z} \end{pmatrix} = 0\,, \tag{4.4.14}$$

$$S_1^T \tilde{W} + \Omega \left[S_2^T \tilde{W}_{,ZZ} + S_3^T \tilde{W}_{,Z} + S_4^T \tilde{W} + S_5^T \tilde{\theta} \right] = 0\,. \tag{4.4.15}$$

The linearized equation (3.6) for the balances of couples leads to the following ODE,

$$I_1 \tilde{W}_{,ZZ} + I_2 \tilde{W}_{,Z} + I_3 \tilde{W} + I_4 \tilde{\theta}_{,ZZ} + I_5 \tilde{\theta} + I_6 \tilde{\Psi}_{,Z} + I_7 \tilde{\Psi} = 0\,. \tag{4.4.16}$$

The expressions for the coefficients I_i are provided in the appendix. The linearized boundary condition for director angle at NS ($Z = 0$) and NI ($Z = \bar{H}$) interfaces are,

$$\tilde{\theta} = 0\,, \tag{4.4.17}$$

$$\tilde{\theta} = \mathbf{i}K\tilde{W}/\Omega\,. \tag{4.4.18}$$

The linearized equations for the electric field potential of the nematic film and air are,

$$J_1 \tilde{\theta}_{,Z} + J_2 \tilde{\theta} + J_3 \tilde{\Psi}_{,ZZ} + J_4 \tilde{\Psi}_{,Z} + J_5 \tilde{\Psi} = 0\,, \tag{4.4.19}$$

$$\tilde{\Psi}_{a,ZZ} + J_6 \tilde{\Psi}_a = 0\,. \tag{4.4.20}$$

The expressions for the coefficients J_i s are provided in the appendix. The linearized boundary conditions for the electric field potentials at the cathode ($Z = 0$) and anode ($Z = D$) are,

$$\tilde{\Psi} = 0 \text{ and } \tilde{\Psi}_a = 0\,. \tag{4.4.21}$$

The linearized normal and the tangential component balances at NI interface ($Z = \bar{H}$) are,

$$S_1^E \tilde{W} + \Omega\left[S_2^E \tilde{\theta} + S_3^E \tilde{\Psi}_{,Z} + S_4^E \tilde{\Psi}_{,Z} + \tilde{\Psi}_{a,Z} \right] = 0, \tag{4.4.22}$$

$$\left(\bar{\Psi}_{,Z} - \bar{\Psi}_{a,Z} \right) \tilde{W} + \Omega\left(\tilde{\Psi} - \tilde{\Psi}_a \right) = 0. \tag{4.4.23}$$

The expressions for the coefficients S_i^E are provided in the appendix. The variables $\tilde{W}$, $\tilde{\theta}$, and $\tilde{\Psi}$ are coupled in the governing equations (4.4.11), (4.4.16), (4.4.19), and (4.4.20) and the boundary conditions (4.4.12) – (4.15), (4.4.17), (4.4.18), and (4.4.21) – (4.4.23). These expressions are solved numerically employing the method discussed in the following section to obtain the time and the length scales for the electric field induced free surface instabilities of nematic films.

The kinematic Eq. (4.3.31) obtained from the lubrication approximation can also be linearized employing the normal linear modes to obtain the following dispersion relation from LWLSA,

$$\Omega = 2I\left(-K^4 - K^2 \Pi_{e,H} - K^2 E_r^{-1} \left(\Delta\theta \right)^2 \right). \tag{4.4.24}$$

The dispersion relation (4.24) provides a preliminary estimate on the length and the time scales of the electric field induced instabilities of thin nematic films. This expression is also employed to validate the results obtained from the GLSA, especially when the instability possesses long-wave characteristics.

4.5 NUMERICAL ANALYSIS

The coupled governing equations (4.4.11), (4.4.16), (4.4.19), and (4.4.20) together with the boundary conditions (4.4.12) – (4.4.15), (4.4.17), (4.4.18), and (4.4.21) – (4.4.23) is an eigenvalue problem and solved numerically employing the spectral collocation[18–20] to obtain the linear growth rate (Ω) and the corresponding wavenumber (K) for the unstable modes. For this purpose, the computational domain is mapped into a space, (-1, 1) with the

help of the transformations, $\xi = 2Z - 1$ and $\chi = \left(-2Z + D\right)/D$, for the equations corresponding to the nematic film and air, respectively. The transformed governing equations motion and electric field are,

$$\begin{aligned} &16L_1\tilde{W}_{,\xi\xi\xi\xi} + 8L_2\tilde{W}_{,\xi\xi\xi} + 4L_3\tilde{W}_{,\xi\xi\xi} + 2L_4\tilde{W}_{,\xi} + L_5\tilde{W} \\ &+L_6\tilde{\theta}_{,\xi\xi} + L_7\tilde{\theta} + L_8\tilde{\Psi}_{,\xi} + L_9\tilde{\Psi} = 0 \end{aligned}, \tag{4.5.1}$$

$$4I_1\tilde{W}_{,\xi\xi} + 2I_2\tilde{W}_{,\xi} + I_3\tilde{W} + 4I_4\tilde{\theta}_{,\xi\xi} + I_5\tilde{\theta} + 2I_6\tilde{\Psi}_{,\xi} + I_7\tilde{\Psi} = 0, \tag{4.5.2}$$

$$2J_1\tilde{\theta}_{,\xi} + J_2\tilde{\theta} + 4J_3\tilde{\Psi}_{,\xi\xi} + J_4\tilde{\Psi}_{,\xi} + J_5\tilde{\Psi} = 0, \tag{4.5.3}$$

$$\left(4/\left(D-1\right)^2\right)\tilde{\Psi}_{a,\chi\chi} + J_6\tilde{\Psi}_a = 0. \tag{4.5.4}$$

The transformed boundary conditions at NS interface ($\xi = -1$) are,

$$\tilde{W} = \tilde{W}_{,\xi} = 0, \tag{4.5.5}$$

$$\tilde{\Psi} = 0, \tag{4.5.6}$$

$$\tilde{\theta} = 0. \tag{4.5.7}$$

The transformed boundary conditions at NI interface ($\xi = 1$ and $\chi = 1$) are,

$$S_1^N\tilde{W} + \Omega\begin{pmatrix} 8S_2^N\tilde{W}_{,\xi\xi\xi} + 4S_3^N\tilde{W}_{,\xi\xi} + 2S_4^N\tilde{W}_{,\xi} + S_5^N\tilde{W} \\ +2S_6^N\tilde{\theta}_{,\xi} + S_7^N\tilde{\theta} + 2S_8^N\tilde{\Psi}_{,\xi} - S_9^N\left(2/\left(D-1\right)\right)\tilde{\Psi}_{a,\chi} \end{pmatrix} = 0, \tag{4.5.8}$$

$$S_1^T\tilde{W} + \Omega\left[4S_2^T\tilde{W}_{,\xi\xi} + 2S_3^T\tilde{W}_{,\xi} + S_4^T\tilde{W} + S_5^T\tilde{\theta}\right] = 0, \tag{4.5.9}$$

$$\Omega\tilde{\theta} + \mathbf{i}K\tilde{W} = 0, \tag{4.5.10}$$

$$S_1^E\tilde{W} + \Omega\left[S_2^E\tilde{\theta} + 2S_3^E\tilde{\Psi}_{,\xi} + S_4^E\tilde{\Psi} - \left(2/\left(D-1\right)\right)\tilde{\Psi}_{a,\chi}\right] = 0, \tag{4.5.11}$$

$$\left(\bar{\Psi}_{,Z} - \bar{\Psi}_{a,Z}\right)\tilde{W} + \Omega\left(\tilde{\Psi} - \tilde{\Psi}_a\right) = 0. \tag{4.5.12}$$

The transformed boundary conditions for electric field at anode (χ = - 1) is,

$$\tilde{\Psi}_a = 0. \qquad (4.5.13)$$

The subscript χ with a preceding comma in the transformed governing equations and boundary conditions denote ordinary differentiation.

The base-state variables are evaluated numerically in (0, *H*) domain and mapped into the transformed (-1, 1) domain. Following this, the transformed four ODEs Eqs. (4.5.1) – (4.5.4) and boundary conditions Eqs. (4.5.5) – (4.5.13) are expanded in terms of Chebyshev polynomials $T_n(z)$. For *N* Chebyshev polynomials, four ODEs and ten boundary conditions form a (4N) × (4N) matrix from where the eigenvalues are obtained. The accuracy of the code is tested by validating the eigenvalues with the LWLSA in the regime of low wavenumber (long-wave). The accuracy of the code is also improved by varying the number of polynomials (~50) and thereafter sorting out the spurious eigenvalues.

4.6. RESULTS AND DISCUSSION

Figure 4.1 schematically describes the diagram of a nematic LC film deforming under the influence of an external electric field. The figure shows that the film rests on the bottom electrode whereas the top-electrode and the film surface are separated by a dielectric material such as air. The soft free surface of the film is expected to deform in presence of the external electric field when the destabilizing effect due to the combined effect of applied field and Ericksen stress overcome the collective stabilizing capillary and bulk elasticity of the liquid crystal film. It may be noted here that although the LWLSA and GLSA is performed employing dimensionless variables and expressions, the results reported in the present work are in the dimensional form to have a better physical understanding on the parameters related to the system.

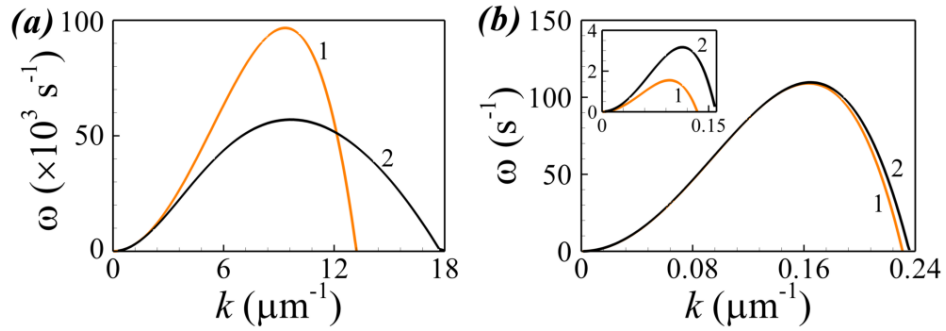

Figure 4.2 Variation of linear growth coefficient (ω) with wave number (k) from the present analysis. Plot (a) shows a comparison between the LWLSA (lighter shade, curve-1) and GLSA (darker shade-curve-2) when the film is isotropic, d = 193 nm, h = 100 nm, ψ = 70 V, μ = 1 Pa s, and ε = 2.5. Plot (b) shows the results from the LWLSA (lighter shade curve-1) and GLSA (darker shade curve-2) for a nematic film when d = 2 μm, h = 1.0 μm, ψ = 20 V, and ε_a = 0.5. The inset in the plot (b) shows a situation where GLSA and LWLSA varies significantly when h = 0.5 μm. The other necessary parameters for the plot (b) are shown in the Table 4.1.

TABLE 4.1 Typical parametric values used in the calculations for the nematic film[11,21,22]

Variables	Values
α_1 (Pa s)	0.0065
α_2 (Pa s)	-0.007
α_3 (Pa s)	- 0.001
α_4 (Pa s)	0.085
α_5 (Pa s)	0.050
γ (N m^{-1})	0.030
K_f (N)	5.0 × 10^{-12}
$\varepsilon_\perp$	2.0 – 8.0
ε_a	-1.0 – 7.0
d (μm)	2.0

Figure 4.2 shows the variations in the growth coefficient (ω) with wavenumber (k) for a number of interesting cases. Plots (a) and (b) shows a comparison between the long-wave (lighter shade) and general analysis (darker shade) when the film is isotropic and nematic, respectively. The curves in this plot corroborate the accuracy of the code as the eigenvalues matches for LWLSA and the GLSA especially in the regime where the instability has long-wave characteristics ($k \rightarrow 0$). The plots also show the necessity of GLSA over LWLSA in predicting the length and time scales when instabilities shift towards the shorter wavelength regime. Interestingly, even with the finite bulk elasticity originating from the orientational order, the nematic film display long-wave characteristics ($\omega \rightarrow 0$ as $k \rightarrow 0$), as usually observed for the EHD instabilities of isotropic thin films.[3,23,24] This is in stark contrast to the similar elastic films with both positional and orientational orders, which leads to the finite wavenumber instabilities.[25]

Figure 4.3 summarizes the stabilizing or destabilizing influences of the Frank's bulk elastic constant (K_f) and Leslie coefficients (α_i where $i = 1, 2, 3,$ and 5) on the electric field induced instabilities of the nematic LC films. The curves show the variations of ω with k from GLSA when the director field at NS ($z = 0$) and NI ($z = h$) interfaces are in homeotropic alignment ($\theta_i = 0^o$). The plot (a) in this figure shows the influence of ε_a on the time and the length scales of the instability. In this plot, the curves corresponding to the nematic film has finite values of K_f and α_i. The curves 1 – 3 represent, $\varepsilon_a < 0$, $\varepsilon_a = 0$, and $\varepsilon_a > 0$, respectively. The plot suggest that as compared to an isotropic film (curve *i*), the nematic film with zero dielectric anisotropy (curve 2, $\varepsilon_a = 0$) is more stable due to the bulk elasticity originating from the orientational order inside the film. However, the length and time scales can be significantly smaller (larger) for the situation when the film

has a positive (negative) dielectric anisotropy, $\varepsilon_a > 0$ ($\varepsilon_a < 0$), as shown by the curve 3 (curve 1). For example, $\varepsilon_a > 0$ ensures that the induced charge separation of the molecules

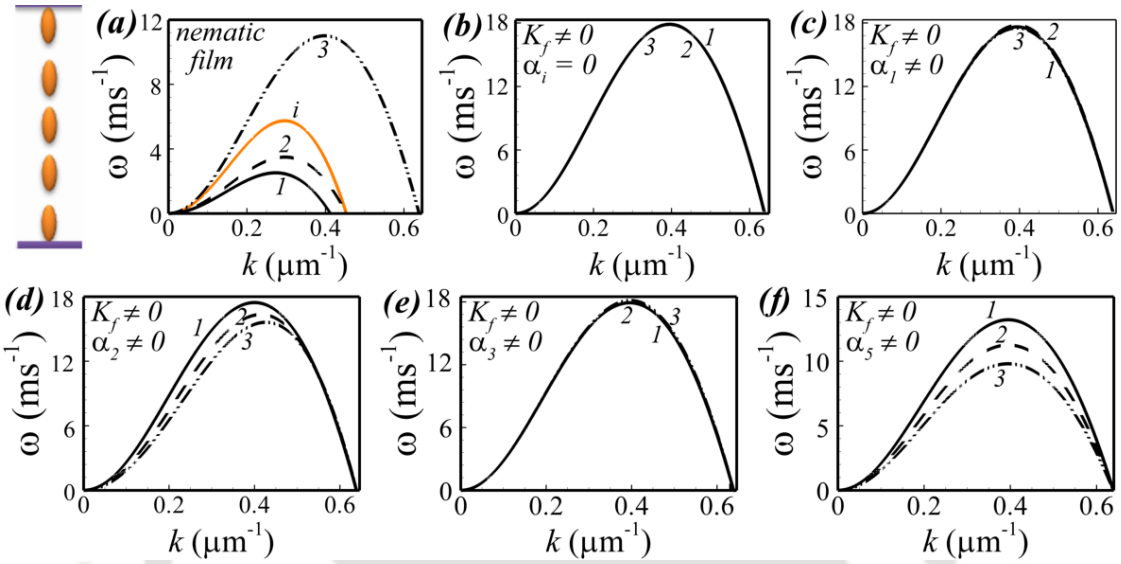

Figure 4.3 The GLSA plots show the variations of ω with k for the electric field induced instabilities (ψ = 20 V) of a thin nematic film (h = 1.5 μm). The director fields at NS (z = 0) and NI ($z = h$) interfaces are in homeotropic alignment ($\theta_i = 0^o$), as schematically shown in the left hand side or the first row. In plot (a) the lines 1 – 3 represent ε_a = – 0.7, 0, and 5, respectively. The curve '*i*' show a comparative ω vs. k plot for a similar isotropic film (ε = 6). Plots (b) – (f) show the influences of the bulk elastic constant (K_f) and the Leslie coefficients (α_i) on the length and time scales. In the plot (b), $K_f, \alpha_4 \neq 0$ and $\alpha_1, \alpha_2, \alpha_3, \alpha_5 = 0$ in which curves 1–3 represent K_f = 3×10^{-12} N, 6×10^{-12} N, and 10×10^{-12} N, respectively; plot (c) $K_f, \alpha_4, \alpha_1 \neq 0$ and $\alpha_2, \alpha_3, \alpha_5 = 0$ in which curves 1–3 represent α_1 = 0.003 Pa s, 0.007 Pa s, and 0.01 Pa s, respectively; plot (d) $K_f, \alpha_4, \alpha_2 \neq 0$ and $\alpha_1, \alpha_3, \alpha_5 = 0$ in which curves 1–3 represent α_2 = – 0.007 Pa s, – 0.03 Pa s, and – 0.05 Pa s, respectively); plot (e) $K_f, \alpha_4, \alpha_3 \neq 0$ and $\alpha_1, \alpha_2, \alpha_5 = 0$, in which the curves 1–3 represent α_3 = – 0.001 Pa s, – 0.003 Pa s, and – 0.006 Pa s, respectively; and plot (f) $K_f, \alpha_4, \alpha_5 \neq 0$ and $\alpha_1, \alpha_2, \alpha_3 = 0$ in which the curves 1–3 represent α_5 = 0.03 Pa s, 0.05 Pa s, and 0.07 Pa s, respectively. The other necessary parameters for the plots are shown in the Table 4.1.

are aligned in the direction of the applied field, which leads to a smaller time and length scales of instability as compared to the situation where $\varepsilon_a = 0$. Thus, the materials such as

nCB (4-n-alkyl-cyanobiphenyl) with $\varepsilon_a > 0$ are expected show a smaller length and time scales for the EHD patterns as compared to the electric field induced patterns on the isotropic polymeric liquid films composed of PS (poly-styrene) or PMMA (poly-methyl-methacrylate). In contrast, when $\varepsilon_a < 0$, the induced charge separation of the molecules aligns in the normal direction of the applied field, which leads to a larger time and length scales of instability as compared to the situation where $\varepsilon_a = 0$. For example, PAA (p-azoxyanisole) is expected to have an induced charge separation in the normal direction to the applied field which in turn will reduce the electric field stress at the interface.[11] In such situations, patterns with larger spacing are expected from a liquid crystal films as compared to the similar isotropic films. Concisely, the curves in the plot (a) infers that presence of dielectric anisotropy inside a nematic film can indeed reduce the periodicity of the patterns to be fabricated on the surface of the film as compared to a similar isotropic film. In the plots (b) – (f) of Figure 4.3 we show the effects of the Frank's bulk elastic constant (K_f) and Leslie coefficients (α_i where $i = 1, 2, 3,$ and 5) individually and for this purpose we turn on one parameter and set others to zero to unveil their importance. It may be noted here that α_4 is the Newtonian viscosity of the films and it has a finite value in all the plots. The curves in plot (b) suggest that the Frank's bulk elastic constant (K_f) has no influence on the length and time scales when the molecules are oriented homeotropically in the bulk as well as at the boundaries. The plots (c) – (f) show that among the Leslie constants, α_5 has the most pronounced influence on the time scale of the instability while the others have either marginal or no influence. Importantly, all the Leslie constants do not influence the length scale, as previously observed for other kinetic parameters such as viscosity and relaxation time of a viscous or viscoelastic liquid films.[24,26]

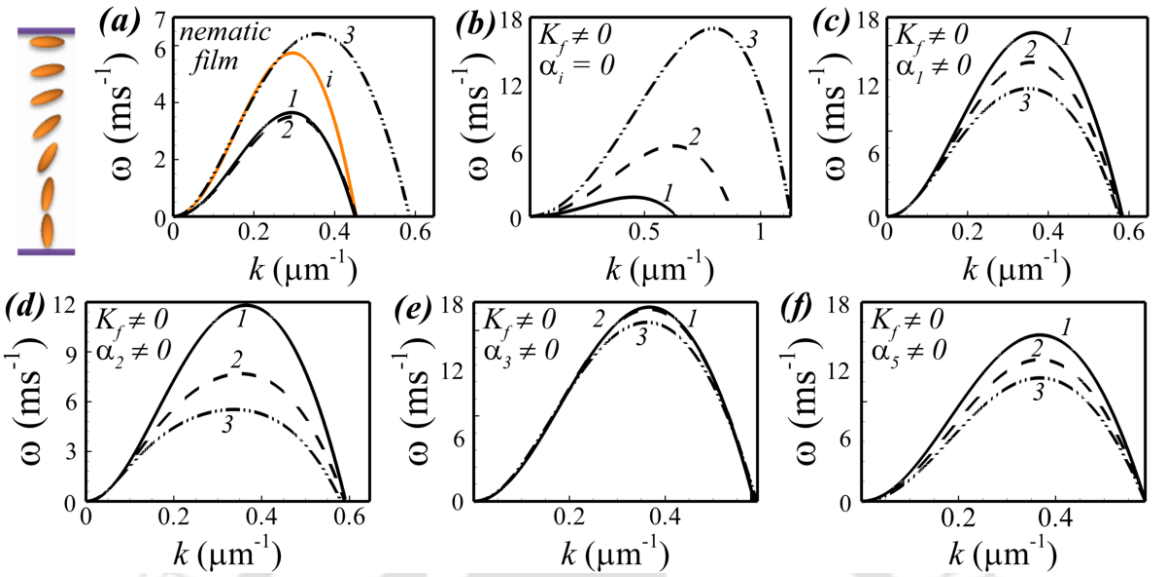

Figure 4.4 The GLSA plots show the variations of ω with k for the electric field induced instabilities (ψ = 20 V) of a thin nematic film (h = 1.5 μm). The director fields at NS (z = 0) is in homeotropic alignment ($\theta_1 = 0^o$) and at NI ($z = h$) interface is in planer alignment ($\theta_2 = 90^o$), as schematically shown in the left hand side or the first row. In plot (a) the lines 1–3 represent ε_a = – 0.7, 0, and 5, respectively. The curve '*i*' show a comparative ω vs. k plot for a similar isotropic film (ε = 6). In the plot (b), h = 0.1 μm , $K_f, \alpha_4 \neq 0$ and $\alpha_1, \alpha_2, \alpha_3, \alpha_5 = 0$, in which the curves 1–3 represent K_f = 3×10^{-12} N, 6×10^{-12} N, and 10×10^{-12} N, respectively; plot (c) $K_f, \alpha_4, \alpha_1 \neq 0$ and $\alpha_2, \alpha_3, \alpha_5 = 0$ in which the curves 1–3 represent α_1 = 0.003 Pa s, 0.007 Pa s, and 0.01 Pa s, respectively; plot (d) $K_f, \alpha_4, \alpha_2 \neq 0$ and $\alpha_1, \alpha_3, \alpha_5 = 0$ in which the curves 1–3 represent α_2 = – 0.007 Pa s, 0.015 Pa s, and 0.02 Pa s, respectively; plot (e) $K_f, \alpha_4, \alpha_3 \neq 0$ and $\alpha_1, \alpha_2, \alpha_5 = 0$ in which the curves 1–3 represent α_3 = - 0.001 Pa s, - 0.003 Pa s, and - 0.006 Pa s, respectively; and plot (f) $K_f, \alpha_4, \alpha_5 \neq 0$ and $\alpha_1, \alpha_2, \alpha_3 = 0$ in which the curves 1–3 represent α_5 = 0.03 Pa s, 0.05 Pa s, and 0.07 Pa s, respectively. The other necessary parameters for the plots are shown in the Table 4.1.

Figure 4.4 summarizes the influences of K_f and α_i (where i = *1*, *2*, *3*, and *5*) when the director field at NS (z = 0) interface is in homeotropic alignment ($\theta_i = 0^o$) and NI ($z = h$) interface is in planer alignment ($\theta_i = 90^o$). The curves 1 – 3 in the plot (a) in this figure show the influence of ε_a on the time and the length scales of the instability at finite values of K_f and α_i. Again, similar to the previous figures, the plot suggest that as compared to

an isotropic film (curve *i*), the nematic film with zero dielectric anisotropy (curve 2, ε_a = 0) is more stable due to the bulk elasticity originating from the orientational order inside the film. The length and time scales can be significantly smaller (larger) for the situation when the film has a positive (negative) dielectric anisotropy, $\varepsilon_a < 0$ ($\varepsilon_a > 0$), as shown by the curve 3 (curve 1). In the plots (b) – (f) of Figure 4.4 we show the effects of the K_f and α_i (where *i* = *1*, *2*, *3*, and *5*) individually and for this purpose we turn on one parameter at a time and set others to zero to unveil their importance. Similar to the previous figure, the Newtonian viscosity α_4 has a finite value in all the plots. The curves in plot (b) suggest that the Frank's bulk elastic constant (K_f) has now significant influence on the length and time scales, as the molecules change their orientation from homeotropic to planer across the film leading to a finite, $\theta_{,z}$. The plots (c) – (f) show that a finite $\theta_{,z}$ also ensures that all the Leslie constants have pronounced influence on the time scale of the instability. Importantly, again the Leslie constants do not influence the length scale. Thus, the figures 3 and 4 together uncover that when the molecular orientation is not changing across a nematic film, ε_a and α_5 are the major contributing factors in changing the length and the time scales for the EHD instabilities. In comparison, when the changing molecular orientation ensures a finite $\theta_{,z}$, all the parameters ε_a, K_f, and α_i is capable of changing the time and the length scales of the EHD instabilities in which the Leslie coefficients contribute only to the change in the time scale.

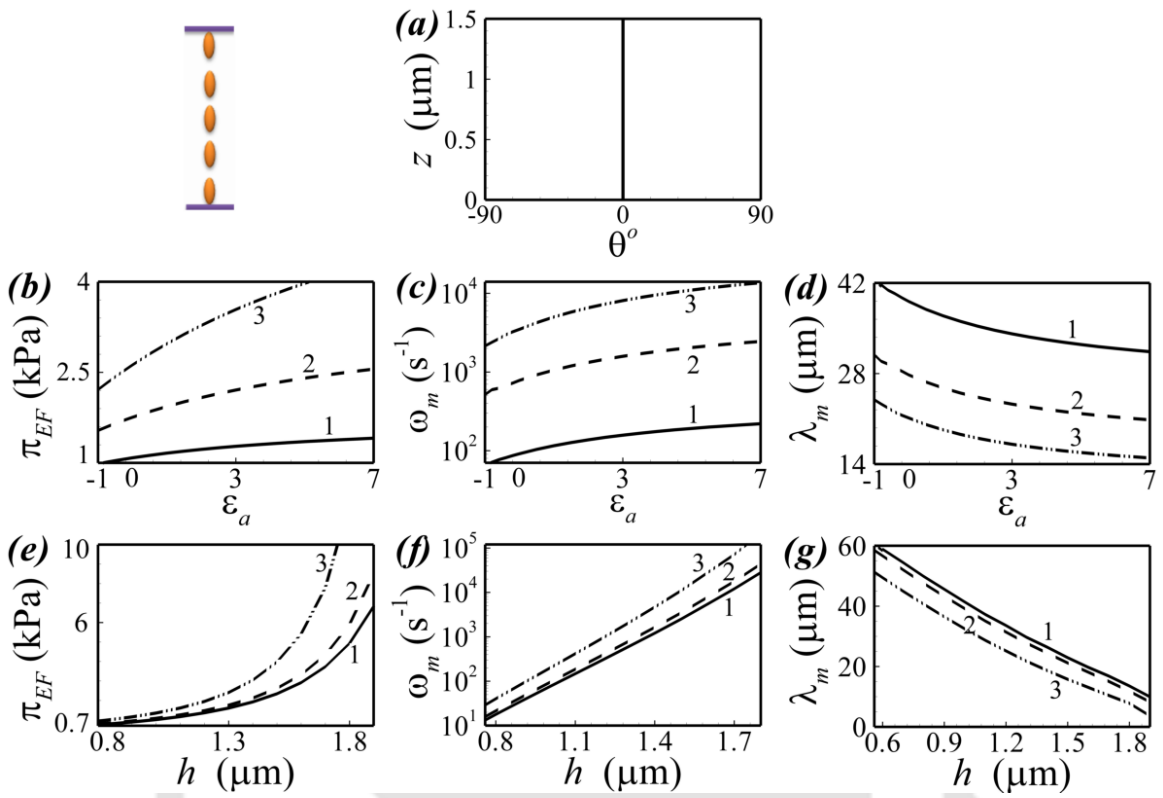

Figure 4.5 The GLSA results when the director fields at NS ($z = 0$) and NI ($z = h$) interfaces are in homeotropic alignment ($\theta_i = 0^o$). The applied field strength is $\psi = 20$ V. Plot (a) shows the variation of θ at the base-state along the z-axis, as schematically shown in the left hand side or the first row. The plots (b) – (d) show the variations of π_{EF}, ω_m, and λ_m with ε_a. The solid, evenly broken and solid curves represent, h = 1.0 μm, 1.3 μm, and 1.5 μm, respectively. The plots (e) – (g) show the variations in π_{EF}, ω_m, and λ_m with h. The solid, evenly broken, and unevenly broken curves represent $\varepsilon_a = -0.7$, 0, and 5, respectively. The other necessary parameters for the plots are shown in the Table 4.1.

Figure 4.5 shows the GLSA results when the director fields at nematic-solid ($z = 0$) and nematic-air ($z = h$) interfaces are in homeotropic alignment ($\theta_i = 0^o$), as schematically shown in the left hand side of the first row. Plot (a) shows the base-state arrangement of the molecules with homeotropic alignment even inside the film alongside the boundary. The plots (b) – (d) show the variations in the destabilizing pressure due to electric field (π_{EF}), destabilizing tangential component of the Ericksen elastic stress (π_{ES}), dominant grow rate (ω_m), and dominant wave length (λ_m) with ε_a whereas the plots (e) – (g) show

the variations in π_{EF}, π_{ES}, ω_m, and λ_m with h. The base-state expressions for π_{EF} and π_{ES} are measures of the strength of the destabilizing stress at the nematic-air interface,

$$\pi_{EF} = 0.5\varepsilon_0\left[\psi_{a,zz}^2 - \left(\varepsilon_\perp + \varepsilon_a \cos^2\theta\right)\psi_{,zz}^2\right]. \tag{4.6.1}$$

$$\pi_{ES} = K_f \theta_{,z}^2. \tag{4.6.2}$$

The expressions indicate that when the molecular orientation homeotropic inside the film and at the boundaries, π_{ES} cannot influence the length and time scales of the instabilities. Plots (b) and (e) together show that the destabilizing stress inside the film increases with increase in π_{EF} which eventually reduces the time and the length scales with progressive increase in ε_a and *h*, as reflected in the plots (c), (d), (f), and (g). In particular, a thicker nematic film with $\varepsilon_a > 0$ ensures a significant reduction in the length scale of the instability, which can be exploited to develop field induced miniaturized patterns on the liquid crystal films.

Figure 4.6 shows another situation where the director fields at NS (z = 0) and NI (z = *h*) interfaces are in planer alignment (θ_i = 90°), as schematically shown in the left hand side of the first row. Plot (a) shows that the arrangement of the molecules inside the film is also planer. The plots (b) – (d) [(e) – (g)] show the variations π_{EF}, ω_m, and λ_m with ε_a [*h*]. The parameter π_{ES} is expected to be zero because the molecular arrangement inside the film ensures that $\theta_{,z}$ is non-existent. Interestingly, when the molecules inside the nematic film is arranged in the planer configuration $\varepsilon_\perp$ of the film has influence on π_{EF}, ω_m, and λ_m, as shown by the plots (b) – (d). However, with the increase in thickness as the electric

field stress at the nematic-air interface increases [plot (e)] the length and the time scales reduces, as depicted in the plots (f) and (g).

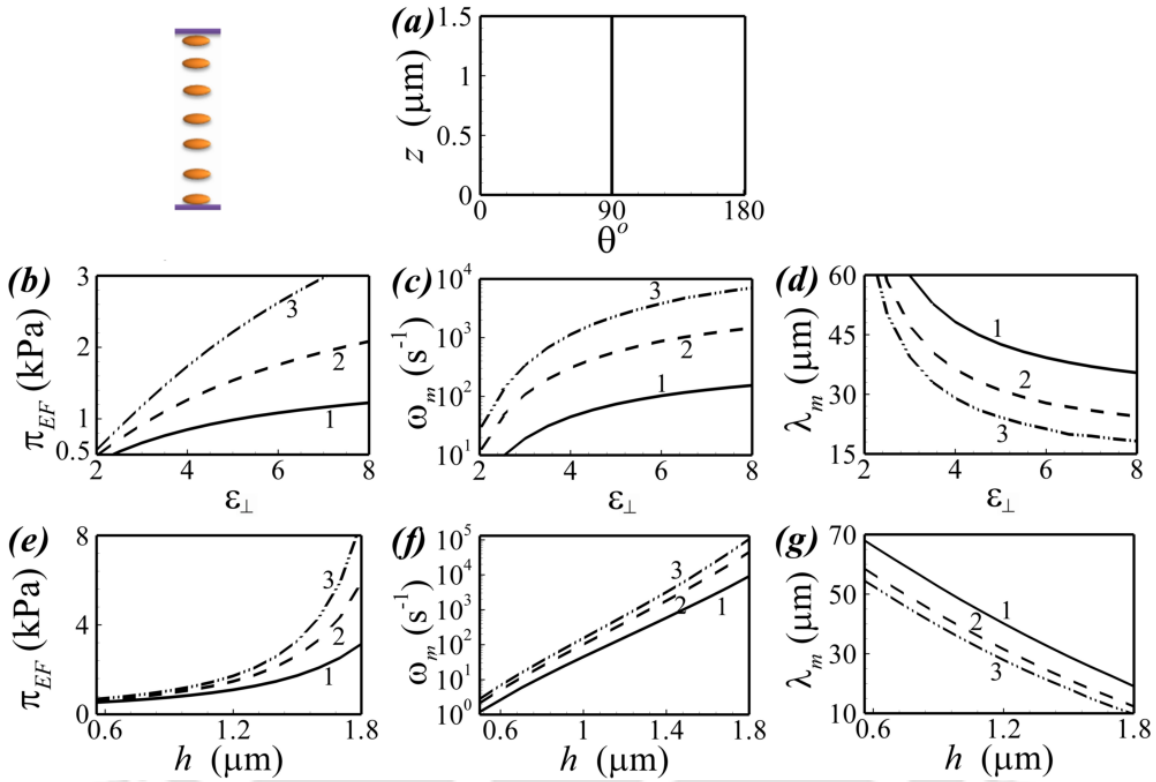

Figure 4.6 The GLSA results when the director fields at NS (z = 0) and NI (z = h) interfaces are in planer alignment (θ_i = 90°). The applied field strength is ψ = 20 V. Plot (a) shows the variation of θ at the base-state along the z-axis, as schematically shown in the left hand side or the first row. The plots (b) – (d) show the variations in π_{EF}, ω_m, and λ_m with ε_a. The solid, evenly broken and unevenly broken curves represent h = 1.0 μm, 1.3 μm, and 1.5 μm, respectively. The plots (e) – (g) show the variations in π_{EF}, ω_m, and λ_m with h. The solid, evenly broken, and unevenly broken curves represent $\varepsilon_\perp$ = 4, 6, and 8, respectively. The other necessary parameters for the plots are shown in the Table 4.1.

Unlike Figures 4.5 and 4.6 where the molecular orientations does not change across the film, Figures 4.7 and 4.8 show examples where the director field varies across the film. Figure 4.7 shows a situation where the director field at NS (z = 0) is in homeotropic alignment (θ_1 = 0°) and at NI (z = h) interface is in planer alignment (θ_2 = 90°), as schematically shown in the left hand side of the first row. Plots (a) and (b) show the

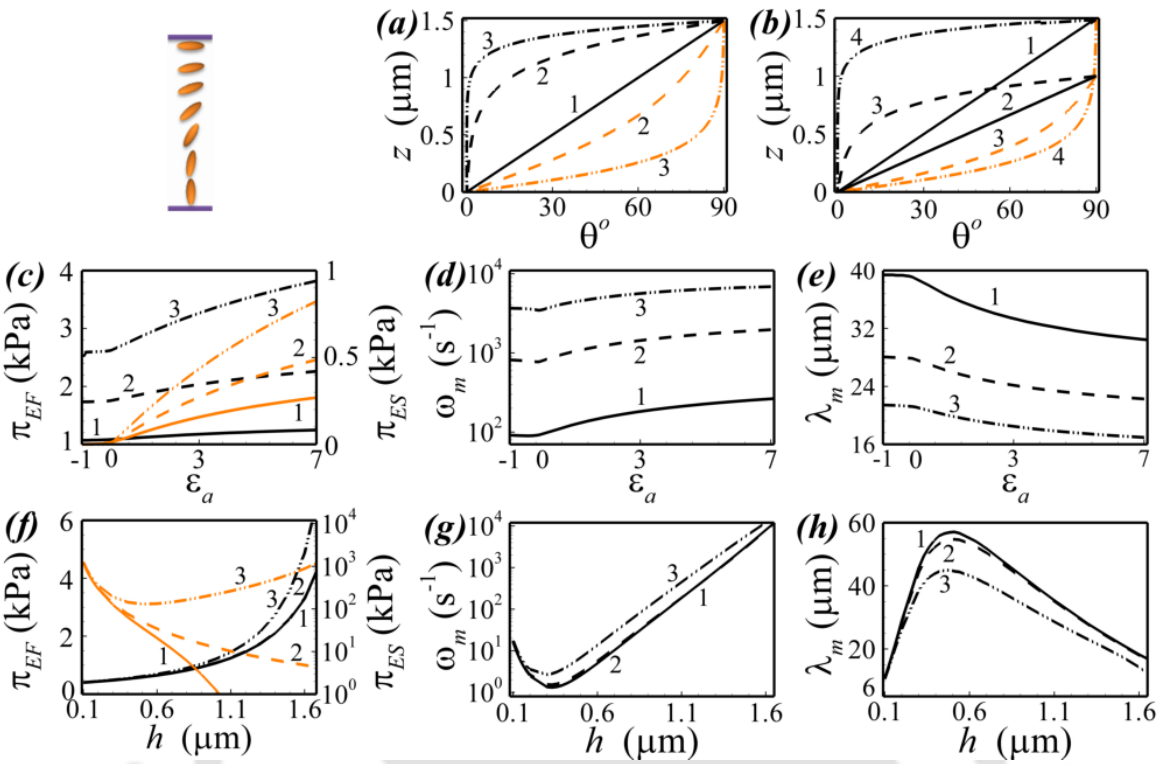

Figure 4.7 The GLSA results when the director fields at NS (z = 0) is in homeotropic alignment (θ_1 = 0°) and at NI (z = h) interface is in planer alignment (θ_2 = 90°). The applied field strength is ψ = 20 V. Plots (a) and (b) shows the variation of θ at the base-state along the z-axis with the change in the ε_a and h, respectively, as schematically shown in the left hand side or the first row. In plot (a) the curve 1 represent ε_a = 0, the evenly broken and unevenly broken curves 2 and 3 of darker shade (lighter shade) represent ε_a = 0.5 and 5 (– 0.1 and – 0.7), respectively. In plot (b) the solid curves 1 and 2 represent ε_a = 0. The evenly broken and unevenly broken curves 3 and 4 of darker shade represent (lighter shade) h = 1 μm, and 1.5 μm, respectively and ε_a = 0, 5 (– 0.1 and – 0.7), respectively. The plots (c) – (e) show the variations in π_{EF}, π_{ES}, ω_m, and λ_m with ε_a. The solid, evenly broken and unevenly broken curves represent h = 1.0 μm, 1.3 μm, and 1.5 μm, respectively. In plot (b) the curves with darker shades (lighter shade) show the variation of π_{EF} (π_{ES}) and y-axis to the left (right) contains the range of variation. The plots (f) – (h) show the variations in π_{EF}, π_{ES}, ω_m, and λ_m with h. The solid, evenly broken, and unevenly broken curves represent ε_a = – 0.7, 0, and 5, respectively. The other necessary parameters for the plots are shown in the Table 4.1.

of θ at the base-state along the z-axis with the change in the ε_a and h, respectively. Plot (a) shows that the change in θ is linear across the film when ε_a = 0. However, for the

condition $\varepsilon_a > 0$ ensures that the molecules are oriented along the direction of the electric field excepting the zone near NI interface where a sharp change of molecular orientation takes place from homeotropic to planer. In contrast, the condition $\varepsilon_a < 0$ ensures that the molecules are mostly oriented along the normal direction to the applied field except for the zone near NS interface where a sharp change of molecular orientation takes place from planer to homeotropic. Among all these conditions, $\varepsilon_a > 0$ strengthens the electric field stresses at the interface while $\varepsilon_a < 0$ tends to weaken the same. Importantly, since the molecular orientations change across the film the destabilizing Ericksen stress, $\pi_{ES} = f\left(\theta_{,z}\right)$, also contribute to the length and time scales of the instabilities. The plots (c) – (e) [(f) – (h)] show the variations π_{EF}, π_{ES}, ω_m, and λ_m with ε_a [h]. The plot (c) shows that the variation is ε_a has less influence on π_{ES} whereas π_{EF} progressively increases with increase in the positive dielectric anisotropy of the film. In contrast, plot (f) suggests that the destabilizing influence from π_{ES} is dominant when the nematic film thickness is smaller and the influence progressively decays with increase in h because of the reduction in $\theta_{,z}$. Beyond a threshold film thickness, π_{EF} become the dominant influence as compared to the contribution from π_{ES}. The interplay between the two destabilizing influences is reflected in ω_m and λ_m plots in the Figure 4.6. Plots (d) and (e) suggest that the time and the length scales of the instability reduce as ε_a is progressively increased. In comparison, plots (g) and (h) shows that the nematic films are found to be unstable by the dominant Ericksen stress at the lower thicknesses. With progressive increase in the film thickness ω_m reduces and λ_m increases, as the strength of the Ericksen

stress reduces (reduction in $\theta_{,z}$). At higher values of *h*, when π_{EF} becomes the dominant destabilizing influence, ω_m increases and λ_m reduces with increase in *h*.

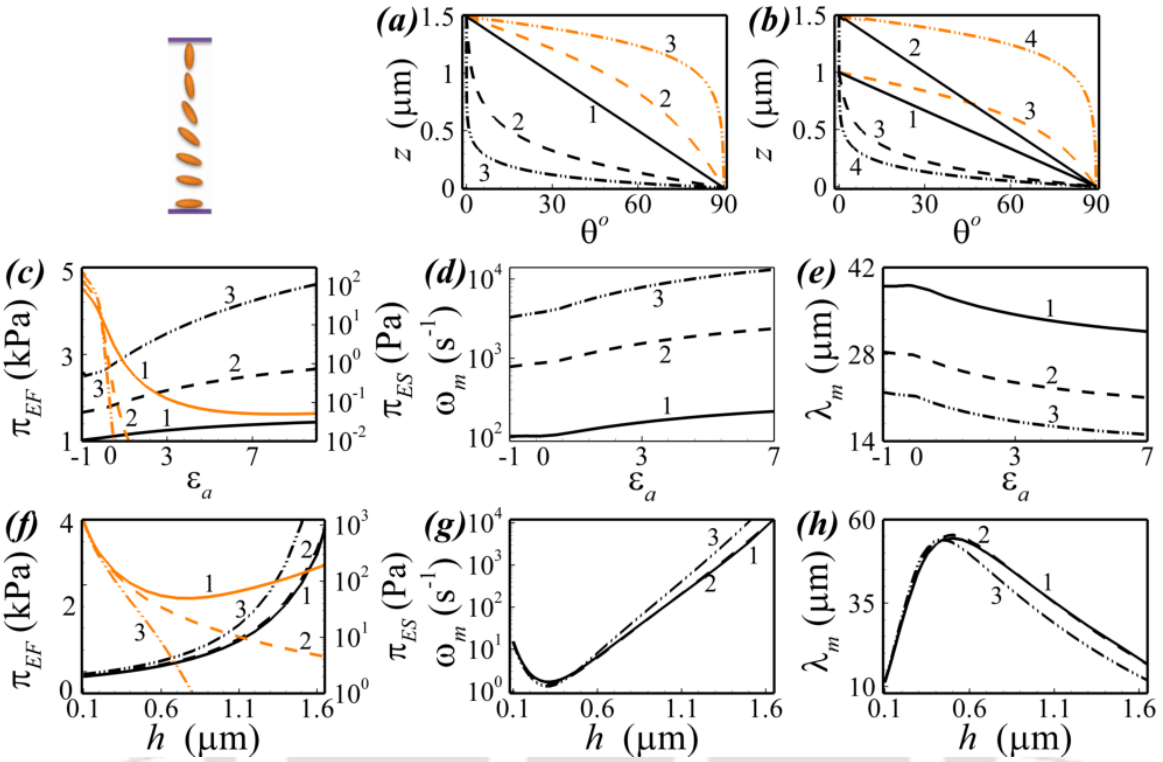

Figure 4.8 The GLSA results when the director fields at the NS (*z* = 0) is in planer alignment (θ_1 = 0°) and at NI (*z* = *h*) interface is in homeotropic (θ_2 = 90°). The applied field strength is ψ = 20 V. Plots (a) and (b) shows the variation of θ at the base-state along the *z*-axis with the change in the ε_a and *h*, respectively, as schematically shown in the left hand side or the first row. In plot (a) the curve 1 represent ε_a = 0, the evenly broken and unevenly broken curves 2 and 3 of darker shade (lighter shade) represent ε_a = 0.5 and 5 (– 0.1 and – 0.7), respectively. In plot (b) the solid curves 1 and 2 represent ε_a = 0. The evenly broken and unevenly broken curves 3 and 4 of darker shade represent (lighter shade) *h* = 1 μm, and 1.5 μm, respectively and ε_a = 0, 5 (– 0.7), respectively. The plots (c) – (e) show the variations in π_{EF}, π_{ES}, ω_m, and λ_m with ε_a. The solid, evenly broken and unevenly broken curves represent *h* = 1.0 μm, 1.3 μm, and 1.5 μm, respectively. In plot (b) the curves with darker shades (lighter shade) show the variation of π_{EF} (π_{ES}) and *y*-axis to the left (right) contains the range of variation. The plots (f) – (h) show the variations in π_{EF}, π_{ES}, ω_m, and λ_m with h. The solid, evenly broken, and unevenly broken curves represent ε_a = – 0.7, 0, and 5, respectively. The other necessary parameters for the plots are shown in the Table 4.1.

Figure 4.8 shows a situation where the director field at the NS (z = 0) is in planer alignment (θ_1 = 90^o) and at NI ($z = h$) interface is in homeotropic alignment (θ_2 = 0^o), as schematically shown in the left hand side of the first row. Plots (a) and (b) show the variation of θ at the base-state along the z-axis with the change in the ε_a and h, respectively. Similar to Figure 4.7, for this case also the plot (a) shows that the change in θ is linear across the film when $\varepsilon_a = 0$. However, for the condition $\varepsilon_a > 0$ ensures that the molecules are mostly oriented along the direction of the electric field barring the zone near NS interface where a sharp change of molecular orientation takes place from homeotropic to planer. In contrast, the condition $\varepsilon_a < 0$ ensures that the molecules are largely oriented along the normal direction to the applied field barring the zone near NI interface where a sharp change of molecular orientation takes place from planer to homeotropic. Again, since the molecular orientations change across the film the destabilizing Ericksen stress, $\pi_{ES} = f\left(\theta_{,z}\right)$, also contribute to the length and time scales of the instabilities. The plots (c) – (e) [(f) – (h)] show the variations π_{EF}, π_{ES}, ω_m, and λ_m with ε_a [h]. The plot (c) shows that the variation in ε_a has less influence on π_{ES} whereas π_{EF} progressively increases with increase in ε_a. In contrast, plot (f) suggests that π_{ES} is dominant when the nematic film thickness is smaller and the influence progressively decays with increase in h. The parameter π_{EF} becomes the dominant influence as compared to π_{ES} when the nematic films are thicker. Plots (d) and (e) suggest that the time and the length scales of the instability reduce as ε_a is progressively increased. In comparison, plots (g) and (h) shows that instability is dictated by the dominant Ericksen stress at lower h. With progressive increase in h, as the strength of π_{ES} reduces (reduction in $\theta_{,z}$), ω_m reduces and

λ_m increases. At higher values of *h*, when π_{EF} becomes the dominant destabilizing influence, ω_m increases and λ_m reduces with increase in *h*.

4.7 SUMMARY

The electric field induced instabilities of thin liquid crystal films has been explored through linear stability analysis. The Ericksen-Leslie governing equations for the flow field of the liquid crystals together with the full descriptions of the Maxwell stresses for the anisotropic electric field are employed to uncover that the time and the length scales of the electric field induced free surface deformation of a liquid crystal film. Enforcing a host of different boundary conditions at NS and NI interfaces, the domain of dominance of the destabilizing Ericksen elastic stress and the external electrostatic field have been identified. Alongside the boundary conditions, the variation in the applied voltage, film thickness, dielectric anisotropy of the film, and distance between the electrodes are also found to significantly influence the molecular orientations inside the film to change the spatiotemporal scales of the instabilities of nematic films. The major conclusions are,

(i) Smaller length and time scales of instabilities are observed as compared to the similar isotropic cases when the film has a positive dielectric anisotropy. In contrast, larger length and time scales of instabilities are observed when the film has a negative dielectric anisotropy.

(ii) The planer-planer or the homeotropic-homeotropic conditions at the boundaries ruled out the influnces arising from the destabilizing Ericksen stress at the interface. In comparison, a planer-homeotropic or homeotropic-planer combination at the NI and NS interfaces showed the importance of destabilizing Ericksen stress especially when the film

thickness is smaller. In such situations, the stresses due to electric field tend to dominate the destabilizing field when the films are relatively thicker.

(iii) Leslie coefficients are found to influence the kinetics of the instabilities. The influence is more pronounced when planer-homeotropic or homeotropic-planer combination is enforced at the NI and NS interfaces. In comparison, the bulk elastic constant for splay and bend is found to alter both time and length scales when planer-homeotropic or homeotropic-planer combination is enforced at the NI and NS interfaces.

(iv) The general analysis could asymptotically reproduce the analytical results obtained for the long-wave analysis of the EHD instabilities of the nematic and isotropic films.

Concisely, the study highlights the influence of molecular orientations on the electric field induced instabilities of a thin nematic film.

4.8 REFERENCES

1. P. Oswald, EPL **90**, 16005 (2010).
2. P. Oswald, Eur. Phys. J. E **33**, 69 (2010).
3. E. Schäffer, T. Thurn-Albrecht, T. P. Russell and U. Steiner, Nature (London) **403**, 874 (2000).
4. F. C. Frank, Discuss. Faraday Soc. **25**, 19 (1958).
5. J. L. Ericksen, Archive for Rational Mechanics and Analysis **9**, 371 (1962).
6. J. L. Ericksen, Trans. Soc. Rheol. **11**, 5 (1967).
7. F. M. Leslie, Continuum Mech. Thermodyn. **4**, 167 (1992).
8. S. Chandrasekhar, *Liquid Crystals* (Cambridge University Press, 1992).
9. T.-S. Lin, L. J. Cummings, A. J. Archer, L. Kondic, and U. Thiele, Phys. Fluids **25**, 082102 (2013).
10. T.-S. Lin, L. Kondic, U. Thiele, and L. J. Cummings, J. Fluid Mech. **729**, 214 (2013).
11. P. G. de Gennes, and J. Prost, The Physics of Liquid Crystals (Oxford University Press, Walton Street, 1993).
12. A. D. Rey, and M. M. Denn, Annu. Rev. Fluid Mech. **34**, 233 (2002).

13. S. J. Tavener, T. Mullin, G. I. Blake, and K. A. Cliffe, Phys. Rev. E **63**, 011708 (2000).
14. H. Yokoyama, S. Kobayashi, and H. Kamei, Mol. Cryst. Liq. Cryst. **129,** 109 (1985).
15. T. Qian, and P. Sheng, Phys. Rev. E **58**, 7475 (1998).
16. M. Ben Amar, and L. J. Cummings, Phys. Fluids **13**, 1160 (2001).
17. L. J. Cummings, Euro. J. Applied Mathematics **15**, 651 (2004).
18. J. A. C. Weideman, and S. C. Reddy, ACM Trans. Math. Soft. **26**, 465 (2000).
19. D. Gottlieb, and S. A. Orszag, (CBMS Regional Conference Series in Applied Mathematics, 1977).
20. S. A. Orszag, J. Fluid Mech. **50**, 689 (1971).
21. M. J. Stephen and J. P. Straley, Rev. Mod. Phys. **46,** 617 (1974).
22. I. W. Stewart, *The Static and Dynamic Continuum Theory of Liquid Crystals* (Taylor & Francis, London, 2004).
23. E. Schäffer, T. Thurn-Albrecht, T.P.Russell and U. Steiner, Europhys. Lett. **53**, 518 (2001).
24. R. Verma, A. Sharma, K. Kargupta and J. Bhaumik, Langmuir **21**, 3710 (2005).
25. J. Sarkar, V. Shenoy, and A. Sharma, **93**, 018302 (2004).
26. G. Tomar, V. Shankar, S. K. Shukla, A. Sharma and G. Biswas, Eur. Phys. J. E **20**, 185 (2006).

Chapter 5

Self-organized pathways to nanopatterns exploiting the instabilities of ultrathin confined bilayers

ABSTRACT

Self-organized interfacial instabilities of an ultrathin bilayer confined between a pair of rigid surfaces is explored. The bilayers are classified based on the macroscopic dewetting behaviors of the liquid films sandwiched between a pair of confining surfaces having surface energy higher or lower than the liquid films. Linear and nonlinear analyses employing the governing equations originating from the continuum description together with molecular dynamics (MD) simulations unveil the salient spatiotemporal features of the dewetting process. The study uncovers that, under the destabilizing influence of the intermolecular interactions, the interface of a confined bilayer can deform into interesting embedded and encapsulated patterns with nanoscale periodicity. The continuum and MD simulations collectively show the detailed route to dewetting starting from the formation of holes in the early stage, their growth to achieve equilibrium contact angle at the intermediate phase, and then to evolve into the equilibrium morphologies at the later stage. Examples are shown where the length and the time scales of the simulated nanostructures from both the continuum and MD approaches are found to agree with the same obtained from the linear stability analysis. We also highlight the deviations that are observed in the continuum and MD approaches. The study confirms that the reduced stabilizing interfacial tension at the liquid-liquid interface together with enhanced intermolecular interaction because of the thinness of the layers can be an alternative strategy for pattern miniaturization exploiting the instabilities of a thin confined bilayer. Further, the study shows that use of topographical patterns on the bounding surfaces can impose periodic order to the holes, droplets, columns, and channels, which can find important applications in the diverse areas of nanotechnology. By varying thickness of topographical pattern or

width of chemical patterns on the substrates we are able to capture from the non-correlated to correlated structure.

This chapter is published in Phys. Rev. E, **87** 022405 (2013).

In this chapter, Molecular Dynamics simulation results are done in collaboration with **Mr. Abhiram Hens, Scientist,** Micro System Technology Laboratory, CSIR - Central Mechanical Engineering Research Institute, Durgapur-713209, India.

5.1 INTRODUCTION

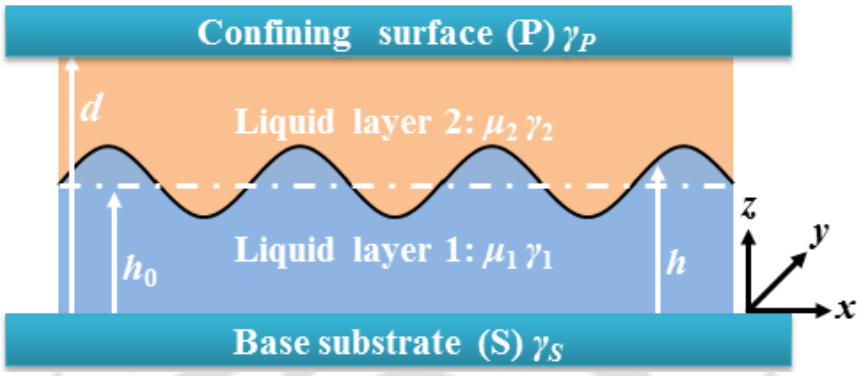

Figure 5.1 Schematic diagram of a bilayer confined between two rigid substrates. The mean and the local thicknesses of the lower layer are denoted by h_0 and $h(x,t)$, respectively. The symbols γ_i and μ_i denote the surface energy and viscosity of the lower (*i* = *1*) and upper (*i* = *2*) layers, respectively. The distance between the substrates is *d*. The surface energy of base substrate and confining surface are γ_S, and γ_P, respectively.

In the present chapter, with the help of MD simulations, we illustrate the instability and spatiotemporal dynamics of an ultrathin confined bilayer (Figure 5.1). The major focus here is to explore the different routes to nanostructure formation exploiting the instabilities of a confined bilayer composed of extremely thin (<5 nm) liquid films. The bilayers are classified based on the high to low surface energies of the confining surfaces and the films. For this purpose, we have chosen benzene (B) and water (W) as liquid films having low and high surface energies confined between (a) case I–a pair of high surface energy substrates (e.g., platinum, Pt), (b) case II – a pair of low surface energy substrates (e.g., rubber, R), and (c) case III – a combination of high- and low-surface-energy substrates. The MD simulations of these configurations clearly show the different spatiotemporal stages of dewetting, such as the hole formation in the short time, then the hole growth followed by the hole-coalescence stage, and finally the formation of nanostructures at the

later phase. The length scales of the patterns from the MD simulations are compared with a linear stabilities analysis (LSA) and nonlinear simulations based on the continuum description. Interestingly, the LSA together with the continuum and MD simulations convey that indeed the increased destabilizing intermolecular interaction due to the thinness of the films together with a weak interfacial tension at the deformable water-benzene interface leads to structures with nanoscale periodicity. In addition, the study shows that the dewetted structures can be guided by the topographic patterns on the substrates to form ordered nanoscale droplets, stripes, and channels, which can be of significant technological importance. The study also highlights the limitations and strengths of the continuum approach as compared to the MD approach in the quantitative prediction of the time and length scales of the dewetted structures. The results reported can encourage future experiments on the patterning and fabrication of nanostructures employing ultrathin confined bilayers.

The chapter is organized in the following manner. In Sec. 5.2, the theoretical formulations for the continuum and the MD approaches are described. In the continuum description, the methodologies employed for the LSA and the nonlinear simulations are shown. In Sec. 5.3, the interesting results are compared and contrasted from all the approaches before our conclusions in Sec. 5.4.

5.2 PROBLEM FORMULATION

In this section, we briefly discuss the formulations from the different approaches. In the continuum approach, starting with continuity and equations of motions for the films, we perform linear stability analysis and nonlinear simulations to study the length and time scales together with the spatiotemporal evolution of the films. Further, MD simulations

are performed to study the dynamics of dewetting of the films and to compare the results obtained from the continuum simulations.

5.2.1 Continuum modeling

5.2.1.1 Governing Equations

Figure 5.1 schematically shows a typical confined bilayer where the notations *x* and *y* are considered as the horizontal axes and *z* is the vertical axis of the coordinate system. The liquid films are assumed Newtonian and incompressible. Inertia is neglected in the formulation owing to the small thicknesses of the films. The resulting equations of motion in the Stokes flow regime, $-\nabla P_i + \nabla \cdot \boldsymbol{\tau}_i = 0$, together with the continuity equation, $\nabla \cdot \mathbf{u}_i = 0$, describe the dynamics of the i^{th} liquid layer (*i = 1* and *2* are lower and upper layer). The symbols $\boldsymbol{\tau}_i$ and $\mathbf{u}_i$ are the Newtonian stress tensor $\mu_i(\nabla \mathbf{u}_i + \nabla \mathbf{u}_i^T)$, and velocity vector $(u_i^{(x)}, u_i^{(z)})$, respectively, where the superscripts in parentheses denote the components of the vector. The notations μ_i, γ_i, π_i, p_i, and P_i are the viscosity, surface tension, excess pressure because of intermolecular forces, isotropic static pressure, and the effective non-body-force pressure inside the films ($p_i - \pi_i$), respectively.

The bilayer is assumed non-slipping and impermeable ($\mathbf{u}_1 = 0$, $\mathbf{u}_2 = 0$) at the solid-liquid interfaces (*z* = 0; *z* = *d*). At the confined interface ($z = h$), continuity of *x* and *z* components of velocities $(\mathbf{u}_1 = \mathbf{u}_2)$, balances shear $(\mathbf{t} \cdot \boldsymbol{\tau}_2 \cdot \mathbf{n} = \mathbf{t} \cdot \boldsymbol{\tau}_1 \cdot \mathbf{n})$ and normal $(-p_2 + \mathbf{n} \cdot \boldsymbol{\tau}_2 \cdot \mathbf{n} + p_1 - \mathbf{n} \cdot \boldsymbol{\tau}_1 \cdot \mathbf{n} = \gamma_{21}\kappa)$ stresses, and the kinematic conditions $\left(\dot{h} + u_1^{(x)} h_x = u_1^{(z)}\right)$ are employed as boundary conditions. Here *h* is the thickness of the lower film, γ_{21} is the interfacial tension at the liquid-liquid interface, and *d* is the distance between the confining surfaces. The unit outward normal and tangent vectors at the liquid-

liquid interface **n** and **t** are expressed as $\left[-h_x/\sqrt{\left(1+h_x^2\right)},1/\sqrt{\left(1+h_x^2\right)}\right]$ and $\left[1/\sqrt{\left(1+h_x^2\right)},h_x/\sqrt{\left(1+h_x^2\right)}\right]$, respectively. The scalar $\kappa\left(=\nabla_S\cdot\mathbf{n}\right)$ is the curvature of the confined interface. The superscript dot and subscript *x* in the expressions represents the time and space derivatives of the variables.

The excess disjoining pressure because of the intermolecular forces at the interface in terms of effective Hamaker constants is $\pi(h)=-A_2/6\pi h^3+A_1/6\pi\left(d-h\right)^3$.[1] The effective Hamaker constants are derived from the binary Hamaker constants, $A_2=A_{11}+A_{S2}-A_{S1}-A_{12}$ and $A_1=A_{22}+A_{P1}-A_{P2}-A_{12}$ where the subscripts *S*, *1*, *2*, and *P* represent the bottom substrate, lower layer, upper layer, and top surface, respectively. The disjoining pressure π can be expressed in terms of the equilibrium spreading coefficients $\left(S_{ijk}=\gamma_{jk}-\gamma_{ik}-\gamma_{ij}\right)$ to make a better understanding on the film instability of the bilayer system as $A_1=-12\pi d_0^2S_{2P1}$ and $A_2=-12\pi d_0^2S_{1S2}$. Here S_{ijk} denotes the spreading coefficient of layer *i* sandwiched between the layers *j* and *k* where $\gamma_{ij}=\left(\sqrt{\gamma_i}-\sqrt{\gamma_j}\right)^2$ denotes interfacial tension of layers *i* and *j*, and d_0 (~0.158 nm) is the van der Waals equilibrium distance between the two surfaces.[2,3] Please note here that the interfacial tension calculated in this manner is approximate and takes into account the contribution from the Lifshitz–van der Waals interactions of the compounds *i* and *j*. A positive (negative) effective Hamaker constant $\left(A_i>0\right)$ is synonymous to a negative (positive) spreading coefficient $\left(S_{ijk}<0\right)$ and both thermodynamically imply an effective attractive (repulsive) van der Waals force leading to spinodal instability (stability).[4–6]

5.2.1.2 Linear stability analysis

The governing equations and the boundary conditions are linearized by perturbing with the normal linear modes to the quiescent base-state, $\mathbf{u}_i = \tilde{\mathbf{u}}_i e^{\omega t + \mathbf{i}kx}$, $P_i = \tilde{P}_i e^{\omega t + \mathbf{i}kx}$, and $h = h_0 + \tilde{\delta} e^{\omega t + \mathbf{i}kx}$. Here the symbols ω and k represent the linear growth coefficient and wave number. The notations $\tilde{\mathbf{u}}_i$, $\tilde{P}_i$, and $\tilde{\delta}$ are the small amplitude perturbations and h_0 is the base-state lower film thickness. The expressions for the linearized momentum and continuity equations are as follows,

$$-\mathbf{i}k\tilde{P}_i + \mu_i\left(-k^2\tilde{u}_i^{(x)} + \frac{d^2\tilde{u}_i^{(x)}}{dz^2}\right) = 0, \tag{5.2.1}$$

$$-\frac{d\tilde{P}_i}{dz} + \mu_i\left(-k^2\tilde{u}_i^{(z)} + \frac{d^2\tilde{u}_i^{(z)}}{dz^2}\right) = 0, \tag{5.2.2}$$

$$\mathbf{i}k\tilde{u}_i^{(x)} + \frac{d\tilde{u}_i^{(z)}}{dz} = 0. \tag{5.2.3}$$

Eliminating $\tilde{P}_i$ from the linearized governing Eqs. (5.2.1) – (5.2.3) leads to the following biharmonic equation for each layer,

$$\frac{d^4\tilde{u}_i^{(z)}}{dz^4} - 2k^2\frac{d^2\tilde{u}_i^{(z)}}{dz^2} + k^4\tilde{u}_i^{(z)} = 0. \tag{5.2.4}$$

The general solution of Eq. (5.2.4) is,

$$\tilde{u}_i^{(z)} = (B_{1i} + B_{2i}z)e^{kz} + (B_{3i} + B_{4i}z)e^{-kz}. \tag{5.2.5}$$

Here the coefficients B_{ji} (i = *1*, *2* and j = *1* to *4*) are constants. The boundary conditions are linearized employing the normal linear modes. The linearized no-slip and impermeability conditions at $z = 0$ and $z = d$ are,

$$\tilde{u}_1^{(x)} = \tilde{u}_1^{(z)} = 0,\ \tilde{u}_2^{(x)} = \tilde{u}_2^{(z)} = 0. \tag{5.2.6}$$

The linearized continuity of velocities, the tangential and normal stress balances, and the kinematic conditions at $z = h_0$ are,

$$\tilde{u}_1^{(x)} = \tilde{u}_2^{(x)},\ \tilde{u}_1^{(z)} = \tilde{u}_2^{(z)}, \tag{5.2.7}$$

$$\mu_1\left(\frac{d\tilde{u}_1^{(x)}}{dz} + \mathbf{i}k\tilde{u}_1^{(z)}\right) - \mu_2\left(\frac{d\tilde{u}_2^{(x)}}{dz} + \mathbf{i}k\tilde{u}_2^{(z)}\right) = 0, \tag{5.2.8}$$

$$\tilde{P}_1 - \tilde{P}_2 - 2\mu_1\left(\frac{d\tilde{u}_1^{(z)}}{dz}\right) + 2\mu_2\left(\frac{d\tilde{u}_2^{(z)}}{dz}\right) + \left(\frac{d\pi}{dh} - k^2\gamma_{21}\right)\tilde{\delta} = 0, \tag{5.2.9}$$

$$\tilde{\delta} = \tilde{u}_1^{(z)} / \omega. \tag{5.2.10}$$

Replacing the expression for $\tilde{u}_i^{(z)}$ from Eq. (5.2.5) to Eq. (5.2.3) the expression for $\tilde{u}_i^{(x)}$ is obtained. Further, $\tilde{P}_i$ is obtained by replacing $\tilde{u}_i^{(x)}$ in Eq. (5.2.1). Substituting the expressions for $\tilde{u}_i^{(x)}$, $\tilde{u}_i^{(z)}$ and $\tilde{P}_i$ in the linearized boundary conditions Eqs. (5.2.6) – (5.2.10) leads to a set of eight homogeneous linear algebraic equations involving eight unknown constants (B_{ji}). The following dispersion relation is obtained by equating the determinant of the coefficient matrix to zero,

$$\begin{vmatrix}
1 & \frac{1}{k} & -1 & \frac{1}{k} & 0 & 0 & 0 & 0 \\
1 & 0 & 1 & 0 & 0 & 0 & 0 & 0 \\
e^{h_0 k} & J_{32} & -e^{-h_0 k} & J_{34} & -e^{h_0 k} & J_{36} & e^{-h_0 k} & J_{38} \\
e^{h_0 k} & h_0 e^{h_0 k} & e^{-h_0 k} & h_0 e^{-h_0 k} & -e^{h_0 k} & -h_0 e^{h_0 k} & -e^{-h_0 k} & -h_0 e^{-h_0 k} \\
J_{51} & J_{52} & J_{53} & J_{54} & J_{55} & J_{57} & J_{56} & J_{58} \\
J_{61} & J_{62} & J_{63} & J_{64} & J_{65} & J_{67} & J_{66} & J_{68} \\
0 & 0 & 0 & 0 & e^{dk} & J_{76} & -e^{-dk} & J_{78} \\
0 & 0 & 0 & 0 & e^{dk} & de^{dk} & e^{-dk} & de^{-dk}
\end{vmatrix} = 0, \tag{5.2.11}$$

Here $J_{32} = \left(1 + kh_0\right)e^{h_0 k} / k$; $J_{34} = -\left(-1 + kh_0\right)e^{-h_0 k} / k$; $J_{36} = -\left(1 + kh_{10}\right)e^{h_0 k} / k$;

$J_{38} = \left(-1 + kh_0\right)e^{-h_0 k} / k$; $J_{51} = 2k\mu_1 e^{h_0 k}$; $J_{52} = 2\mu_1\left(1 + h_0 k\right)e^{h_0 k}$; $J_{53} = 2k\mu_1 e^{-h_0 k}$;

$J_{54}=2\mu_1\left(-1+h_0k\right)e^{-h_0k}$; $J_{55}=-2k\mu_2e^{h_0k}$; $J_{56}=-2\mu_2\left(1+h_0k\right)e^{h_0k}$; $J_{57}=-2k\mu_2e^{-h_0k}$;

$J_{58}=-2\mu_2\left(-1+h_0k\right)e^{-h_0k}$; $J_{61}=\left(-k^2\gamma_{21}+\varphi-2k\mu_1\omega\right)e^{h_0k}/\omega$; $\varphi=d\pi/dh$;

$J_{62}=-h_0\left(k^2\gamma_{21}-\varphi+2k\mu_1\omega\right)e^{h_0k}/\omega$; $J_{63}=\left(-k^2\gamma_{21}+\varphi+2k\mu_1\omega\right)e^{-h_0k}/\omega$;

$J_{64}=h_0\left(-k^2\gamma_{21}+\varphi+2k\mu_1\omega\right)e^{-h_0k}/\omega$; $J_{65}=2k\mu_2e^{h_0k}$; $J_{66}=2kh_0\mu_2e^{h_0k}$;

$J_{67}=-2k\mu_2e^{-h_0k}$; $J_{68}=-2kh_0\mu_2e^{-h_0k}$; $J_{76}=e^{dk}\left(1+dk\right)/k$; $J_{78}=-e^{-dk}\left(-1+dk\right)/k$.

The solution of the general dispersion relation is an analytical expression involving the linear growth coefficient and the wave number, $\omega=f(k)$, when the physical properties and the thicknesses of the films are known. The dominant growth coefficient (ω_m) and the corresponding wavelength (λ_m) are obtained by finding out the maximum of ω and the corresponding wavelength from the dispersion relation. All the algebraic operations and the numerical calculations are performed employing the commercial software Mathematica™. The dispersion relation is verified under different asymptotic limits and analytical expression of the dispersion relation corresponding to single layer dewetting is recovered.

5.2.1.3 Nonlinear evolution equation

The evolution equation of liquid-liquid interface for the nonlinear simulations is derived with the assumptions that (i) the layers are thin enough that inertia can be neglected, and (ii) the interface deforms with a small slope to ensure that the long-wave approximation is valid. The resulting momentum equations [$\mu_i u_i^{(x)}{}_{zz}=\left(p_i-\pi_i\right)_x$, $\mu_i u_i^{(y)}{}_{zz}=\left(p_i-\pi_i\right)_y$ and $\left(p_i-\pi_i\right)_z=0$] and continuity equations ($u_{ix}^{(x)}+u_{iy}^{(y)}+u_{iz}^{(z)}=0$) for the liquid layers[7] and the kinematic boundary condition for the liquid-liquid interface ($h_t+u_i^{(x)}h_x+u_1^{(y)}\big|_h h_y=u_1^{(z)}$)

lead to the evolution equation for the liquid-liquid interface, $h = h(x, y, t)$. The boundary conditions enforced to derive the evolution equation are no-slip and impermeability ($\mathbf{u}_1 = 0$ and $\mathbf{u}_2 = 0$) at the bounding surfaces [$z = f(x, y)$ and $z = d$]. The continuity of the velocity ($\mathbf{u}_1 = \mathbf{u}_2$), shear stress ($\mu_2 u_2^{(y)}{}_z = \mu_1 u_1^{(y)}{}_z$ and $\mu_2 u_2^{(x)}{}_z = \mu_1 u_1^{(x)}{}_z$), and normal stress ($P_1 = P_2 - \gamma_{21} h_{xx} - \pi$) balances at the liquid-liquid interface ($z = h$). The evolution equation thus obtained is,

$$\frac{\partial h}{\partial t} + \nabla \cdot \left(\frac{1}{6\mu_1} \frac{q_1}{q_2} \nabla \left(\gamma_{21} \nabla^2 h + \pi \right) \right) = 0 . \qquad (5.2.12)$$

where $q_1 = (d-h)^2 (h-f)^2 \left[2(d-h)^2 (h-f) + \left(2d(h-f)^2 + h\left(f^2 + 4fh - 2h^2 \right) \right) \mu \right]$, and

$$q_2 = d^4 + 4dh^3(\mu - 1) + 4d^3\left[h(\mu - 1) - \mu f \right] + d^2\left[3\mu f^2 - 6(\mu - 1)h^2 \right] + (\mu - 1)h^2\left[(\mu - 1)h^2 + 3\mu f^2 - 4\mu fh \right] .$$

In these expressions the symbol $\mu = \mu_2 / \mu_1$. For a homogeneous surface ($f = 0$), the above evolution equation asymptotically reduces to the form shown elsewhere,[1,8] which also provides the detailed steps for the derivation. To avoid contact line singularity at the late stages of evolution we incorporate Born repulsion terms into the following expression of the disjoining pressure,[1,8]

$$\pi = \frac{2d_0^2 S_{1S2}}{(h-f)^3} - \frac{2d_0^2 S_{2P1}}{(d-(h-f))^3} + \frac{3B_1}{(h-f)^4} - \frac{3B_2}{(d-(h-f))^4} . \qquad (5.2.13)$$

The cumbersome expressions for B_1 and B_2 are obtained in the limits (i) $\pi \to 0$ when $h \to l_0$, and (ii) $\pi \to 0$ when $(d-h) \to l_0$ and are not shown with the text. The disjoining pressure for an unstable confined bilayer resting on a topographically patterned substrate

is a function of the film thickness and spatial coordinates, $\pi = g(x, y, h)$. Thus, the gradient of disjoining pressures can arise from two different mechanisms,[9,10]

$$d\pi = \left.\frac{\partial \pi}{\partial h}\right|_{x,y} dh + \left.\frac{\partial \pi}{\partial x}\right|_{y,h} dx + \left.\frac{\partial \pi}{\partial y}\right|_{x,h} dy. \tag{5.2.14}$$

Here $\alpha|_{\beta}$ implies a variable α evaluated at constant β. The first term in Eq. (5.2.14) represents the spinodal dewetting [$\pi = g(h)$] whereas the last two terms represent the forces because of the wettability gradient originating from the physical heterogeneities on the substrate [$\pi = g(x, y)$]. For an unstable confined bilayer on a heterogeneous substrate, both the modes compete and the latter becomes increasingly important as the spinodal parameter ($\partial\pi / \partial h$) becomes weaker.[9,10]

The nonlinear evolution equation [Eq. (5.2.12)] is made dimensionless employing the following variables,

$$(X, Y) = K_1 (x, y)/h_0,\ (Z, H, D, D_0) = (z, h, d, d_0)/h_0,\ T = K_2 \left(t\nu_1 / h_0^2\right),$$

$$(\mathrm{P}_1, \mathrm{P}_2, \Pi) = (P_1, P_2, \pi)/\hat{P},\ \hat{P} = K_1^2 \gamma_{21}/h_0,\ S'_{2P1} = S_{2P1}/S_{1S2},\ K_1 = (BC)^{0.5},\ K_2 = B^2 C,$$

$$B = 2D_0 |S_{1S2}| h_0 / 3\rho_1 \nu_1^2,\ C = 3\rho_1 \nu_1^2 / \gamma_{21} h_0,\ \mu = \mu_2/\mu_1, \text{ and } \nu_1 = \mu_1/\rho_1.$$

The resulting dimensionless evolution equation is,

$$\frac{\partial H}{\partial T} + \nabla \cdot \left(\frac{1}{2} \frac{Q_1}{Q_2} \nabla \left(\nabla^2 H + \Pi \right) \right) = 0. \tag{5.2.15}$$

where

$$Q_1 = (D-H)^2 (H-F)^2 \left[2(D-H)^2 (H-F) + \left(2D(H-F)^2 + H\left(F^2 + 4F - 2H^2\right)\mu \right) \right],$$

and

$$Q_2 = D^4 + 4DH^3(\mu-1) + 4D^3\left[H(\mu-1) - \mu F\right] + D^2\left[3\mu F^2 - 6(\mu-1)H^2\right] + (\mu-1)H^2 \left[(\mu-1)H^2 + 3\mu F^2 - 4\mu HF\right]$$

.

The resulting dimensionless evolution equation is Eq. (5.2.15) was solved numerically in order to obtain the spatiotemporal morphologies at the liquid-liquid interface of the confined bilayer under varied conditions. The equation was initially discretized using a central difference scheme in space with half-node interpolation. Following this, periodic boundary conditions were enforced at the spatial boundaries. The resulting set of stiff ordinary differential equations was time marched employing Gear's algorithm (D02NCF subroutine in the NAG library) with an initial volume preserving random perturbation at the liquid-liquid interface.[11,12] The grid independence of the solutions was ensured by increasing the number of grid points and then comparing the solutions. The influence of the physical heterogeneity on the substrate was incorporated by locally changing the film thickness.

5.2.2 Molecular modeling

The universal force field (UFF)[13–15] from the commercial package Materials Studio of Accelrys, Inc., was employed to perform the MD simulations. UFF is a general force field employed for MD studies, which takes into account the energies corresponding to a set of (i) hybridization dependent atomic radii (E_R), (ii) hybridization angles (E_θ), (iii) van der Waals parameters (E_{VDW}), (iv) torsional and inversion barriers (E_ϕ and E_ω), and (v) effective nuclear charges (E_{EL}), for all the elements present in the periodic table. In UFF, the potential energy of a molecular system is expressed as a sum of all bonded and nonbonded interactions,

$$E = E_R + E_\theta + E_\phi + E_\omega + E_{VDW} + E_{EL}. \qquad (5.2.16)$$

The bonded interactions consist of bond stretching, E_R, which is either a harmonic oscillator $0.5k_{IJ}\left(r-r_{IJ}\right)^2$ or a Morse function $D_{IJ}e^{\left(k_{IJ}/2D_{IJ}\right)^{0.5}\left(r-r_{IJ}\right)^2}$. Here D_{IJ} is the bond dissociation energy and r_{IJ} is the bond length, which is the sum of atom specific single bond radii with bond order and electronegativity corrections. The distortions includes angle bending, $E_\theta = K_{IJK}\sum_{n=0}^{m} C_n \cos n\theta$, dihedral angle torsion, $E_\phi = K_{IJKL}\sum_{n=0}^{m} C_n \cos n\phi_{IJKL}$, inversion terms, $E_\omega = K_{IJKL}\left[C_0 + C_1\cos\omega_{IJKL} + C_2\cos 2\omega_{IJKL}\right]$, where K_{IJK} and K_{IJKL} are the force constants. The non-bonded interactions include van der Waals, $E_{VDW} = D_{IJ}\left[-2\left(x_{IJ}/x\right)^6 + \left(x_{IJ}/x\right)^{12}\right]$, where and D_{IJ} and x_{IJ} are the wall depth and van der Waals bond length. The other non-bonded interaction is the electrostatic term, $E_{EL} = 332.0637\left[Q_IQ_J/\varepsilon R_{IJ}\right]$, where Q_I and Q_J are charges in electron units, R_{IJ} is the distance, and ε is the dielectric constant.

In the beginning of each MD simulation, the initial configurations of atomic and/or molecular layers were constructed. Following this, the geometry optimization for each layer was performed separately employing a "smart" algorithm, which initiated with the steepest descent method, then followed the conjugate gradient method, and finally ended with a Newton's method. The length of the *x* and *y* directions of each layer was restricted to 8.8 nm and the heights of the individual films were varied from 0.5 to 2 nm. The confining Pt surface contained 9941 atoms whereas that of the rubber surface contained 11 200 carbon atoms. Typically, a water film of thickness 1, 0.75, and 0.5 nm contained 2600, 1950, and 1300 molecules, respectively, whereas 1.0, 0.75, and 0.5 nm benzene films contained 500, 390, and 260 molecules, respectively. Initial configurations of water and benzene films ensured the density of 1 g/cm^3 and 0.86 g/cm^3, respectively, which

were in reasonably good agreement with the standard density water and benzene at 298 K. The molecular dynamics simulations were performed for a canonical (NVT) ensemble keeping number of atoms (*N*), volume (*V*), and temperature (*T*) of the system fixed. All the simulations were performed at 298 K under isothermal conditions. The Berendsen[16] method of temperature-bath coupling was used with a decay constant of 0.1 ps. Periodic boundary conditions were applied at the spatial boundaries in the *x* and *y* directions. The equations of motions were time integrated using the Verlet algorithm[17] with a time step of 1 fs, which was found to be small enough to capture the dynamics. The coordinates of the atoms of the confining surfaces were kept fixed in all the planes and the force field on the movable atoms was calculated by including their contribution to the energy expression. For computation of the nonbonding energies (electrostatic and van der Waals interactions) the Ewald[18] summation method was used with an accuracy of the order of 0.001 kcal/mol. In each MD simulation, an initial cushion of 3000 steps was employed to equilibrate, which was indicated by the energy and temperature profile and thereafter, the simulations were time marched until 45–100 ps.

A comparison between the continuum and MD morphologies was performed employing a widely used open source image analysis software ImageJ, developed at the US National Institutes of Health and available in the public domain.[19] The simulation images were taken into this software and the average spacing between the structures (holes or columns) was obtained employing the "plot profile" option from the Analyze menu, which generated the plots with the gray scale intensities for a selected area. The areas of the images were kept fixed at 8.8 nm × 8.8 nm and the number of cycles that appear in the plots determines the average spacing between the structures. It may be noted that the MD

image analysis was always found to be noisy because of its discrete nature in terms of gray scale intensity.

5.3 RESULTS AND DISCUSSION

Ultrathin films confined between a pair of solid substrates are always under either attractive (destabilizing) or repulsive (stabilizing) influence of the Lifshitz–van der Waals interaction together with the stabilizing surface tension force. It may be noted here that the attractive or repulsive interactions discussed in this section originate from the effective Lifshitz-van der Waals forces. The nature of the effective van der Waals force acting on the films can be predicted through the well-known wettability criterion for a single thin layer confined between two semi-infinite solid or liquid substrates. The criterion states that a layer is unstable and dewets under the influence of attractive van der Waals force when it has either the highest or the lowest surface energy as compared to the semi-infinite bounding surfaces ($A_i > 0$ and $S_{ijk} < 0$). Further, the layer can be stable or wetting under the influence of repulsive van der Waals interaction when the surface energy has an intermediate value as compared to the bounding surfaces ($A_i < 0$ and $S_{ijk} > 0$). The criterion helps in the classification of thin confined bilayers into the following cases,

(i) Case I (Pt-W-B-Pt): The benzene (B) and water (W) films are confined between high-energy Pt substrates. The typical surface energies of the materials (γ_{Pt} = 2489 mN m^{-1}, γ_B = 28.8 mN m^{-1}, and γ_W = 72 mN m^{-1})[20–23] ensure that the benzene layer is thermodynamically unstable between the water layer and the Pt surface because it has the lowest surface energy ($S_{BWPt} < 0$). In contrast, the water layer is stable between the Pt surface and the benzene layer because it has intermediate surface energy ($S_{BWPt} > 0$). Thus, for this configuration, only the benzene film is expected to dewet the Pt surface.

(ii) Case II (R-W-B-R): The liquid films are confined between low-energy rubber substrates. The typical surface energy of rubber (γ_R = 60 mN m^{-1}) ensures that both benzene and water layers are thermodynamically unstable ($S_{BWR} < 0$ and $S_{WBR} < 0$) in this configuration.

(iii) Case III (R-W-B-Pt): The liquid films are confined between low-surface-energy rubber and high-surface-energy Pt substrates, which ensures that both the layers are thermo-dynamically unstable ($S_{BWP} < 0$, $S_{WBR} < 0$). In what follows, the results from LSA, continuum, and MD simulations are described systematically for each case to uncover the salient features of the self-organized instabilities of the confined bilayers.

TABLE 5.1 The following Hamaker constants, surface energies, and viscosities are used for calculations of the reported different cases.[20-23]

Properties	*Case* I	*Case* II	*Case* III
A_1 (J)	2.89×10^{-19}	3.68×10^{-20}	2.89×10^{-19}
A_2 (J)	-2.25×10^{-19}	2.66×10^{-20}	2.89×10^{-20}
γ_1 (N m^{-1})	0.072	0.072	0.072
γ_2 (N m^{-1})	0.028	0.028	0.028
γ_{21} (N m^{-1})	0.033	0.033	0.033
μ_1 (Pa s)	8.94×10^{-4}	8.94×10^{-4}	8.94×10^{-4}
μ_2 (Pa s)	6.04×10^{-4}	6.04×10^{-4}	6.04×10^{-4}

5.3.1 Linear stability analysis

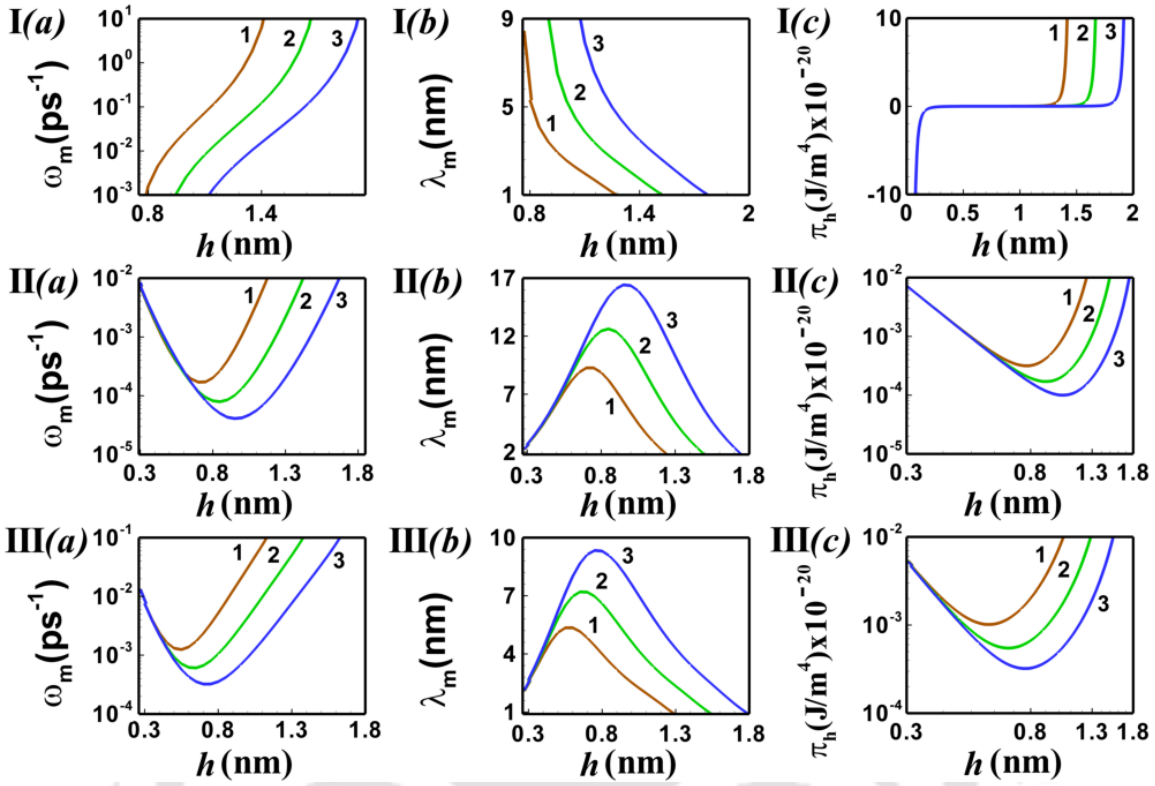

Figure 5.2 The LSA results for the confined bilayers. Plots (a) – (c) show the variations of ω_m, λ_m and $\partial\pi/\partial h$ with h. Rows (I) – (III) correspond to cases (I) – (III). Curves 1 – 3 represent a constant d = 1.5 nm, 1.75 nm, and 2.0 nm, respectively. The other parameters required for the plots are shown in Table 5.1.

Figure 5.2 shows the LSA plots in which the typical length and time scales of the instabilities of the confined bilayers are discussed. In this figure, the plots (a) – (c) show the variations in the dominant growth coefficient ω_m, corresponding wavelength λ_m, and pressure gradient due to the van der Waals interaction ($\partial\pi/\partial h$), respectively, with the water layer thickness (h) at constant d. Rows (I) – (III) show the results for cases (I) – (III) in which the lower layer is water and the upper layer is benzene unless mentioned otherwise. Table 5.1 shows a list of typical parametric values employed to generate the plots in Figure 5.2. The results for case I show that increase in the thickness of the benzene layer (decreasing h) leads to a reduction in ω_m [plot (Ia)] and increase in λ_m [plot

(Ib)]. As discussed previously, the instability of the case I bilayer is dictated by the instability of the benzene layer because the water layer is stable between the benzene layer and the Pt surface. Thus, increasing the thickness of the benzene layer (decreasing *h*) leads to a reduction in the net destabilizing van der Waals force [plot (Ic)], which increases the time and the length scales of the instability. The plots for case II show that when the water layer is very thin (low *h*) the instability is controlled by the stronger destabilizing van der Waals interaction at the water layer. With increase in the water layer thickness ω_m decreases [plot (IIa)] and λ_m increases [plot (IIb)]. However, beyond a threshold thickness ratio of the layers, the destabilizing van der Waals interaction due to the thinness of the benzene layer fuels up and instability is dictated by the dewetting of the benzene layer. Thus, ω_m (λ_m) again increases (decreases) as the benzene layer thickness is reduced (increasing *h*). Plot (IIc) shows that the pressure gradient due to the van der Waals interaction passes through a minimum where both the layers are equally unstable, which also corresponds to the minimum and maximum of ω_m and λ_m in plots (IIa) and (IIb). Case III shows a similar trend as observed for case II. In this situation, again, at lower *h* the instability is dictated by the stronger van der Waals interaction at the water layer. With increase in *h* initially ω_m decreases [plot (IIIa)] and λ_m increases [plot (IIIb)]. Beyond a threshold *h*, the destabilizing van der Waals interaction due to the benzene layer fuels up and consequently, ω_m (λ_m) increases (decreases) as the benzene layer thickness is reduced (increasing *h*). Plot (IIIc) shows that the pressure gradient due to the van der Waals interaction passes through a minimum, which also corresponds to the minimum of ω_m and maximum of λ_m in plots (IIIa) and (IIIb).

The plots in Figure 5.2 summarize that the length scale of the instabilities of ultrathin bilayers can indeed be less than 20 nm when the films are really thin (< 5 nm) and the time scale, $t \infty (1/\omega_m)$, is of the order of picoseconds. In the following sections, we show that the MD simulations also closely follow the order of length and time scales as obtained from the LSA.

5.3.2 Molecular dynamics and continuum simulations

1. Case I (Pt-W-B-Pt)

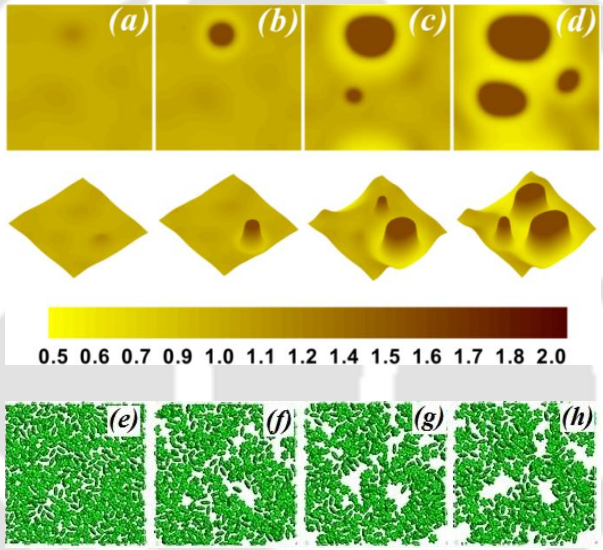

Figure 5.3 The simulation results for case I (Pt-B-W-Pt). Images (a) – (d) show the continuum evolution over a 3Λ × 3Λ domain when the benzene (water) film is 0.75 nm (1.0 nm) thick (λ_m = 3.14 nm). Images in the first (second) row show the top view (3D surface profiles) at *T* = 4.8, 5.2, 5.8, and 6.4, respectively. Images (e) – (h) show the spatiotemporal MD evolution, where the first, second, and third rows show the evolution of the benzene, water, and combined layers, after *t* = 0, 15, 30, and 45 ps, respectively. In images (a) – (h), the benzene (water) layer is 0.75 nm (1.0 nm) thick.

Figure 5.3 summarizes the results obtained from both continuum and MD approaches. Images (a) – (d) show the spatiotemporal continuum simulations where the first row shows the top view and the second row depicts the three-dimensional (3-D) view of the evolving liquid-liquid interface. In all the images, the darker shades represent higher *h*.

Images (e) – (h) show the time evolution of the same system following the MD approach where the first and second rows represent the benzene and the water layer, respectively, and the third row depicts the combined 3-D evolution after removing the top surface. Images (i) – (k) show the influence of the variation in the film thickness on the interfacial patterns. It may be noted here that all the continuum simulations are performed employing a $3\Lambda \times 3\Lambda$ lateral domain where is the dimensionless dominant length scale. The lateral dimension for the MD simulations are kept fixed at 8.8 nm × 8.8 nm. Unless mentioned otherwise the lower layer of the bilayer is water and the upper layer is benzene.

Images (a) – (d) show the evolution of a case I confined bilayer with a 0.75-nm-thick benzene layer resting on a 1.0-nm-thick water layer. In response to the initial random perturbations, in a short time the benzene film dewets the top Pt substrate [darker zones in images (a) and (b)]. Following this, as the holes formed in the benzene layer grow to achieve equilibrium contact angle [images (b) – (d)] the water layer fills out these holes to form columnar structures. Near equilibrium, a collection of holes in the benzene layer filled by the water columns is observed. It may be noted here that among the initial nine waves [image (a)] only three grow to form holes in the benzene layer [image (d)].

The bilayer considered in images (a) – (d) is also simulated employing the MD approach and the results are shown in images (e) – (h). Interestingly, the MD approach also shows that in a short time holes are formed in the benzene layer [image (e)], which grow in time while the water remains stable after a sufficient amount of time marching [images (f) – (h)]. The MD morphology shown in image (h) closely resembles the continuum morphology shown in image (d).

The MD and continuum simulations in Figure 5.3 together convey that the instability of a benzene-water bilayer confined between two high-energy surfaces initiates with the

dewetting of the benzene layer followed by filling of the dewetted zones by the water layer at the zones where the benzene layer dewets the top surface. The simulations also show that strength of the van der Waals interaction can indeed be modulated by changing the film thickness of the water and benzene layers, which can have a marked influence on the hole formation, hole spacing, and subsequent dewetted morphologies. The figure also corroborates interesting nanoscale patterns such as encapsulated or embedded holes and columns can be decorated on the solid surfaces employing this configuration.

2. Case II (R-W-B-R)

In this case, again, the benzene layer is confined between two higher-surface-energy materials, rubber and water, which ensure an unstable benzene layer (S_{BWR}<0). However, as compared to the previous case, the lower energies of the bounding surfaces induce a weaker destabilizing van der Waals interaction to the benzene layer. Further, unlike the previous case, the water layer is now confined between two lower-surface-energy materials, rubber and benzene, which ensures that the water layer is also unstable (S_{WBR} < 0).

Figure 5.4 summarizes the simulated results for this case. Images (a) – (d) show the continuum simulation of a confined bilayer when benzene and water films are equally thick. In this case, a larger destabilizing van der Waals interaction breaks the benzene layer first [darker shades, image (a)]. It may be noted here that the water columns are formed at the places where the benzene layer is dewetted. Following this, as the holes in the benzene layer (columns in the water layer) grow to achieve equilibrium contact angle the hole rims (depressions adjacent to the columns) grow towards the lower rubber surface and break the water layer [images (c) and (d)]. Breakup of the water layer also leads to the formation of benzene columns. Near equilibrium, a morphology composed of the columns

of water (columns of benzene) embedded inside the dewetted benzene (water) layer is observed. Images (e) – (h) show that increase in the thickness reduces the destabilizing van der Waals interaction in the benzene layer. In consequence, the initial stage of instability is dictated by the dewetting of the water layer on the lower rubber surface. At the later stages of the evolution, again the benzene film is found to dewet the upper rubber surface. The final morphology in image (h) is composed of a collection of benzene columns embedded inside the dewetted water film.

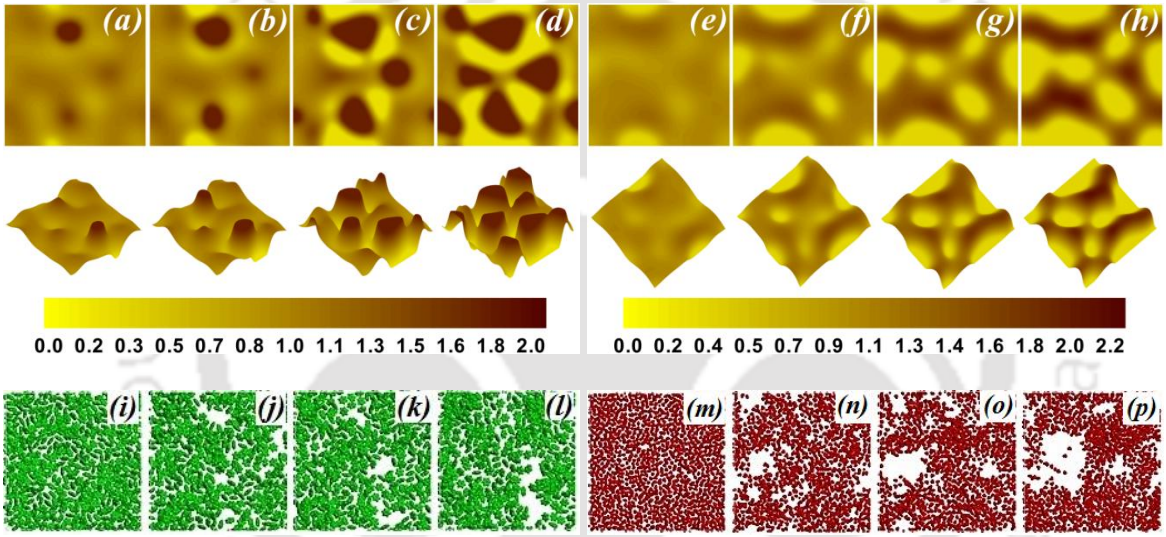

Figure 5.4 The results for case II (R-W-B-R). Images (a) – (d) show the continuum evolution over a 3Λ × 3Λ domain (λ_m = 9.13 nm) of a confined bilayer when the benzene and water films are equally thick (0.75 nm). Images in the first (second) row show the top view (3-D surface profiles) at *T* = 4.5, 4.73, 5.08, and 5.4, respectively. Images (e) – (h) show the continuum simulation when the benzene (water) film is 1.0 nm (0.5 nm) thick over a 3Λ × 3Λ domain (λ_m = 6 nm). Images in the first (second) row show the top view (3-D surface profiles) at *T* = 13.4, 15.1, 16.3, and 17.6, respectively. Images (i)–(p) show the MD evolution. Images show the evolution of the benzene layers after *t* = 0 ps, 25 ps, 50 ps, and 100 ps, respectively. In images (i) – (l), the benzene (water) layer is 0.75 nm (0.75 nm) thick and in images (m) – (p), the benzene (water) layer is 1 nm (0.5 nm) thick.

Images (i) – (l) show the MD evolution of the bilayer considered in images (a) – (d). Interestingly, similar to the continuum simulations, the MD simulations suggest that in this situation the benzene layer dewets the upper rubber surface in a short time. However,

unlike the continuum simulations the water layer does not dewet the lower rubber surface simultaneously and remains stable until about 100 ps. The stability of the water layer can be kinetic in nature and a longer time marching can lead to its breakdown. Importantly, the MD and continuum simulations differ significantly at this point because the continuum simulation infers a simultaneous dewetting of both layers, whereas the MD simulations predict the dewetting of the benzene layer at the initial stages and breaking down of the water layer at the later stages. In order to test the instability of the water layer, we simulated another bilayer where it is much thinner and the benzene layer is thicker, similar to the continuum case shown in images (e) – (h). In such a situation, images (m)–(p) suggest that increase in thickness can suppress the instability at the benzene layer and the dewetting can progress by hole formation, hole growth, and hole coalescence in the water layer on the lower rubber surface. In this situation, the weaker destabilizing van der Waals interaction leads to the kinetic stability of the benzene layer.

Concisely, the simulations in Figure 5.4 convey that when a benzene-water bilayer is confined between a pair of low-energy rubber surfaces, both the layers can dewet (or form columns) on the solid surfaces. Although the continuum simulations show similar hole spacing as the MD simulations at the initial stages, the final morphology is found to be somewhat different. In particular, the MD simulations show that the liquid layers can break up sequentially rather than simultaneously under these conditions as predicted by the continuum simulations. However, both approaches convey that by tuning the thickness of the films the spacing and location of the nanoscale patterns can be modulated employing this configuration.

3. Case III (R-W-B-Pt)

Figure 5.5 summarizes the results from the continuum for this case. Images (a) – (d) show that when the liquid layers are equally thick the initial holes form at the benzene layer (darker regions) because of the larger destabilizing van der Waals interaction. At the later stage the water film also breaks up and an array of water columns encapsulated by the dewetted benzene layer is observed near equilibrium. Images (e) – (h) show that increase in the thickness reduces the strength of the destabilizing van der Waals interaction at the benzene layer, which leads to the dewetting of the benzene layer with a larger spacing between the holes. At the later stage the water film also breaks up and a collection of randomly placed water columns embedded inside the dewetted benzene layer can be observed.

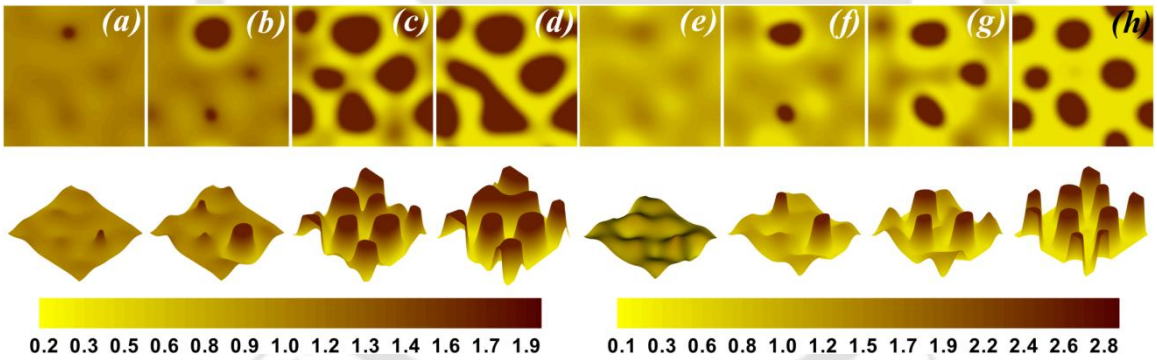

Figure 5.5 The simulation results for case III (R-W-B-Pt). Images (a) – (d) show the continuum evolution over a 3Λ × 3Λ domain (λ_m = 4.1 nm) when the benzene and water films are 0.75 nm thick. Images in the first (second) row show the top view (3-D) surface profiles) at *T* = 0.15, 0.17, 0.201, and 0.23, respectively. Images (e) – (h) show the continuum simulation over a 3Λ × 3Λ domain (λ_m = 4.8 nm) when the benzene (water) film is 1.0 nm (0.5 nm) thick. Images in the first (second) row show the top view (3-D surface profiles) at *T* = 4.8, 5.2, 5.7, and 6.7, respectively.

Figure 5.5 conveys that the dewetting of the benzene-water bilayer confined between a low- and high-energy surface progresses with breakdown of both the layers. The figure

also conveys that interesting pattern–such as a hole at the upper layer filled by the lower can be fabricated employing this configuration.

5.3.3 Spatiotemporal scales and morphologies from the continuum and MD approaches

TABLE 5.2 Length and time scales, morphologies from continuum (CD) and MD approaches for different cases. The lighter shades in the images show smaller height.

Case	$h_0 - d$ (nm)	CD image	MD image	LWLSA/GLSA		CD		MD	
				l (nm)	t (ps)	l (nm)	t (ps)	l (nm)	t (ps)
I	1.0 - 1.75	**Fig.-** 5.6(a)	**Fig.-** 5.6(b)	3.15/5.27	308/394.3	4.4	3.5×10^3	4.4	45
II	0.5 - 1.5	**Fig.-** 5.6(c)	**Fig.-** 5.6(d)	6.0/6.22	1533/1700	4.4	2.3×10^4	4.4	50
III	0.5 - 1.5	**Fig.-** 5.6(e)	**Fig.-** 5.6(f)	4.8/5.1	630/760	4.4	7.7×10^3	4.4	15

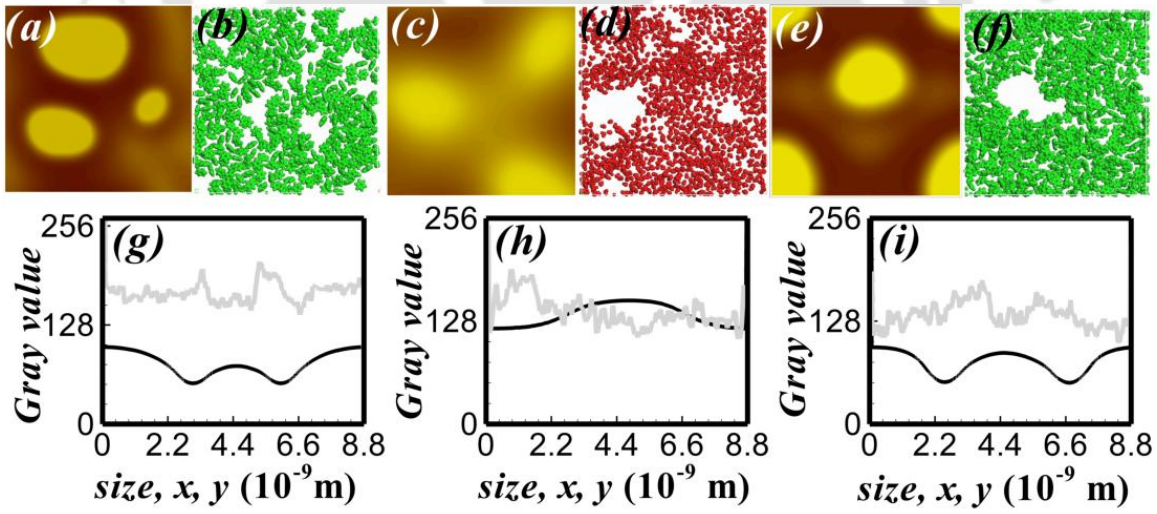

Figure 5.6 Images (a) – (f) are referenced in Table 5.2. Plots (g) – (i) show gray scale vs distance plots obtained from the image analysis of plots (a) – (f). Plot (g) corresponds to images (a) and (b) of case (I), plot (h) corresponds to images (c) and (d) of case (II), and plot (i) corresponds to images (e) and (f) of case (III). The line with darker (lighter) shade corresponds to the continuum (MD) simulations.

A comparative analysis on the time and length scales obtained from the continuum and MD approaches is presented in Table 5.2. The continuum and MD simulations images in the table are of the same size and the length scales are obtained by the image analysis method mentioned in Sec. 5.2.2. It may be noted that the domain size limitations for the MD simulations might influence the hole or column spacing reported, although the periodic boundary conditions are enforced at the spatial boundaries. Larger area MD simulations may uncover more quantitative information in this regard. Images (a) – (f) in Figure 5.6 show the plots mentioned in Table 5.2 under varied conditions. Plots (g) – (i) in Figure 5.6 show the comparison of the length scale plots for the cases presented in Table II. We present three different approaches to compare the time and length scales from the continuum: (i) GLSA–the general linear stability analysis presented earlier in Sec. 5.2.1.2, (ii) LWLSA–long-wave linear stability analysis, which is performed by linearizing the thin film Eq. (5.2.12) using standard procedure,[9] and (iii) from the image analysis of the continuum simulations. The results obtained from these approaches are compared and contrasted with the data obtained from the MD simulations. The case I configuration in Table 5.2 shows matching in both morphology and length scales from all the continuum and MD approaches. For example, both morphologies in the continuum and MD simulations in row 1 show that there are multiple holes in the benzene layer with similar average spacing [Figure 5.6(a)]. The time scale estimate differs only by an order of magnitude for the LSA and MD approaches. However, the time scales predicted by the continuum simulations are about two to three orders of magnitude higher as compared to the MD predictions. In fact, for all the cases (rows 1 – 3) the time scales obtained from the continuum simulations are considerably higher, whereas the length scales are quite similar. The time scales obtained from the LSA in all the rows are intermediate between

the values observed for the continuum and MD simulations. The length scales obtained from the LSA differ marginally from the continuum and MD simulations in rows 2 and 3. Concisely, Figure 5.6 and Table 5.2 show that the predictions from continuum and MD approaches match in some cases and deviate fairly in some situations. The deviations can be attributed to the approximations made while developing the continuum model. For example, we always consider the films to be incompressible in the continuum description. However, NVT ensemble allows local compressibility of the films, which can lead to different interfacial morphologies, as shown with the results of case III. Further, the intermolecular force in the continuum domain employs the DLVO approximation to calculate the contribution from the intermolecular force, which is more comprehensively calculated in the MD simulations. While the interface of the continuum description is considered very sharp, the MD simulations may allow nontrivial intermixing of the layers near the interface, which can also change the spatiotemporal dynamics of the films by changing the interfacial properties.

5.3.4 Patterning of dewetted structures

The dewetted structures obtained in the previous section can be ordered employing a lateral wettability gradient by means of decorating topographical patterns on the substrate surface. Figure 5.7 shows the dewetting of a case I (Pt-W-B-Pt) bilayer when the Pt surface near the benzene layer is decorated with either a cross pattern [image (a)] or a stripe [image (e)]. It may be noted here that benzene (water) is considered as the lower (upper) layer in the following simulations. Images (a) – (h) show the results obtained from the continuum simulations and images (i) – (j) show the same from the MD simulations. The continuum simulations depict that in the presence of a cross pattern [images (a) – (d)] or stripe [images (e) – (h)] the benzene layers breaks up near the patterns owing to larger

van der Waals interaction due to the local thinness of the film. As the dewetting front moves to achieve equilibrium contact angle, droplets are formed over the grooves on the cross-patterned surface [image (d)] whereas a channel is formed on the ridge of the striped surface [image (h)]. Interestingly, the size and periodicity of the droplets and channels formed are in the nanoscale regime and use of repeated periodic patterns on the substrate can lead to a large area ordering of these patterns. The continuum simulations have shown in images (a) – (h) have striking resemblance with the similar MD simulations shown in images (i) – (j).

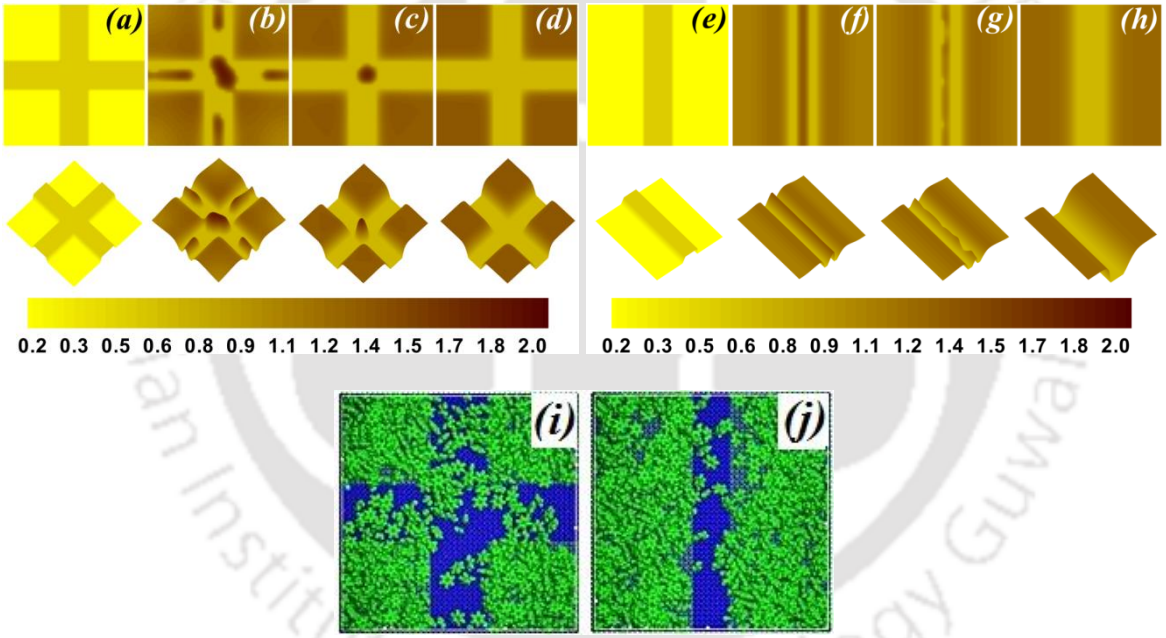

Figure 5.7 The simulation results for a case I (Pt-W-B-Pt) bilayer on physically patterned surfaces. Images (a) – (d) show the continuum evolution of a confined bilayer over $\Lambda \times \Lambda$ domain on cross-patterned surface. Image (a) in the first (second) row shows the top view (3-D profiles) of cross-patterned surface and images (b) – (d) in the first (second) row show the top view (3-D profiles) of the evolving interface at T = 3.3, 12.4, and 28.05, respectively. Images (e) – (h) show the continuum simulation over $\Lambda \times \Lambda$ domain on striped patterned surface. Image (e) in the first (second) row shows the top view (3-D profiles) of striped patterned surface and images (f) – (h) in the first (second) row show the top view (3-D profiles) of the evolving interface at T = 2.03, 5.3, and 37.7, respectively. Images (i) and (j) show the MD morphologies of the benzene layer after 50 ps. In all plots, h = 1.0 nm, d = 2.0 nm, and the defect height is 0.4 nm.

Figure 5.7 conveys that physically heterogeneous nanopatterns on the confining surface can locally expedite the dewetting of the unstable liquid layers and indeed direct the dewetting pathway to form interesting ordered nanostructures. The kinetics of dewetting is found to be much faster on the patterned surfaces owing to the stronger influence from the lateral wettability gradient as compared to the van der Waals interactions on the homogeneous surfaces.

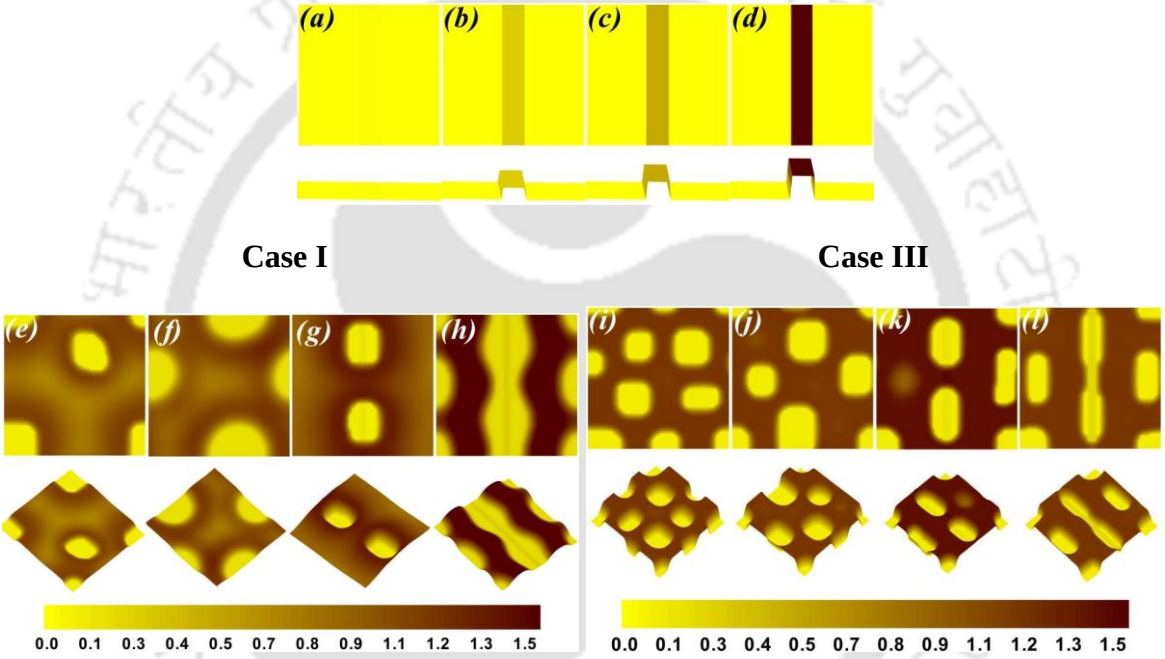

Figure 5.8 The continuum simulation results of spatiotemporal evolution of liquid-liquid interface for case I (Pt-W-B-Pt) and case III (Ru-W-B-Pt) bilayers composed of water ($d - h$ = 1 nm) and benzene (h = 2 nm) layers on a striped Pt substrate with varying height of striped. The first (second) row in images (a) – (d) show top view (side view) of striped Pt substrate. Width of the striped in all the cases is 1.50 nm and its height increases from left to right and for case I (Case III) are 0.0 nm, 0.02 nm, 0.1 nm, and 0.2 nm, (0.0 nm, 0.02 nm, 0.1 nm, and 0.3 nm) respectively. Images (e) - (h) show the morphologies after T = 93.8, 31.2, 66.1 and 23.8 respectively and images (i) - (l) show that after T = 69.0, 79.4, 75.2 and 31.1 respectively. Other necessary parameters are $A_1 = -1.2 \times 10^{-19}$, $A_2 = 2.67 \times 10^{-19}$ for Case I and $A_1 = 4.41 \times 10^{-21}$, $A_2 = 2.67 \times 10^{-19}$ for Case III.

The Figures 5.8 and 5.9 explore the salient features of the defect induced dewetting of the confined bilayers employing continuum dynamic simulations (CD). In the process we capture the diverse nanoscale structures that arise during the transition from the spinodal

to the defect induced dewetting of confined bilayers. The chemical impurities at the solid surface can create a wettability gradient because of the sharp change in the magnitudes of A_i or S_{ijk} across the defect. In such situations, the holes are nucleated near the chemical defects when the film is thermodynamically unstable ($A_i > 0$ and $S_{ijk} < 0$). The chemical heterogeneity on the substrate is created by embedding layers with another material of higher Hamaker constant (A_{2C}). Again, the depth and width of the embedding layers stripe are varied to change the dimensions of the chemical defects. In may be noted here that in all the simulations reported in this work the water (benzene) layer is considered to be the upper (lower) layer.

The Figures 5.8 summarize the effect of the height of the stripe on the change in the dewetting pathway from spinodal to heterogeneous nucleation. In this figure, the first two rows show the substrate top and side views and 3rd and 4th rows of images (e) – (h) [(i) – (l)] show the top and isometric views of the interface for case I (case II). The images in the columns (a) – (d) suggest that the CD simulations can also qualitatively predict the transition from spinodal to the pattern directed pathway when the height of the stripe is varied for the cases I and III. However, for the CD simulations the transition takes place at a much smaller height of the stripe. Interestingly, the CD simulations predict an array of beaker and channel shaped nanoscale patterns with the change in the height of the stripe pattern, which can find diverse applications once large area ordering is achieved employing functional materials as films.

Figures 5.9 display a similar transition in the dewetting mechanism when the Pt surface is decorated with a stripe of chemical heterogeneity. In this case the width and the height of the chemical patterns are changed to identify the regimes for the dominance of the spinodal and the pattern directed pathways. In this figure, the first row show the substrate

side views and 2rd and 3th rows of images (d) – (f) [(g) – (i)] show the top and isometric views of the interface for case I (case III). The CD simulations clearly suggest that a transition from randomly placed holes to the nanochannel can take place when the width of the chemical patch is increased. Again, the CD simulations under predicts the patch width for the transition from the spinodal to the pattern directed pathway.

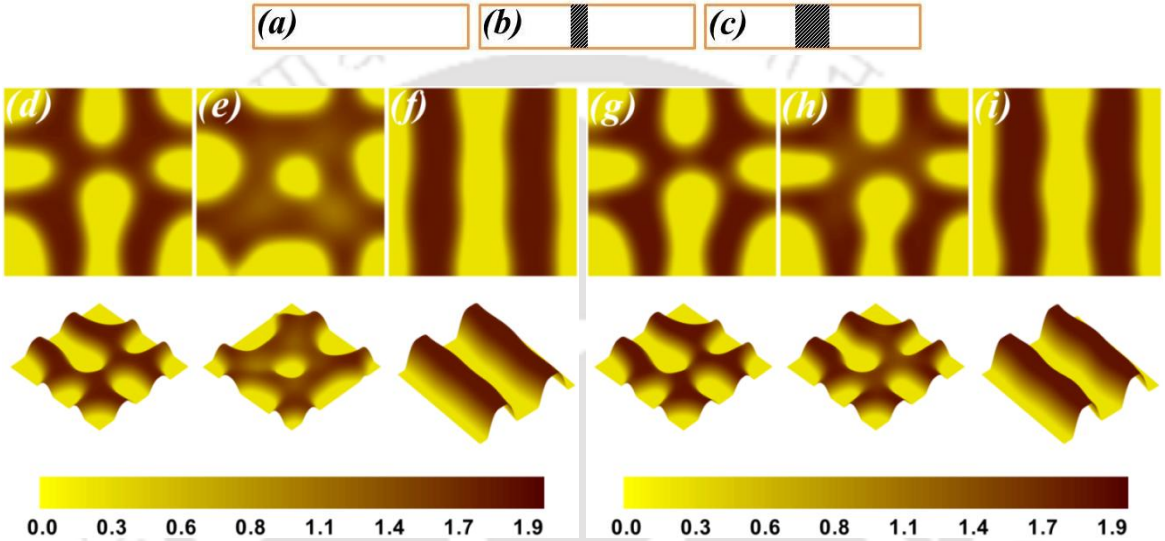

Figure 5.9 The continuum simulation results of spatiotemporal evolution of liquid-liquid interface for case I (Pt-W-B-Pt) and case III (Ru-W-B-Pt) bilayers composed of water (*d* – *h* = 1 nm) and benzene (*h* = 1 nm) layers on a chemically striped Pt substrate. Images (a) – (c) show side view of a chemically patterned substrate with different patterned width (0.0 nm, 0.08 nm and 0.2 nm). Images (d) - (f) show the morphologies after *T* = 44.1, 37.8, and 44.6, respectively, and images (g) - (i) show that after *T* = 44.6, 36.0, and 39.8, respectively. The bottom row shows the side view of the respective Pt substrates. Other necessary parameters are $A_1 = -1.2\times10^{-19}$, $A_2 = 2.67 \times 10^{-19}$, and $A_{2C} = 4.0 \times 10^{-19}$ for Case I and $A_1 = 4.41 \times 10^{-21}$, $A_2 = 2.67\times10^{-19}$, and $A_{2C} = 4.0 \times 10^{-19}$ for Case II.

5.4 SUMMARY

We report a combined continuum and MD analysis to study the pathways to dewetting of an ultrathin confined bilayer resting on homogeneous and topographically patterned surfaces. The major conclusions are as follows:

(i) The confined bilayers are classified into different cases based on the dewetting behaviors of the films between a pair bounding high- to low-energy surfaces. Both the

continuum and MD approaches show that only the benzene layer (case I) or both the layers (cases II and III) can be unstable under varied conditions. In particular, the MD simulations predict that for cases II and III, the films can dewet the confining surfaces either periodically or simultaneously, under varied conditions. This is in contrast to the predictions from the approximate continuum approach, which always show a simultaneous dewetting of the layers. Further, the MD simulations predict a thermodynamic stability in case I and conditional kinetic stability in cases II and III, for the water layer. Importantly, the MD simulations show the different stages of the dewetting such as the hole formation, hole growth, and hole coalescence in the layers, as observed in the experiments for the ultrathin single films. The predictions from the MD simulations encourage future experiments on the various dewetting pathways of the ultrathin confined bilayers for nanostructure formation.

(ii) The continuum and MD simulations show striking resemblance in predicting the short-time length and time scales of the instabilities. Further, the shape of the holes, spacing between the holes, and hole-growth phenomena match very closely for both the continuum and MD simulations. However, the results of the later stages of the evolution differ significantly, which can be attributed to the approximations associated with the continuum approach. The study highlights the importance of the MD simulations in predicting accurately the short- to long-time features of the instabilities of these nanoscale systems.

(iii) The instabilities of a confined bilayer can be exploited to develop technologically important nanoscale patterns. In this direction, the important factors are the thinness of the liquid layers and the weak interfacial tension at the liquid-liquid interface. A host of interesting patterns such as arrays of holes, columns, droplets, stripes, and channels can be fabricated on the solid surfaces tuning the surface energies of the building blocks and

thicknesses of the films. A large area ordering can be imposed on the patterned structures by decorating periodic topographical patterns on the substrates. Importantly, the dewetting confined bilayers are capable of developing encapsulated and embedded nanoscale patterns, which are otherwise difficult to fabricate employing conventional lithographic techniques or from the self-organized instabilities of a single layer. The MD simulations are computationally intensive and require long-time number crunching even when simple liquids such as benzene or water are simulated. Thus, simulating the dewetting polymeric materials as thin layers, which are in general employed for experiments or for technological purposes, is beyond the scope of this work. However, the length scales and morphologies reported for the simple liquids remain valid even for the films with complex fluids, especially when they exhibit Newtonian behavior. The kinetic influences such as the viscous dissipation or the elastic relaxation in the materials can only time-shift the various features of the dewetting process, as shown by the previous studies.[9,25,26,27] Instead of the MD approach, the time dynamics of the technologically important complex fluids can be accurately studied employing the computationally less intensive coarse-grained approach, which will motivate future works in these areas.

(iv) In the present study we excluded the elliptic equation which is coupled with the evolution equation that gives the effect of vertical vorticity[1]. For radially symmetric structures like, perfectly circular drops, holes or column are not affected by the additional vorticity contribution even in the strongly nonlinear regime.

5.5 REFERENCES

1. D. Merkt, A. Pototsky, M. Bestehorn, and U. Thiele, Phys. Fluids **17**, 064104 (2005).
2. C. J. van Oss, M. K. Chaudhuty, and R. J. Good,Chem. Rev. **88** , 927 (1988).

3. J. N. Israelachvili, Intermolecular and Surface Forces (Academic Press, London, 1992).
4. A. Sharma, Langmuir **9**, 861 (1993).
5. A. Oron, S. H. Davis, and S. G. Bankoff, Rev. Mod. Phys. **69**, 931 (1997).
6. A. Sharma and R. Khanna, Phys. Rev. Lett. **81**, 3463 (1998).
7. E. Ruckenstein and R. K. Jain, J. Chem. Soc., Faraday Trans. 2 **70**, 132 (1974).
8. R. Verma, A. Sharma, I. Banerjee, and K. Kargupta, J. Colloid Interface Sci. **296**, 220 (2006).
9. K. Kargupta and A. Sharma, J. Colloid Interface Sci. **245**, 99 (2002).
10. A. Sharma, Eur. Phys. J. E **12**, 397 (2003).
11. D. Bandyopadhyay and A. Sharma, J. Phys. Chem. B **112**, 11564 (2008).
12. D. Bandyopadhyay and A. Sharma, J. Phys. Chem. C **114**, 22377 (2010).
13. A. K. Rappé, C. J. Casewit, K. S. Colwell, W. A. Goddard, and W. M. Skid, J. Am. Chem. Soc. **114**, 10024 (1992).
14. A. K. Rappé, K. S. Colwell, and C. J. Casewit, Inorg. Chem. **32**, 3438 (1993).
15. Materials Studio 4.2 Manual (Accelrys, Inc., San Diego, CA, 2007).
16. H. J. C. Berendsen, J. P. M. Postma, W. F. V. Gunsteren, A. DiNola, and J. R. Haak, J. Chem. Phys. **81**, 3684 (1984).
17. L. Verlet, Phys. Rev. E **159**, 98 (1967).
18. N. Karasawa, I. William, and A. Goddard, Macromolecules **25**, 7268 (1992).
19. E. Gering and C. T. Atkinson, J. Parasitol. **90**, 879 (2004).
20. R. K. Wanchoo, J. Narayan, G. K. Raina, and V. K. Rattan, Chem. Eng. Commun. **81**, 145 (1989).
21. J. A. Dean, Lange's Handbook of Chemistry (McGraw-Hill, New York, 1967).
22. W. R. Tyson and W. A. Miller, Surf. Sci. **62**, 267 (1977).
23. K. Moran, A. Yeung, and J. Masliyah, Langmuir **15**, 8497 (1999).
24. G. Tomar, V. Shankar, S. K. Shukla, A. Sharma, and G. Biswas, Eur. Phys. J. E **20**, 185 (2006).
25. R. Konnur, K. Kargupta, and A. Sharma, Phys. Rev. Lett. **84**, 931 (2000).
26. K. Kargupta and A. Sharma, Phys. Rev. Lett. **86**, 4536 (2001).

27. G. Tomar, V. Shankar, S. K. Shukla, A. Sharma, and G. Biswas, Eur. Phys. J. E **20**, 185 (2006).

Chapter 6

Conclusions and scope for future work

6.1 CONCLUSIONS

Interfacial instabilities of thin films have been studied for four different configurations. The length and time scales at the early stage of instabilities have been predicted using liner stability analysis. The late stage of morphologies is captured using nonlinear simulation for some of the configurations. The major observations from each of the analysis are discussed below.

6.1.1. Electro-capillary instabilities of thin elastic-viscous bilayer: A general linear stability analysis of the electric field induced instabilities of elastic-viscous bilayers uncovers the following key features,

(i) Presence of a leaky elastic or viscous layer in the bilayer can impart additional electrostatic stress due to the presence of free charges at the interface, which can significantly reduce the length scales to develop submicron patterns. Unlike the purely dielectric bilayers where the accumulation of induced dipoles due to the dielectric-contrast across the interface dictates the direction of the interfacial deformation, for leaky bilayers the presence of the free charge (positive or negative) can determine the deformation towards or away from the electrodes (anode or cathode).

(ii) The study uncover that a transition from long- to short-wave instabilities take place with progressive increase in the strength of the destabilizing stress, reduction in the capillary forces at the interface, and with increase in the thickness of the leaky layer.

(iii) The general analysis shown here could reproduce the previously predicted length scales especially with a long-wave potential. Further, the use of a more generic potential in the present work can indeed predict the recently reported experimental length scales of the electric field induced instabilities of elastic viscous bilayers.

(iv) A recent experiment has already shown the reduction in the length scales in an elastic-viscous bilayer with a leaky viscous bilayer. The present work predicts that instead of the viscous layer, use of elastic layer can further reduce the length scales of the features. In addition, the study uncovers that the elastic-viscous configurations with one leaky layer can indeed lead to sub-micron scale patterns at reasonably low field intensity on the surface of the elastic film.

6.1.2. Electric field induced instabilities of thin leaky bilayers: The influence of charge leakage on the electric field induced interfacial instabilities of thin bilayers has been explored with the help of linear stability analysis together with nonlinear simulations. The study highlights,

(i) The general linear stability analysis considers the full descriptions of the Maxwell stresses in the formulation and uncovers the short-wave features of the electric field induced instabilities of thin bilayers with leaky dielectric films. In this regard, the inadequacy of the long-wave analysis is highlighted especially when stronger destabilizing electrical stresses reduce the length scale to the order of film thickness.

(ii) When a bilayer is exposed to an external electrostatic field, a weakly conducting lower layer can develop free charges at the liquid-liquid interface whereas a leaky upper layer can develop free charges at both the interfaces. Importantly, introduction of weakly conducting liquid layers in a bilayer can fuel up coupled electrical stresses at the interface(s) due to the accumulation of the free charges together with the induced charge separation. The GLSA uncovers that the presence of weak conductivity at any of the layers or both the layers can significantly reduce the length scale of the instability. In particular, when the instability is dominated by the deformation of the liquid-liquid

interface with a weaker stabilizing interfacial tension, the wavelength of instability can be pushed to the nanoscale regime.

(iii) The charge concentration(s) are found to vary spatiotemporally at the interface(s) to develop a wide range of destabilizing force field with the variations in the thickness, viscosity, and dielectric permittivity of the films. A host of interesting patterns such as arrays of (i) holes or columns or droplets or a combination of these embedded inside the columns, (ii) columns encapsulated by a 'cage' of columns, (iii) core-shell columns, and (iv) holes embedded inside unperturbed layer are obtained by tuning the charge concentrations at the interfaces. Although the patterns shown here are rather randomly distributed, a large area ordering can easily be expected when the electrodes are pre-decorated with physicochemical patterns. Importantly, a wide range of interesting patterns such as an ordered array of open/closed pores, cavities, and channels can be obtained from these embedded/encapsulated structures when one of the layers is selectively removed. The self-organized encapsulated and embedded patterns obtained in this work are difficult to obtain employing the conventional lithographic techniques or from the electric field induced instabilities of a single layer.

6.1.3 Electro-capillary instabilities of thin liquid crystal films: The electric field induced instabilities of thin liquid crystal films have been explored through linear stability analysis. The Ericksen-Leslie governing equations for the flow field of the liquid crystals together with the full descriptions of the Maxwell stresses for the anisotropic electric field are perturbed to obtain that the time and the length scales of the electric field induced free surface deformation of a liquid crystal film. The major conclusions are,

(i) Smaller length and time scales of instabilities are observed as compared to the similar isotropic cases when the film has a positive dielectric anisotropy. In contrast, larger length

and time scales of instabilities are observed when the film has a negative dielectric anisotropy.

(ii) The planer-planer or the homeotropic-homeotropic conditions at the boundaries ruled out the influences arising from the destabilizing Ericksen stress at the interface. In comparison, a planer-homeotropic or homeotropic-planer combination at the NI and NS interfaces showed the importance of destabilizing Ericksen stress especially when the film thickness is smaller. In such situations, the stresses due to electric field tend to dominate the destabilizing field when the films are relatively thicker.

(iii) Leslie coefficients are found to influence the kinetics of the instabilities. The influence is more pronounced when planer-homeotropic or homeotropic-planer combination is enforced at the NI and NS interfaces. In comparison, the bulk elastic constant for splay and bend is found to alter both time and length scales when planer-homeotropic or homeotropic-planer combination is enforced at the NI and NS interfaces.

(iv) The general analysis could asymptotically reproduce the analytical results obtained for the long-wave analysis of the EHD instabilities of the nematic and isotropic films.

6.1.4. Self-organized nanopatterns from the unstable ultrathin confined bilayers: A combined continuum and MD analyses unveils the pathways to nano-patterns from a dewetting ultrathin confined bilayer resting on homogeneous and topographically patterned surfaces. The important outcomes of the study are,

(i) The confined bilayers are classified into different cases based on the dewetting behaviors of the films between a pair bounding high- to low-energy surfaces. Both the continuum and MD approaches show that only the benzene layer (case I) or both the layers (case II) can be unstable under varied conditions. In particular, the MD simulations

predict that for case II, the films can dewet the confining surfaces either periodically or simultaneously, under varied conditions. This is in contrast to the predictions from the approximate continuum approach, which always show a simultaneous dewetting of the layers.

(ii) The continuum and MD simulations show striking resemblance in predicting the short-time length and time scales of the instabilities. Further, the shape of the holes, spacing between the holes, and hole-growth phenomena match very closely for both the continuum and MD simulations. However, the results of the later stages of the evolution differ significantly, which can be attributed to the approximations associated with the continuum approach.

(iii) The instabilities of a confined bilayer can be exploited to develop technologically important nanoscale patterns. In this direction, the important factors are the thinness of the liquid layers and the weak interfacial tension at the liquid-liquid interface. A host of interesting patterns such as arrays of holes, columns, droplets, stripes, and channels can be fabricated on the solid surfaces tuning the surface energies of the building blocks and thicknesses of the films. A large area ordering can be imposed on the patterned structures by decorating periodic topographical and chemical patterns on the substrates. Importantly, the dewetting confined bilayers are capable of developing encapsulated and embedded sub-micron patterns, which are otherwise difficult to fabricate employing conventional lithographic techniques or from the self-organized instabilities of a single layer.

In summary, the thesis showcases a comprehensive theoretical study on the electric field and intermolecular force induced instabilities of thin single or bilayer of films having isotropic and anisotropic physical properties. The major outcomes of the research can motivate many novel future experiments and computations related to the self-organized

instabilities and subsequent patterning, which can find important applications in the domain of nanoscience and nanotechnology.

6.2 FUTURE SCOPE OF RESEARCH

The thesis can be extended in many different ways. Some of the interesting configurations remains to be explored are,

(i) Chapter 2 showed an additional reduction of length and time scale when the elastic-viscous confined bilayer with weak conducting elastic layer is exposed beyond a critical electric field strength. In this regard, the nonlinear evolution of the configuration alongside the experimental work to obtain patterns in sub-micron scale is an open problem.

(ii) In most of the thin film experiments high molecular weight polymers are used, which in general slips on the bounding surface while evolving. The influence of slippage on length and time scale and the final morphology of electric field induced instability of dielectric or leaky bilayers are some open problems from both theoretical and experimental point of view.

(iii) The long-wave nonlinear equation for the free surface of the electric field induced deformation of a thin nematic liquid crystal film has been derived in the present work. The equation can be solved numerically in 2-D and 3-D to obtain the interfacial patterns and then compared and contrasted with the experiments.

(iv) The instability and dynamics of the bilayers composed of isotropic and anisotropic materials is another exciting area of research, which has not been explored in detail from both computational as well as experimental fronts.

(v) Experiments with thin films of thickness less than 5 nm is another area needs attention. The major issue here might be to coat the films on the surfaces. Employing techniques

such as the layer by layer coating through Langmuir-Blodgett (LB) trough and then studying the dynamics of the instabilities can be another interesting area to touch upon.

(vi) A number of the theoretical results obtained in the thesis are yet to be established through experiments, which hold the key to the successful applications of the concepts developed. Thus, in the recent future, a more intensive comparison with experiments is needed to put these works in perspective.

APPENDIX

The variables A_i, B_i, C_i, and D_i, in the dimensionless equations of motions Eqs. (3.2) and (3.3) are,

$$A_1 = \left(\hat{\alpha}_1 \sin^4\theta + \hat{\alpha}_4 + \left(\hat{\alpha}_5 + \hat{\alpha}_6\right)\sin^2\theta\right), \tag{A1}$$

$$A_2 = 0.25\sin 2\theta\left(2\hat{\alpha}_1 \sin^2\theta - \hat{\alpha}_2 - \hat{\alpha}_3 + \hat{\alpha}_5 + \hat{\alpha}_6\right), \tag{A2}$$

$$A_3 = 0.25\sin 2\theta\left(2\hat{\alpha}_1 \sin^2\theta + \hat{\alpha}_2 + \hat{\alpha}_3 + \hat{\alpha}_5 + \hat{\alpha}_6\right), \tag{A3}$$

$$A_4 = 0.25\hat{\alpha}_1 \sin^2 2\theta, \tag{A4}$$

$$B_1 = 0.5\sin 2\theta\left(\hat{\alpha}_1 \sin^2\theta + \hat{\alpha}_5\right), \tag{A5}$$

$$B_2 = 0.5\left(0.5\hat{\alpha}_1 \sin^2 2\theta + \left(\hat{\alpha}_5 - \hat{\alpha}_2\right)\cos^2\theta + \left(\hat{\alpha}_3 + \hat{\alpha}_6\right)\sin^2\theta + \hat{\alpha}_4\right), \tag{A6}$$

$$B_3 = 0.5\left(0.5\hat{\alpha}_1 \sin^2 2\theta + \left(\hat{\alpha}_2 + \hat{\alpha}_5\right)\cos^2\theta + \left(\hat{\alpha}_6 - \hat{\alpha}_3\right)\sin^2\theta + \hat{\alpha}_4\right), \tag{A7}$$

$$B_4 = 0.5\sin 2\theta\left(\hat{\alpha}_1 \cos^2\theta + \hat{\alpha}_6\right), \tag{A8}$$

$$C_1 = 0.5\sin 2\theta\left(\hat{\alpha}_1 \sin^2\theta + \hat{\alpha}_6\right), \tag{A9}$$

$$C_2 = 0.5\left(0.5\hat{\alpha}_1 \sin^2 2\theta + \left(\hat{\alpha}_2 + \hat{\alpha}_5\right)\sin^2\theta + \left(\hat{\alpha}_6 - \hat{\alpha}_3\right)\cos^2\theta + \hat{\alpha}_4\right), \tag{A10}$$

$$C_3 = 0.5\left(0.5\hat{\alpha}_1 \sin^2 2\theta + \left(\hat{\alpha}_5 - \hat{\alpha}_2\right)\sin^2\theta + \left(\hat{\alpha}_6 + \hat{\alpha}_3\right)\cos^2\theta + \hat{\alpha}_4\right), \tag{A11}$$

$$C_4 = 0.5\sin 2\theta\left(\hat{\alpha}_1 \cos^2\theta + \hat{\alpha}_5\right), \tag{A12}$$

$$D_1 = 0.5\hat{\alpha}_1 \sin^2 2\theta, \tag{A13}$$

$$D_2 = 0.25\sin 2\theta\left(2\hat{\alpha}_1 \cos^2\theta + \hat{\alpha}_2 + \hat{\alpha}_3 + \hat{\alpha}_5 + \hat{\alpha}_6\right), \tag{A14}$$

$$D_3 = 0.25\sin 2\theta\left(2\hat{\alpha}_1 \cos^2\theta - \hat{\alpha}_2 - \hat{\alpha}_3 + \hat{\alpha}_5 + \hat{\alpha}_6\right), \tag{A15}$$

$$D_4 = \left(\hat{\alpha}_1 \cos^4\theta + \hat{\alpha}_4 + \left(\hat{\alpha}_5 + \hat{\alpha}_6\right)\cos^2\theta\right). \tag{A16}$$

In the above expressions the dimensionless variables, $\hat{\alpha}_i = 2\alpha_i / \alpha_4$.

The expressions for the variables L_i^X, L_i^Z, and L_i in the linearized Eqs. (4.4.8) – (4.4.11) are provided as follows,

$$L_1^X = \bar{B}_2, \tag{A17}$$

$$L_2^X = \mathbf{i}K\delta_1\left(\bar{A}_2 + \bar{B}_1 - \bar{B}_4\right) + \bar{B}_{2,Z}, \tag{A18}$$

$$L_3^X = -K^2\delta_1^2\left(\bar{A}_1 - \bar{A}_4 - \bar{B}_3\right) + \mathbf{i}K\delta_1\left(\bar{B}_1 - \bar{B}_4\right)_{,Z}, \tag{A19}$$

$$L_4^X = \mathbf{i}K^3\delta_1^3\bar{A}_3 + \delta_1^2K^2\bar{B}_{3,Z}, \tag{A20}$$

$$L_5^X = -K^2E_r^{-1}\bar{\theta}_{,Z}, \tag{A21}$$

$$L_1^Z = \delta_1\bar{D}_2, \tag{A22}$$

$$L_2^Z = \mathbf{i}K\delta_1^2\left(\bar{C}_2 + \bar{D}_1 - \bar{D}_4\right) + \delta_1\bar{D}_{2,Z}, \tag{A23}$$

$$L_3^Z = -K^2\delta_1^3\left(\bar{C}_1 - \bar{C}_4 - \bar{D}_3\right) + \mathbf{i}K\delta_1^2\left(\bar{D}_1 - \bar{D}_4\right)_{,Z}, \tag{A24}$$

$$L_4^Z = K^2\delta_1^4\bar{C}_3 - \mathbf{i}K\delta_1^3\bar{D}_{3,Z}, \tag{A25}$$

$$L_5^Z = 2\mathbf{i}KE_r^{-1}\bar{\theta}_{,Z}, \tag{A26}$$

$$L_6^Z = \mathbf{i}KE_r^{-1}\bar{\theta}_{,ZZ}, \tag{A27}$$

$$L_7^Z = -\mathbf{i}K^3\delta_1^2E_r^{-1}\bar{\theta}_{,Z} - 2\mathbf{i}K\varepsilon_a\cos 2\bar{\theta}\,\bar{\theta}_{,Z}\bar{\Psi}_{,Z}{}^2, \tag{A28}$$

$$L_8^Z = -2\mathbf{i}K\varepsilon_a\sin 2\bar{\theta}\,\bar{\theta}_{,Z}\bar{\Psi}_{,Z}, \tag{A29}$$

$$L_9^Z = -2K^2\delta_1\varepsilon_a\cos 2\bar{\theta}\,\bar{\theta}_{,Z}\bar{\Psi}_{,Z}, \tag{A30}$$

$$L_1 = \bar{B}_2, \tag{A31}$$

$$L_2 = \mathbf{i}K\delta\left(\bar{A}_2 + \bar{B}_1 - \bar{B}_4 - \bar{D}_2\right) + 2\bar{B}_{2,Z}, \tag{A32}$$

$$L_3 = -K^2\delta_1^2\left(\bar{A}_1 - \bar{A}_4 - \bar{B}_3 - \bar{C}_2 - \bar{D}_1 + \bar{D}_4\right) + \mathbf{i}K\delta_1\left(\bar{A}_2 + 2\left(\bar{B}_1 - \bar{B}_4\right) - \bar{D}_2\right)_{,Z} + \bar{B}_{2,ZZ}, \tag{A33}$$

$$L_4 = \mathbf{i}K^3\delta_1^3\left(\bar{A}_3 + \bar{C}_1 - \bar{C}_4 - \bar{D}_3\right) - K^2\delta_1^2\left(\bar{A}_1 - \bar{A}_4 - 2\bar{B}_3 - \bar{D}_1 + \bar{D}_4\right)_{,Z} + \mathbf{i}K\delta_1\left(\bar{B}_1 - \bar{B}_4\right)_{,ZZ}, \tag{A34}$$

$$L_5 = K^4\delta_1^4\bar{C}_3 + \mathbf{i}K^3\delta_1^3\left(\bar{A}_3 - \bar{D}_3\right)_{,Z} + K^2\delta_1^2\bar{B}_{3,ZZ}, \tag{A35}$$

$$L_6 = K^2E_r^{-1}\bar{\theta}_{,Z}, \tag{A36}$$

$$L_7 = -K^4\delta_1^2E_r^{-1}\bar{\theta}_{,Z} - 2K^2\varepsilon_a\cos 2\bar{\theta}\,\bar{\theta}_{,Z}\bar{\Psi}_{,Z}{}^2, \tag{A37}$$

$$L_8 = -2K^2\varepsilon_a\sin 2\bar{\theta}\,\bar{\theta}_{,Z}\bar{\Psi}_{,Z}, \tag{A38}$$

$$L_9 = 2\mathbf{i}K^3\delta_1\,\varepsilon_a\cos 2\bar{\theta}\,\bar{\theta}_{,Z}\bar{\Psi}_{,Z}. \tag{A39}$$

The expressions for the variables S_i^N, and S_i^T in the linearized Eqs. (4.4.14) – (4.4.15) are provided as follows,

$$S_1^N = CaK^4 - \mathbf{i}K^3\delta_1\varepsilon_a\sin 2\bar{\theta}\,\bar{\Psi}_{,Z}{}^2, \tag{A40}$$

$$S_2^N = -\bar{B}_2, \tag{A41}$$

$$S_3^N = -\mathbf{i}K\delta_1\left(\bar{A}_2 + \bar{B}_1 - \bar{B}_4 - \bar{D}_2\right) - \bar{B}_{2,Z}, \tag{A42}$$

$$S_4^N = K^2\delta_1^2\left(\bar{A}_1 - \bar{A}_4 - \bar{B}_3 - \bar{D}_1 + \bar{D}_4\right) - \mathbf{i}K\delta_1\left(\bar{B}_1 - \bar{B}_4\right)_{,Z}, \tag{A43}$$

$$S_5^N = -\mathbf{i}K^3\delta_1^3\left(\bar{A}_3 - \bar{D}_3\right)\tilde{W} - K^2\delta_1^2\bar{B}_{3,Z}, \tag{A44}$$

$$S_6^N = -K^2E_r^{-1}\bar{\theta}_{,Z}, \tag{A45}$$

$$S_7^N = -K^2\varepsilon_a\sin 2\bar{\theta}\,\bar{\Psi}_{,Z}{}^2, \tag{A46}$$

$$S_8^N = 2K^2\left(\varepsilon_\perp + \varepsilon_a\cos^2\bar{\theta}\right)\bar{\Psi}_{,Z}, \tag{A47}$$

$$S_9^N = -2K^2\bar{\Psi}_{a,Z}, \tag{A48}$$

$$S_1^T = K^2 E_r^{-1}\bar{\theta}_{,Z}{}^2, \tag{A49}$$

$$S_2^T = -\bar{B}_2, \tag{A50}$$

$$S_3^T = -\mathbf{i}K\delta_1\left(\bar{B}_1 - \bar{B}_4\right), \tag{A51}$$

$$S_4^T = -K^2\delta_1^2\bar{B}_3, \tag{A52}$$

$$S_5^T = K^2 E_r^{-1}\bar{\theta}_{,Z}. \tag{A53}$$

The expressions for the variables I_i in the linearized Eq. (4.16) are provided as follows,

$$I_1 = 0.5\delta_1\left(\Lambda_1 - \Lambda_2\cos 2\bar{\theta}\right), \tag{A54}$$

$$I_2 = -\mathbf{i}K\delta_1^2\Lambda_2\sin 2\bar{\theta}, \tag{A55}$$

$$I_3 = -0.5K^2\delta_1^3\left(\Lambda_1 + \Lambda_2\cos 2\bar{\theta}\right), \tag{A56}$$

$$I_4 = -\mathbf{i}KE_r^{-1}, \tag{A57}$$

$$I_5 = \mathbf{i}K^3\delta_1^2 E_r^{-1} + 2\mathbf{i}K\Delta\varepsilon\cos 2\bar{\theta}\,\bar{\Psi}_{,Z}^2, \tag{A58}$$

$$I_6 = 2\mathbf{i}K\varepsilon_a\sin 2\bar{\theta}\,\bar{\Psi}_{,Z}, \tag{A59}$$

$$I_7 = 2K^2\delta_1\varepsilon_a\cos 2\bar{\theta}\,\bar{\Psi}_{,Z}. \tag{A60}$$

The expressions for the variables J_i in the linearized Eq. (4.19) are provided as follows,

$$J_1 = \varepsilon_a\sin 2\bar{\theta}\,\bar{\Psi}_{,Z}, \tag{A61}$$

$$J_2 = \varepsilon_a\sin 2\bar{\theta}\,\bar{\Psi}_{,ZZ} + 2\varepsilon_a\cos 2\bar{\theta}\,\bar{\theta}_{,Z}\bar{\Psi}_{,Z} - \mathbf{i}K\varepsilon_a\delta_1\cos 2\bar{\theta}\,\bar{\Psi}_{,Z}, \tag{A62}$$

$$J_3 = -\left(\varepsilon_\perp + \varepsilon_a\cos^2\bar{\theta}\right), \tag{A63}$$

$$J_4 = \varepsilon_a\sin 2\bar{\theta}\,\bar{\theta}_{,Z} - \mathbf{i}K\delta\varepsilon_a\sin 2\bar{\theta}. \tag{A64}$$

$$J_5 = K^2\delta_1^2\left(\varepsilon_\perp + \Delta\varepsilon \sin^2\bar{\theta}\right) - \mathbf{i}K\delta_1\,\varepsilon_a \cos 2\bar{\theta}\,\bar{\theta}_{,Z}\,, \tag{A65}$$

$$J_6 = -K^2\,\delta_1^2\,. \tag{A66}$$

The expressions for the variables S_i^E in the linearized Eq. (4.4.22) are provided as follows,

$$S_1^E = 0.5\delta_1 \mathbf{i}K\varepsilon_a \sin 2\bar{\theta}\bar{\Psi}_{,Z}\,, \tag{A67}$$

$$S_2^E = \varepsilon_a \sin 2\bar{\theta}\,\bar{\Psi}_{,Z}\,, \tag{A68}$$

$$S_3^E = -\left(\varepsilon_\perp + \varepsilon_a \cos^2\bar{\theta}\right), \tag{A69}$$

$$S_4^E = -0.5\delta\mathbf{i}K\varepsilon_a \sin 2\bar{\theta}\,. \tag{A70}$$